



HAL
open science

Bioinspired semi-hemic iron(III) complex for chemical and photochemical oxygen atom transfer reactions

Nhat Tam Vo

► **To cite this version:**

Nhat Tam Vo. Bioinspired semi-hemic iron(III) complex for chemical and photochemical oxygen atom transfer reactions. Catalysis. Université Paris Saclay (COMUE), 2019. English. NNT : 2019SACLS319 . tel-02615260

HAL Id: tel-02615260

<https://theses.hal.science/tel-02615260>

Submitted on 22 May 2020

HAL is a multi-disciplinary open access archive for the deposit and dissemination of scientific research documents, whether they are published or not. The documents may come from teaching and research institutions in France or abroad, or from public or private research centers.

L'archive ouverte pluridisciplinaire **HAL**, est destinée au dépôt et à la diffusion de documents scientifiques de niveau recherche, publiés ou non, émanant des établissements d'enseignement et de recherche français ou étrangers, des laboratoires publics ou privés.

Bioinspired semi-hemic iron(III) complex for chemical and photochemical oxygen atom transfer reactions

Thèse de doctorat de l'Université Paris-Saclay
Préparée à Université Paris Sud

École doctorale n°571 Sciences chimiques : Molécules, Matériaux,
Instrumentation et Biosystèmes (2MIB)

Spécialité de doctorat : Chimie

Thèse présentée et soutenue à Orsay, le 27 septembre 2019, par

M. Nhat Tam VO

Composition du Jury :

Bruno Andrioletti Professeur, Université de Lyon 1 (ICBMS)	Président du jury
Elodie Anxolabéhère-Mallart Directrice de Recherche, CNRS, Université Paris Diderot (LEM)	Rapportrice
Bernard Boitrel Directeur de Recherche, CNRS, Université de Rennes 1 (ISCR)	Rapporteur
Kim Larmier Chercheur, IFP Energies Nouvelles, Solaize	Examineur
Benedikt Lassalle Ingénieur de recherche, Synchrotron SOLEIL	Examineur
Ally Aukauloo Professeur, Université Paris Sud (LCI)	Directeur de thèse
Marie Sircoglou Maître de Conférence, Université Paris Sud (LCI)	Co-Encadrante de thèse

Université Paris-Saclay

Espace Technologique / Immeuble Discovery

Route de l'Orme aux Merisiers RD 128 / 91190 Saint-Aubin, France



Remerciements

Ce travail de thèse a été réalisé dans le cadre du projet Multiplet, financé par l'Agence Nationale de la Recherche (ANR) et effectué à l'Institut de Chimie Moléculaire et des Matériaux d'Orsay (ICMMO) dans le Laboratoire de Chimie Inorganique (LCI).

Je souhaite tout d'abord remercier Pr. David AitKen, Directeur de l'ICMMO, et Pr. Talal Malah, Responsable du LCI, de m'avoir accueilli et permis d'y travailler pendant les trois années de ma thèse.

Je tiens à remercier les membres de mon jury de thèse : les directeurs de recherche Elodie Anxolabéhère-Mallart (CNRS - Université Paris Diderot), Bernard Boitrel (CNRS - Université Rennes 1) ainsi que Pr. Bruno Andrioletti (Université de Lyon 1) et les ingénieurs de recherche Kim Larmier (IFP Energies nouvelles), Benedikt Lassalle (Synchrotron SOLEIL). Merci d'avoir accepté de juger ce travail avec bienveillance et pour vos interventions très pertinentes qui m'ont permis de mettre en valeur l'étendue de mes travaux.

Je voudrais adresser particulièrement mes remerciements à mes encadrants Pr. Ally Aukauloo et Dr. Marie Sircoglou pour la connaissance, la disponibilité et la confiance qu'ils m'ont prodiguées m'ont permis d'enrichir autant sur le plan professionnel que personnel. Merci à Ally pour tes leçons très importantes dans la vie de la recherche : « le foot de science » et « le hasard ne sourit qu'aux esprits bien préparés ». Marie, merci de ta présence et ton soutien à tout moment difficile pendant les trois ans de ma thèse, notamment pendant la rédaction de ce manuscrit et les répétitions de ma soutenance.

Je tiens à associer mes remerciements également à deux personnes super-gentilles dans notre groupe de recherche « Photosynthèse Artificielle », Zakaria Halime et Winfried Leibl, pour ses qualités humaines et scientifiques. Son expérience m'a permis de m'épanouir dans mon apprentissage de la recherche.

Le travail présenté dans ce manuscrit est en collaboration entre plusieurs équipes de recherche, j'aimerais donc remercier Thierry Tron, Yasmina Mekmouche, Jalila Simaan à l'Institut des Sciences Moléculaires de Marseille ; Annamaria Quaranta à CEA Saclay ;

Geneviève Blonde à CEA Grenoble ; Frédéric Banse au LCI pour l'intérêt et la disponibilité qu'ils m'ont accordés.

Je remercie également toutes les personnes avec qui j'ai été amené à travailler à l'ICMMO : Christian Herrero pour les analyses RPE, Régis Guillot pour les analyses de cristallographie aux rayons X sur monocristal, Jean-Pierre Baltaze de l'équipe RMN et Tanya Inceoglu pour les analyses de masse. J'aimerais aussi remercier Wadih Ghattas et Yoan Chevalier qui m'ont fait connaître comment utiliser la chromatographie en phase liquide et gazeuse. Je souhaite remercier également Thomas Pino et Minh Huong Ha Thi à l'Institut des Sciences Moléculaires d'Orsay pour la participation à l'analyse du Raman de mes échantillons.

Je voudrais ensuite remercier mon stagiaire Jafeng pour sa motivation et ses travaux. Je souhaite remercier l'ensemble permanences du LCI : Jean-Noël, Eric, Katell, Yu, Anne, Amélie, Sandra, Marie-Laure, Anne, Giulia, Vincent, Cyril et ainsi les postdocs, les doctorants, les stagiaires croisés : Khaled, Phillip, Clémence, Stéphanie, Linh, Antoine, Yiting, Feng, Benjamin, Jully, Maria, Julien, Tania, Rajaa, Jeremy, Gabriel. Je continuerai ma liste avec les futurs docteurs : Asma, Axel, Adama, Amanda, Niccolo, Laura. Bon courage pour la suite les jeunes. Merci à tous pour vos soutiens ou juste simplement pour les bons moments partagés.

Enfin, je souhaite remercier chaleureusement ma famille que j'aime très fort. Un grand merci à mes parents qui me font toujours confiance tout au long de mes études dans un pays lointain. Je termine le remerciement adressé à la femme de ma vie Nhàn qui a toujours été là pour moi. Nhàn, Merci pour ton soutien sans limites.

Abstract

Oxidation of hydrocarbons such as olefin epoxidation and alkane hydroxylation plays an important role in the industry for the production of drugs, materials and energy. These chemical transformations are major challenges because of the inert carbon - carbon bonds (BDE = 80-90 kcal / mol) and carbon - hydrogen bonds (BDE = 80-90 kcal / mol). In current processes, they are often carried out in a harsh and dangerous condition associated to high temperature and high pressure in the presence of a costly catalyst such as metallic salts of palladium and ruthenium which massively produces the polluting wastes. It is therefore urgent to seek a new safe and clean process. Nature shows us that these difficult reactions can be catalyzed in the mild condition thanks to metalloenzymes. These enzymatic catalysts containing an active site based on transition metal are capable of activating the sources of green oxygen atom such as dioxygen and water in order to generate a highly oxidized active metal-oxo species. This active species is an intermediate capable of effectuating the oxidation of hydrocarbons. In the context of sustainable development, cheaper and green methods for these transformations have been developed using a bio-inspired catalyst based on transition metal, in particular iron thanks to its high abundance, and support by sophisticated ligands.

In this manuscript we report the synthesis and characterization of an iron(III) complex supported by a non-innocent hemi-porphyrinic ligand, constructed with a dipyrin fragment and two pyridine functions. This ligand was designed to combine the structural features of well-known catalyst platforms such as porphyrins and poly-nitrogen ligands. The iron(III) complexes have been prepared and characterized by a variety of spectroscopic techniques, with a focus on their electrochemical behavior and their potential use as catalysts in the activation of green oxygen source such as dioxygen and water for hydrocarbon oxidation. We found that these complexes can catalyze the oxidation of a fair variety of substrates using oxidant agent such as iodosylbenzene. Intriguingly, our gathered results point to a reactivity pattern that stems from a low-oxidation state iron species. Electron Paramagnetic Resonance and Mössbauer analyses support a high spin iron(III) reactive species. Furthermore, data from mass spectrometry and Infra-red spectroscopy supported by DFT calculations helped us to propose the chemical formulation of this chemically generated intermediate where the ligand has been reversibly oxidized.

Additionally, these complexes were used as catalysts in a photocatalytic system in aqueous media under aerobic condition using a photosensitizer a reversible electron acceptor to preclude the “evil necessity” of a sacrificial electron donor. ^{18}O isotopic labelling experiments were undertaken to confirm that the origin of oxygen atom in oxidized product is dioxygen while Laser Flash Photolysis experiments allow us to understand the reactional mechanism. Our study provides a new paradigm to perform photoinduced oxygen atom transfer reactions with solely light as energy input and dioxygen as oxygen atom source in aqueous solution.

Résumé

L'oxydation des hydrocarbures telles que l'époxydation de l'oléfine et l'hydroxylation de l'alcane joue un rôle important dans le monde de l'industrie pour la production de médicament, de matériaux et d'énergie. Ces transformations chimiques sont des grands défis à cause de liaison inerte de carbone - carbone (BDE = 80-90 kcal/mol) et de carbone - hydrogene (BDE = 80-90 kcal/mol). Dans les procédés actuels, elles sont souvent réalisées dans une condition dure et dangereuse liée à haute température et haute pression en présence d'un catalyseur coûteux comme des sels métalliques de palladium et ruthénium qui produit massivement le déchet polluant. Il est alors urgent de chercher un nouveau procédé doux et propre. La nature nous montre que ces difficiles réactions peuvent être catalysées à la condition douce grâce aux métalloenzymes. Ces catalyseurs enzymatiques contenant un site actif à base de métal de transition sont capables d'activer les sources d'atome d'oxygène verte comme le dioxygène et l'eau afin de générer une espèce active métal-oxo en de haut degré d'oxydation. Cette espèce est un intermédiaire capable d'effectuer l'oxydation des hydrocarbures. Au contexte de développement durable, des méthodes moins onéreux, moins dangereux et non polluant pour ces transformations sont en cours développées en utilisant d'un catalyseur bio-inspirée à base de métal de transition, en particulière de fer grâce à son abondant, et de support des ligands sophistiqués.

Dans ce manuscrit, nous rapportons la synthèse et la caractérisation d'un complexe de fer (III) supporté par un ligand hémi-porphyrinique non innocent, construit avec un fragment dipyrriane et deux fonctions pyridines. Ce ligand est désigné de se combiner les caractères structuraux des familles de ligand connus tels que le porphyrine et le ligand poly-azoté neutre utilisés très courant pour le catalyseur bio-inspiré d'oxydation d'hydrocarbure. Les complexes de fer (III) ont été préparés et caractérisés par plusieurs techniques spectroscopiques, en mettant l'accent sur leur comportement électrochimique et leur utilisation potentielle en tant que catalyseurs pouvant achever des sources d'oxygène vertes telles que le dioxygène et l'eau en vue d'oxyder des hydrocarbures. Nous avons constaté que ces complexes peuvent catalyser l'oxydation d'une grande variété de substrats en utilisant un agent oxydant tel que l'iodosylbenzène. Curieusement, nos résultats rassemblés suggèrent un schéma de réactivité qui découle d'une espèce de fer de bas degré d'oxydation. Les analyses de résonance paramagnétique électronique et de Mössbauer confirment l'existence d'une espèce réactive de fer (III) haut

spin. De plus, les données de spectrométrie de masse et de spectroscopie infrarouge appuyées par des calculs de DFT nous ont aidés à proposer la formulation chimique de cet intermédiaire généré chimiquement où le ligand a été oxydé de manière réversible.

En outre, ces complexes ont été utilisés comme catalyseurs dans un système photocatalytique pour oxyder styrène à diol et benzaldéhyde à la condition aérobie dans milieux aqueux en utilisant un photosensibilisateur et un accepteur d'électron réversible permettant d'éviter le recours néfaste à un donneur d'électron sacrificiel. L'étude avec l'oxygène marqué O^{18} nous permet de confirmer la source d'atome d'oxygène comme provenant le dioxygène tandis que l'expérience de Laser Flash Photolysis clarifie le mécanisme réactionnel et le transfert d'électron entre le photosensibilisateur, l'accepteur d'électron réversible, le dioxygène et le catalyseur dans l'activation du dioxygène. La présence de notre complexe de fer est indispensable d'activer dioxygène et de former une espèce active à base de fer qui est responsable d'oxyder le styrène. Notre étude fournit un nouveau paradigme pour effectuer des réactions photoinduites de transfert d'atome d'oxygène utilisant la lumière comme la source d'énergie et le dioxygène comme la source d'atome d'oxygène en solution aqueuse.

TABLE OF CONTENTS

LIST OF ABBREVIATIONS	13
CHAPTER I : INTRODUCTION.....	15
I.1 Enzymatic systems performing oxidation in nature.....	18
I.1.1 Cytochrome P-450	18
I.1.2 α - ketoglutarate dependent hydroxylases.....	20
I.1.3 Soluble methane monooxygenases	21
I.2 Synthetic iron catalysts for oxidation reaction	23
I.2.1 Ligand design	23
I.2.1.1 Biomimetic approach	23
I.2.1.2 Bioinspired approach.....	27
I.2.2 Activation strategies and mechanistic insights	31
I.2.2.1 Using chemical oxygen donor agents	31
I.2.2.2 Using dioxygen as oxygen atom source.....	33
I.2.2.3 Using water as oxygen atom source.....	38
I.2.3 Quest for the active iron species	41
I.3 Context and objective	46
CHAPTER II : SYNTHESIS, CHARACTERIZATION AND ELECTROCHEMICAL STUDY OF IRON DPY COMPLEXES.....	49
II.1 Presentation of the DPy Ligand	51
II.2 Synthesis and characterization of the iron complex Fe^{III}DPyCl₂.....	53
II.2.1 Synthesis of Fe ^{III} DPyCl ₂ complex	53
II.2.2 Characterization of Fe ^{III} DPyCl ₂ complex	54
II.2.2.1 UV-visible Absorption spectroscopy.....	54
II.2.2.1 Structure determination in the solid state by X-Ray diffraction crystallography.....	55
II.2.2.2 ESI-HRMS measurement.....	57
II.2.2.3 EPR spectroscopy.....	58
II.2.2.4 Mössbauer spectroscopy.....	60
II.2.3 Electrochemical study	61

II.2.3.1	Electroactivity in reduction	62
II.2.3.2	Electroactivity upon oxidation.....	67
II.3	Synthesis and characterization of diiron complex (Fe^{III}DPy)₂O(OTf)₂.....	74
II.3.1	Synthesis & characterization.....	74
II.3.1.1	Absorption spectroscopy.....	75
II.3.1.2	Structure determination in the solid state by X-Ray diffraction crystallographie	75
II.3.1.3	ESI-HRMS measurement.....	77
II.3.1.4	Electrochemical study	78
II.3.2	Dimer to monomer interconversion	80
II.3.2.1	Dimer to monomer conversion upon ligand exchange	81
II.3.2.2	Reversible μ -oxo-bridge cleavage by acid and base addition.....	83
II.4	Conclusion	86

CHAPTER III : REVERSIBLE ELECTRON RELAY TO EXCLUDE SACRIFICIAL ELECTRON DONOR IN PHOTOCATALYTIC OXYGEN ATOM TRANSFER REACTION WITH O₂ IN WATER..... 89

III.1	State of the art	91
III.2	Photocatalytic systems using iron(III) DPy catalyst	95
III.2.1	Reactivity.....	95
III.2.2	Study of the photocatalytic mechanism	97
III.2.2.1	Study of subsystem [Ru ^{II}] + O ₂	97
III.2.2.2	Study of subsystem [Ru ^{II}] + [MV ²⁺] + O ₂	100
III.2.2.3	Role of catalyst	104
III.2.2.4	Proposed mechanism for the full system	107
III.2.2.5	Influence of the pH media	111
III.2.2.6	Limiting step in the proposed mechanism	112
III.2.3	Isotope labelling study	113
III.2.4	Quantum yield	115
III.3	Photosystem using iron(II) catalyst.....	117
III.3.1	Reactivity.....	117
III.3.2	Photo-generation of the active iron species.	118
III.3.3	Characterization of the active iron species	124
III.3.4	Proposed mechanism for the photocatalytic system using [L ₅ Fe ^{II}] ²⁺ catalyst	125
III.4	Conclusion & Perspective	128

CHAPTER IV : CHEMICAL GENERATION OF AN ACTIVE LOW OXIDATION STATE IRON SPECIES BASED ON NON-INNOCENT DPY LIGAND.....	131
IV.1 Low oxidation state iron(III) species related to iron-oxo species	133
IV.1.1 Fe-O-X adducts.....	133
IV.1.1.1 Fe-O-Cl.....	133
IV.1.1.2 Fe-O-OC(O)-R.....	135
IV.1.1.3 Fe-OiAr.....	136
IV.1.2 Ligand-oxygenated iron(III) species	139
IV.2 Chemical oxidation of Fe^{III}DPyCl₂ and evidence of a reversible ligand oxidation	143
IV.2.1 Oxidation with m-CPBA.....	143
IV.2.2 Oxidation with NaClO.....	149
IV.2.2.1 Characterization of the generated iron species	149
IV.2.2.1.1 UV-visible spectroscopy.....	149
IV.2.2.1.2 EPR spectroscopy.....	151
IV.2.2.1.3 High resolution mass spectroscopy (HRMS)	152
IV.2.2.1.4 Infra-red spectroscopy.....	156
IV.2.2.2 Studying the reactivity of the N-oxide iron(III) species	158
IV.2.2.3 Catalytic tests	160
IV.2.3 Oxidation with iodosylarenes	162
IV.2.3.1 Characterization of generated iron species.....	162
IV.2.3.1.1 UV-visible spectroscopy.....	162
IV.2.3.1.2 EPR spectroscopy.....	163
IV.2.3.1.3 Mössbauer spectroscopy.....	164
IV.2.3.1.4 HRMS	166
IV.2.3.1.5 Infrared spectroscopy	169
IV.2.3.1.5 Resonance Raman spectroscopy	172
IV.2.3.1.6 DFT Calculation	174
IV.2.3.2 Preparation of oxidized DPyN _{py} O ligand.....	176
IV.2.3.3 Catalytic activity study.....	177
IV.3 Conclusion	180
 CHAPTER V : CONCLUSION & PERSPECTIVES	 181
 EXPERIMENTAL SECTION	 187

Instrumentation	189
Experimental procedures	192
Synthesis.....	192
Crystal structure determination.....	195
Catalytic procedure	202
Quantification of oxidized products by HPGC	202
Photocatalytic procedure	205
REFERENCES.....	211

LIST OF ABBREVIATIONS

ε	Extinction molar coefficient
λ	Wavelength
$^{\circ}$	Degree
$^{\circ}\text{C}$	Celsius Degree
A	Ampère
Å	Angstrom
Abs	Absorbance
BDE	Bond Dissociation Energy
bpy	2,2'-bipyridine
C-C	Bonding between two carbons
C-H	Bonding between carbon and oxygen
C-O	Bonding between carbon and oxygen
CAN	Ceric Ammonium Nitrate
cm	Centimeter
CV	Cyclic Voltammetry
Cyt	Cytochrome
DFT	Density Functional Model
DPV	Differential pulse voltammetry
DPy	3,5-dipyridine-8- pentafluorophenyldipyrrin
EA	Electron Acceptor
E_a	Anodic potential
E_c	Cathodic potential
$E_{1/2}$	Half-wave potential
ED	Electron Donor
E_p	Peak potential
EPR	Electron Paramagnetic Resonance
ESI-MS	Electrospray Ionisation Mass Spectrometry
EtOH	Ethanol
G	Gauss
g	gram
h	Hour
HAA	Hydrogen atom abstraction
HPGC	High Performance Gaz Chromatography

HPLC	High Performance Liquid Chromatography
GHz	Gigahertz
K	Kelvin
k_i	Rate constant
L	Liter
LED	Light-emitting diode
LMCT	Ligand to Metal Charge Transfer
M	Mole per liter
m-	Milli
μ	Micro
m-CPBA	Meta-chloroperbenzoic acid
MeCN	Acetonitrile
min	Minute
MLCT	Metal to Ligand Charge Transfer
MMO	Methane Mono Oxygenase
n-	Nano
NaClO	Sodium hypochlorite
NMR	Nuclear Magnetic Resonance
OAT	Oxygen Atom Transfer
OTf	Triflate (Trifluoromethanesulfonate)
PCET	Proton–Coupled Electron transfer
Ph	Phenyl
pH	Hydrogen Potential
PhIO	Iodosylbenzene
s	Second
SCE	Saturated Calomel Electrode (Reference)
T	Temperature
TAML	Tetra–amido macrocyclic ligand
TBAPF ₆	Tetrabutylammonium hexafluorophosphate
TOF	Turnover frequency
TON	Turnover number
Uv-vis	Ultraviolet Visible Spectroscopy
V	Volt
X-Ray	X–ray diffraction Spectroscopy

Chapter I : Introduction

Oxidation reactions involving oxygen atom transfer reaction (thioether oxidation, olefin epoxidation) and hydrogen atom abstraction reaction (alkane hydroxylation) are a challenging transformation in chemical synthesis. Those reactions are often associated to expensive metals (palladium, iridium, rhodium),^{1,2} toxic reagents (chromates, permanganates, organic peroxides) and generate a high amount of undesired products (moderate selectivity). Consequently, the development of “green” and cheaper metal-based systems inspired from natural enzymes capable to catalyze such reactions is becoming more and more important in research. A wide variety of biological systems can make this challenging reaction under mild condition by activating dioxygen and forming highly oxidized active metal–oxo species that react with substrates. Especially, most natural systems contain a green abundant transition metal such as iron. The study of such systems is desirable to understand the details of biological oxygen activation and transfer, and to imitate their reactivity. It is also important to develop more sustainable methodologies.

In this chapter, we will present natural systems based on iron metal and most significant synthetic systems. Common methods used to generate and characterize high active iron-oxo will be also reported.

I.1 Enzymatic systems performing oxidation in nature

Catalytic enzymes performing oxidation reaction can be classified in two groups: hemic proteins for example cytochrome P450, and non-hemic proteins such as soluble methane-monooxygenases and α - ketoglutarate dependent hydroxylases (Table I-1).

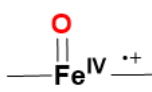
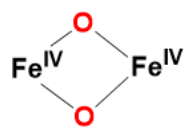
Catalytic metalloenzyme	Active species	Catalytic reaction
Cytochrome P450		$\text{C}-\text{C} / \text{C}-\text{H} + \text{O}_2 \xrightarrow[2e^-]{2\text{H}^+} \text{C}-\overset{\text{O}}{\text{C}} / \text{C}-\text{OH} + \text{H}_2\text{O}$
α - ketoglutarate dependent hydroxylases.		$\text{RH} + \text{R}'\text{COCO}(\text{OH}) + \text{O}_2 \longrightarrow \text{ROH} + \text{R}'\text{COOH} + \text{CO}_2$
Soluble methane-monooxygenases		$\text{CH}_4 + \text{O}_2 \xrightarrow[2e^-]{2\text{H}^+} \text{CH}_3\text{OH} + \text{H}_2\text{O}$

Table I-1 : Selection of metalloenzymes involved in biological oxidation

I.1.1 Cytochrome P-450

Cytochrome P-450s are an important family of heme (iron porphyrin) metalloenzymes that are present in all forms of life such as bacteria, plants, yeasts, insects and mammals. These heme enzymes are mono-oxygenases capable to activate dioxygen and to incorporate oxygen atom in a wide variety of substrates under mild condition.³ Cytochrome P-450s catalyze aromatic and aliphatic hydroxylation, olefin epoxidation and sulfoxide formation using dioxygen as oxygen source and nicotinamide adenine dinucleotide phosphate (NADPH) as reducing agent. Especially, the reactions catalyzed by cytochrome P-450s intrigue chemists because of their high selectivity. In fact, these enzymes are active enough to hydroxylate inert substrates such as cyclohexane without damaging the relatively fragile enzyme organic superstructure.

The active site of cytochrome P-450s (Figure I-1) is an iron protoporphyrin IX center coordinated to a cysteine thiolate in axial position. The last coordination site is occupied by a labile molecule such as solvent allowing the system to activate dioxygen at this position.

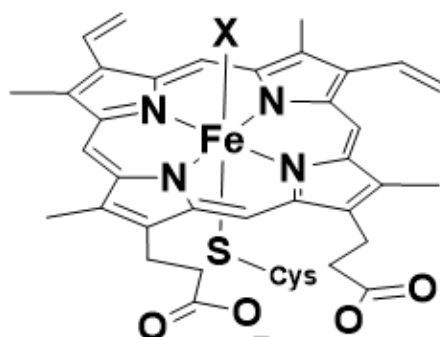
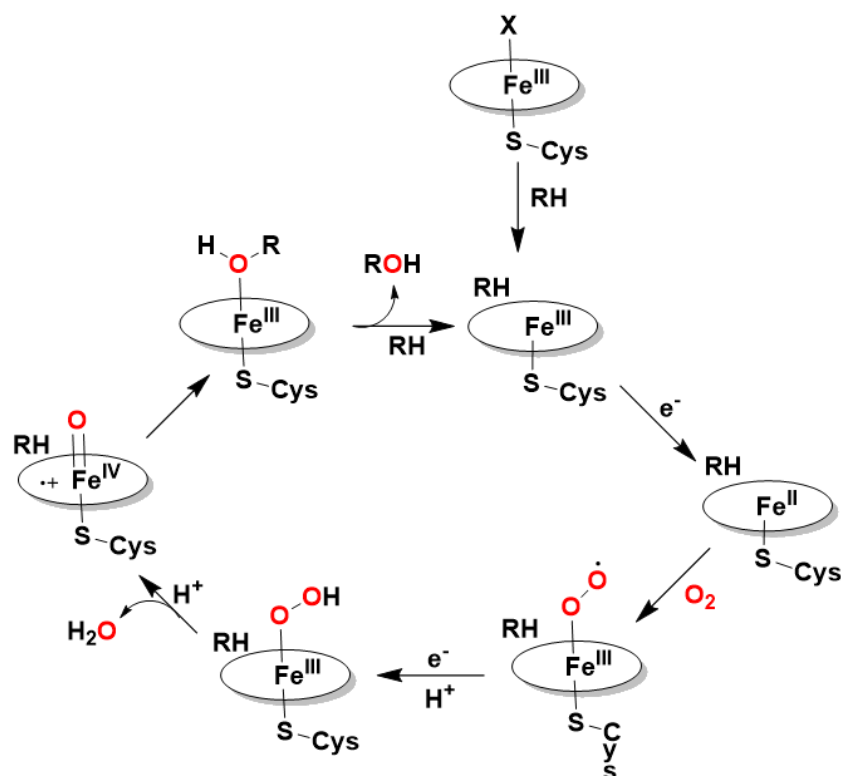


Figure I-1 : Iron protoporphyrin IX active site of cytochromes P-450s, X: labile ligand.

The principal features of the mechanism of cytochrome P-450s are illustrated in Scheme I-1.⁴ The catalytic reaction starts with the binding of substrate to the enzyme leading to the release of the labile ligand, sometimes accompanied with a spin state change of the iron center. Molecular oxygen coordinates to the reduced Fe(II) form of cytochrome P-450s obtained by the first reduction of iron(III) form by reducing agent NADPH. Then, a second one-electron reduction and protonation give the Fe(III)-hydroperoxo species. The high valent active iron(IV)-oxo porphyrin cation radical species called Compound I is obtained by protonation and heterolytic cleavage of the O-O bond. Compound I is identified and characterized in a number of heme enzymes by a variety of spectroscopic analyses such as Mössbauer spectroscopy ($\delta = 0.05\text{-}0.14$ mm/s; $\Delta E_Q = 0.90\text{-}1.33$ mm/s characterizing a low spin ($S = 1$) Fe^{IV} species), EPR spectroscopy ($g \approx 2$ assigned to radical species) and Raman spectroscopy ($750\text{-}790$ cm^{-1} attributed to Fe-O vibration).⁵ Finally, oxygen atom transfer is realized from this iron-oxo species to the bound substrate to form the oxygenated product.

Some calculations suggested that the radical may reside to a greater or lesser extent on the thiolate ligand⁶ or other protein residues. In any case, the iron(IV)-oxo porphyrin radical intermediate is believed to be the species responsible for the reactivity of cytochrome P-450s according to a variety of spectroscopic studies.⁷



Scheme I-1 : Catalytic cycle for oxygen activation and transfer by cytochrome P-450s.

I.1.2 α - ketoglutarate dependent hydroxylases

Iron(II) α - ketoglutarate dependent hydroxylases are mononuclear non-heme metalloenzymes capable to catalyze an amazing diversity of hydroxylation reactions using the α - ketoglutarate co-substrate. These enzymes possess an active site that contains one iron center bound to three water molecules and three amino acid side chains (Figure I-2).

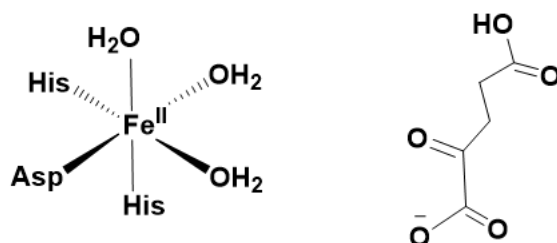


Figure I-2 : Active site of α - ketoglutarate dependent hydroxylases (left) and α - ketoglutarate (right)

The activation of dioxygen through the oxidative decarboxylation of α - ketoglutarate leads to

the generation of the highly active iron(IV)-oxo species that hydroxylates various types of substrates such as methylated nucleotides and lipids. The consensus mechanism of the catalytic reaction shown on Figure I-3 is proposed based on spectroscopic studies of enzymes such as Clavaminate Synthase 2 and Taurine dioxygenase.⁹⁻¹¹ The first conclusive spectroscopic evidence for a non-heme high spin ($S = 2$) iron(IV)-oxo was reported by Bollinger and Krebs in 2003 and detected in the Taurine dioxygenase using Mössbauer spectroscopy.¹² The high oxidation state of iron center was identified by an isomer shift of $\delta = 0.31$ mm/s and a quadrupolar splitting of $\Delta E_Q = 0.88$ mm/s. Additionally, resonance Raman studies revealed a Fe-O vibration at 821 cm^{-1} that shifted to 787 cm^{-1} upon labelling with ^{18}O .¹³

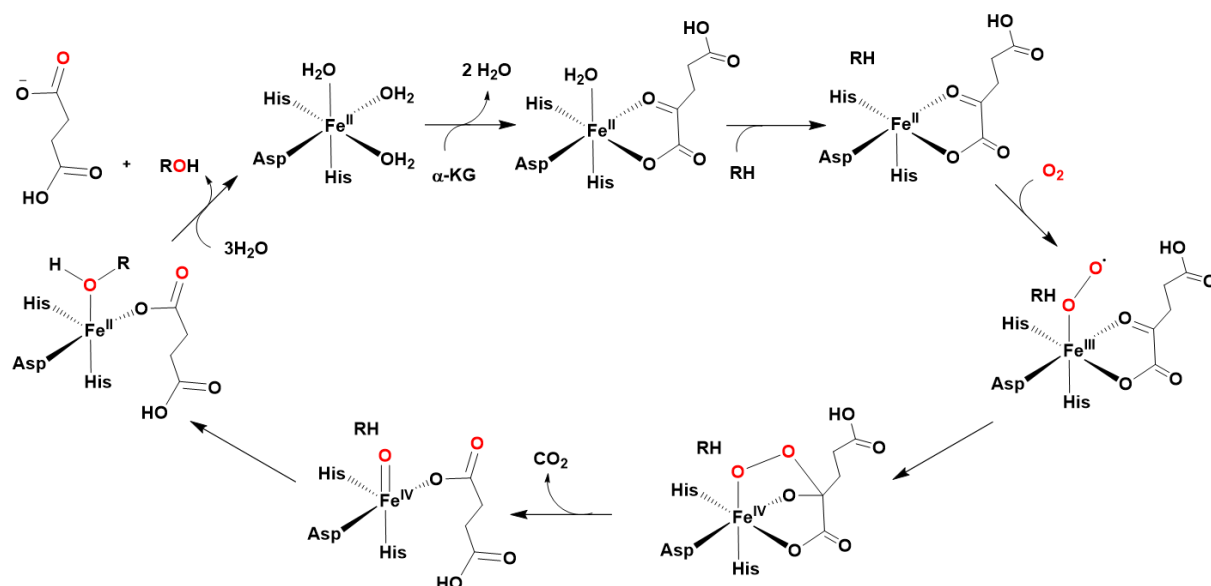


Figure I-3 : Proposed mechanism of catalytic cycle for α - ketoglutarate dependent hydroxylases.

I.1.3 Soluble methane monooxygenases

Soluble methane monooxygenases (sMMO)¹⁴ found in some bacteria, have some analogy with cytochrome P-450s and α - ketoglutarate dependent hydroxylases in their ability to hydroxylate un-activated C-H bonds of methane ($BDE_{C-H} = 105\text{kcal/mol}$) using dioxygen as oxygen source and NADP as reducing agent. sMMO contain dinuclear iron units in the active site, each one in a non-heme environment (Figure I-4).

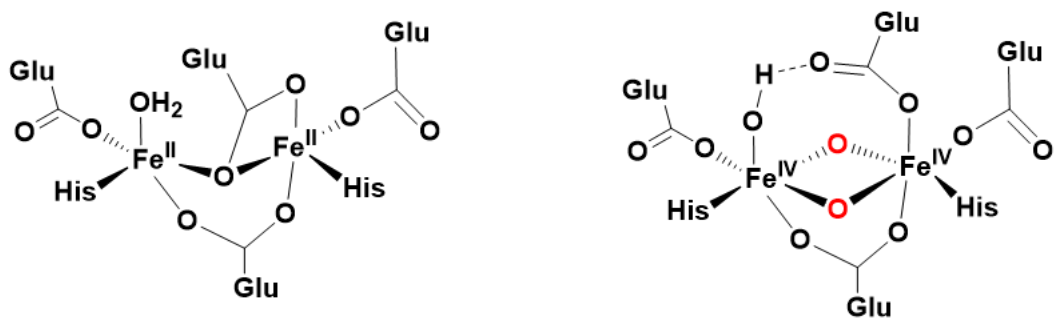


Figure I-4 : Dinuclear iron active site in sMMO : (left) reduced form, (right) oxidized form.

Unlike un mononuclear metalloenzymes, the active form of sMMO is a bis μ -oxo diiron(IV) species with a diamond core structure, which was trapped and spectroscopically characterized in catalytic reaction.¹⁵⁻¹⁷ The main features of the catalytic mechanism are shown on Figure I-5. Dioxygen is activated by both metals to give a peroxo bridge between two iron(III) centers. Then, homolytic O-O bond cleavage leads to the generation of an active bis- μ -oxo diiron(IV) that can react with methane.

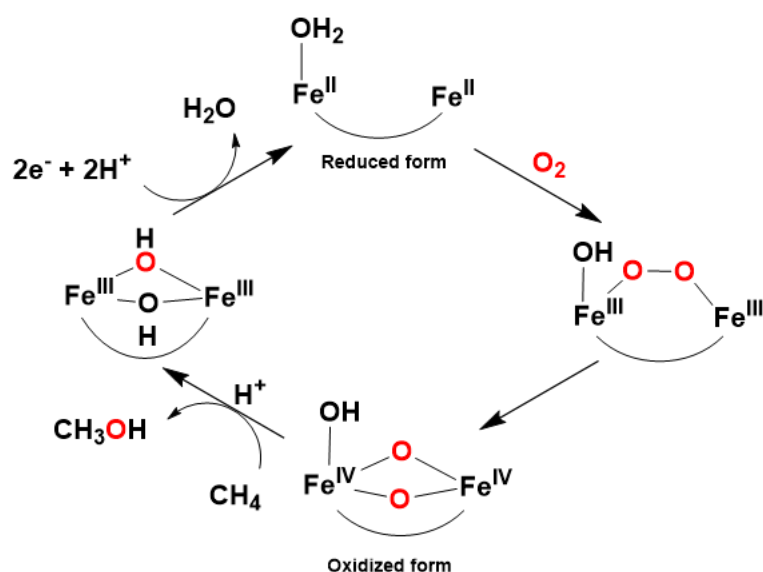


Figure I-5 : Proposed mechanism for methanol conversion using sMMO.

In brief, nature's enzymes can oxygenate hydrocarbon under normal pressure and temperature conditions by activating dioxygen molecule to generate high valent active iron oxo species with the help of the reducing agent (NADP) or co-factor such as α - ketoglutarate. Although natural metalloenzymes are highly efficient and selective in oxidation of hydrocarbons, the isolation of these enzymes from plants is extremely difficult. Indeed, only in recent years

have genes of cytochrome P-450s been isolated.¹⁸ Consequently, the search for robust model systems mimicking these metalloenzymes may help to overcome the intrinsic difficulties of working with enzymes. Besides, the studies of synthetic systems as models for metalloenzymes have afforded important insights into the nature of enzymatic processes themselves.

I.2 Synthetic iron catalysts for oxidation reaction

Once the metal center chosen, chemists have to select two important parameters that will impact on the reactivity of the catalyst. The ligand permits to modulate the electronic properties and steric environment of the metal center and thereby the activation strategies.

Below we will discuss these two factors.

I.2.1 Ligand design

In recent years, the development of efficient synthetic systems for oxidation reaction that mimic the catalytic metalloenzymes has attracted much attention. It is known that the main power of catalytic metalloenzymes comes from the protein environment, in particular from the structural ligand coordinating the metal center. Synthetic ligands can be also classified in two groups: biomimetic ligands and bioinspired ligands depending on their design strategy.

I.2.1.1 Biomimetic approach

A biomimetic ligand is a structural analogue exhibiting spectroscopic features close to the enzyme's factor. For example, Porphyrin, the best-know biomimetic ligand has been developed by copying the ligand core of protoporphyrin IX at the heart of Cytochrome-P450s to mimic a similar electronic density with four nitrogen coordination sites (Figure I-6). Since the first synthetic metalloporphyrin, chloro-5,10,15,20-tetraphenylporphyriniron(III) ($\text{Fe}^{\text{III}}\text{TPPCl}$), reported by Groves and co-workers in 1979 to catalyze the alkene epoxidation and alkane hydroxylation using iodobenzene as an oxygen donor,¹⁹ the use of metalloporphyrin as catalysts has received increasing attention during the past four decades.

Substitutions in meso and β position were operated on the next generations of metalloporphyrins which allowed enhanced efficiency in oxidation reactions (Figure I-6). One example of the influence of these distal substituents on their reactivity will be discussed in the next paragraph.

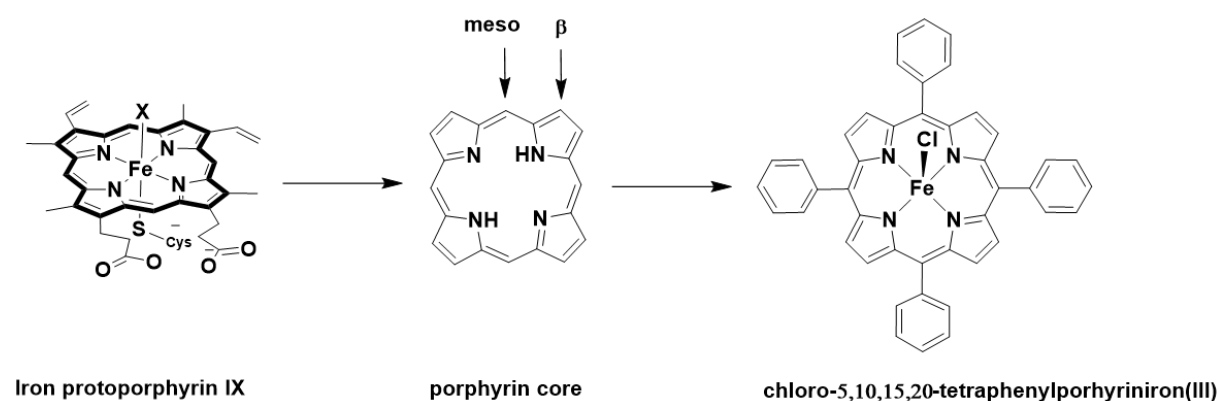


Figure I-6 : Porphyrin core used for synthetic porphyrin ligand and formula of metalloporphyrin of the first generation used in model system of Cytochrome P450s.

One of the remarkable features of cytochrome P-450s is the presence of a thiolate ligand. This function is believed to have a strong influence on the chemistry of the heme iron complex. Thus, synthetic models carrying a thiolate RS^- moiety were developed to reveal their relative effect. In order to avoid the replacement of the thiolate ligand by any other ligand present in solution, the thiolate ligand was attached at the tetraphenylporphyrin by a “ S^- -bridge” or a “ S^- -tail” (Figure I-7).^{20,21} The first iron porphyrin coordinated by an alkylthiolate anion used for catalytic oxidation was reported by Hirobe in 1990.²² His work demonstrated that the thiolate ligand induces around 100 fold increase of the rate of oxidation of 2,4,6-tri-tert-butylphenol and 1,1-diphenyl-2-picrylhydrazine compared to $Fe^{III}TPPCl$, using alkyl hydroperoxides as oxidant. Indeed, the oxidation mechanism consists of several steps: the formation of an alkyl peroxide iron porphyrin, the O-O bond cleavage leading to the formation of an active iron-oxo species and the reaction between iron-oxo and substrate. The oxidation rate was accelerated probably because the large electron donating alkyl thiolate enhances the cleavage of the O-O bond and stabilizes the high-valent iron-oxo.²³ The electron donor effect of thiolate ligand was clearly revealed by the change in the potential of Fe^{III}/Fe^{II} redox couples. An important negative shift (-200 mV) for the Fe^{III}/Fe^{II} process compared to that of the iron porphyrin without thiolate ligand ($Fe^{III}TPPCl$) was observed by cyclic voltammetry.²⁴

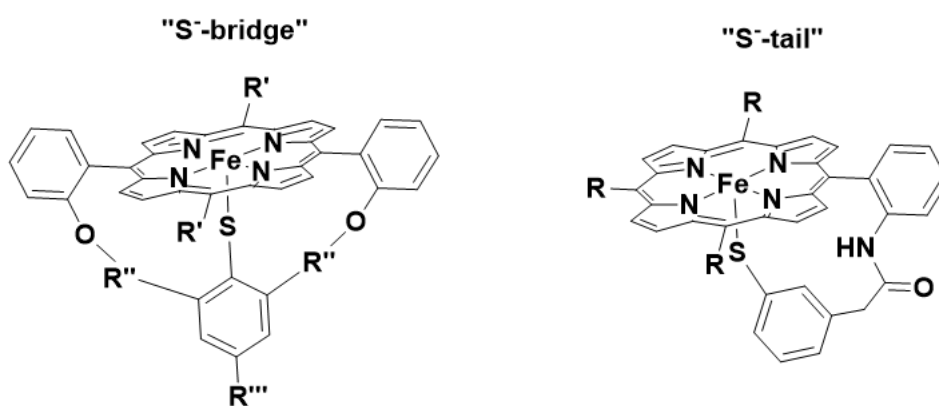


Figure I-7 : Synthetic metalloporphyrins containing a « S- bridge » ligand (left) and « S- tail » ligand (right).

Despite the promising result of Hirobe's group, development of the synthetic heme metalloporphyrins with thiolate ligand was limited by the outstanding difficulty in their synthesis because of the facile oxidation of thiolate ligand to disulfide. The presence of an electron donating thiolate ligand decreases the stability of such synthetic complex in highly oxidizing condition.²⁵ Consequently, these models were not further explored.

Alternatively, electron withdrawing groups (EWGs) were introduced in meso or β position with good improvement in reactivity of the cyclohexene oxidation as shown in Table I-2 and Figure I-8.²⁶ In fact, EWGs increase the electrophilic property of Fe=O moiety that enhances the reactivity of catalysts in reaction with the electron rich nucleophiles such as alkenes. On the other hand, EWGs can make the catalysts more robust against oxidation.

Catalysts	Substrate	Product	TON
Fe ^{III} (TPP)Cl			32
Fe ^{III} (TDCPP)Cl	cyclooctene	Cyclooctene epoxyde	72
Fe ^{III} (β -F ₈ TPP)Cl			81

Table I-2 : Cyclohexene epoxidation by PhIO catalyzed by iron porphyrin complex. Cyclohexene/PhIO/catalyst = 100/100/1, solvent: DCM. TON based on PhIO in 2h.

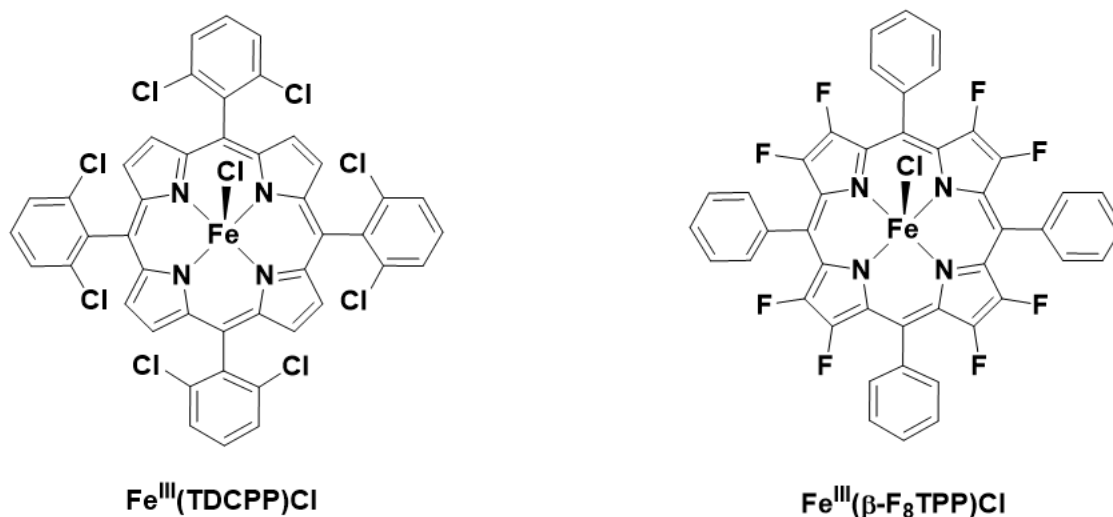


Figure I-8 : Structure of iron(III) porphyrins with electron withdrawing group in meso and β position.

Over the last two decades, a number of biomimetic non-heme models of metalloenzymes have been reported in order to generate an iron-oxo species able to catalyze the oxidation reaction.²⁷ In 2003, Que reported a synthetic model for α - ketoglutarate dependent hydroxylases based on a tridentate ligand Tp^{Ph_2} (hydrotris(3,5-diphenylpyrazol-1-yl)borate) (Figure I-9) to mimic the three amino acid ligands, and an α - keto acid as the sacrificial electron donor to provide the two electrons needed to activate dioxygen.²⁸ This non-heme model is able to react with dioxygen to undergo an oxidative decarboxylation of α - keto acid and displays a versatile reactivity such as sulfide oxidation, alkene cis-hydroxylation and alkane hydroxylation.²⁹ But in absence of any organic substrate, the intramolecular hydroxylation of the phenyl group of Tp^{Ph_2} ligand is also observed, probably because the phenyl group is directly maintained above the iron site. Unfortunately, no intermediates could be trapped or characterized.

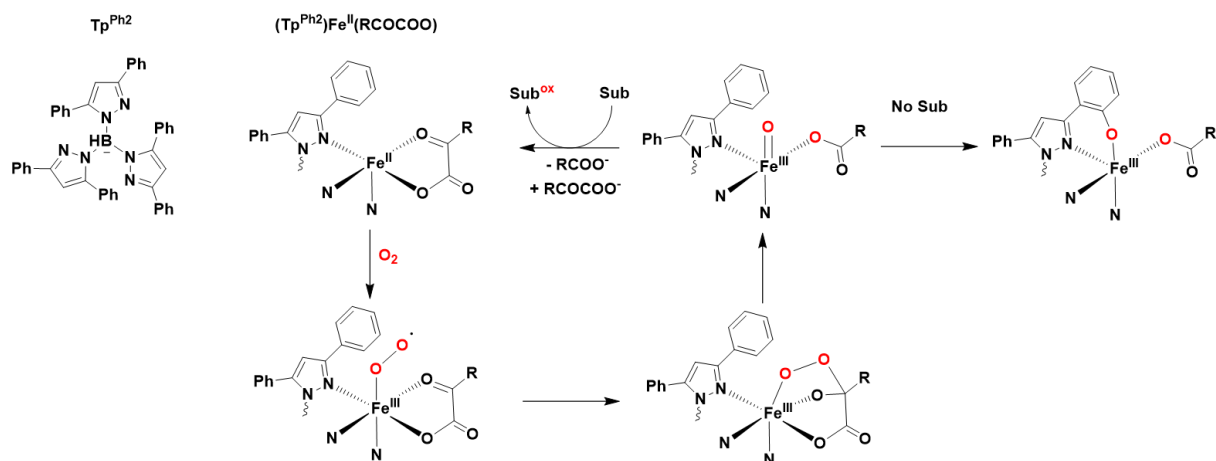


Figure I-9 : Synthetic model for α - ketoglutarate dependent iron enzymes.

In brief, by replicating structural aspects of biological system, the biomimetic approach can produce good oxidation catalysts capable of oxygenating alkene and alkane although their catalytic reactivity is rather moderate due to their short life-time in oxidation condition. In fact, reproducing partially some structural features of the enzyme without the complex protein environment necessarily changes the property of the active site. However, the study of biomimetic system is very helpful to understand how catalytic metalloenzymes work in nature and to find out the important aspects contributing to their amazing catalytic reactivity. Thus, the result obtained with biomimetic model provides useful insights for the development of bioinspired oxidation catalysts.

1.2.1.2 Bioinspired approach

In contrast with biomimetic approach, bioinspired strategy aims at discovering and capturing the essential idea that underpins a biological system. High-valent iron-oxo identified to be key oxidized intermediate in the mechanism of iron enzymes for a variety of oxidation reaction, is stabilized by a sophisticated proteinic structure. In chemistry, researchers make use of various coordinating functions to stabilize highly oxidized species. Electron-rich ligand having nitrogen or oxygen binding sites are the most abundantly developed .

One of the best know bioinspired system is based on tetradentate Salen ligand containing two phenol and two iminic bindings groups, leaving two coordination sites on the metal ion

available for coordination of exogenous ligand and activation of terminal oxidant. These ligands are dianionic like porphyrins allowing to stabilize high valent metal centers. Furthermore, their structure and electronic density can be easily modulated by functionalizing the substituents due to their simple preparation. Thus, reactivity and durability of Salen-based catalyst are more and more improved at each new generation. Due to similar planar and tetradentate nature of Salen, a large number of metal centers such as ruthenium, iron, manganese have been used to study the Salen-based catalysts.^{30,31} The most attractive example of Salen-based catalyst is Jacobsen's, a complex with manganese as metal center associated with a chiral Salen ligand able to catalyze asymmetric epoxidation of alkenes. This catalyst is used in industrial synthesis of Indinavir, an HIV protease inhibitor (Figure I-10),³² which shows that oxidation reaction catalyzed by bioinspired systems have a really great potential.

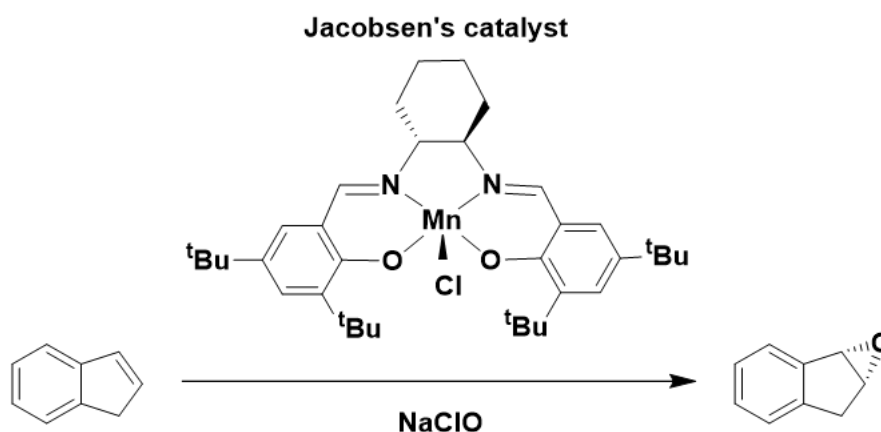


Figure I-10 : Jacobsen's catalyst used for asymmetric epoxidation in Industrial synthesis of Indinavir.

Inspired by Salen ligand and the macrocyclic tetraamine ligand reported by Margerum,³³ another well-known ligand family based on tetraamido macrocyclic molecule has been developed and continuously improved against oxidative degradation and hydrolysis for over forty years by the group of Collins and then Gupta.^{34,35} TAML (TetraAmido Macrocyclic Ligands) are tetraanionic ligands providing a strong electron-donor ligand field to stabilize highly oxidized metal center. TAMLs are quite robust thanks to their geometric cyclic rigidity that prevents an intramolecular isomerization process that could lead to their degradation.³⁶ Until now, seven generations of TAMLs have been developed.³⁷ Especially the fifth generation is able to support the generation of an active iron(V)-oxo species $[(b\text{-TAML})\text{Fe}^{\text{V}}=\text{O}]^{1-}$ at room temperature (Figure I-11). Moreover, this iron(V)-oxo has shown a

powerful reactivity in the activation of the inert C-H bond of cyclohexane with high selectivity, yet while maintaining a remarkable operational stability.³⁸

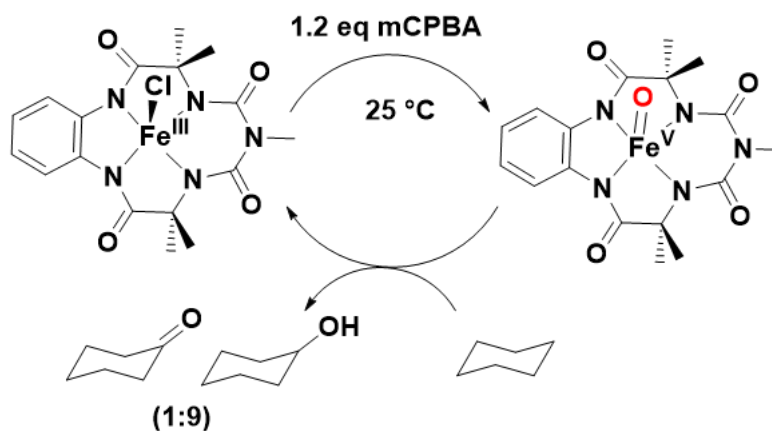


Figure I-11 : Operationally stable, highly active iron(V)-oxo supported by b-TAML and their reactivity toward cyclohexane oxidation.

Using negatively charged ligand shown in precedent paragraph is not the only way to generate highly oxidized metal-oxo. Synthetic neutral polynitrogen ligand bioinspired by the proteinic neutral ligands such as His have also been explored. Since the end of the 1980s, a number of synthetic systems based on polynitrogen ligands have been studied to generate active metal-oxo and catalyze oxidation reactions.^{39,40} These polydentate ligands may contain π -acceptor nitrogen binding group such as pyridine, benzimidazole, imidazole and the tertiary amines providing σ -donor ligands. They are presented in Figure I-12 with their acronyms. Their flexible geometry can adapt to the preferred geometry of the metal. The absence of negative charge probably decreases the stability of the high valent metal oxo, but it may allow to generate a more active metal oxo species due to a lower electronic density environment around metal center. Indeed, in 2011, Nam reported a nonheme iron(IV)-oxo species supported by Me_3NTB ligand capable of activating the C-H bond of alkanes and transferring oxygen atom to thianisole. Especially, his work showed the first synthetic nonheme iron-oxo species that was more active than iron(IV)-oxo porphyrin π -cation radical $(\text{Por}\bullet)\text{Fe}^{\text{IV}}=\text{O}$ species (compound I). The facility in the synthesis and modulation of the poly-nitrogen ligand allowed to improve further the reactivity of iron-oxo species. In 2015, Costas reported an $\text{Fe}^{\text{V}}=\text{O}$ species based on the poly-nitrogen macrocyclic ligand PyNMe_3 that exhibited the highest reactivity in the hydroxylation of cyclohexane among all iron-oxo species reported so far.⁴¹

I.2.2 Activation strategies and mechanistic insights

I.2.2.1 *Using chemical oxygen donor agents*

Over the past decade, several synthetic high valent iron-oxo complexes with a wide range of ligands have been prepared by different methods. The general synthesis is carried out by oxidizing iron complex precursor by oxygen atom donor oxidant, such as iodosylbenzene (PhIO), sodium hypochlorite (NaClO), peracids (m-CPBA) and hydroperoxides (H₂O₂, ^tBuOOH).⁴³ Among these oxidants used to generate active iron-oxo species, the two electron oxidant like PhIO, NaClO, mCPBA oxidize directly iron(II) precursor to iron(IV)-oxo species and iron(III) precursor to iron(V)-oxo or iron(IV)-oxo ligand cation radical species. Generally, the mechanism occurs by two consecutive steps: the adduct formation followed by oxygen atom transfer triggered by heterolytic O-X bond cleavage (Figure I-14).

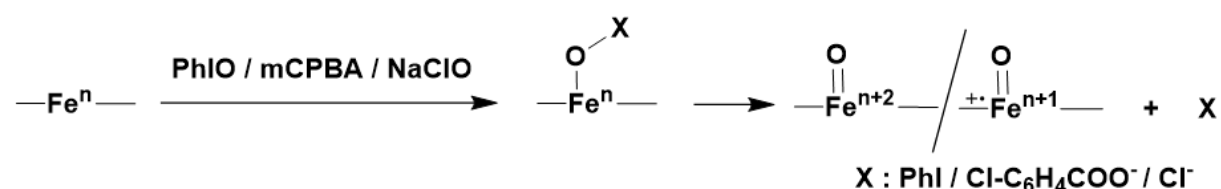


Figure I-14 : Proposed mechanism for the iron-oxo species formation using a two-electron oxidant.

For instance, a number of studies using H₂O₂ as an oxidant have been conducted to get insight into how O-O bond cleavage proceeds in nature. In presence of an excess H₂O₂ in acetonitrile, iron(II) precursor is believed to be oxidized by half an equivalent of H₂O₂ to an iron(III) complex, that rapidly reacts with another equivalent of H₂O₂ to form hydropero iron(III) species. Heterolytic O-O bond cleavage follows to generate iron(V)-oxo species (Figure I-15).^{44,45} Consequently, generating an iron(V)-oxo species from an iron(III) precursor needs only one equivalent of H₂O₂.⁴⁶

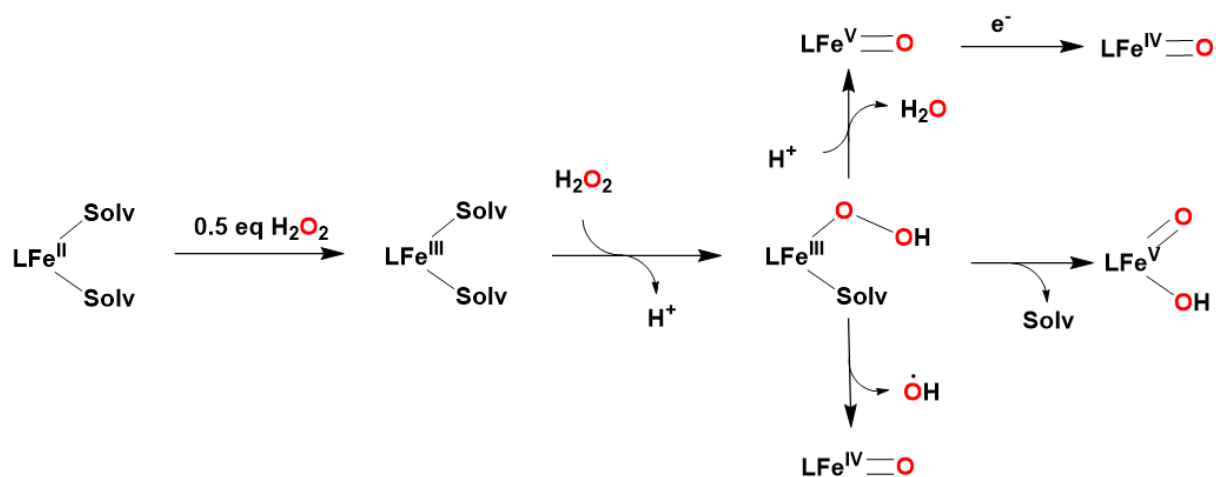


Figure I-15 : Proposed mechanism for generation of an iron(V)-oxo species from iron(II) precursor using H_2O_2

However, Que and co-workers reported in 2011 the full characterization of an $[(Fe^{IV}=O)TMC]^{2+}$ species generated by reaction of $[Fe^{II}(TMC)]^{2+}$ with an excess H_2O_2 in presence of acid and the rate of formation for $[(Fe^{IV}=O)TMC]^{2+}$ was dependent on the proton concentration.⁴⁷ Consequently, the formation of $[(Fe^{IV}=O)TMC]^{2+}$ was suggested to proceed through proton assisted heterolytic O-O bond cleavage of $Fe^{III}OOH$ intermediate generating a short-lived $[(Fe^V=O)TMC]^{3+}$ species that would ultimately be reduced by one electron. Alternatively, iron(IV)-oxo species could also be obtained by the decomposition of $Fe^{III}OOH$ by homolytic O-O bond cleavage,⁴⁸ but a DFT calculation suggested this pathway was not energetically favored.⁴⁹

On the other hand, Que reported that the stoichiometric reaction of $[Fe^{II}(TMC)]^{2+}$ / $[Fe^{II}(TMC-py)]^{2+}$ with H_2O_2 in presence of a base affords the corresponding $Fe^{IV}=O$ species in 90 % yield.⁵⁰ This high conversion was obtained from only one equivalent of H_2O_2 probably revealing the formation of iron(II) peroxo precursor followed by an heterolytic O-O bond cleavage (Figure I-16).⁵¹ The iron(II) peroxo species formation can be questioned because iron(II) precursor is also probably oxidized by one-electron by H_2O_2 to the iron(III) product.

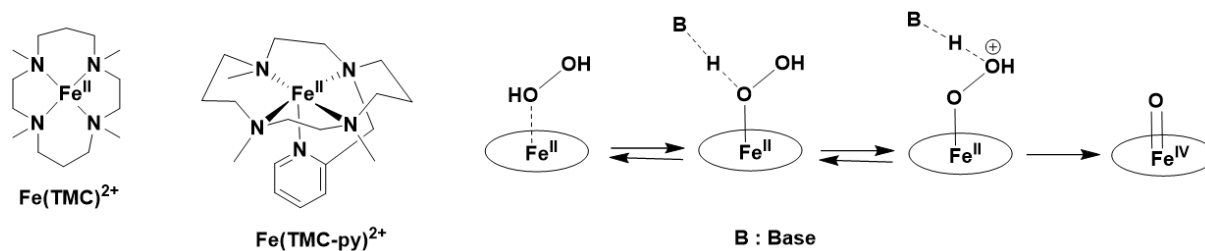


Figure I-16 : Proposed mechanism for the base-catalyzed formation of iron(IV)-oxo from iron(II) precursor and H_2O_2

Other strategies using mCPBA, NaClO and PhIO as oxidant will be discussed in detail in chapter IV.

1.2.2.2 Using dioxygen as oxygen atom source

Chemical oxidants with a controlled quantity allow to properly generate active iron species in order to characterize these short-lived iron species and study the mechanistic activation in oxidation reaction. However, using environmentally friendly oxygen source is highly desirable. Dioxygen is known to be an abundant and green oxygen source that is identified as a terminal oxidant in many natural oxidation processes catalyzed by heme and non-heme metalloenzymes. Inspired from cytochrome P-450s, synthetic iron precursor can activate dioxygen and convert into an active iron-oxo species with the help of a proton source and a reducing agent such as NADPH, BNAH, cobaltocene, BH_4^- . For instance, Banse and co-workers reported clearly this promising strategy using a well-known $[\text{Fe}^{\text{II}}(\text{TMC-py})]^{2+}$ precursor, BPh_4^- as an electron source and HClO_4 as a proton source.⁵² In presence of H^+ and BPh_4^- , dioxygen is reductively activated at iron(II) center, yielding a iron(III) superoxo species that converts into a $\text{Fe}^{\text{III}}\text{OOH}$ intermediate which ultimately decomposes into the iron(IV)-oxo species by O-O bond cleavage (Figure I-17). The O-O cleavage can be an homolytic process or an heterolytic process followed by a fast decomposition to afford iron(IV)-oxo species as previously observed with H_2O_2 in presence of acid. The $[\text{Fe}^{\text{IV}}=\text{O}(\text{TMC-py})]^{2+}$ species generated in the study was fully characterized by a variety of spectroscopic analyses, especially by X-Ray diffraction on single crystal.

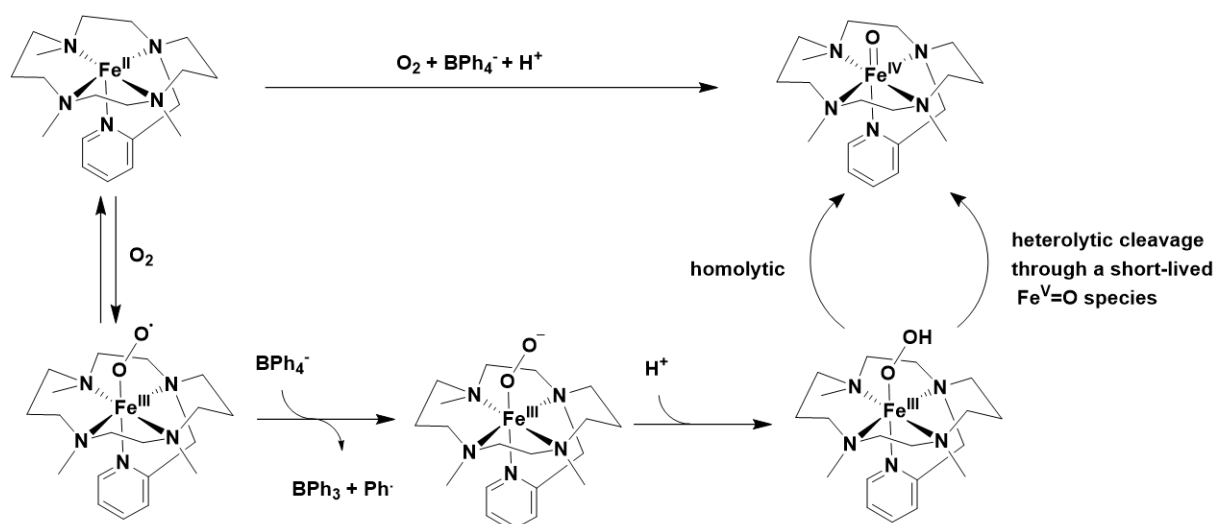


Figure I-17 : Proposed dioxygen activation mechanism using $[Fe^{II}(TMC-Py)]^{2+}$.

Murray and coll first introduced the idea of electroactivation of O_2 .⁵³ The group of Dey reported in 2013 the study of dioxygen activation by iron(III) porphyrin by electrolysis coupled to resonance Raman spectroscopy is reported.⁵⁴ Using ^{18}O isotopical labelling, these combined techniques allowed to directly identify the corresponding iron(III) peroxo and iron(IV) oxo intermediates involved in $Fe^{II}-O_2$ adduct reduction at -0.5 V vs Ag/AgCl (Figure I-17). However, their report can also be questioned. According to their study, the Fe-O bond of the $Fe^{IV}=O$ species was identified by the vibration at 780 cm^{-1} , but the Fe-O vibration of all the heme and nonheme iron-oxo species reported until then was experimentally determined in the range of $800-850\text{ cm}^{-1}$, as will be presented in next paragraph.

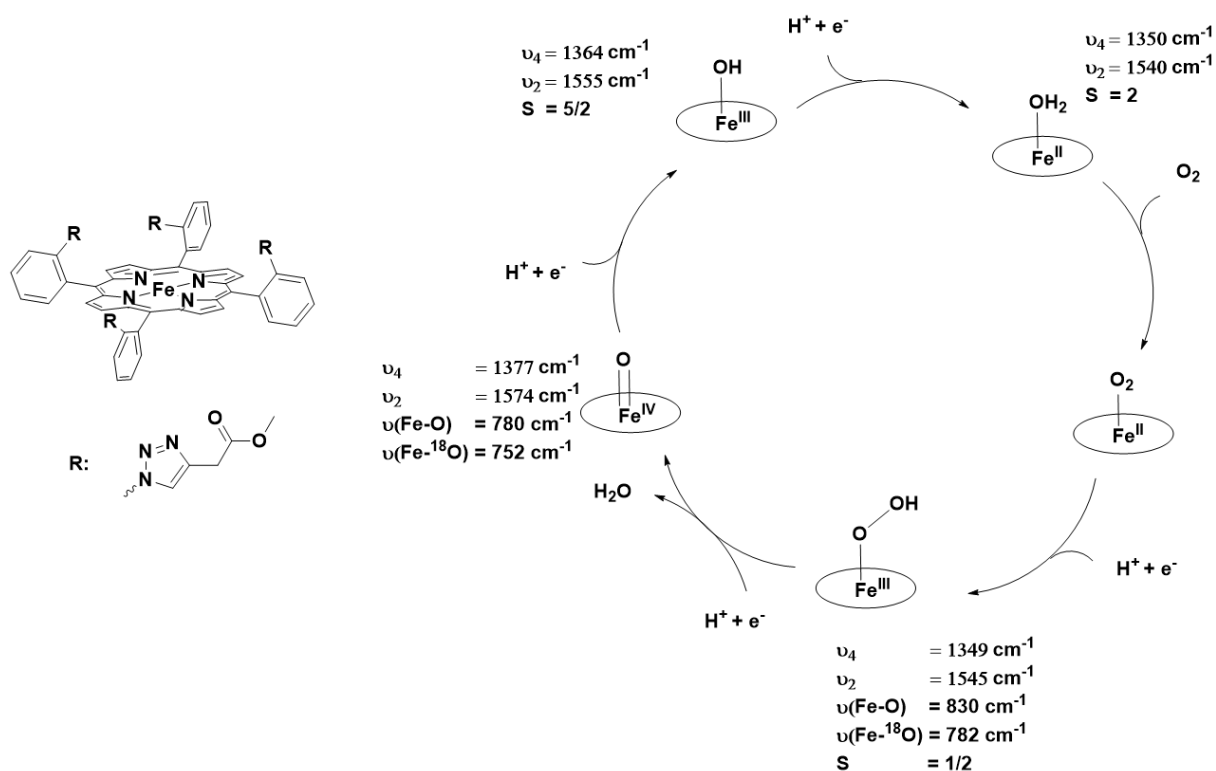


Figure I-18 : Proposed mechanism for electro-reductive dioxygen activation and the Raman bands of each detected species.

This electro-reductive activation approach was again reported in 2015 by Banse and Anxolabéhère-Mallart with a non-heme $[\text{Fe}^{\text{II}}(\text{TPEN})]^{2+}$ precursor. The corresponding intermediates $[\text{Fe}^{\text{III}}(\text{OO})(\text{TPEN})]^+$, $[\text{Fe}^{\text{III}}(\text{OOH})(\text{TPEN})]^{2+}$ and $[\text{Fe}^{\text{IV}}(\text{O})(\text{TPEN})]^{2+}$ were chemically generated in high yield and characterized electrochemically.⁵⁵ The mechanistic study of the reaction of $[\text{Fe}^{\text{II}}(\text{TPEN})]^{2+}$ with O_2 was then carried out by cyclic voltammetry. Analysis and simulation of the data obtained revealed that the iron(III) peroxo species $[\text{Fe}^{\text{III}}(\text{OO})(\text{TPEN})]^+$ is formed by reducing a rarely observed $\text{Fe}^{\text{II}}\text{-O}_2$ adduct by one electron at -0.62 V vs SCE while dioxygen was reduced to superoxide at much lower potential -0.87 V (Figure I-19). However, unlike in the previously discussed system, no O-O bond cleavage from the iron(III) peroxo species $[\text{Fe}^{\text{III}}(\text{OO})(\text{TPEN})]^+$ was detected on the time scale and condition of the electrochemical study.

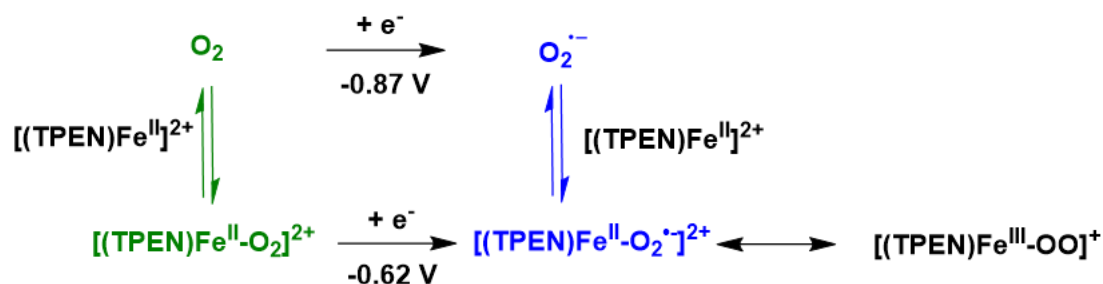


Figure I-19 : Proposed reductive activation mechanism of O_2 at $[\text{Fe}^{\text{II}}(\text{TPEN})]^{2+}$ based on modelisation of experimental CVs.

The dioxygen activation can also occur by an autooxidation reaction at a synthetic catalyst. This approach is attractive because it doesn't require electron donor. The mechanism was elucidated in 1980s. The reaction was shown to proceed through a μ -peroxo diiron(III) species, followed by an homolytic O-O bond cleavage to form an iron(IV)-oxo intermediate.⁵⁶⁻⁵⁸ The μ -peroxo diiron(III) porphyrin was trapped and shown to slowly convert to iron(IV)-oxo species at low temperature (-80 to -30 °C) by ^1H NMR and UV-visible spectroscopy. In presence of 50 eq of triphenylphosphine (PPh_3), $\text{Fe}^{\text{II}}\text{TPP}$ is thus capable of transferring oxygen atom to PPh_3 , forming $\text{O}=\text{PPh}_3$ in 27 successful turnover numbers (TON) before inactivation occurs (Figure I-20).⁵⁶ The deactivation is caused by the formation of inactive μ -oxo diiron(III) porphyrin identified in solution at the end of catalytic reaction.

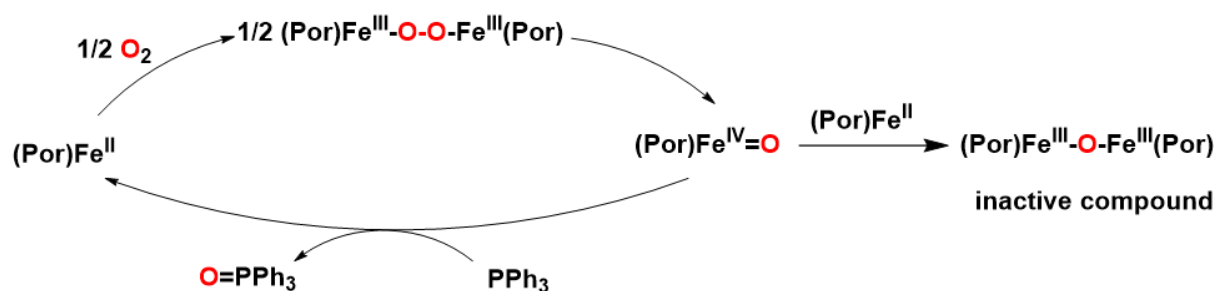


Figure I-20 : Proposed mechanism for dioxygen activation by iron porphyrin complex

However, it's interesting that the inactive μ -oxo diiron(III) porphyrin can be activated by homolytic photocleavage of the Fe-O bonds using visible light to form an iron(II) porphyrin and a reactive iron(IV)-oxo intermediate capable of oxygenating substrates. Nocera and co-workers reported a photoinduced oxidation of sulfides, olefins et alkanes using μ -oxo diiron(III) porphyrin as an active catalyst in aprotic solvent such as benzene and toluene.⁵⁹⁻⁶¹

Especially, a μ -oxo diiron(III) Pacman porphyrin was found much more reactive than the unbridged analogue probably due to the fact that dioxygen easily meets two iron centers to make μ -peroxo bond thanks to the bridged diporphyrin ligand. However, the mechanism of μ -oxo diiron(III) Pacman porphyrin formation from dioxygen and diiron(II) Pacman porphyrin is not clarified yet (Figure I-21).

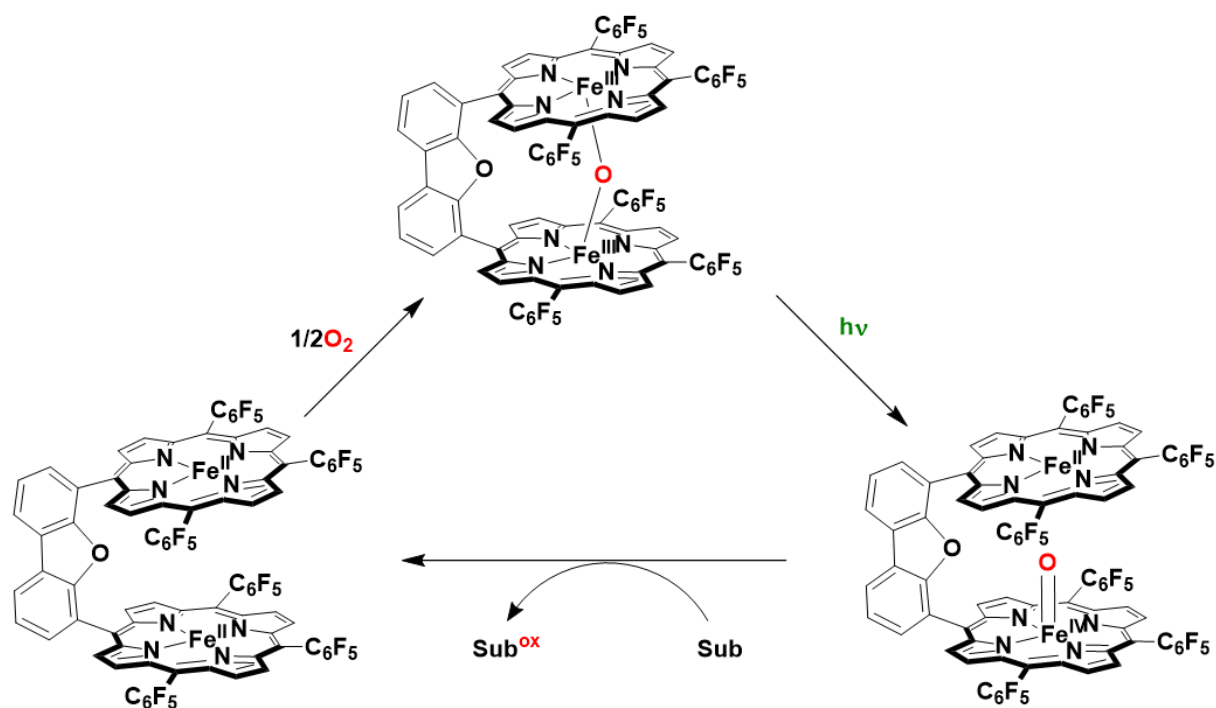


Figure I-21 : Photocycle of the catalytic oxidation of substrates by μ -oxo diiron(III) Pacman porphyrin using dioxygen without need for an external coreductant.

The nonheme synthetic complex $[\text{Fe}^{\text{II}}(\text{TMC})(\text{OTf})_2]$ can also activate dioxygen to convert iron(IV)-oxo species probably through μ -peroxo diiron(III) intermediate. However, its reactivity is moderate. For example, it converts PPh_3 into O=PPh_3 with a TON = 8, thioanisole into methyl phenyl sulfoxide with TON = 7 and benzyl alcohol to benzaldehyde with TON = 6. The formation of μ -oxo diiron(III) complex might be a deactivation pathway responsible for this low activity although it was never detected. Moreover, Nam and co-workers reported that the high electronic density of these iron(II) complexes exhibiting relatively low $\text{Fe}^{\text{III}}/\text{Fe}^{\text{II}}$ redox potential (< -0.1 V vs Fc^+/Fc) is an important factor in dioxygen activation to form iron(IV)-oxo species.⁶² For this reason, other non-heme iron(II) complexes such as $[\text{Fe}^{\text{II}}(\text{TPA})]^{2+}$, $[\text{Fe}^{\text{II}}(\text{N4Py})]^{2+}$, $[\text{Fe}^{\text{II}}(\text{BPMEN})]^{2+}$ do not react with O_2 to generate iron(IV)-oxo.

The μ -oxo diiron(IV) 1-TAML (first generation of TAML) complex firstly reported in 2004 by Collins and co-workers is also capable of oxygenating substrates.⁶³ The formation of the μ -oxo diiron(IV) 1-TAML complex from iron(III) 1-TAML complex and dioxygen, proceeds probably through μ -peroxo diiron(IV) and iron(V)-oxo intermediates as in the mechanism of formation of μ -oxo diiron(III) complex previously described. This amazing behavior for an iron(III) complex toward dioxygen is probably due to the four strong electron donating amidato nitrogens allowing to stabilize to a great extent the oxidized metal. The structure of the μ -oxo bis iron(IV) was confirmed by X-Ray structure characterization. Its reactivity toward oxidation reaction is believed to come from the decomposition of the μ -oxo diiron(IV) 1-TAML complex into iron(III) and iron(V)-oxo species in presence of the substrate (Figure I-22). The latter was identified and characterized as the active species.^{64,65} Thus, The μ -oxo diiron(IV) 1-TAML complex can catalytically oxidize a variety of substrates in the presence of dioxygen as oxygen atom source.

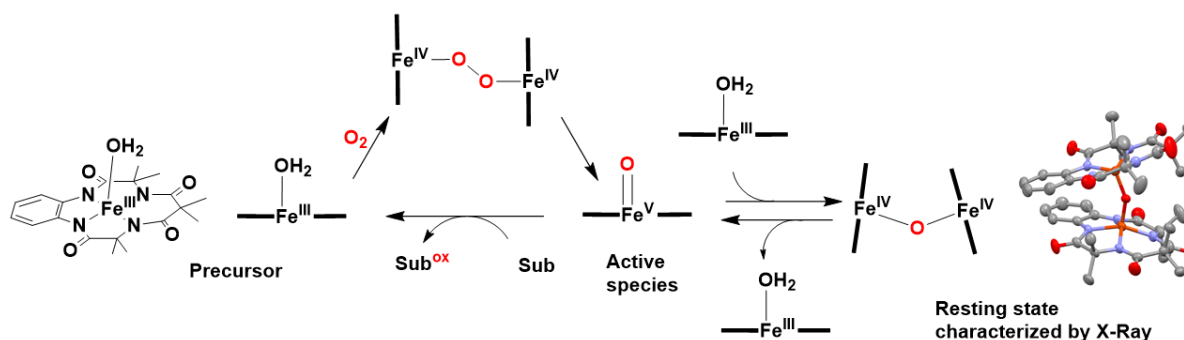


Figure I-22 : Proposed mechanism for the oxygenation of substrates by dioxygen catalyzed by iron(III) TAML complex in the presence of O_2 .

Other photocatalytic strategies using a chromophore and an electron donor to photoactivate O_2 at an iron center will be discussed in detail in chapter III.

1.2.2.3 Using water as oxygen atom source

Like dioxygen, water is known as green supply of oxygen atom that is used to generate of the manganese(V)-oxo species in the natural oxidation process of Photosystem II, the enzyme responsible for water slitting, oxygen evolution and plastoquinone reduction. A number of studies of the oxygen-evolving complex in Photosystem II demonstrated that the $Mn^V=O$

species can be formed by two-electron oxidation of a water bound molecule via a proton-coupled electron transfer (PCET) mechanism (Figure I-23).^{66,67} In Photosystem II, the visible light activates a chromophore which in turn successively oxidizes the manganese-aqua complex to manganese-oxo species through a series of proton coupled electron transfer reaction.

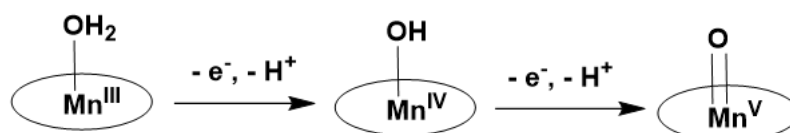


Figure I-23 : Formation of $\text{Mn}^{\text{V}}=\text{O}$ species in PCET mechanism using water as an oxygen source.

Various synthetic metallic systems including iron systems were developed to attempt to generate highly oxidized metal-oxo species using water as an oxygen source. A first synthetic iron-oxo species $[\text{Fe}^{\text{IV}}=\text{O}(\text{N4Py})]^{2+}$, generated from $[\text{Fe}^{\text{II}}(\text{H}_2\text{O})(\text{N4Py})]^{2+}$ by using water as oxygen source in presence of cerium(IV) as a strong one-electron oxidant, was reported by Fukuzumi and Nam in 2009 to catalytically oxygenate organic substrates such as thioanisol, benzyl alcohol, cyclohexen and ethylbenzene (Figure I-24).⁶⁸ Following this successful work, Fukuzumi developed a photocatalytic system containing the same $[\text{Fe}^{\text{II}}(\text{H}_2\text{O})(\text{N4Py})]^{2+}$ catalyst, $[\text{Ru}(\text{bpy})_3]^{2+}$ as a chromophore and $[\text{Co}^{\text{III}}(\text{NH}_3)_5]\text{Cl}$ as a sacrificial electron acceptor for the same purpose. The work of Fukuzumi demonstrated that the active iron-oxo species $[\text{Fe}^{\text{IV}}=\text{O}(\text{N4Py})]^{2+}$ can be produced by using a weak oxidant such as $[\text{Co}^{\text{III}}(\text{NH}_3)_5]\text{Cl}$ through a light-driven reaction with water as an oxygen source (Figure I-24).⁶⁹

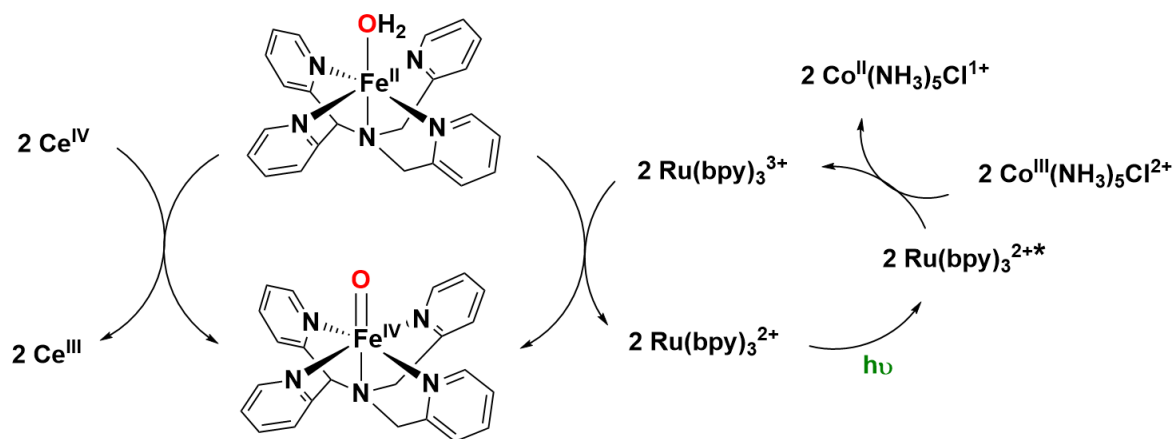


Figure I-24 : Formation of $[\text{Fe}^{\text{IV}}=\text{O}(\text{N}_4\text{Py})]^{2+}$ by water chemical activation using Cerium(IV) (left) as an oxidant or by water photoactivation using a chromophore and a sacrificial electron donor (right).

In similar manner, the iron(V)-oxo species $[\text{Fe}^{\text{V}}=\text{O}(\text{TAML})]^{1-}$ was generated by oxidation of the corresponding iron(III)-aqua complex $[\text{Fe}^{\text{III}}(\text{OH}_2)(\text{TAML})]^{1-}$ by a strong oxidant Cerium(IV),⁷⁰ or by light-driven activation using $[\text{Ru}(\text{bpy})_3]^{2+}$ as a chromophore and $\text{Na}_2\text{S}_2\text{O}_4$ as a sacrificial electron acceptor.⁷¹ Another strategy consists in electroactivating the metal-bound water molecule. Stahl and co-workers reported the sequential formation of $[\text{Fe}^{\text{IV}}(\text{OH})(1\text{-TAML})]^{1-}$ and $[\text{Fe}^{\text{V}}=\text{O}(1\text{-TAML})]^{1-}$ species by electrochemically oxidizing $[\text{Fe}^{\text{III}}(\text{OH}_2)(1\text{-TAML})]^{1-}$ at increasing potential of 0.34 and 0.79 V vs Fc^+/Fc , respectively and their catalytic application in electrochemical oxidation of organic molecules such as alkyl benzene, benzyl alcohol.⁷²

Similarly, a series of high valent iron(IV)-oxo species based on a number of non-heme polynitrogen ligands were quantitatively generated by bulk electrolysis in acetonitrile with 0.1 to 1 M water as an oxygen source.^{73,74} The redox behavior of these iron(II) precursor studied by cyclic voltammetry in dry acetonitrile, showed only a $\text{Fe}^{\text{III}}(\text{CH}_3\text{CN})/\text{Fe}^{\text{II}}(\text{CH}_3\text{CN})$ redox couple. In presence of water, the coordinated acetonitrile was replaced by water as confirmed by a new reduction wave at a potential more negative than that of the $\text{Fe}^{\text{III}}(\text{CH}_3\text{CN})/\text{Fe}^{\text{II}}(\text{CH}_3\text{CN})$ couple. This feature is assigned to the $\text{Fe}^{\text{III}}/\text{Fe}^{\text{II}}$ couple of the $\text{Fe}^{\text{II}}(\text{OH}_2)(\text{L})$ complex. The iron(II)-aqua precursor was oxidized by two one-electron processes coupled to a series of deprotonation at two different potentials. For example, $[\text{Fe}^{\text{II}}(\text{H}_2\text{O})(\text{N}_4\text{Py})]^{2+}$ is oxidized for the first one-electron oxidation process at 0.6 V vs Fc^+/Fc to $[\text{Fe}^{\text{III}}(\text{OH})(\text{N}_4\text{Py})]^{2+}$ and the second oxidation to $[\text{Fe}^{\text{IV}}=\text{O}(\text{N}_4\text{Py})]^{2+}$ at 0.9 V vs Fc^+/Fc . The

potential value of the redox $\text{Fe}^{\text{IV}}=\text{O}/\text{Fe}^{\text{III}}-\text{OH}$ couple could reveal their oxidative activity toward organic substrates. Indeed, Comba, Costas and Que demonstrated that the higher this redox couple potential is the more actively the $\text{Fe}^{\text{IV}}=\text{O}$ species oxygenates substrates such as thioanisole, benzyl alcohol and 1,3-cyclohexadiene (CHD).⁷³

I.2.3 Quest for the active iron species

High valent iron-oxo species have been tracked for a few decades to understand the chemistry of the active sites of enzymes and improve the efficiency of synthetic environmentally friendly catalyst for oxidation reactions such as alkene epoxidation and alkane hydroxylation. Iron-oxo species can be characterized by a combination of various spectroscopic analyses such as absorption spectroscopy, Mössbauer, EPR, Raman, NMR, MS. The oxidation state of iron and the ligand field are mainly characterized by Mössbauer and EPR spectroscopy. Raman resonance spectroscopy is usually used to observe the energy of Fe=O bond vibration. The structure of iron-oxo species can be deduced from Mass spectroscopy and precisely determined by X-Ray Diffraction although the instability of the highly active high-valent iron-oxo species often prevents their crystallization even at low temperature. The result from EXAFS study is useful to characterize the oxidation state of iron center and the ligand environment such as the Fe-O bond distance.

They were fully characterized and some rationalization were drawn to correlate their structure with their activity. Some of them will be discussed in the next paragraph.

It's interesting to note that a non-heme iron(III) complex based on a tridentate carbazole ligand can also lead upon oxidation by the two-electron oxidant PhIO, to an iron(IV) cation radical species capable of epoxydizing alkenes.⁸¹ As in porphyrin, the π -conjugated system of the carbazole-based tridentate ligand was demonstrated to be essential for the generation of iron(IV) cation radical species and its catalytic reactivity. This iron(IV) cation radical species was proposed to be the active intermediate responsible for oxygenating substrates, based on the detection of an absorption band at 660 nm ($\epsilon = 1.4 \times 10^4 \text{ M}^{-1} \cdot \text{cm}^{-1}$) typically observed for iron(IV)-oxo porphyrin cation radical species,^{82,83} and a sharp symmetrical EPR signal at g value of 2.0 assigned to a π -cation radical in the ligand. However, the electronic structure of an iron(IV) cation radical species can be questioned. Indeed, the EPR signal observed at g = 2 is justified in the report by the absence of coupling between the Fe^{IV} center and the π -cation which is in deep contrast with what was observed with porphyrin iron-oxo species previously described.

A series of non-heme iron(IV)-oxo species were prepared and characterized over twenty years. The first $\text{Fe}^{\text{IV}}=\text{O}$ species reported in 2000 by Grapperhaus and co-workers was generated by ozonolyzing $[\text{Fe}^{\text{III}}(\text{cyclam-acetato})(\text{CF}_3\text{SO}_3)]^+$ at $-80 \text{ }^\circ\text{C}$ in acetone/water (95/5) mixture.⁸⁴ This intermediate is stable for around 30 min at $-80 \text{ }^\circ\text{C}$ and quickly decomposes above $-40 \text{ }^\circ\text{C}$. The Mössbauer study revealed an iron(IV)-oxo species with $S = 1$ while the EPR spectrum became silent upon oxidation. However, the instability prevented characterizing the $[\text{Fe}^{\text{IV}}=\text{O}(\text{cyclam-acetato})]^+$ by other spectroscopic techniques.

Some years later, by using methyl substituted cyclam (TMC) with increased ligand field compared to cyclam ligand, Que succeeded in generating an iron(IV)-oxo species, stable for at least 1 month at $-40 \text{ }^\circ\text{C}$, from the reaction of $[\text{Fe}^{\text{II}}(\text{TMC})(\text{CH}_3\text{CN})]^{2+}$ complex with PhIO in acetonitrile.⁸⁵ The relative stability of this intermediate allowed to obtain its full characterization especially by X-ray diffraction spectroscopy. The X-ray structure of $[\text{Fe}^{\text{IV}}=\text{O}(\text{TMC})(\text{CH}_3\text{CN})]^{2+}$ demonstrated a terminal Fe-O distance of 1.64 Å comparable to the average terminal Fe-O double bond distance in $\text{K}_2\text{Fe}^{\text{VI}}\text{O}_4$. Since then, a number of non-heme iron(IV)-oxo species were synthesized and spectroscopically characterized.⁴⁰

Probably due to the instability of iron-oxo species in high oxidation state, a few iron(V)-oxo species were prepared and characterized. Indeed, as explained in the previous literature survey, the formation of a $\text{Fe}^{\text{V}}=\text{O}$ species was suggested proceeding via the degradation of a short-lived $\text{Fe}^{\text{V}}=\text{O}$ species. Moreover, the high oxidative power of $\text{Fe}^{\text{V}}=\text{O}$ species was supported by high potential value of $\text{Fe}^{\text{V}}=\text{O}/\text{Fe}^{\text{IV}}-\text{OH}$ couple.^{72,86} Consequently, almost $\text{Fe}^{\text{V}}=\text{O}$ species were generated and characterized at very low temperature (-60 to -80 °C), except $[\text{Fe}^{\text{V}}=\text{O}(\text{b-TAML})]^{1-}$ (Table I-3).³⁹

The first iron(V)-oxo species using a strong electron donor ligand 1-TAML was reported by Collins in 2007.⁸⁷ The high oxidation state of this species was confirmed by a negative isomer shift ($\delta = -0.46$ mm/s) measured by Mössbauer spectroscopy, that is more negative than those of iron(IV)-oxo species reported. The EPR signal, observed at g value of 1.99, 1.97 and 1.74, was assigned to a low spin ($S = 1/2$) species. Furthermore, the EXAFS study revealed a Fe-O bond distance of 1.58 Å that is 0.04 to 0.10 Å shorter than those reported for iron(IV)-oxo species. All these data are consistent with a low spin iron(V)-oxo species. Among the iron(V)-oxo species synthesized and characterized until now, there is no the high spin ($S = 3/2$) iron(V)-oxo species yet, probably due to a strong field created by the electron donor ligand used to support the generation of iron(V)-oxo species. Unfortunately, no X-ray crystal structure of iron(V)-oxo species was neither reported, probably because of their high reactivity toward oxidation reaction.

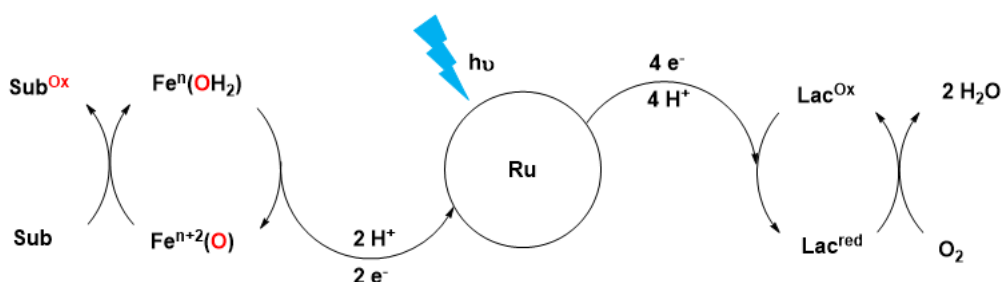
Proposed formulation	λ_{\max} (nm) (ϵ) ($M^{-1}.cm^{-1}$)	EPR g values	Mössbauer δ ($mm.s^{-1}$)	Raman $\nu(Fe-O)$ (cm^{-1})	Fe-O bond (Å)	Ref
$Fe^V=O(1-TAML)$	445 (5400) 630 (4200)	1.99, 1.97, 1.74	-0.42	-	1.58	87
$Fe^V=O(b-TAML)$	441 (4350) 613 (3420)	1.98, 1.94, 1.73	-0.44	-	-	38
$Fe^V=O(TPA)$	-	2.71, 2.42, 1.53	-	-	-	88
$Fe^V=O(BPMEN)$	-	2.69, 2.42, 1.70	-	-	-	89
$Fe^V=O(PDP)$	-	2.66, 2.42, 1.71	-	-	-	90
$Fe^V=O(PyTACN)$	-	2.66, 2.43, 1.74	-	-	-	91
$Fe^V=O(PyNMe_3)$	490	2.07, 2.01, 1.95	-	-	-	41
$Fe^V=O(TMC)(NCOCH_3)$	410 (4000) 780 (430)	2.05, 2.01, 1.97	0.1	798	-	92

Table I-3 : Spectroscopic characterizations of $Fe^V=O$ species.

Interestingly, in chase the $Fe=O$ species, other revealed that short-lived iron intermediates $Fe-O-X$ ($X = Cl, OH, O, OAc$), identified as precursors of $Fe=O$ species can be detected and characterized. Some of them, have even been identified as the active species capable of oxygenating substrates. They will be discussed in chapter IV.

I.3 Context and objective

The work presented in this manuscript started in the context of our ANR project MULTIPLET. The aim of this project was to promote clean photooxydation reactions by using a chromophore in combination with an iron catalyst and water as an oxygen source on one side, and a Laccase, an enzyme able to reduce dioxygen in water, as a sustainable electron acceptor on the other side (Scheme I-2). The feasibility of the electron transfer between the $[\text{Ru}(\text{bpy})_3]^{2+}$ chromophore and the Laccase was reported by our group in 2015.⁹³



Scheme I-2 : Proposed mechanism for our clean photooxydation.

This strategy was found to be limited by the efficiency of the electron transfer to the laccase. Nonetheless, while studying the photoactivation of the iron complex in aerobic conditions, we discovered a new paradigm that allowed us to promote photoinduced OAT reaction using O_2 as an oxygen source in the absence of sacrificial electron donor or acceptor. Meanwhile, we sought to chemically generate potent oxidizing intermediate in order to get insight in the nature of these species and reactivity schemes of this new class of iron complexes.

The system we picked for these studies is based on the previous literature survey that revealed that $\text{Fe}^{\text{V}}=\text{O}$ species, or their isoelectronic $\text{Fe}^{\text{IV}}=\text{O}(\text{L}^\bullet)$ analogues are potent active species due to their high oxidizing properties. However, what we know of their chemistry is still limited by the paucity of artificial $\text{Fe}^{\text{V}}=\text{O}$ species characterized by contrast with $\text{Fe}^{\text{IV}}=\text{O}$ species. To bring our piece to this field we chose to use an anionic hemiporphyrinic dipyrin-dipyridine DPy^- ligand recently developed in our lab as an organic platform to coordinate $\text{Fe}(\text{III})$ precursor and contain higher oxidation states.

The synthesis of two new DPy-based monomeric and a dimeric iron complexes are described in Chapter II together with their full characterization using various spectroscopic techniques such as absorption spectroscopy, HRMS, EPR and Mössbauer spectroscopy, and study of their redox properties by electrochemistry.

In Chapter III, we will present the study we led to decipher the mechanism of the photocatalytic system containing a $[\text{Ru}(\text{bpy})_3\text{Cl}_2]$ chromophore, an iron catalyst and a reversible methylviologen chloride $[(\text{MV})\text{Cl}_2]$ as a reversible electron relay, that can promote OAT reaction with no need for sacrificial electron acceptor or donor.

Chapter IV will describe the strategies employed to chemically generate and characterize potentially active species from the Fe(III) precursors using different oxidants. The nature of these active species will be investigated and the reversible oxidation of the ligand platform will be evidenced. We will also present the interesting catalytic activity stemming from this unusual behavior.

Chapter II : Synthesis, characterization and electrochemical study of iron DPy complexes

II.1 Presentation of the DPy Ligand

In the development of oxidation catalysts, we've seen in chapter I that the structure of the ligand has a predominant influence on the reactivity and the stability of the catalyst. Several different types of ligands have been used to successfully form metal-based oxidation catalyst having a promising reactivity towards oxo transfer to nucleophiles (PPh_3 , SR_2) and hydrocarbons. Although sometimes limited by their turnover numbers, these systems are helpful to identify and rationalize the important structural factors to develop robust and efficient catalyst. For example, the conjugated system of porphyrin ligand facilitates the modulation of the electronic property of catalyst, the four negative charges of TAML contributes largely to stabilize the highly oxidized metal-oxo intermediate, while neutral polydentate nitrogen containing ligands have been designed mainly to investigate the structure/reactivity pattern.

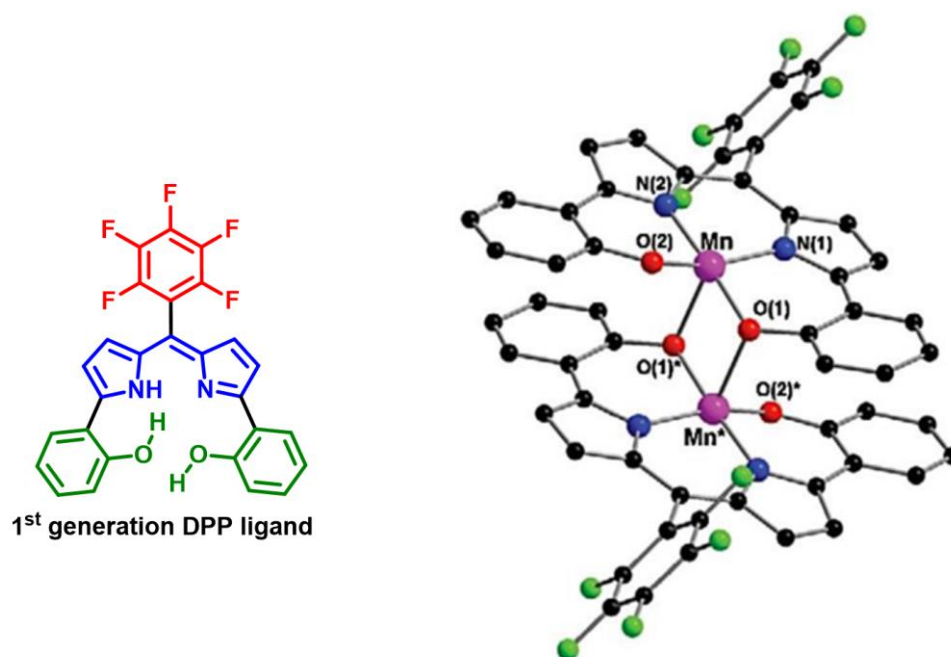


Figure II-1 : X-Ray structure of $[\text{Mn}^{\text{III}}(\text{DPP})]_2$ complex.

In order to design a new ligand family able to support metal-based oxidation catalysts, the Artificial Photosynthesis Group at ICMMO we reasoned to combine structural features from different families of ligands. We targeted a dipyrin skeleton with an aryl group in meso position to avoid auto-oxidation and two coordinating groups in α -position of each pyrrolic

cycle allowing to obtain a tetradentate acyclic ligand. The first ligand synthesized was DPP ligand (pentafluoroDiPyrinPhenol) which has a pentafluorophenyl group in meso position, as in F₂₀-TPP porphyrin, to enhance the stability towards oxidative conditions, and two phenolate groups in α -position reminiscing that of the Salen ligand.⁹⁴ The manganese complex based on DPP ligand was synthesized. Although X-Ray structure showed a dimeric complex, EPR and HRMS analyses revealed a monomer in solution (Figure II-1). This complex is capable of transferring oxygen atom from PhIO to cyclooctene, but its reactivity was not to our expectations.

The next generation of this family was synthesized by replacing phenolate groups with pyridine, groups usually incorporated in poly-nitrogen ligands, to generate a monoanionic DPy ligand (pentafluoroDiPyrinPyridine).⁹⁵ The pyridine groups allow to conserve the ligand structure and decrease the negative charge of ligand in order to enhance the reactivity of catalyst.

In my thesis, DPy ligand was used to prepare the corresponding iron complexes in order to investigate their catalytic properties towards oxidation reactions. Iron metal was chosen because it's abundant, non-toxic and the highly oxidized iron-oxo species are known to be an active intermediate to perform hydrocarbon oxidation. Given that iron(IV)-oxo species in octahedral geometry usually exhibit moderated reactivity compared to iron(IV)-oxo species in trigonal bipyramid geometry,⁴⁰ while DPy as a tetradentate planar ligand, would only create a octahedral geometry, we decided to target the hot iron(V)-oxo intermediate and thus to start with iron(III) DPy precursor.

II.2 Synthesis and characterization of the iron complex $\text{Fe}^{\text{III}}\text{DPyCl}_2$

II.2.1 Synthesis of $\text{Fe}^{\text{III}}\text{DPyCl}_2$ complex

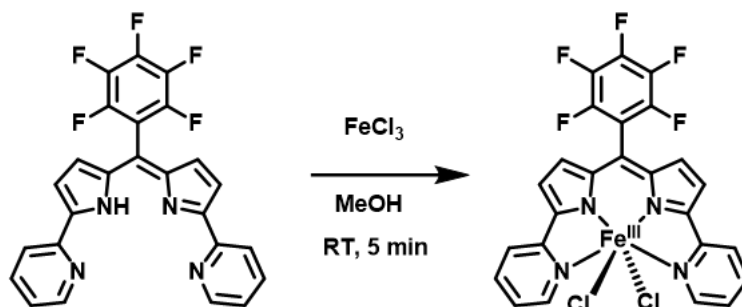


Figure II-2: Scheme of the synthesis of the iron (III) complex $\text{Fe}^{\text{III}}\text{DPyCl}_2$

The preparation of DPy ligand was developed by Dr. Clemence Duclouset in our team.⁹⁵ The $\text{Fe}^{\text{III}}\text{DPyCl}_2$ complex was isolated after metalation of DPy ligand and iron(III) chloride in methanol at room temperature (Figure II-2). The following synthetic tactics was used, a solution of DPy ligand was added dropwise into the solution of iron (III) chloride to avoid two ligands to coordinate on one iron center. Upon mixing, the solution turned immediately blue, revealing that the metalation was effective. The reaction was monitored by UV-visible spectroscopy shown in Figure II-3 to ensure that the complexation was complete. Remarkably, the metalation was realized without the help of base. Probably upon coordination there is spontaneous deprotonation. This complex was isolated in 90% yield by precipitation with diethyl ether.

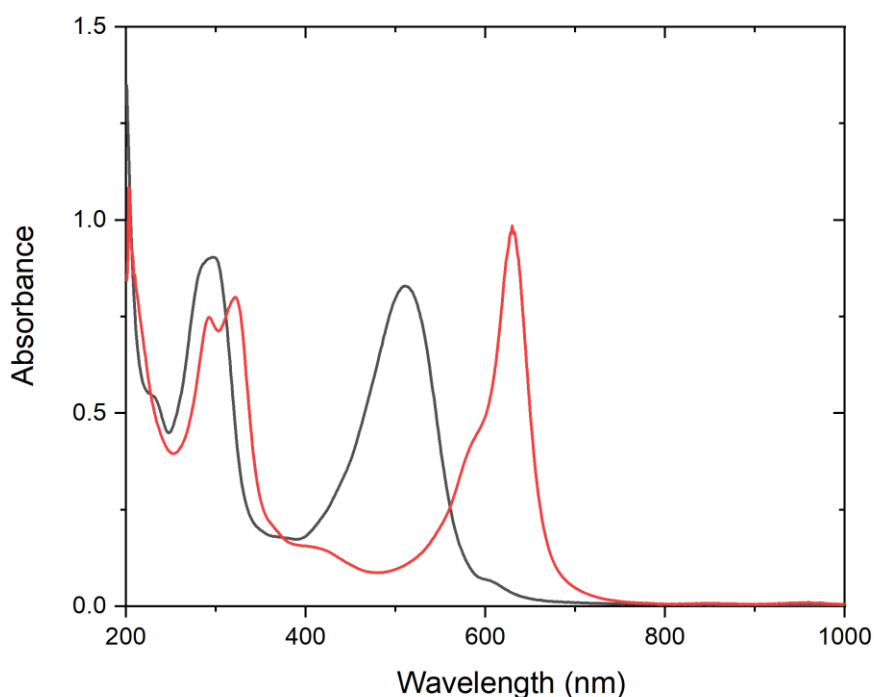


Figure II-3 : UV-vis spectral changes during metalation of DPy ligand (black) with $FeCl_3$ (red) in MeOH.

The paramagnetic $Fe^{III}DPyCl_2$ complex was characterized by UV-vis, ESI-HRMS, EPR & Mössbauer spectroscopies, X-Ray diffraction on single crystals. Its redox behavior was also studied towards electrochemical activation of water.

II.2.2 Characterization of $Fe^{III}DPyCl_2$ complex

II.2.2.1 UV-visible Absorption spectroscopy

Like the porphyrin chromophore, DPy ligand contains a conjugated system, leading to strong absorption in the visible region. UV-vis spectrum (Figure II-4) of $Fe^{III}DPyCl_2$ in acetonitrile shows four intense bands ($\epsilon = 10100$; 21600 ; 27200 and $27700 M^{-1}.cm^{-1}$) at 666 ; 584 ; 316 and 295 nm, respectively that probably stem from ligand to ligand ($\pi \rightarrow \pi^*$) transition given their high molar extinction coefficient. A broad band ($\epsilon = 6000 M^{-1}.cm^{-1}$) is also observed at round 440 nm that can be attributed to metal to ligand transfer (MLCT) transition.

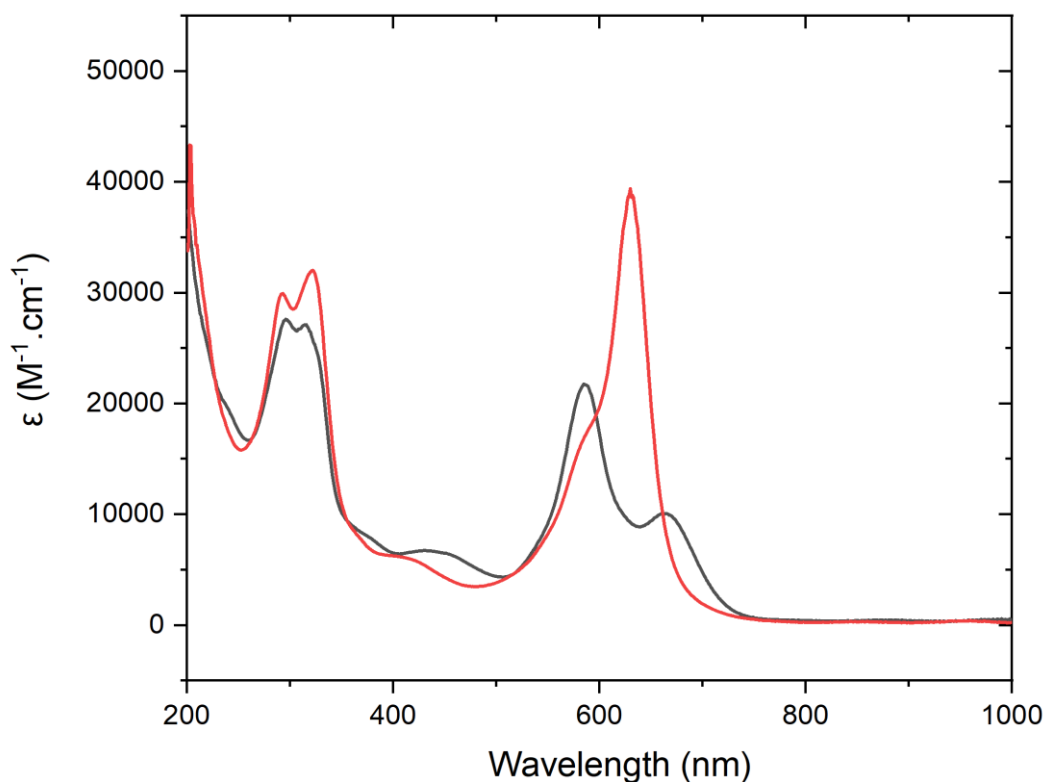


Figure II-4 : UV-vis spectrum of $\text{Fe}^{\text{III}}\text{DPyCl}_2$ in acetonitrile (blue) and in methanol (red).

Interestingly $\text{Fe}^{\text{III}}\text{DPyCl}_2$ complex absorbs differently in methanol a band at 630 nm ($38600 \text{ M}^{-1}\text{cm}^{-1}$) and a shoulder at 585 nm, probably because the axial labile sites are occupied by methanol or methanolate ligand in this case.

II.2.2.1 Structure determination in the solid state by X-Ray diffraction crystallography

Purple mono-crystals suitable for single crystal X-ray diffraction analysis were grown by slow diffusion of diethyl ether into a saturated solution of $\text{Fe}^{\text{III}}\text{DPyCl}_2$ complex in acetonitrile. Figure II-5 shows the ORTEP diagrams of the complex and Table 1 displays selected bond lengths and angles for the crystallographically determined structure. The complex contains an iron center situated in a distorted octahedral geometry. The four equatorial coordination sites are occupied by the nitrogen atoms of DPy ligand with iron-nitrogen bond lengths in typical range for a high spin complex (longer than 2.05 \AA).^{96,97} The Fe-N1 (N_{pyrrol}) distance of 2.050 \AA in $\text{Fe}^{\text{III}}\text{DPyCl}_2$ is comparable to the Fe- N_{pyrrol} distance found in high spin iron (III)

porphyrin complexes.^{98,99} The Fe–N2 (N_{Py}) bond length of 2.235 Å is significantly longer than Fe–N_{Py} (~1.97 Å) found in other iron complex based on pyridine containing ligands such as TPA, N4Py.^{100,101} The dipyrin-pyridine skeleton is almost planar (N_{py} dihedral angle of 3.86°). Two axial sites are occupied by chloride ligands. The Fe–Cl bonds (2.317 Å) are much longer than that of monochloride iron(III) porphyrin complex ClFeTPP (2.192 Å),¹⁰² and much closer to that of trans-dichloride iron(III) such as in oxaporphyrin iron complex (2.302 Å)¹⁰³, (β-PPh₃-TPP)Fe^{III}Cl₂ (2.348 and 2.429 Å)¹⁰⁴ and non heme iron(III) complex Fe^{III}(dpa) (2.285 and 2.315 Å).⁻ The considerable lengthening of the Fe–Cl bonds can be ascribed to the mutual trans influence of the chloride ligand. These axial Fe–Cl bonds are deviated from the z axis by about 13.98°. The C–C and C–N bond distances are very homogenous over the ligand backbone which indicates a strong delocalization of the electron density over the whole skeleton.

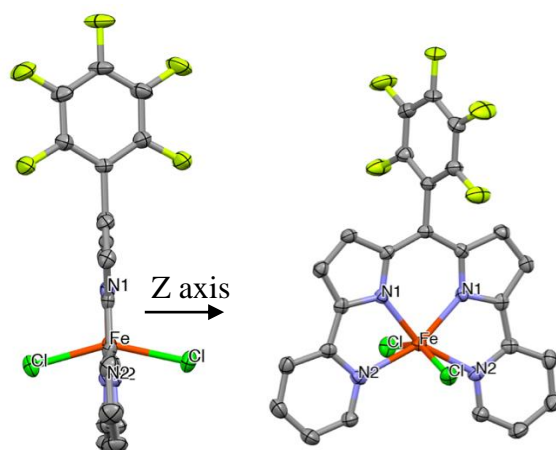


Figure II-5 : ORTEP representation of X-Ray structure of Fe^{III}DPyCl₂ complex. Thermal ellipsoids are shown at 30 % level of probability. Hydrogen atoms and solvent molecules are omitted for clarity. Symmetry code: (i) $x-y+2/3, -y+4/3, -z+5/6$.

Bond distances		Angles	
Fe- N1	2.048(3)	N1-Fe-N1	82.36(19)
Fe- N2	2.238(4)	N1-Fe-N2	75.29(13)
Fe- Cl	2.3187(11)	Cl-Fe-Cl	152.03(7)
		N1-Fe-Cl	102.35(10)
		N2-Fe-Cl	84.31(10)

Table II-1 : Selected Bond Distances (Å) and Angles (°) for $Fe^{III}DPyCl_2$ complex with estimated standard deviation's in parenthesis.

Of note, the molecules are packed head to tail which might indicate the presence of π -stacking interactions in the solid state.

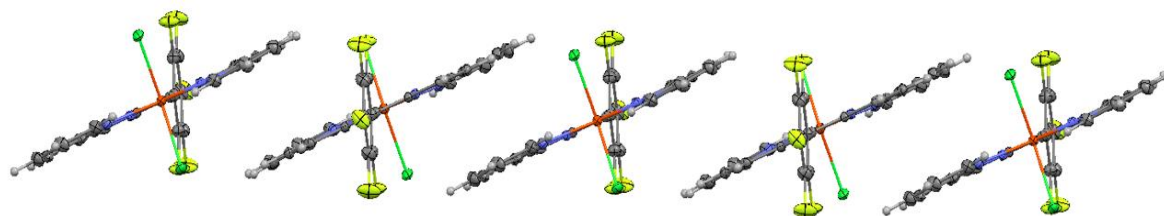


Figure II-6 : $Fe^{III}DPyCl_2$ chain observed by X-Ray diffraction.

II.2.2.2 ESI-HRMS measurement

The structure of the complex in solid state was revealed by the above X-Ray determination. However, its structure in solution can be modified, for example solvent molecules can replace labile chloride ligands. The ESI-HRMS analysis of a $Fe^{III}DPyCl_2$ solution in acetonitrile showed a prominent peak at $m/z = 553.9995$ with charge and isotopic distribution assigned to the monochloride $[Fe^{III}DPyCl]^+$ complex (Figure II-7). A second prominent peak at $m/z = 611.9583$ was attributed to the sodium adduct $[(Fe^{III}DPyCl_2)(Na)]^+$. No peak corresponding to a complex with coordinated acetonitrile molecule $[Fe^{III}DPy(MeCN)_{1-2}]^{2+}$ was observed. Therefore, the structure of complex in acetonitrile was probably not changed compared to its structure in solid state with two axial chloride ligands.

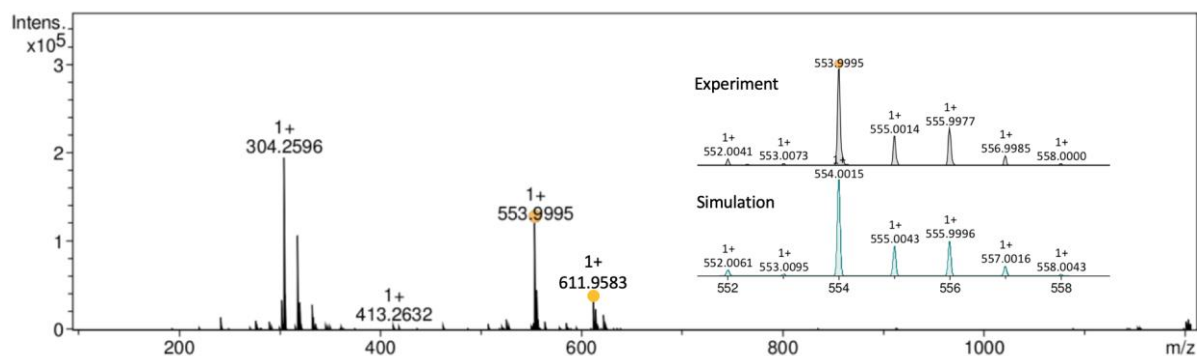


Figure II-7: ESI+-HRMS spectrum of the $\text{Fe}^{\text{III}}\text{DPyCl}_2$ solution in acetonitrile. Inset: comparison of experimental and theoretical peak for the isotopic distributions.

On the contrary, when the ESI-HRMS analysis was performed on a $\text{Fe}^{\text{III}}\text{DPyCl}_2$ solution in methanol, two peaks at $m/z = 550.0499$ and 604.0570 attributed to $[\text{Fe}^{\text{III}}\text{DPy}(\text{OMe})]^+$ and $[\text{Fe}^{\text{III}}\text{DPy}(\text{OMe})_2\text{Na}]^+$ were observed, that allows us to consider that the chloride ligands in axial position can be replaced by the methanolate ligands in methanol solution. The change of axial ligand probably leads to the shift of the absorption bands observed in methanol compared to acetonitrile (Figure II-4).

II.2.2.3 EPR spectroscopy

EPR measurement was used to verify the oxidation state of iron center and characterize the ligand field. The X-band spectrum of the complex recorded at 10 K in acetonitrile showed a broad signal. Broad signals can be obtained if the frozen solution does not constitute a good “glass”. We reasoned that microcrystals might form in acetonitrile due to $\pi - \pi$ stacking interactions such as evidenced in the previous section on the X-Ray structure (Figure II-6).

We thus decided to add TBAPF_6 in the acetonitrile solution of $\text{Fe}^{\text{III}}\text{DPyCl}_2$ to prevent the formation of these chains of complexes by intercalation of the bulky salt and allow the formation of a good “glass”. The EPR spectrum in presence of TBAPF_6 showed clearly three intense signals at $g = 9.1, 5.1, 3.7$ and a broad weak signal at g value around 2 which are in good agreement with a d^5 iron center in a rhombic environment (Figure II-8). The effective g value could be described when considering a $S = 5/2$ high spin with $E/D = 0.2$ rhombicity. This description predicts $g \approx 5.1, 3.7, 3.4$ for the $|\pm 3/2\rangle$ doublet excited state and $g \approx 9.1,$

2.0, 1.2 for the $|\pm 1/2\rangle$ doublet ground state. However, a series of EPR spectra recorded at different temperatures revealed that the intensity of the signals at $g = 5.1$ and 3.7 changed in the same trend with the signal at $g = 9.1$ (Figure II-9, left), and thus cannot belong to two different Kramers doublets of a same species but rather to 2 different species. We thus attempted to simulate the EPR spectrum on the basis of 2 sets of signals (Figure II-9, right). The effective g values could be fitted with a mixture in ratio 1:1 of two high spin ($S = 5/2$) iron(III) species in 0.2 rhombicity probably corresponding to our $\text{Fe}^{\text{III}}\text{DPyCl}_2$ in two different geometries. The first set is characterized by three signals at $g = 5.1, 3.7$ and 2.0 while the second one is characterized by three signals at $g = 9.1, 4.2$ and 3 .

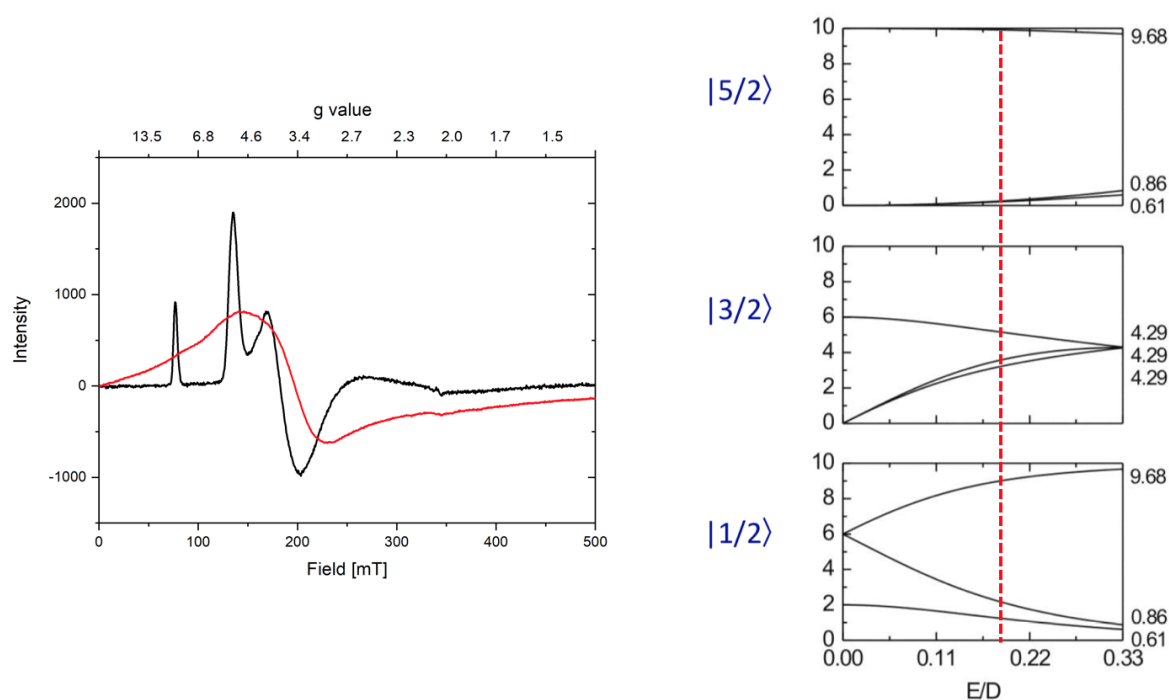


Figure II-8 : (Left) EPR spectrum of $\text{Fe}^{\text{III}}\text{DPyCl}_2$ (1 mM) in acetonitrile in absence (red) and in presence (black) of TBAPF_6 (0.1 mM) at 10 K after subtraction of cavity signal. (Right) Rhombogram for an $S = 5/2$ system.

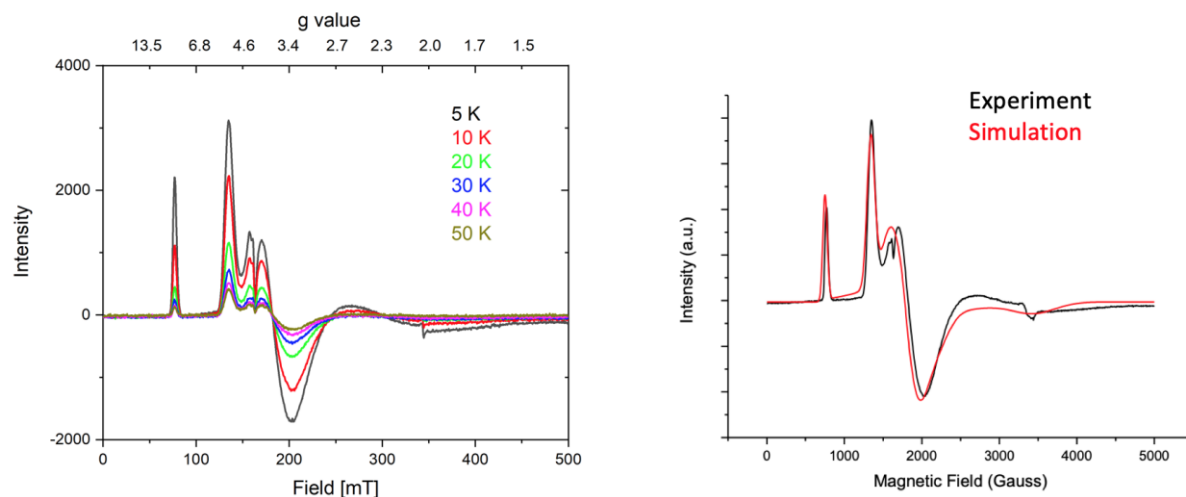


Figure II-9: (Left) EPR spectrum of $\text{Fe}^{\text{III}}\text{DPyCl}_2$ (1 mM) in acetonitrile in absence at different temperature after subtraction of cavity signal. (Right) Simulation of EPR spectrum based on the experimental signals.

II.2.2.4 Mössbauer spectroscopy

The magnetic properties of iron complex $\text{Fe}^{\text{III}}\text{DPyCl}_2$ were also assessed by Mössbauer measurement in collaboration with Dr. Geneviève Blondin from the CEA Grenoble. Mössbauer spectra of $^{56}\text{Fe}^{\text{III}}\text{DPyCl}_2$ in solid state (15 mg) under zero magnetic field—applied at 80 K showed a doublet that could be fitted with an isomer shift of $\delta = 0.46 \text{ mm}\cdot\text{s}^{-1}$ and quadrupolar splitting of $\Delta E_Q = 0.7 \text{ mm}\cdot\text{s}^{-1}$. While, Mössbauer spectra of $^{57}\text{Fe}^{\text{III}}\text{DPyCl}_2$ in frozen acetonitrile solution (2 mL) showed a single broad doublet that was tentatively fitted with an isomer shift of $\delta = 0.45 \text{ mm}\cdot\text{s}^{-1}$ and quadrupolar splitting of $\Delta E_Q = 0.54 \text{ mm}\cdot\text{s}^{-1}$. These parameters fall within the expected range for a high spin ($S = 5/2$) iron (III) compound (Figure II-10). The abnormal width of doublet was probably due to the present of different sites of close geometries, as stated before by the formation of complex chains mentioned.

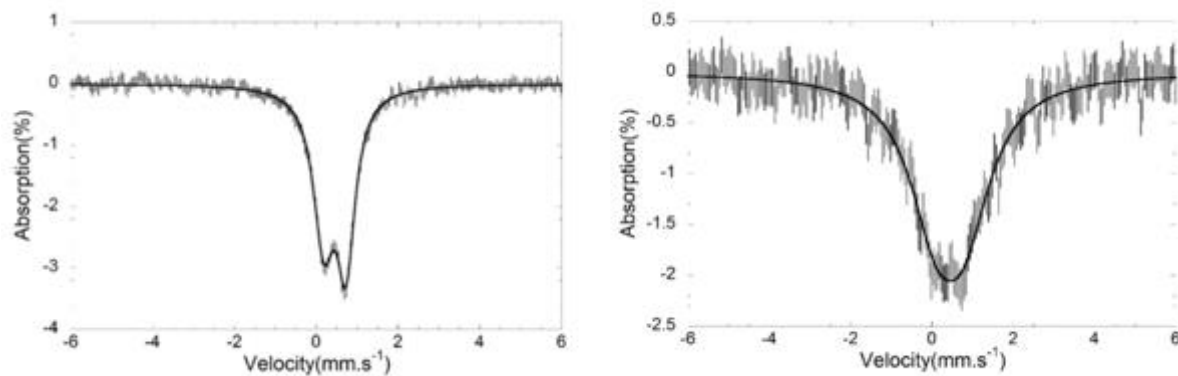


Figure II-10 : Zero-field Mössbauer spectra at 80 K of $^{56}\text{Fe}^{\text{III}}\text{DPyCl}_2$ in solid state (15 mg) (left) and $^{57}\text{Fe}^{\text{III}}\text{DPyCl}_2$ in a frozen acetonitrile solution (2 mM) (right) with their simulation.

II.2.3 Electrochemical study

The electrochemical behavior of $\text{Fe}^{\text{III}}\text{DPyCl}_2$ complex was evaluated by cyclic voltammetry and differential pulse voltammetry at a glassy carbon electrode in argon-degassed acetonitrile containing 0.1 M of tetra-N-butylammonium hexafluorophosphate as electrolyte using platinum wire as auxiliary electrode and saturated calomel reference electrode. The voltammograms are illustrated in Figure II-11. The cyclic voltammogram (CV) shows two reversible cathodic waves at -0.04 V ($\Delta E_p = 80$ mV) and -0.72 V ($\Delta E_p = 80$ mV) vs SCE and two irreversible anodic waves at 1.32 V and 1.53 V.

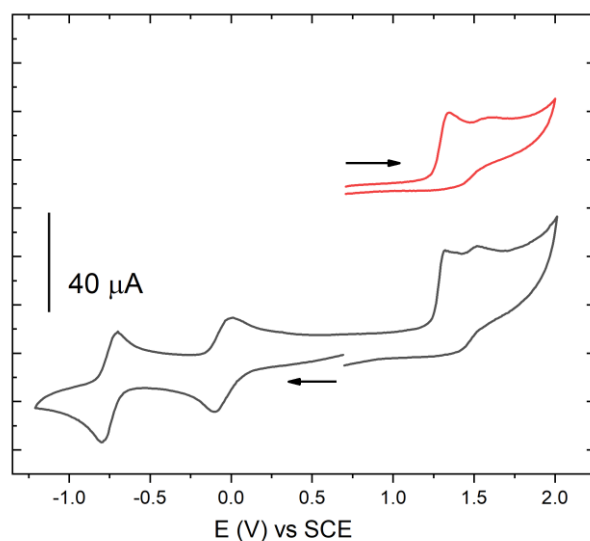


Figure II-11 : Cyclic voltammetry at $\nu = 100$ mV/s (black: reduction direction, red: oxidation direction) of 1 mM $\text{Fe}^{\text{III}}\text{DPyCl}_2$ in acetonitrile.

The shape of this voltammogram led us to investigate more deeply the redox behavior of this complex to reveal its catalytic potential towards reductive and oxidative process.

II.2.3.1 Electroactivity in reduction

The first one-electron reduction process at -0.04 V was assigned to the $\text{Fe}^{\text{III}}/\text{Fe}^{\text{II}}$ couple. The iron(II) complex obtained by reducing the $\text{Fe}^{\text{III}}\text{DPyCl}_2$ complex by one electron at -0.4 V vs SCE was confirmed by the recording of a silent EPR spectrum at 10 K (Figure II-12). The second reduction process occurs at the same potential as the reduction of the free ligand and the d^{10} Zn complex, which suggests that in this case, the reduction may take place at the ligand rather than at the metal center (Figure II-13). To investigate on the electronic nature of the doubly reduced form, we performed a second electrolysis at -1.2 V. Unfortunately, attempts to electrochemically reduce $\text{Fe}^{\text{III}}\text{DPyCl}_2$ at -1.2 V in acetonitrile led to the formation of a dark precipitate. EPR of the suspension only revealed the presence of a weak signal at $g = 2.00$ (Figure II-12), the intensity of which could be explained by the degradation of the species upon the time-scale of the experiment. A weak signal at $g = 4.3$ was also observed, corresponding probably to reoxidized iron(III) product upon sample preparation.

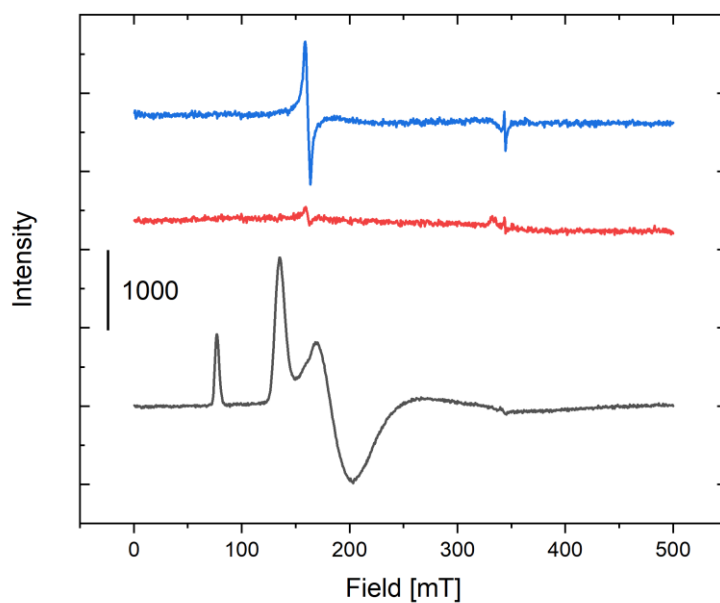


Figure II-12: EPR spectra at 10 K of a $\text{Fe}^{\text{III}}\text{DPyCl}_2$ solution (black) and after controlled potential electrolysis at -0.4 V (red) and -1.2 V (blue) vs SCE in acetonitrile at 10 K.

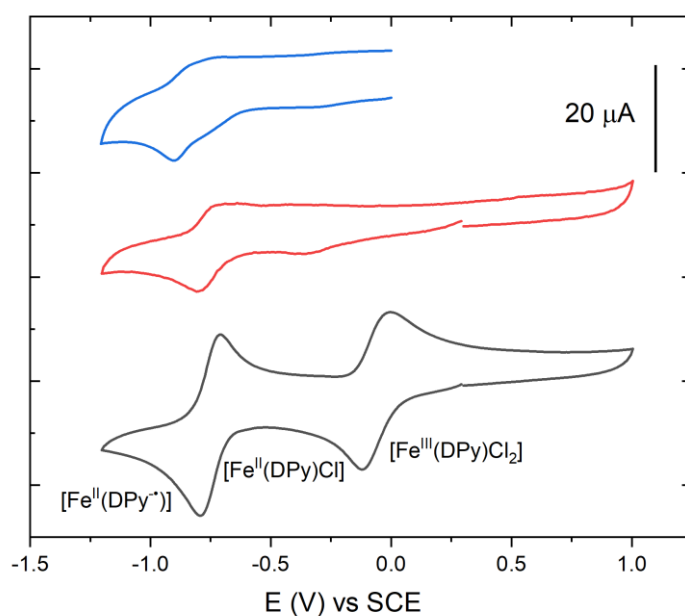


Figure II-13 : Cyclic voltammograms of 1 mM DPy ligand (blue), 1 mM ZnDPyCl (red) and 1 mM $\text{Fe}^{\text{III}}\text{DPyCl}_2$ (black) measured in acetonitrile.

Although the second reduction probably takes place at the ligand, the reversibility of two reduction waves reveals that the $\text{Fe}^{\text{III}}\text{DPyCl}_2$ complex could be used as an electrocatalyst for proton or carbon dioxide reduction. Indeed, the reduction behavior of $\text{Fe}^{\text{III}}\text{DPyCl}_2$ was similar to that of the iron porphyrin complex $\text{Fe}^{\text{III}}\text{TPPCl}$ which exhibits an interesting reactivity in dioxide carbon reduction (Figure II-16).

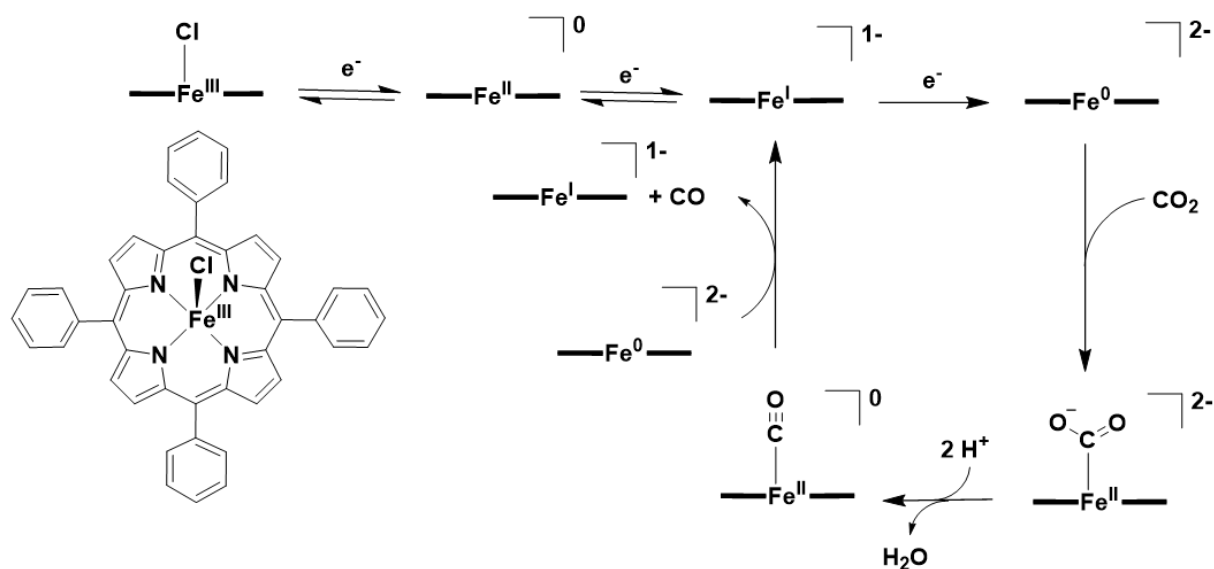


Figure II-14 : Proposed mechanism for carbon dioxide reduction electro-catalyzed by $\text{Fe}^{\text{III}}\text{TPPCl}$.

$\text{Fe}^{\text{III}}\text{TPPCl}$ needs to be reduced by three one-electron processes to yield a formally iron(0) species capable to reduce carbon dioxide by two-electron to form carbon monoxide and water in presence of proton source (Figure II-14).^{106,107} The presence of a hydrogen source such as water, methanol, trifluoroethanol (TFE) is highly important to diminish the cost of carbon dioxide reduction (Figure II-15).

Reduction potentials of CO ₂	E° [V] vs SHE at pH 7
CO ₂ + e ⁻ → CO ₂ ⁻	-1.9
CO ₂ + 2H ⁺ + 2e ⁻ → HCOOH	-0.61
CO ₂ + 2H ⁺ + 2e ⁻ → CO + H ₂ O	-0.52
2CO ₂ + 12H ⁺ + 12e ⁻ → C ₂ H ₄ + 4H ₂ O	-0.34
CO ₂ + 4H ⁺ + 4e ⁻ → HCHO + H ₂ O	-0.51
CO ₂ + 6H ⁺ + 6e ⁻ → CH ₃ OH + H ₂ O	-0.38

Figure II-15 : Standard electrochemical potentials for CO₂ reduction.¹⁰⁸

Although CO₂ reduction was not the heart of this thesis project, our group is interested in this field. Therefore, we decided to investigate on the ability of Fe^{III}DPyCl₂ to promote electro-catalytic reduction of carbon dioxide.

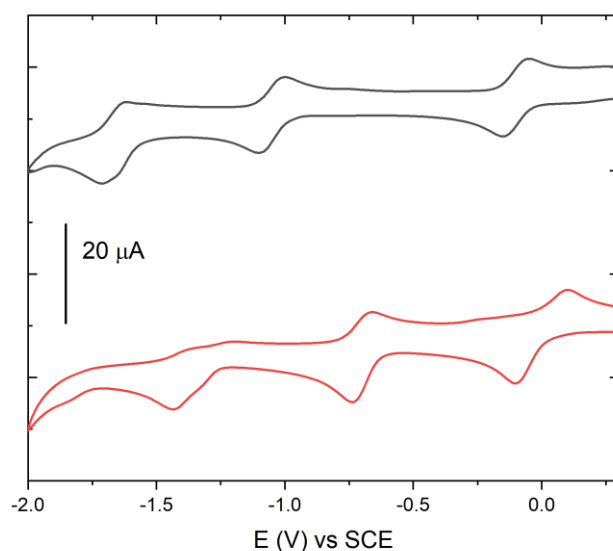


Figure II-16 : Cyclic voltammograms of 1 mM Fe^{III}TPPCL (black) and Fe^{III}DPyCl₂ (red) measured in DMF.

Given the high solubility of CO₂ in DMF, this solvent was chosen for the study. As Fe^{III}TPPCL, Fe^{III}DPyCl₂ presented in its CV a 3rd reduction wave at a more positive value of -1.4 V vs SCE. Next, TFE (trifluoroethanol) was added as a proton source. The CV of Fe^{III}DPyCl₂ complex in DMF with 4 M TFE under argon atmosphere showed a catalytic wave at -1.8 V that was attributed to hydrogen reduction (Figure II-17). When the CV was

performed under CO₂ atmosphere, a catalytic wave at a more positive potential of -1.3 V was detected, indicating CO₂ reduction by the Fe^{III}DPyCl₂ complex. The CO₂ reduction was observed at the 3rd reduction wave of the Fe^{III}DPyCl₂ complex, supporting the fact that the formally reduced [Fe⁰(DPy)] was responsible for CO₂ reduction.

To identify the products obtained from CO₂ reduction, a controlled potential electrolysis was run at -1.6 V in CO₂ saturated solution of 1 mM Fe^{III}DPyCl₂ as catalyst for 2 h with 4 M TFE as proton source. Bubbles were observed at the electrode surface. The gases contained in the headspace were regularly analyzed by HPGC. Carbon monoxide CO was detected to be a product from carbon dioxide reduction especially at the beginning of the electrolysis (Figure II-18). However, the main gas detected was dihydrogen. The low Faradaic efficiency around 40 % might indicate that other products may have formed in solution such as formate which cannot be detected by HPGC. No further analysis of soluble reduced forms of CO₂ was performed. Optimization of the potential applied during the electrolysis was not explored either, but it can be expected that a better selectivity could be achieved at lower potential.

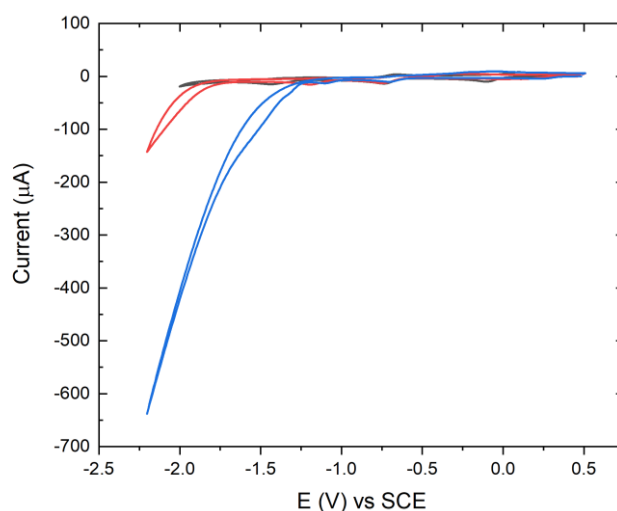


Figure II-17 : Cyclic voltammograms of 1 mM Fe^{III}DPyCl₂ (black) in presence of TFE (4 mM) in saturated argon solution in DMF (red) and in saturated carbon dioxide solution in DMF (blue).

In brief, Fe^{III}DPyCl₂ was able to reduce both proton and carbon dioxide to form dihydrogen and carbon monoxide, respectively. As DPy ligand is an active redox ligand in reduction, our results point that the first reduction was centered at iron center to form [Fe^{II}DPy]⁺, while the

second and third reduction are probably centered at the DPy ligand to form $[\text{Fe}^{\text{II}}(\text{DPy}\bullet\bullet)]^{1-}$ species such as suggested in the case of iron porphyrin.

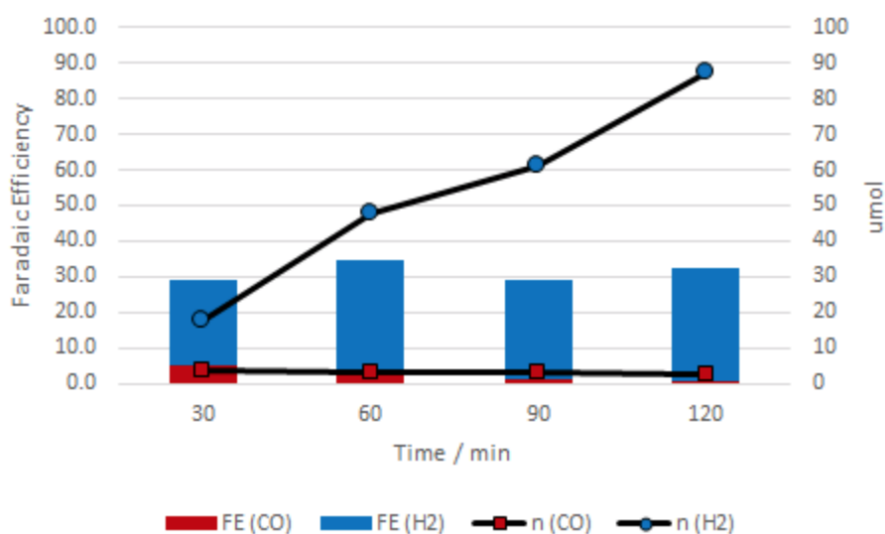


Figure II-18: CO , H_2 evolution traces and the corresponding faradaic efficiency in the bulk electrolysis of a $\text{Fe}^{\text{III}}\text{DPyCl}_2$ (0.5 mM) solution in DMF containing 0.1M TBAPF_6 at -1.7 V vs SCE under CO_2 atmosphere.

II.2.3.2 Electroactivity upon oxidation

To understand the nature of the two irreversible oxidation waves of $\text{Fe}^{\text{III}}\text{DPyCl}_2$, the redox behavior of DPy ligand complex was studied in acetonitrile. The non-innocent DPy ligand shows two irreversible oxidations at 1.21 V and 1.36 V while the $\text{Fe}^{\text{III}}\text{DPyCl}_2$ complex shows two irreversible oxidation waves at 1.32 V and 1.53 V (Figure II-19). The presence of the metal center decreases the electronic density at the ligand and makes its oxidation more difficult. Thus, the two oxidation waves of the ligand coordinated to the iron center can be positively shifted to 1.32 V and 1.53 V. However, the current amplitude observed by CV for the first oxidation at 1.32 V is two times more important than the one observed for the one-electron reduction of Fe^{III} to Fe^{II} , suggesting that the first oxidation is a multi-electron process (Figure II-11). Additionally, DPV of $\text{Fe}^{\text{III}}\text{DPyCl}_2$ complex revealed that the current amplitude of oxidation wave at 1.32 was 3 times that at 1.53 V (Figure II-19). Therefore, the first oxidation at 1.32 V was not only assigned to the one electron of the oxidation ligand but also probably to iron or chloride oxidation. Measuring the cyclic voltammetry of tetra-N-

butylammonium ($[\text{Bu}_4\text{N}]\text{Cl}$) shows that free chloride ions are oxidized at 1.05 V (Figure II-19), but as mentioned before, iron coordinated-chloride can also be oxidized at a higher potential due to a decreased electronic density upon coordination.

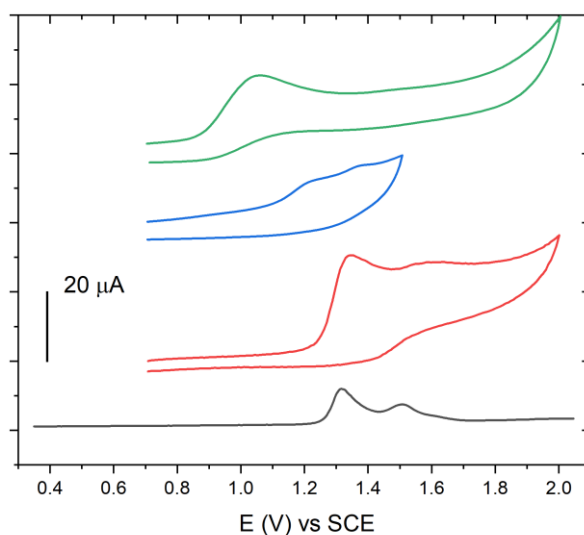


Figure II-19 : Cyclic voltammetry at $v = 100 \text{ mV/s}$ of $[\text{Bu}_4\text{N}]\text{Cl}$ (green), 1 mM DPy ligand (blue), 1 mM $\text{Fe}^{\text{III}}\text{DPyCl}_2$ (red) and Differential pulse voltammetry with step potential of 5 mV and intergration time of 1 s of $\text{Fe}^{\text{III}}\text{DPyCl}_2$ (black) in acetonitrile.

To distinguish between these 2 possibilities, EPR spectroscopy was used to monitor the electrolysis of a $\text{Fe}^{\text{III}}\text{DPyCl}_2$ solution at 1.45 V. A signal with g value at 4.3 corresponding to a rhombic high spin iron(III) species together with a signal pointing at g value at 2.00 assigned to a probable radical species were detected. Of note the initial EPR signal disappeared (Figure II-20). The radical signal is very broad probably because the organic radical is partially delocalized on the iron center. This signal could also be attributed to an Fe(V) species, that usually exhibits a set of signal around $g = 2$.⁸⁷⁻⁹² Iron IV formation cannot be ruled out since this species would be EPR silent. Oxidation of an Fe-bound chloride into the EPR silent chlorine and a new Fe(III) species can however explain the presence of the signal at 4.3. Consequently, both the ligand, one coordinated-chloride and the iron center could be oxidized at 1.45 V. A sum up of the different possibilities is given in Figure II-21.

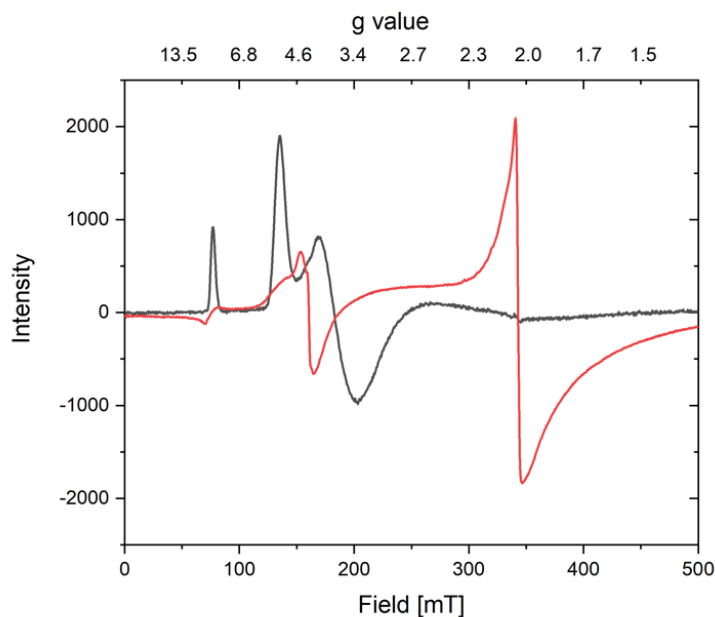


Figure II-20 : EPR spectra of $\text{Fe}^{\text{III}}\text{DPyCl}_2$ (black) and oxidized species (red) obtained by oxidizing $\text{Fe}^{\text{III}}\text{DPyCl}_2$ 1.45 V vs SCE in acetonitrile at 10 K.

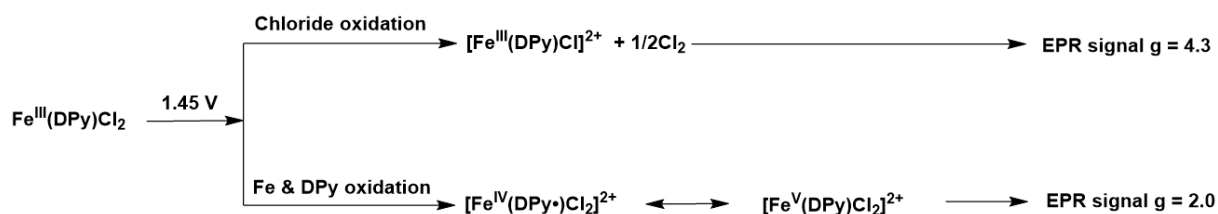


Figure II-21 : Proposition of the oxidized species obtained by electrolyzing at 1.45 V.

The above electrochemical study demonstrated that the $\text{Fe}^{\text{III}}\text{DPyCl}_2$ complex is based on a non-innocent ligand and the electrochemical oxidation of this complex in absence of oxygen source can generate a mixture of oxidized species. However, a highly oxidized iron-oxo species may be electrochemically generated in presence of water as oxygen source, as explained in paragraph I.2.2.3.⁷²⁻⁷⁴ For this reason, the redox behavior of $\text{Fe}^{\text{III}}\text{DPyCl}_2$ complex was also studied in acetonitrile in presence of water (Figure II-22). The CV showed a positive-shift of $\text{Fe}^{\text{III}}/\text{Fe}^{\text{II}}$ couple attesting partial chloride replacement by aqua ligand occurs at axial coordination sites. Indeed, the iron(III)-aqua complex $[\text{Fe}^{\text{III}}\text{DPy}(\text{OH}_2)_2]^{2+}$ with two

positive charges would be more easily reduced than the neutral $\text{Fe}^{\text{III}}\text{DPyCl}_2$ complex. Of note, the reduced wave at -0.72 V was not shifted by addition of water, suggesting that the reduction taking place at the ligand was not affected by change of axial coordination.

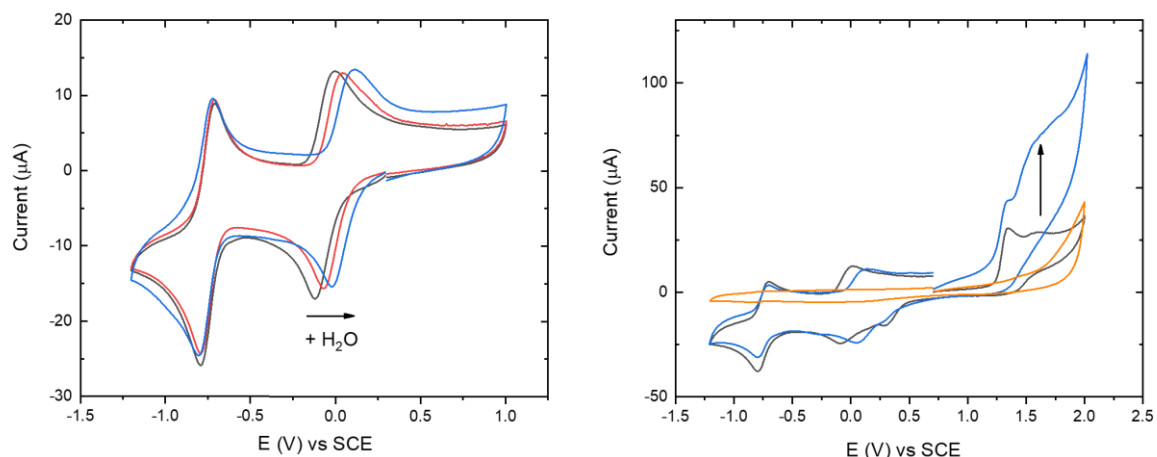


Figure II-22 : (Left) Cyclic voltammograms of $1 \text{ mM Fe}^{\text{III}}\text{DPyCl}_2$ measured in acetonitrile (black) in presence of 0.5 M (red) and 1 M water (blue), scan towards negative potentials; (Right) Cyclic voltammograms measured in acetonitrile with 1 M water in presence (blue) and in absence (orange) of $\text{Fe}^{\text{III}}\text{DPyCl}_2$ and CV of $\text{Fe}^{\text{III}}\text{DPyCl}_2$ in absence of water (black), scan towards positive potentials.

On the other hand, the current amplitude of the oxidation wave at 1.53 V increased upon addition (Figure II-22, right), suggesting a catalytic process is probably undergoing in presence of water. This was confirmed by the controlled potential electrolysis experiment in mixture of acetonitrile and water that showed a higher current consumption in the presence of $\text{Fe}^{\text{III}}\text{DPyCl}_2$ complex than its absence (Figure II-23), suggesting that the catalytic reaction takes place at working electrode in presence of iron complex. To date all attempts to confirm O_2 production by the four electron oxidation of water using a Foxy probe to detect O_2 upon bulk electrolysis were not successful.

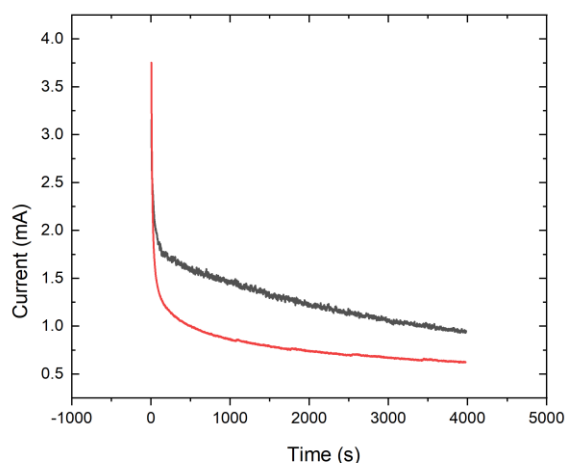


Figure II-23 : Current evolution during controlled potential electrolysis on a glassy carbon at 1.7 V vs SCE with (black) and without (red) 1 mM $\text{Fe}^{\text{III}}\text{DPyCl}_2$ complex in acetonitrile in presence of 2 M water.

We also tried to detect highly oxidized species such an $\text{Fe}^{\text{V}}=\text{O}$ by EPR measurement. The EPR spectrum of a solution obtained by electrolyzing $\text{Fe}^{\text{III}}\text{DPyCl}_2$ (1 mM) at 1.6 V in wet acetonitrile showed a broad signal with g value at 2.00 that could probably be attributed, as already mentioned to a low spin $\text{Fe}^{\text{V}}=\text{O}$ or a $\text{Fe}^{\text{IV}}=\text{O}(\text{DPy}\bullet)$ species (Figure II-24).

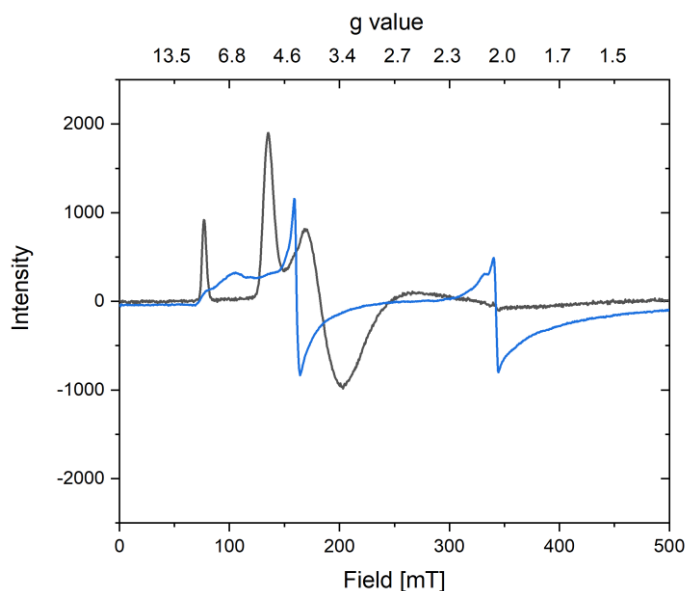


Figure II-24 : : EPR spectra at 10 K of 1 mM $\text{Fe}^{\text{III}}\text{DPyCl}_2$ (black) and oxidized species obtained by oxidizing $\text{Fe}^{\text{III}}\text{DPyCl}_2$ at 1.6 V vs SCE in wet acetonitrile (blue).

Therefore, we can propose that a highly oxidized iron(V)-oxo species can be electrochemically generated at 1.53 V by activation of a water molecule at the iron complex. Indeed, this kind of electrocatalytic water oxidation was reported by Meyer using an iron(III) complex based on dpaq ligand (dpaq = 2-[bis(pyridine-2-ylmethyl)]amino-N-quinolin-8-yl-acetamido) in propylene carbonate solution upon addition of water.⁸⁶ The water oxidation mechanism using iron catalyst was proposed on the basis of the mechanism earlier proposed for a series of Ru polypyridyl catalyst,^{109,110} and is depicted in Figure II-25. In this mechanism, it was found that the rate-limiting step is the O-O bond formation, occurring by reaction of the Fe^V=O species with H₂O. Accordingly, the current amplitude of catalytic wave varies with iron catalyst concentration and water concentration following the rate law given in equation 1 and the expression for the catalytic current (*i*_{cat}) expressed in equation 2.

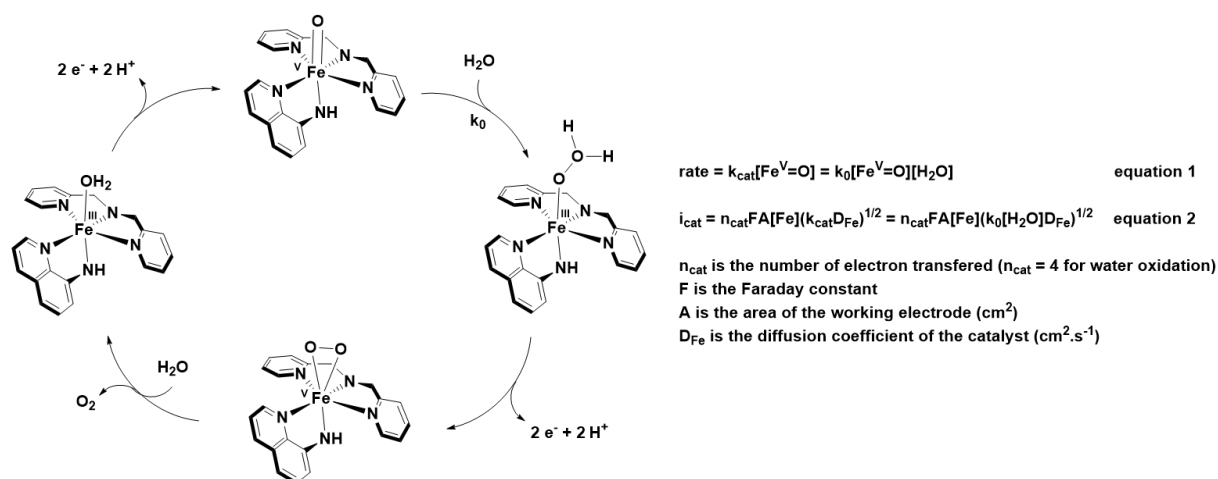


Figure II-25 : (Left) Proposed mechanism for electrocatalytic water oxidation using iron(III) catalyst. (Right) the rate law and catalytic current equations.

In our case, the current amplitude of the catalytic oxidation wave at 1.53 V was also found to vary linearly with iron precursor concentration $[\text{Fe}^{\text{III}}\text{DPyCl}_2]$ and $[\text{H}_2\text{O}]^{1/2}$ (Figure II-26 and Figure II-27). These collected data are also consistent with the generation of an active iron-oxo species generated at 1.53 V, able to catalyze the oxidation of water. Further studies are still required to decipher the electrocatalytic processes observed here, and the nature of the oxidation product (O_2 and H_2O_2).

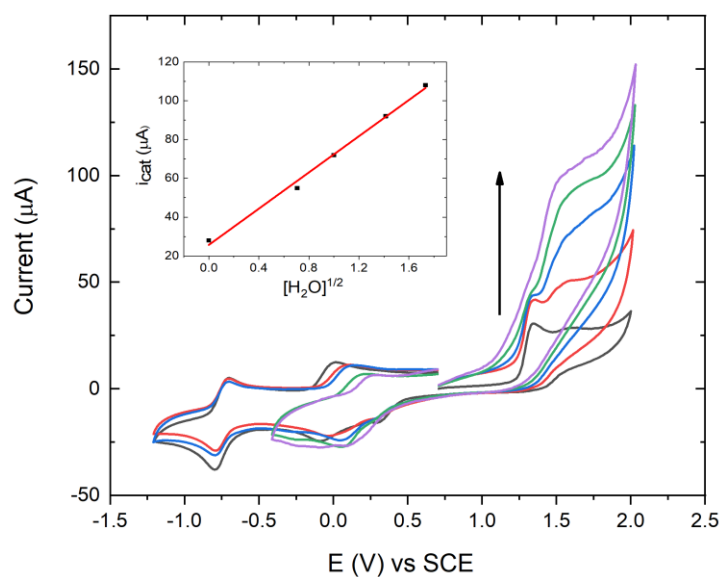


Figure II-26 : Cyclic voltammograms of 1 mM $Fe^{III}DPyCl_2$ measured in acetonitrile (black) in presence of 0.5 M (red), 1 M (blue), 2 M (green) and 3 M (purple) water. Scan towards positive potentials. Inset: Plot of catalytic current at 1.53 V versus water concentration.

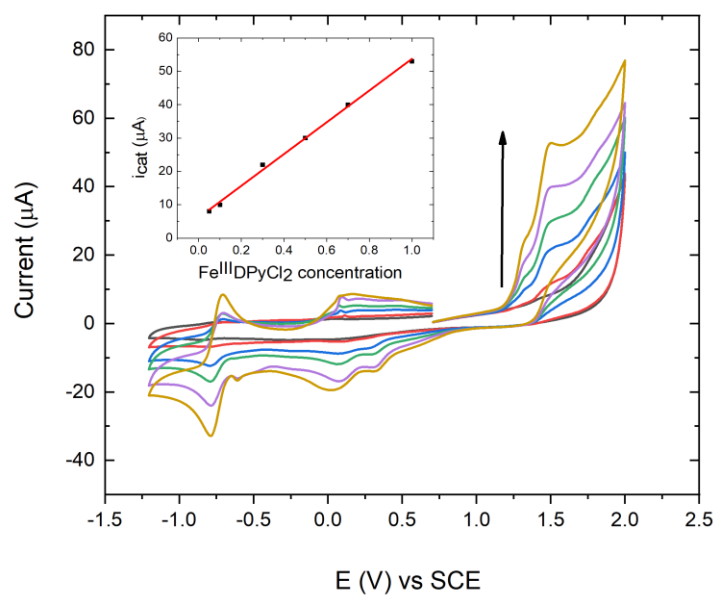


Figure II-27 : Cyclic voltammograms measured in acetonitrile with 2 M water of 0.05 mM (black), 0.1 mM (red), 0.3 mM (blue), 0.5 mM (green), 0.7 mM (purple) and 1 mM (yellow) $Fe^{III}DPyCl_2$. Scan towards positive potentials. Inset: Plot of catalytic current at 1.53 V versus the $Fe^{III}DPyCl_2$ concentration.

II.3 Synthesis and characterization of diiron complex $(\text{Fe}^{\text{III}}\text{DPy})_2\text{O}(\text{OTf})_2$

$\text{Fe}^{\text{III}}\text{DPyCl}_2$ complex was synthesized and characterized with various spectroscopic analyses. Electrochemical study revealed an interesting use of this complex in electrocatalytic reaction. However, the Fe-Cl bond which is rather stable, probably slow down the formation of Fe-OH₂ and Fe-O₂ species required to activate water or dioxygen for oxidation reaction. We thus decided to replace it with a more labile ligand such as triflate by using ferrous triflate $\text{Fe}(\text{OTf})_2$ as iron salt precursor. Triflate being a weaker electron donor ligand than chloride, it should also enhance the electrophilicity of iron complex.

II.3.1 Synthesis & characterization

Iron(II) triflate reacted quickly with DPy ligand in methanol under argon in glove box. The instant color change from red to blue confirmed the formation of iron(II) DPy intermediate, which was then oxidized to Fe^{III} complex upon exposure to air as attested by a color change to cyan (Figure II-28). The iron(III) complex was obtained by evaporating methanol and was recrystallized by slowly diffusing pentane into a saturated solution in ethanol (85% yield).

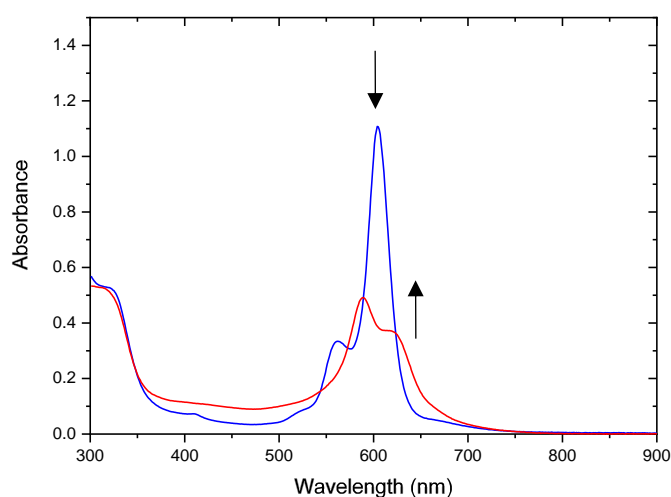


Figure II-28 : UV-visible spectra of $\text{Fe}^{\text{II}}(\text{DPy})(\text{OTf})$ under argon (blue) after exposure to air (red).

II.3.1.1 Absorption spectroscopy

The new UV-vis spectrum (Figure II-29) shows four intense bands ($\epsilon = 23700$; 30500 ; 33700 and $34500 \text{ M}^{-1}.\text{cm}^{-1}$) at 616 ; 588 ; 319 and 295 nm , respectively that correspond probably to $\pi-\pi^*$ charge transfer transitions within the ligand as in $\text{Fe}^{\text{III}}\text{DPyCl}_2$. A broad band ($\epsilon = 8260 \text{ M}^{-1}.\text{cm}^{-1}$) observed at around 420 nm is attributed to metal to ligand charge transfer (MLCT).

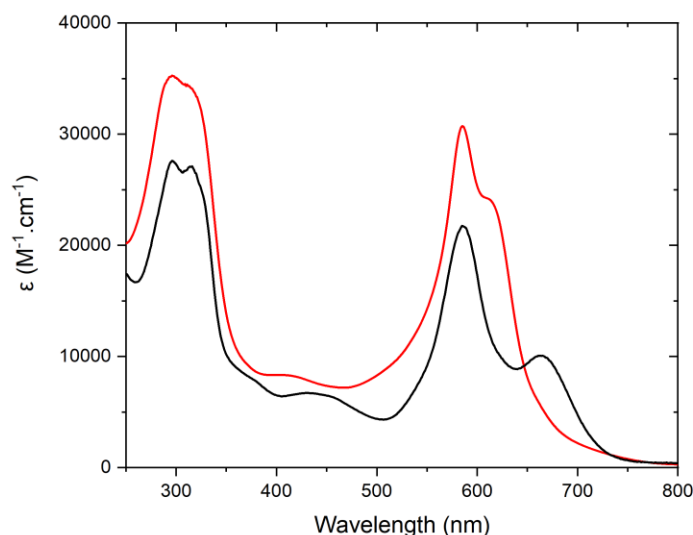


Figure II-29 : UV-vis spectrum of $[\text{Fe}^{\text{III}}(\text{DPy})](\text{OTf})_2$ (red) and $\text{Fe}^{\text{III}}\text{DPyCl}_2$ (black) in acetonitrile.

II.3.1.2 Structure determination in the solid state by X-Ray diffraction crystallographie

Purple monocrystals previously obtained were analyzed by X-Ray diffraction analysis. Resolution of the X-Ray diffraction structure revealed the formation of a μ -oxo diiron(III) dimer instead of a bistriflate monomer. This result was not unexpected and possible mechanism explaining the dimer formation will be discussed in paragraph II.3.2. Figure II-30 shows the ORTEP diagrams of complex and Table 2 display selected bond lengths and angles for the crystallographically determined structures.

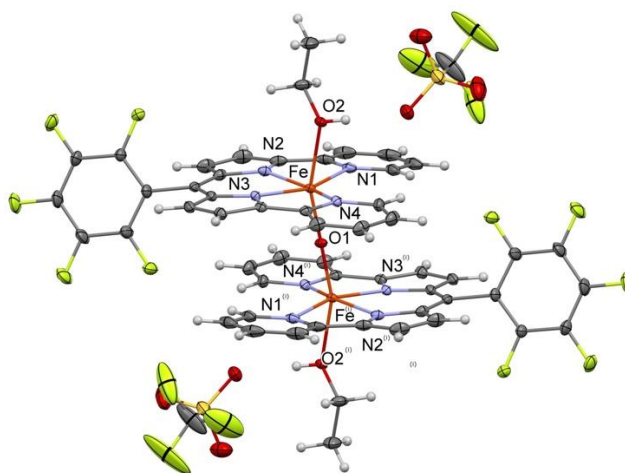


Figure II-30 : An ORTEP drawing of compound complex $\{[Fe^{III}DPy(EtOH)]_2O\}(OTf)_2$. Thermal ellipsoids are shown at the 30% level of probability. (symmetry codes: (i) – x, – y, – z).

Bonds lengths		Angles	
Fe- N1	2.213(3)	N1-Fe-N2	76.02(12)
Fe- N2	2.051(3)	N1-Fe-N3	157.61(11)
Fe- N3	2.055(3)	N1-Fe-N4	124.53(11)
Fe- N4	2.203(3)	N2-Fe-N3	82.12(10)
Fe- O1	1.7710(4)	N2-Fe-N4	157.40(11)
Fe- O2	2.165(2)	N3-Fe-N4	76.38(10)
		O2-Fe-O1	160.24(7)
		Fe-O1-Fe ^(-x;-y;-z)	180

Table II-2 : Selected Bond Distances (Å) and Angles (°) for $Fe^{III}DPyCl_2$ complex with estimated standard deviation's in parenthesis.

Remarkably, the structure of dimer in solid state revealed that triflate ligands have been displaced by ethanol. The coordination sphere of each iron(III) ion is described by the four nitrogen atoms of the DPy ligand in a meridional plane and oxygen atoms from the bridging oxo and one ethanol molecule in apical positions. Two triflate counter anions assure

electroneutrality. The Fe-N bond lengths and the N-Fe-N angles are rather similar to that of $\text{Fe}^{\text{III}}\text{DPyCl}_2$ complex. The bridging Fe-O bond distances (1.77 Å) are within the range of typical diiron μ -oxo distances. The structure of $\{[\text{Fe}^{\text{III}}\text{DPy}(\text{EtOH})_2\text{O}](\text{OTf})_2\}$ is characterized by a linear Fe-O-Fe angle of 180°. Consequently, two planar ligands are quite parallel to each other, leading to a strong π - π stacking interaction between the two parallel rings of ligand. This π - π stacking distance between two plans is 3.542 Å that is close the distance of 3.35 Å known for graphite sheets.¹¹¹ This interligand π - π stacking interaction participate to stabilize the μ -oxo bridged diiron complex,¹¹²⁻¹¹⁴ resulting to the short bridging Fe-O bonds and Fe-Fe distance which probably revealed a strong antiferromagnetic coupling between two iron center predicting a silent EPR spectrum.

II.3.1.3 ESI-HRMS measurement

The ESI- HRMS analysis of a dissolved crystals in acetonitrile confirmed the dimeric nature of the complex in solution. Two peaks were detected; one a peak at $m/z = 527.0278$ which was attributed to $[(\text{Fe}^{\text{III}}\text{DPy})_2\text{O}]^{2+}$ ion and second at $m/z = 519.0329$ which was assigned to $[\text{Fe}^{\text{II}}\text{DPy}]^+$ ion (Figure II-31). No peak corresponding to complex with acetonitrile or triflate adduct was observed.

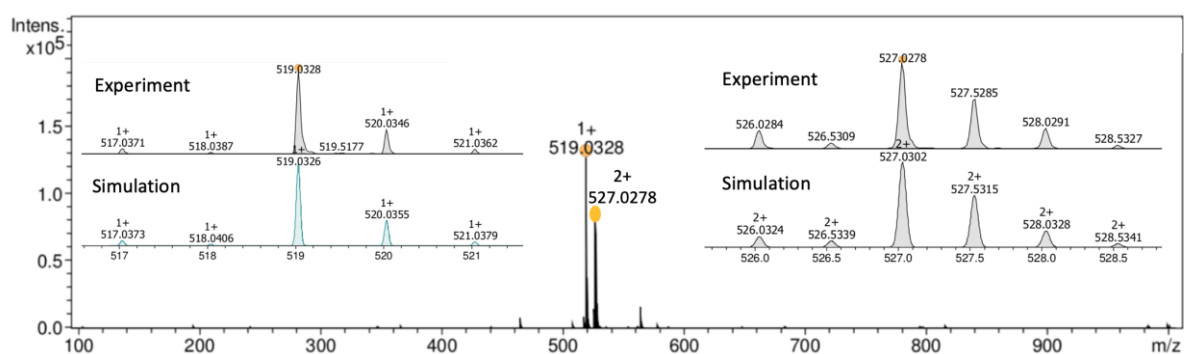


Figure II-31 : ESI⁺-HRMS spectrum of the $[(\text{Fe}^{\text{III}}\text{DPy})_2\text{O}](\text{OTf})_2$ solution in acetonitrile. Inset: comparing experimental and theoretical peaks for the isotopic distribution.

The formation of iron(II) complex can be explained by the decomposition of the diiron(III) μ -oxo complex by homolytic cleavage of a Fe-O bond upon heating at 180 °C to vaporize for

mass spectroscopy analysis (Figure II-32). Unfortunately, the highly active iron-oxo species was not observed in these conditions.



Figure II-32 : Formation of iron(II) complex from diiron complex.

However, this observation revealed the fragility of the Fe-O bond and suggests our diiron complex could be used as a catalyst able to trap and transfer an oxygen atom from dioxygen to a substrate, by generating the active high oxidized iron(IV)-oxo species through an auto-activation or photo-activation strategy such as presented in paragraph I.2.2.2.

II.3.1.4 Electrochemical study

In acetonitrile, the triflate ligands are expected to be displaced by solvent molecule. Accordingly, the Fe^{III}/Fe^{II} oxidation wave is shifted to a higher potential at 0.7 V compared to Fe^{III}DPyCl₂ complex (0 V) while the reduction wave taking place at the ligand at -0.72 V remains (Figure II-33). The two reduction waves observed at 0.57 V and 0.33 V can probably be assigned to reduction of the two iron(III) center in the dimer corresponding to the two Fe^{III}OFe^{III} / Fe^{II}OFe^{III} and Fe^{II}OFe^{III} / Fe^{II}OFe^{II} couples. Finally, we propose that the diiron(II) μ-oxo complex obtained by reducing both iron(III) centers dissociates to two monomer iron(II) complexes, the oxidation wave of which is observed at 0.7 V. The coordination of π-acceptor ligand such as acetonitrile probably causes the positive-shift of Fe^{III}/Fe^{II} couple compared to Fe^{III}DPyCl₂ complex with π-donor chloride ligand. The positive charge of complex when acetonitrile occupies one axial coordination site also participates in increasing the oxidation potential. Finally, the reduction wave was observed at -0.21 V probably corresponds to Fe^{III}/Fe^{II} with triflate on axial coordination site.

Cyclic voltammetry of (Fe^{III}DPy)₂O(OTf)₂ in acetonitrile (Figure II-33) also shows two oxidation waves at 1.32 V and 1.63 V. The intensity of the first one is strongly diminished and probably correspond to the oxidation at the ligand. The second is higher in intensity and might concern the oxidation of the iron center to iron(IV/V) species as discussed above.

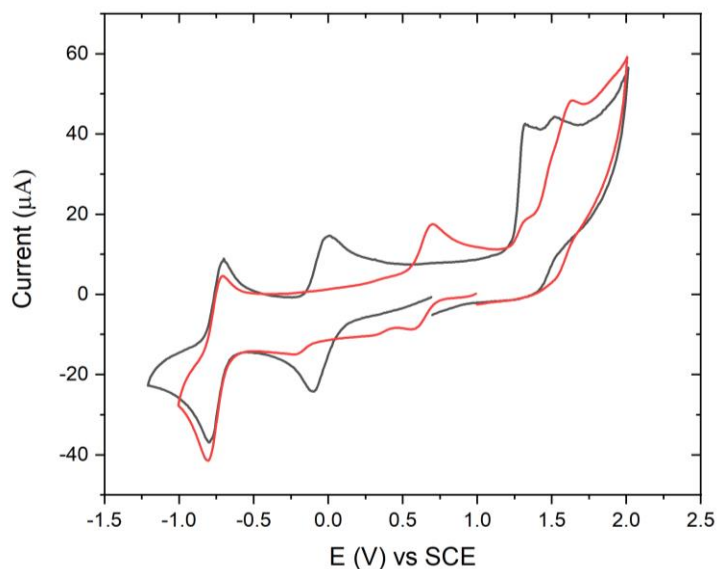


Figure II-33: Cyclic voltammogram of 1 mM $(\text{Fe}^{\text{III}}\text{DPy})_2\text{O}(\text{OTf})_2$ (red) and 1 mM $\text{Fe}^{\text{III}}\text{DPyCl}_2$ (black) measured in acetonitrile.

In presence of water, the $\text{Fe}^{\text{III}}/\text{Fe}^{\text{II}}$ oxidation wave was shifted to 0.38 V while two reduction waves were observed at 0.12 V and -0.15 V. The negative shift of the redox $\text{Fe}^{\text{III}}/\text{Fe}^{\text{II}}$ potential probably reveals that acetonitrile molecules were displaced by water molecules (Figure II-34). Moreover, an intense oxidation wave at 1.53 V was again observed and probably corresponds to the electrocatalytic water oxidation by $(\text{Fe}^{\text{III}}\text{DPy})_2\text{O}(\text{OTf})_2$ as noticed with the $\text{Fe}^{\text{III}}\text{DPyCl}_2$ monomer. Here too, a more in-depth study is needed to underpin the ongoing catalytic electrochemical reactions.

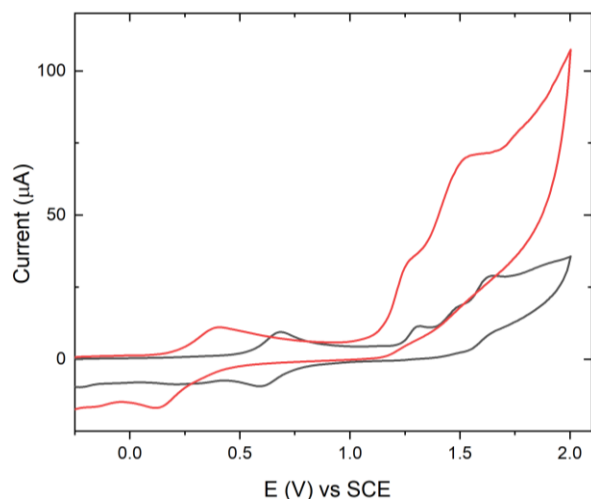


Figure II-34 : Cyclic voltammograms of 1 mM $(Fe^{III}DPy)_2O(OTf)_2$ (black) measured in acetonitrile in presence of 3 M water (red).

II.3.2 Dimer to monomer interconversion

The mechanism of the formation of μ -oxo dimeric iron complex can be envisioned to proceed as mentioned in the well-developed iron porphyrin literature.^{115,116} It would start with the initial coordination of O_2 to Fe^{II} complex to afford a superoxo $Fe^{III}-OO^\bullet$ species. The reaction of this iron(III) superoxo species with the starting iron(II) complex would afford a peroxide-bridged $Fe^{III}-OO-Fe^{III}$ ferric dimer. The O-O bond cleavage would lead to the highly oxidized iron(IV)-oxo species that would ultimately react with the starting iron(II) complex to generate the μ -oxo-bridge ferric dimer (Figure II-35).

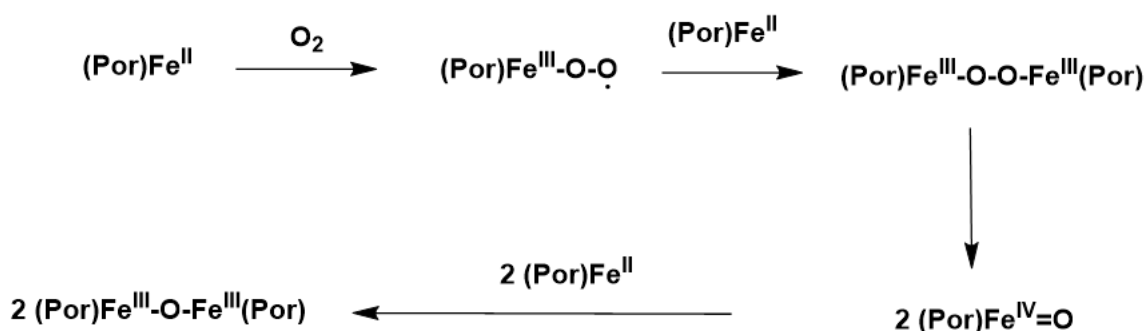


Figure II-35: Proposed mechanism for formation of diiron(III) porphyrin starting from iron(II) complex.

However, the formation of diiron(III) complex $(\text{Fe}^{\text{III}}\text{DPy})_2\text{O}(\text{OTf})_2$ was also observed by using $\text{Fe}^{\text{III}}(\text{OTf})_3$ precursor. In this case, the dimerization would probably proceed via the formation of an iron(III) hydroxo complex, due to water traces in solution, then followed by formation of hydroxo-bridged ferric dimer $\text{Fe}^{\text{III}}\text{-(OH)-Fe}^{\text{III}}$ that would release a μ -oxo diiron(III) complex upon deprotonation (Figure II-36).^{117,118} Alternatively a bis- μ -hydroxo dimer could be formed and lead to the μ -oxo dimer by condensation.¹¹⁹

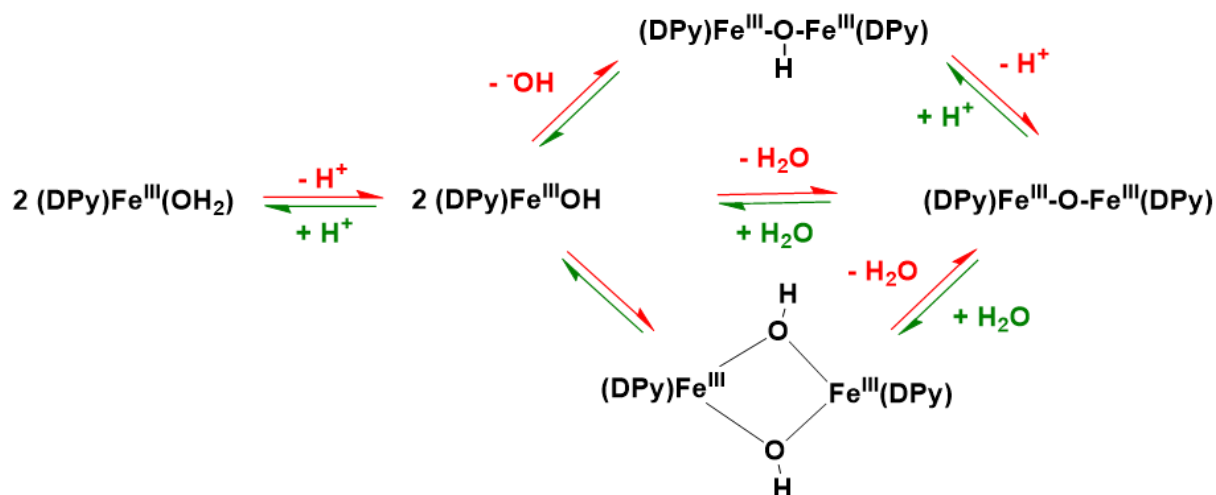


Figure II-36 : One proposed mechanism for formation of μ -oxo diiron(III) DPy starting from iron(III) complex.

These two pathways indicate how the monomer can be converted into a μ -oxo-dimer. Additionally, HRMS analysis of dimer revealed the Fe-O can be activated under certain conditions such as high temperature. Therefore, the dimer to monomer transformation was studied by using different conditions to understand how to activate Fe-O bond.

II.3.2.1 Dimer to monomer conversion upon ligand exchange

In an attempt to crystallize dimer with triflate axial ligand instead of ethanol, the dimer solution in non-coordinating chloroform was slowly evaporated at 30 °C. Interestingly, the X-Ray diffraction analysis of the single crystals obtained showed a monomer iron(III) complex with two triflates ligands occupying the axial positions instead of a dimer. The Fe-O bond was

probably cleaved by heating at 30 °C and the dimer was transformed to a more stable bis(trisflate) monomer form in absence of water or coordinating solvent.

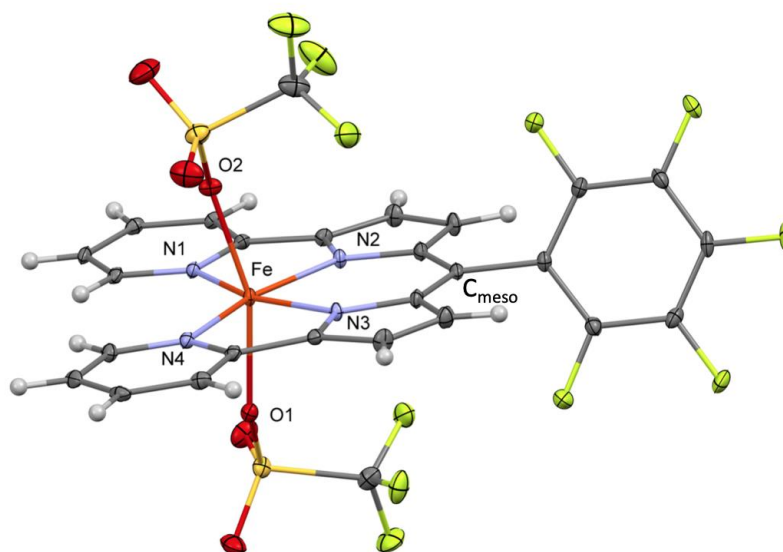


Figure II-37 : An ORTEP drawing of compound complex $[Fe^{III}DPy(OTf)_2]$. Thermal ellipsoids are shown at 30% level of probability.

Bond distances		Angles	
Fe- N1	2.133	N1-Fe-N4	122.88
Fe- N2	2.020	N1-Fe-N2	77.37
Fe- N3	2.023	N2-Fe-N3	82.28
Fe- N4	2.139	O1-Fe-O2	161.03
Fe- O1	2.046	N1-Fe-O1	87.41
Fe- O2	2.050	N2-Fe-O2	82.96

Table II-3 : Selected Bond Distances (\AA) and Angles ($^\circ$) for $Fe^{III}DPyCl_2$ complex.

Figure II-37 shows the ORTEP diagram of the complex and Table II-3 displays selected bond lengths and angles for the crystallographically determined structure. The Fe-N bond lengths of $[Fe^{III}DPy(OTf)_2]$ complex are slightly shorter than that of $Fe^{III}DPyCl_2$ monomer and $\{[Fe^{III}DPy(EtOH)]_2O\}(OTf)_2$ dimer probably because triflate is a weaker ligand compared to strong ligand donor such as chloride and ethanol. As a consequence, the two pyridine arms are closer to each other than in the two latter complexes, the $N_{Py}-C_{meso}-N_{Py}$ angle being of

44.2 ° for this complex versus 47.4 ° for $\text{Fe}^{\text{III}}\text{DPyCl}_2$ monomer and 46.2 ° for $\{[\text{Fe}^{\text{III}}\text{DPy}(\text{EtOH})]_2\text{O}\}(\text{OTf})_2$ dimer.

We also questioned the possibility to prevent the formation of the dimer by adding chloride iron(III). Upon addition of four equivalents of $(^t\text{Bu}_4\text{N})\text{Cl}$ in the $(\text{Fe}^{\text{III}}\text{DPy})_2\text{O}(\text{OTf})_2$ solution in acetonitrile, the instant color change was immediately observed from cyan to blue. UV-visible spectrum after adding $(^t\text{Bu}_4\text{N})\text{Cl}$ showed absorbance at 666 nm and 584 nm characteristic for $\text{Fe}^{\text{III}}\text{DPyCl}_2$ (Figure II-38), indicating that the μ -oxo structure can be cleaved by introducing chloride ligand at the two axial positions of the iron center.

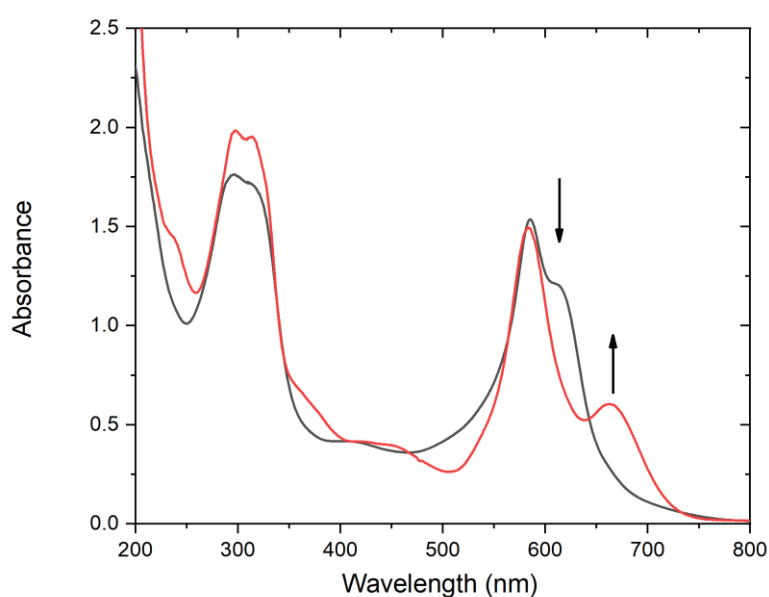


Figure II-38: UV-visible change after adding 4 eq $(^t\text{Bu}_4\text{N})\text{Cl}$ into a 50 μM $(\text{Fe}^{\text{III}}\text{DPy})_2\text{O}(\text{OTf})_2$ solution in acetonitrile.

II.3.2.2 Reversible μ -oxo-bridge cleavage by acid and base addition

The μ -oxo-bridge of $(\text{Fe}^{\text{III}}\text{DPy})_2\text{O}(\text{OTf})_2$ can be reversibly cleaved with acid (HX) to afford either the corresponding anion-bound (Fe-X) or solvent-bound (Fe-MeCN) product or Fe-OH complex. In the following study, triflic acid was used so as to keep the same counter anion (triflate). Therefore, the monomer obtained could be the Fe-MeCN or Fe-OH complex because triflate is a weak ligand compared to acetonitrile and hydroxy coordinating groups.

Indeed, the electrochemical study of the dimer $(\text{Fe}^{\text{III}}\text{DPy})_2\text{O}(\text{OTf})_2$ in acetonitrile revealed that the axial positions on iron coordination were occupied by the solvent molecules and not by triflate ions.

The color change was observed within 10 min by adding 1 eq triflic acid into a solution of the dimeric μ -oxo-bridged complex in acetonitrile at room temperature. This is illustrated in the electronic absorption spectrum shown Figure II-39. UV-visible spectra showed five isosbestic points at 310, 364, 424, 540 and 610 nm indicating a clean chemical transformation. The new spectrum obtained after complete transformation shows an intense band at 621 nm, a broad band around 490 nm and a weak band around 700 nm, that pertains the reversible conversion to the monomeric form of the complex.

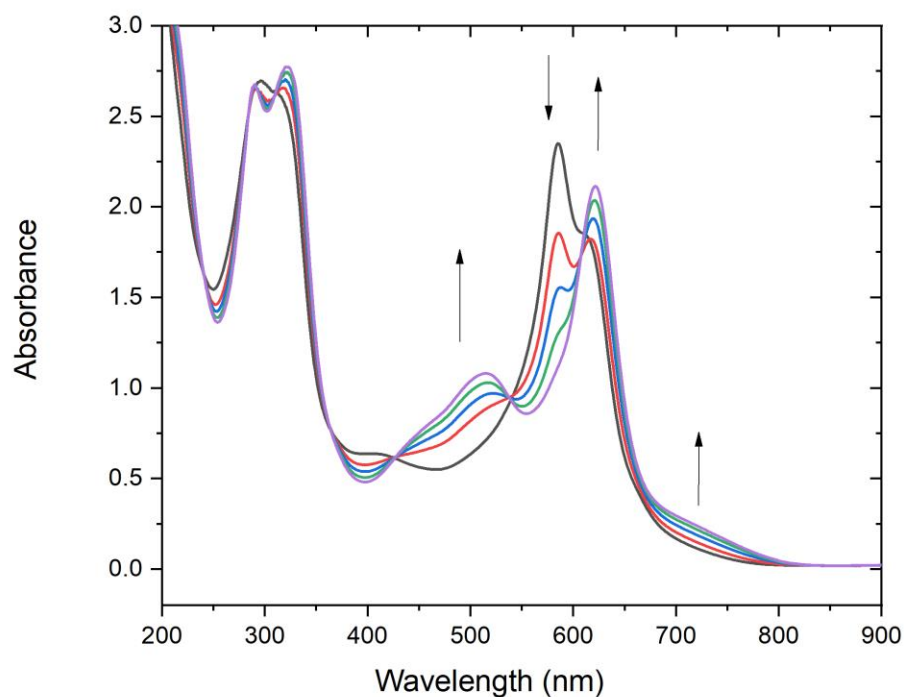


Figure II-39: UV-visible spectrum evolution showing the reaction of 1 eq triflic acid with $(\text{Fe}^{\text{III}}\text{DPy})_2\text{O}(\text{OTf})_2$ in acetonitrile at room temperature in 10 min.

The dimer-to-monomer conversion by 1 eq triflic acid was confirmed by EPR analysis at 10 K. The EPR spectrum of $(\text{Fe}^{\text{III}}\text{DPy})_2\text{O}(\text{OTf})_2$ in acetonitrile is silent due to antiferromagnetically interaction of the μ -oxo bridged diiron cores. The addition of 1 eq triflic

acid gave an EPR active species shown Figure II-40. The signal at $g = 4.3$ assigned a rhombic high spin iron(III) species, indicates the cleavage of Fe-O_{oxo} bond.

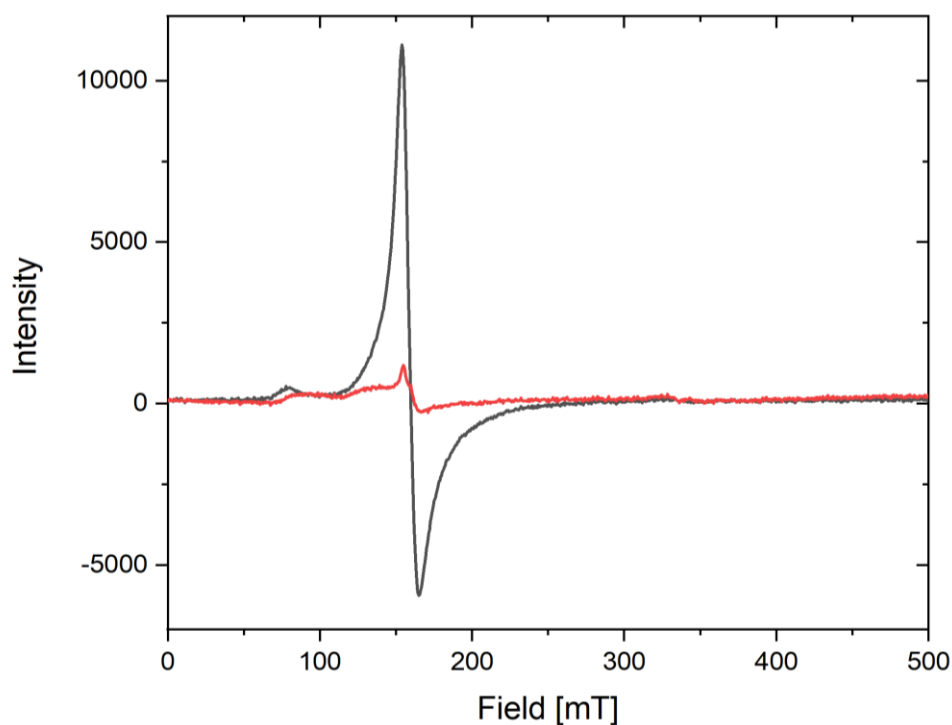


Figure II-40 : EPR spectra of $(Fe^{III}DPy)_2O(OTf)_2$ before (red) and after (black) adding 1 eq triflic acid.

This dimer-to-monomer transformation was optimal upon addition of 1eq of acid per dimer. This indicates that the dimer to monomer transformation proceeds via the protonation of the μ -oxo bridged diiron complex followed by water coordination and condensation (Figure II-36).

Adding 1 eq of $(^tBu_4N)OH$ to the previous solution led to recovery of the initial dimer as monitored by UV-visible absorption spectroscopy (Figure II-41). Based on absorption band, the monomer was completely converted to the μ -oxo bridged dimer by only one equivalent of base in a few seconds. The transformation mechanism was probably through hydroxo bridged dimer again or by condensation as description in Figure II-36.

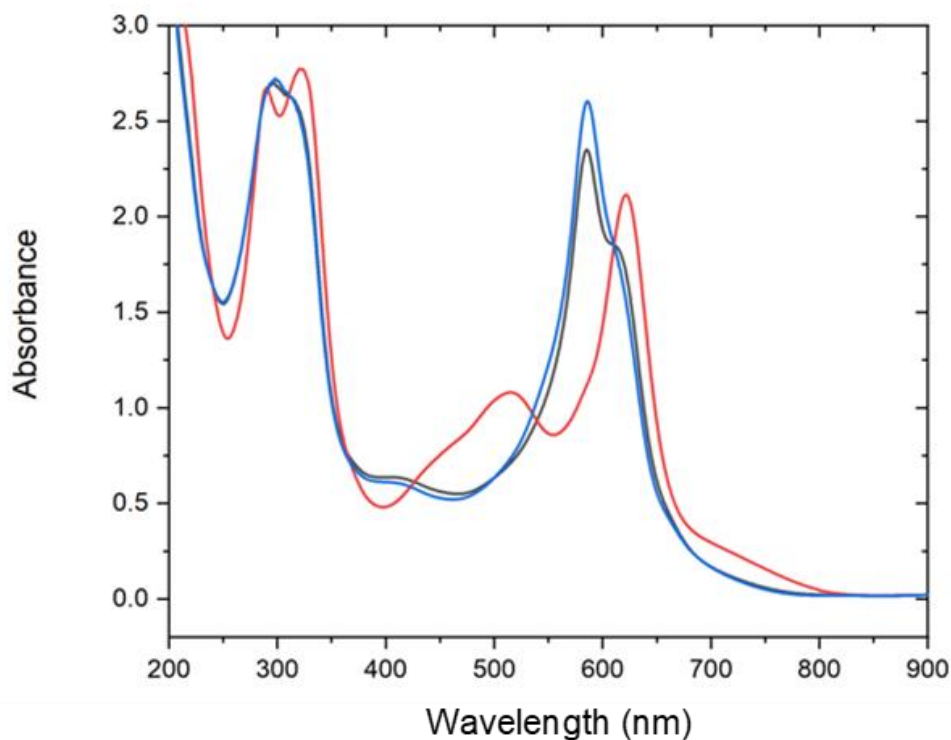


Figure II-41 : UV-visible spectra showing that the reaction of 1 eq ($t\text{Bu}_4\text{N}$)OH with monomer iron(III) complex obtained above (red) in acetonitrile affords the μ -oxo dimer (blue). Black : UV-visible spectrum of the initial dimer.

II.4 Conclusion

The synthesis of iron(III) complex based on DPy ligand was realized by using two different iron salt precursors. A monomeric $\text{Fe}^{\text{III}}\text{DPyCl}_2$ complex was obtained with chloride iron salt while using triflate iron salt led to the formation of a dimer, the μ -oxo bridged diiron(III) complex $\{[\text{Fe}^{\text{III}}\text{DPy}(\text{EtOH})_2\text{O}](\text{OTf})_2\}$. The chloride ions that act as strong electron donor ligands prevent the formation of dimer but also transform dimer to monomer by occupying two axial positions on iron. Moreover, μ -oxo diiron(III) complex can be transformed to the iron(III) monomer under mild temperature in non-coordinating aprotic solvent or upon addition of acid. The lability of Fe-O bridge revealed that this μ -oxo dimer can be a potential catalyst for oxygen atom transfer reaction.

Both iron(III) monomer $\text{Fe}^{\text{III}}\text{DPyCl}_2$ and diiron(III) dimer $\{[\{\text{Fe}^{\text{III}}\text{DPy}(\text{EtOH})\}_2\text{O}](\text{OTf})_2\}$ were electrochemically studied to understand their redox properties before using in catalytic reaction. The EPR analysis of the solutions obtained by oxidizing and reducing complex by electrolysis allowed to characterize the oxidized and reduced species, then to determine if the locus of oxidation and reduction takes place at the iron center or the ligand. The EPR spectra evidenced that the first reduction occurs at the metal center to form iron(II) complex and the second is probably centered at the non-innocent DPy ligand. While, the oxidation processes occurring at very close potentials, probably concerned the DPy ligand but iron center and chloride could also be oxidize. However, iron center seemed be oxidized to a putative iron(V)-oxo species in presence of water as a proton source.

Preliminary electrocatalytic study with monomer $\text{Fe}^{\text{III}}\text{DPyCl}_2$ demonstrated a promising reactivity in activation of inert molecule such as carbon dioxide and water. It is probable that $\text{Fe}^{\text{III}}\text{DPyCl}_2$ could be electro-activated to generate an active iron(V)-oxo species capable of activating water molecules. On the other hand, carbon monoxide was identified as a product in carbon dioxide reduction electrochemically catalyzed by $\text{Fe}^{\text{III}}\text{DPyCl}_2$. Moreover, there were probably other reduced products non-detected in carbon dioxide reduction. Although $\text{Fe}^{\text{III}}\text{DPyCl}_2$ exhibited a moderate selectivity for carbon dioxide reduction compared to hydrogen reduction, its selectivity could be improved either by structural modifications or under optimization of experimental conditions.

In the next chapter, $\{[\{\text{Fe}^{\text{III}}\text{DPy}(\text{EtOH})\}_2\text{O}](\text{OTf})_2\}$ dimer with a fragile Fe-O bond will be used in the study of a photocatalytic oxidation using O_2 as oxygen source. In the following, the well-defined monomer $\text{Fe}^{\text{III}}\text{DPyCl}_2$ will be used as catalyst to perform oxidation using chemical oxidation.

Chapter III : Reversible Electron Relay to
Exclude Sacrificial electron Donor in
Photocatalytic Oxygen Atom Transfer
Reaction with O₂ in Water

III.1 State of the art

Dioxygen is an abundant molecule and the true green oxidant which serves as the main supplier of the oxygen atom in the biosynthesis of essential organic molecules. Although the thermodynamics behind these chemical reactions are favorable, kinetic limitation come from the fundamental paramagnetic state of dioxygen. This limitation can be lifted off when dioxygen is partnered with paramagnetic species or excited triplet states that can undergo single electron transfer reactions. Chemists have taken inspiration from biology to develop metal complexes that can bind and activate dioxygen in presence of co-reductants thereby the active metal-oxo species.¹²⁰

Photoactivating dioxygen at a metal complex through light-induced electron transfer is an even more desirable target. In 2013, Aukauloo and Mahy reported a synthetic diiron(III) complex $[(\text{N-EtHPTB})\text{Fe}^{\text{III}}\text{Fe}^{\text{III}}]^{5+}$ (N-EtHPTB = N,N,N',N'-tetrakis(N-ethyl-2-benzimidazolylmethyl)-2-hydroxy-1,3-diaminopropane) as a model of the MMO enzyme able to activate dioxygen using a ruthenium-polypyridine type complex $[\text{Ru}^{\text{II}}(\text{bpy})_3]^{2+}$ (bpy = bispyridine) as a chromophore and triethylamine (TEA) as a sacrificial electron donor (Figure III-1).¹²¹ Upon light irradiation, the excited state of chromophore $\text{Ru}^{\text{II}*}$ was quenched by TEA to form the powerful reduced Ru^{I} capable of reducing both two iron centers of $[(\text{N-EtHPTB})\text{Fe}^{\text{III}}\text{Fe}^{\text{III}}]^{5+}$ dimer to $[(\text{N-EtHPTB})\text{Fe}^{\text{II}}\text{Fe}^{\text{II}}]^{3+}$ dimer. The reaction of the photoreduced diiron(II) complex with dioxygen leads to formation of an active μ -peroxo diiron(III) intermediate responsible for transferring oxygen atom to triphenylphosphine (PPh_3).

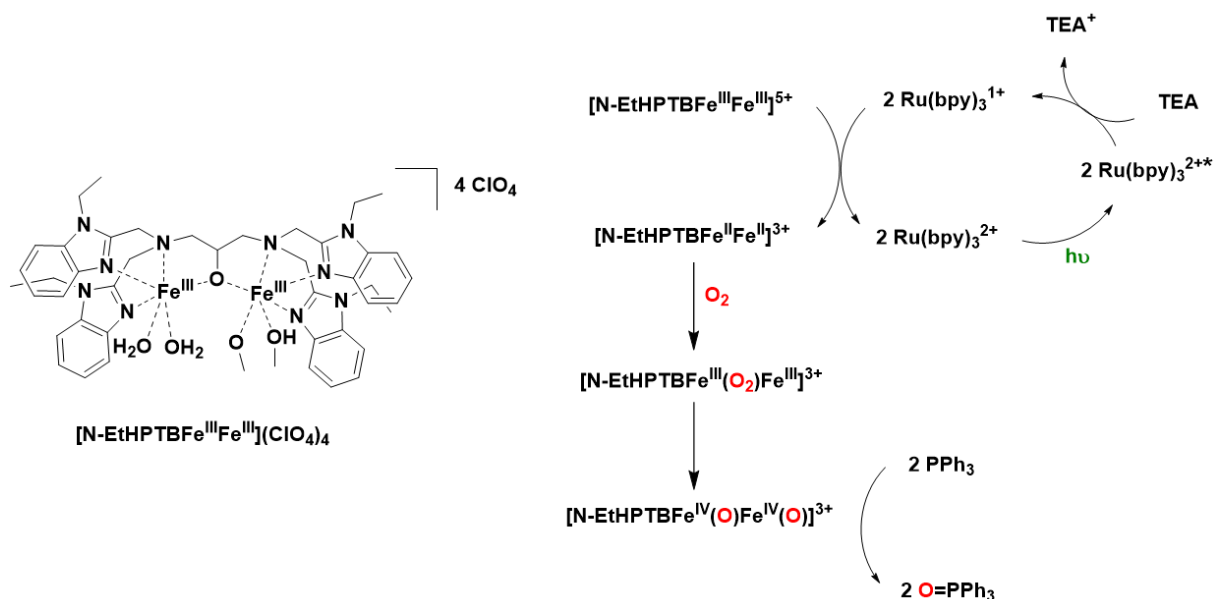


Figure III-1 : Proposed mechanism for the photoinduced dioxygen activation at a dinuclear iron(III) complex.

A dyad containing a Ru^{II} photosensitizer and a Cu^{II} pre-catalyst reported by Iali et al. in 2015 was proven to be efficient for sulfides, phosphines, and alkene light-driven catalytic oxidation in presence of triethanolamine (TEOA) as sacrificial electron donor and O_2 as oxygen atom donor.¹²² Ru^{II} - Cu^{II} absorbs a photon to yield a Ru^{II*} - Cu^{II} excited state followed by an intramolecular electron transfer to form Ru^{III} - Cu^I . Subsequent reduction by TEOA generates Ru^{II} - Cu^I capable of forming the Ru^{II} - $Cu^{II}(O_2)$ adduct responsible for substrate oxygenation (Figure III-2).

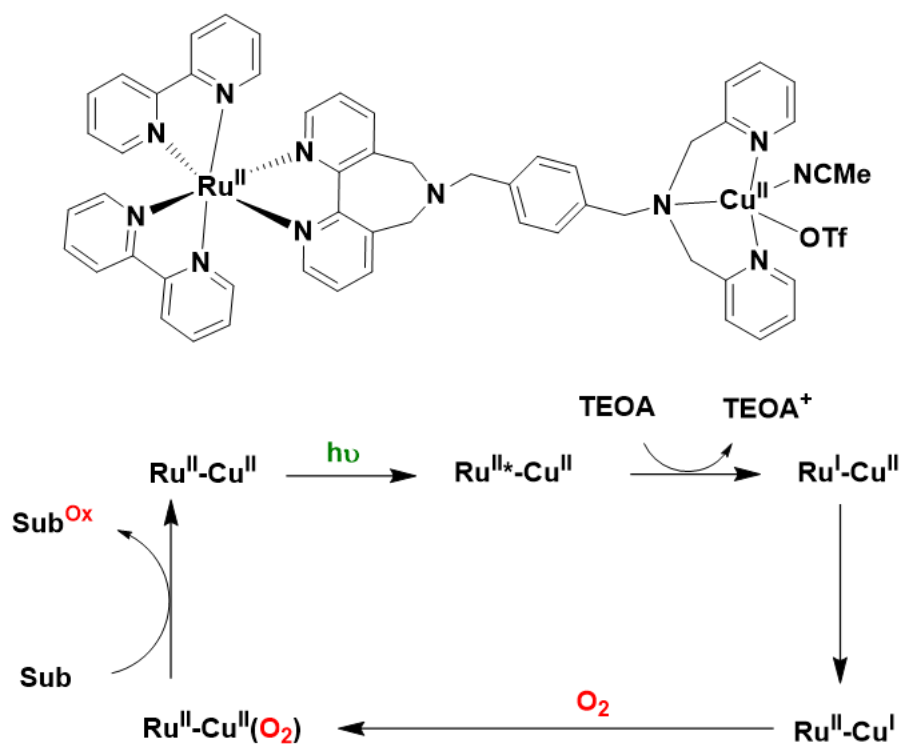


Figure III-2 : Oxygenation of organic substrate by a photosensitizing-precatalyst dyad through light-driven dioxygen activation.

These two classical approaches need a sacrificial electron donor to drive photo-induced reactions. But precluding these necessary “evil” molecules in photocatalytic processes is an urgent issue because they can interfere in the activation pathway and also limit the implementation of these chemical oxidation transformations.¹²³

In a very different approach, Mühldorf and Wolf more recently reported a dual catalytic system containing riboflavin tetraacetate (RFT) and $[\text{Fe}^{\text{II}}(\text{TPA})(\text{MeCN})_2](\text{ClO}_4)_2$ complex that efficiently catalyze photooxygenation of various challenging substrates using dioxygen as oxygen source and with no need for a sacrificial electron donor.¹²⁴ RFT, which is a synthetic flavin analogue is known to be a non-toxic photocatalyst in the aerobic oxidation of alkanes and benzyl alcohol through a radical processes generating hydrogen peroxide as a by-product.^{125,126} The latter reacts with iron(II) complex to generate the active iron-oxo species itself capable of substrate oxidation. These tandem reactions are believed to be the key for high efficiency of this bi-catalytic system (Figure III-3). Indeed, in absence of iron catalyst hydrogen peroxide is a major drawback of photocatalytic RFT system because it degrades RFT upon irradiation.

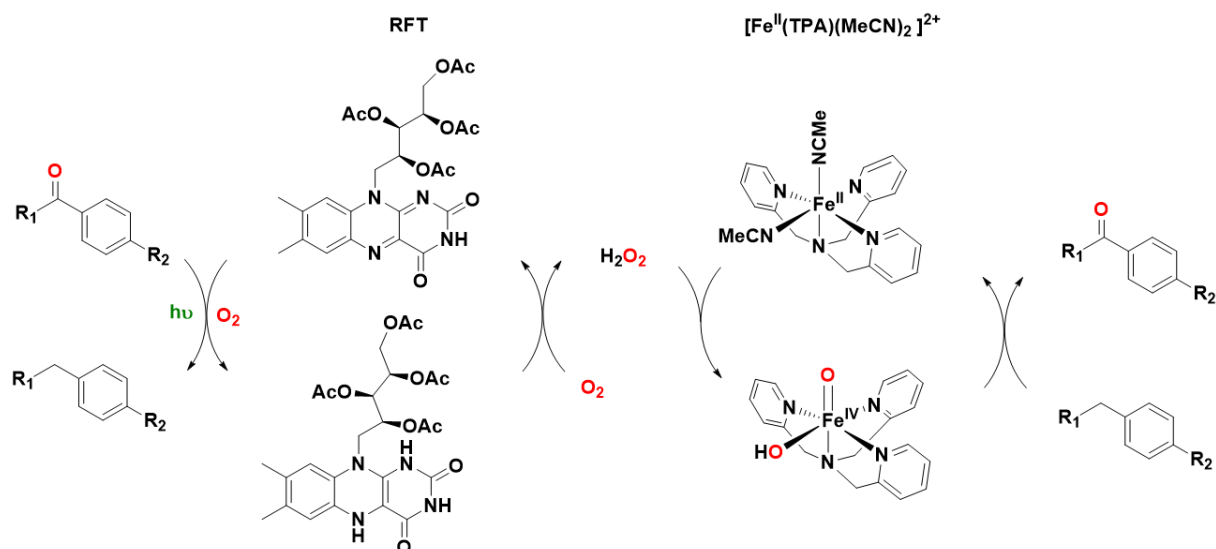


Figure III-3 : Proposed mechanism for photooxidation of substrates catalyzed by dual catalyst system.

On the other hand, it is known that the combination of $[\text{Ru}(\text{bpy})_3]\text{Cl}_2$ and a reversible electron acceptor dichloride methylviologen MV^{2+} can produce hydrogen peroxide upon light irradiation in presence of EDTA as an electron donor in aqueous solution.¹²⁷ Hydrogen peroxide is formed by photo-induced electron transfer from photo-excited state $\text{Ru}^{\text{II}*}$ to dioxygen with the help of MV^{2+} as an electron relay coupled with protonation and the oxidized photosensitizer Ru^{III} is reset to its ground state by oxidizing EDTA (Figure III-4).

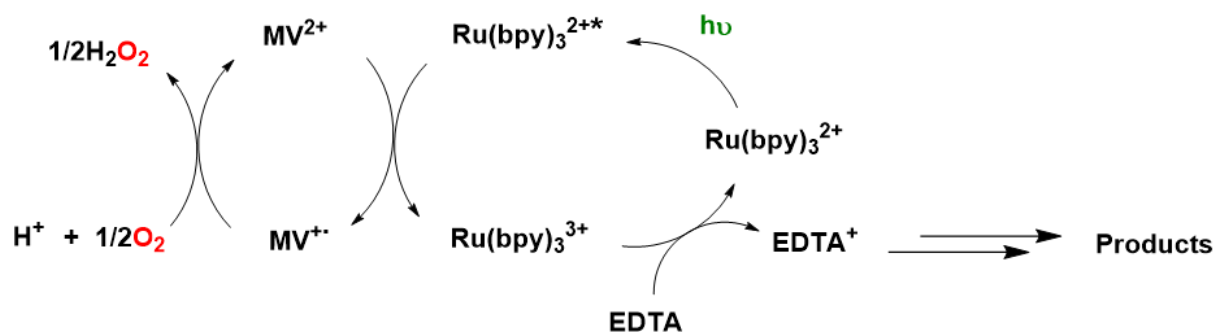


Figure III-4 : Proposed mechanism for producing hydrogen peroxide by light-driven reaction.

The role of $[\text{Ru}(\text{bpy})_3]\text{Cl}_2$ and MV^{2+} in this case can be related to that of RFT photocatalyst producing hydrogen peroxide capable of activating the iron catalyst for oxygenating substrates. Consequently, we reasoned to introduce MV^{2+} in a mixture of the $[\text{Ru}(\text{bpy})_3]\text{Cl}_2$ and iron catalysts to attempt an aerobic photooxidation of alkene substrate in aqueous solution.

In this chapter, we interrogate a counter intuitive approach for the light-driven reductive activation of dioxygen by using $[\text{Ru}(\text{bpy})_3]\text{Cl}_2$ hereby shorthanded as $[\text{Ru}^{\text{II}}]$, as a photosensitizer and MV^{2+} a reversible electron acceptor to preclude the use of sacrificial electron donor in aqueous solution. This work has been submitted to publication by our group simultaneously to the writing of this manuscript, therefore some explanations and scheme have been used as a slightly modified in this chapter.

III.2 Photocatalytic systems using iron(III) DPy catalyst

To explore this reactivity, we chose $[(\text{Fe}^{\text{III}}\text{DPy})_2\text{O}](\text{OTf})_2$ dimer as an analogue of Nocera's μ -oxo diiron porphyrin to play the role of the catalyst in combination with the well-studied photosensitizer tris(bispyridine)ruthenium(II) chloride ($[\text{Ru}^{\text{II}}]$) in presence of methylviologen chloride ($[\text{MV}^{2+}]$) as an electron acceptor and sodium styrene-4-sulfonate (S) as a substrate in a pH = 4 Britton-Robinson B&R buffer aqueous. The aqueous medium was picked because of solubility issues and importantly previous studies have evidenced that methylviologen radical can be quenched by O_2 only in aqueous medium to generate in a first place the superoxide radical. Indeed, such electron transfer process does not happen in organic solvent such as acetonitrile etc... Sodium styrene-4-sulfonate was chosen as a water-soluble substrate. Additionally, its oxidized products can be easily detected and quantified by ^1H NMR (see detail in the experimental section).

The photosensitizer and catalyst were introduced in equimolar amounts (30 μM) while the electron mediate (4 mM) and the substrate (10 mM) were added in excess after testing different condition. Excitation of the photosensitizer $\lambda_{\text{abs}}(\text{max}) = 450 \text{ nm}$ was performed with the combination of a white LED (1.3 $\text{mW}\cdot\text{cm}^{-1}$) and a filter ($T=0$ for $\lambda < 415 \text{ nm}$).

III.2.1 Reactivity

$[(\text{Fe}^{\text{III}}\text{DPy})_2\text{O}](\text{OTf})_2$ (30 μM) was utilized as iron(III) catalyst in a Britton & Robinson pH4 buffer aqueous mixture with the $[\text{Ru}^{\text{II}}]$ photosensitizer (30 μM), the $[\text{MV}^{2+}]$ reversible electron acceptor (4 mM) and an excess of sodium styrene-4-sulfonate (10 mM) (hereby

shorthand as S). Upon continuous illumination using a LED lamp and under an aerobic atmosphere, two oxygenated products were detected, the 4-(1,2-dihydroxyethyl)benzenesulfonate (diol) and the 4-formylbenzenesulfonate (benzaldehyde). ¹H NMR of the reactional mixture revealed the presence of 1.17 mM diol and 1.27 mM of benzaldehyde respectively corresponding to 11.7 % and 12.7 % of oxidation yield based on the substrate with an overall turnover number (TON) of 80 (Table III-1, entry 1). This TON value falls roughly within the range observed for highly oxidized iron species generated upon reaction of iron complex models with O₂ in presence of electron and proton donors.¹²⁸⁻¹³⁰ While, a mixture of [Ru^{II}], S and O₂ was irradiated in presence of [MV²⁺] (Table III-1, entry 4), only trace amounts of oxidized substrate (benzaldehyde) were detected. Moreover, upon addition of iron(III) salt leads also to only trace of benzaldehyde (Table III-1, entry 3). Therefore, the presence of [(Fe^{III}DPy)₂O](OTf)₂ catalyst with the support of exogenous DPy ligand is essential for the observed photocatalytic reaction.

Entry	[Ru(bpy) ₃]Cl ₂	Catalyst	MV ²⁺	Substrate	Product yield ^a			TON ^b
					Diol	Benzaldehyde	Epoxyde	
1	30 μM	30 μM [(Fe ^{III} DPy) ₂ O](OTf) ₂	4 mM	10 mM	11.7%	12.7%	traces	81
3	30 μM	30 μM Fe ^{III} Cl ₃	4 mM	10 mM	0	traces	0	nd
4	30 μM	0	4 mM	10 mM	0	traces	0	nd

Table III-1 : Substrate conversion under different conditions. Oxygenation reactions were carried out under irradiation for 22, under aerobic conditions in B&R bufer at pH 4. ^a The product yield is based on substrate. ^b TON: turnover number is calculated over catalyst.

Of note, the monomer Fe^{III}DPyCl₂ showed a similar reactivity in such condition probably due to its dimerization in aqueous medium.¹³¹ As a result, dimer [(Fe^{III}DPy)₂O](OTf)₂ was utilized in the following studying to clarify the mechanism and active species involved in the reactivity of these systems.

III.2.2 Study of the photocatalytic mechanism

III.2.2.1 *Study of subsystem [Ru^{II}] + O₂*

Upon light irradiation of a reactional mixture containing a [Ru^{II}] photosensitizer, methylviologen [MV²⁺] and semi-hemic iron(III) catalyst [(Fe^{III}DPy)₂O] we succeeded to utilize a reversible electron relay to exclude sacrificial electron donor in the photocatalytic oxygen atom transfer to an alkene with dioxygen in water. Our work provides a new paradigm to perform photocatalytic oxidation of substrates using solely light as energy input and dioxygen as oxygen source. Understanding the chemistry of this new paradigm is indispensable for improving their reactivity. We thus performed a series of experiments to understand the mechanism and identify the active species responsible for substrate oxygenation under our condition.

In 2000, Vaidyalingam and Dutta reported the accumulation of cis-[Ru(bpy)₂(OH₂)₂]²⁺ complex from decomposition of the [Ru(bpy)₃]²⁺ photosensitizer following prolonged irradiation of [Ru(bpy)₃]²⁺.¹³² Cis-[Ru(bpy)₂(OH₂)₂]²⁺ complex can be oxidized to generate highly active Ru^{IV}=O and Ru^{VI}=O species capable of oxygenating substrates.¹³³ However, no photo-degradation of the photosensitizer was observed under our irradiation condition. UV-visible spectrum shown a similar absorption of Ru^{II} photosensitizer at 450 nm before and after irradiation for 22 h (Figure III-5), while cis-[Ru(bpy)₂(OH₂)₂]²⁺ complex is characterized by a absorption band centered at 488 nm. We can thus exclude the participation of chemically altered intermediate such as cis-[Ru(bpy)₂(OH₂)₂]²⁺ as potent photooxidation catalyst.

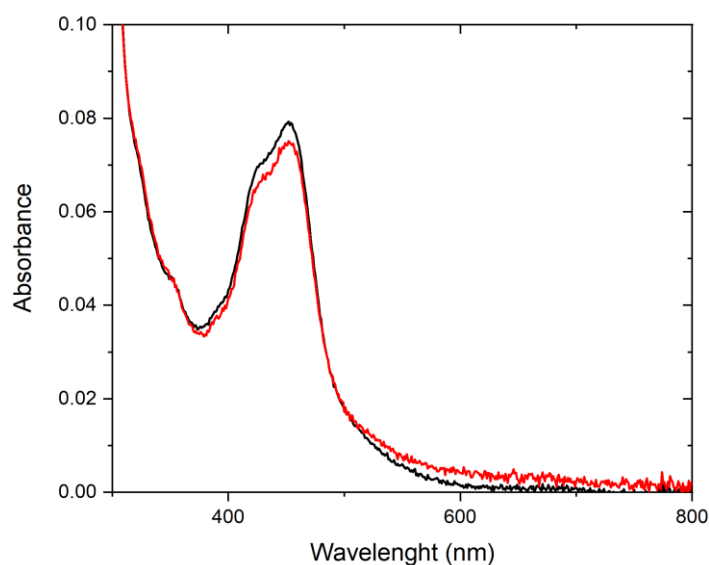


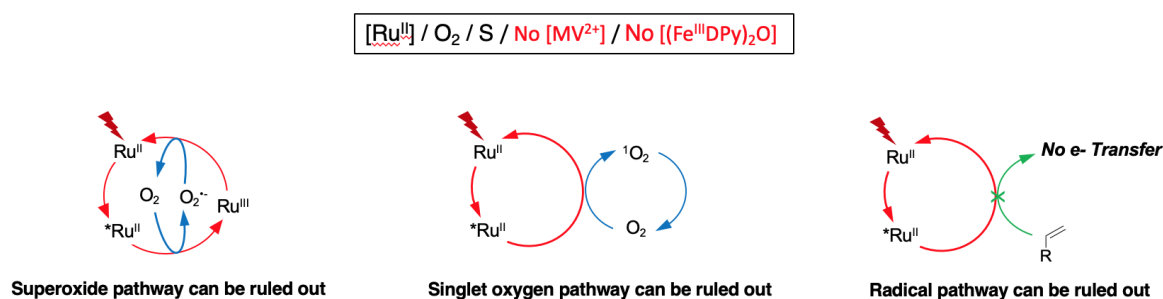
Figure III-5 : UV-visible spectra of $\text{Ru}(\text{bpy})_3\text{Cl}_2$ ($30 \mu\text{M}$) in B&R buffer at pH 4 before (black) and after (red) irradiation for 22h.

We then performed a series of control experiments (Table III-2) combined with the detection of relevant intermediate species by Laser Flash Photolysis (LFP) in order to understand the specific role of each compound in our photocatalytic system.

Entry	$[\text{Ru}(\text{bpy})_3\text{Cl}_2]$	$[(\text{Fe}^{\text{III}}\text{DPy})_2\text{O}](\text{OTf})_2$	MV^{2+}	Substrate	Product yield ^a			TON ^b
					Diol	Benzaldehyde	Epoxyde	
1	$30 \mu\text{M}$	$30 \mu\text{M}$	4 mM	10 mM	11.7%	12.7%	traces	81
2	$30 \mu\text{M}$	0	0	10 mM	0	0	0	0
3	$30 \mu\text{M}$	0	4 mM	10 mM	0	traces	0	nd
4	0	$30 \mu\text{M}$	4 mM	10 mM	0	0	0	0
5	$30 \mu\text{M}$	$30 \mu\text{M}$	0	10 mM	0	0	0	0

Table III-2 : Substrate conversion under different conditions. Oxygenation reactions were carried out under irradiation for 22 hours, under aerobic conditions, in B&R buffer at pH 4. ^a The product yield is based on substrate. ^b TON: turnover number is calculated over catalyst.

In a first control experiment, where both $[(\text{Fe}^{\text{III}}\text{DPy})_2\text{O}]$ catalyst and $[\text{MV}^{2+}]$ were excluded, we decided to examine the role of oxygen species formed upon reaction with excited $[\text{Ru}^{\text{II}*}]$. It is known that $[\text{Ru}^{\text{II}*}]$ can react with O_2 to form the singlet dioxygen $^1\text{O}_2$ or the superoxide radical $\text{O}_2^{\bullet-}$ by an energy or charge transfer, respectively. Although $\text{O}_2^{\bullet-}$ is a highly oxidizing agent ($E^\circ(\text{O}_2^{\bullet-}/\text{H}_2\text{O}_2) = 0.94 \text{ V vs NHE}$)¹³⁴ and $^1\text{O}_2$ is known to react with double bond to form epoxide product and aldehyde.^{135,136} Under our experimental conditions, no oxidized products were detected ruling out this photo driven pathway. (Table III-2, Entry 2). The rapid quenching of the Ru^* state by MV^{2+} probably inhibits the energy transfer to O_2 to form singlet O_2 while $\text{O}_2^{\bullet-}$ under such experimental conditions leads to the rapid back-electron transfer (Scheme 3). Moreover, $\text{O}_2^{\bullet-}$ itself was not capable of oxygenating sodium styrene-4-sulfonate. That was confirmed by the reaction of sodium styrene-4-sulfonate with excess of potassium superoxide (1000 eq) in B&R buffer pH 4, in which no oxidized product was detected.



Scheme 3 : Proposed mechanism for reaction involved in the blank experiment containing only Ru^{II} and substrate upon light irradiation at aerobic atmosphere.

Furthermore, the LFP experiment indicates that $[\text{Ru}^{\text{II}*}]$ was not quenched by the excess of substrate in absence of the electron acceptor (Figure III-6). The control experiment and this LFP experiment revealed that $[\text{Ru}^{\text{II}*}]$ did not oxidize the substrate to an alkenyl radical which could react with triplet O_2 or the activated forms of O_2 to form the oxidized product.¹³⁷

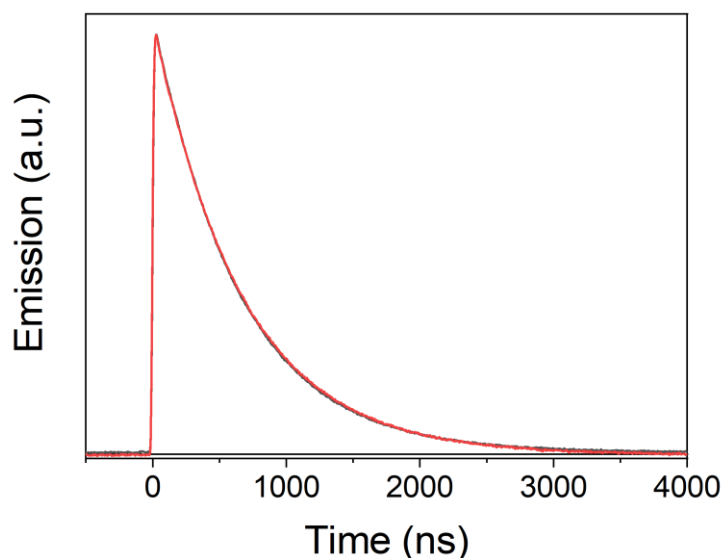


Figure III-6 : Normalized traces of the kinetics of $[Ru^{II*}]$ emission measured at 610 nm in a B&R pH 4 solution of $[Ru(bpy)_3]Cl_2$ ($30 \mu M$) (red) in the absence and (black) presence of sodium styrene-4-sulfonate ($100 mM$).

III.2.2.2 Study of subsystem $[Ru^{II}] + [MV^{2+}] + O_2$

In a subsequent blank experiment (Table III-1, Entry 3), where a mixture of $[Ru^{II}]$, S and O_2 was irradiated in presence of MV^{2+} , only trace amounts of oxidized substrate were detected, bringing again unambiguous support that the presence of the iron complex is essential for the observed photocatalytic reaction. The photoexcitation with a laser pulse at 460 nm of an aqueous mixture of $[Ru^{II}]$ and MV^{2+} in presence and absence of O_2 resulted in both cases in the formation of $MV^{+\bullet}$ detected by its characteristic absorption maximum around 605 nm ($\epsilon = 14600 M^{-1}cm^{-1}$),¹³⁸ and $[Ru^{III}]$ probed by the bleaching of the metal ligand charge transfer (MLCT) band at 450 nm ($\epsilon = 14600 M^{-1}cm^{-1}$) (Figure III-7).¹³⁹ In absence of dioxygen, the charge transfer process between $[Ru^{II*}]$ and $[MV^{2+}]$ to form $[Ru^{III}]$ and $[MV^{+\bullet}]$ was followed the recombination of $[MV^{+\bullet}]$ and $[Ru^{III}]$ (back electron transfer) with a bimolecular rate $k_9 = 9 \cdot 10^9 M^{-1}s^{-1}$ (Scheme 4). This rate was determined by fitting the decay time of reduced methyl-viologen $MV^{+\bullet}$ at 605 nm under argon atmosphere (Figure III-8, green).

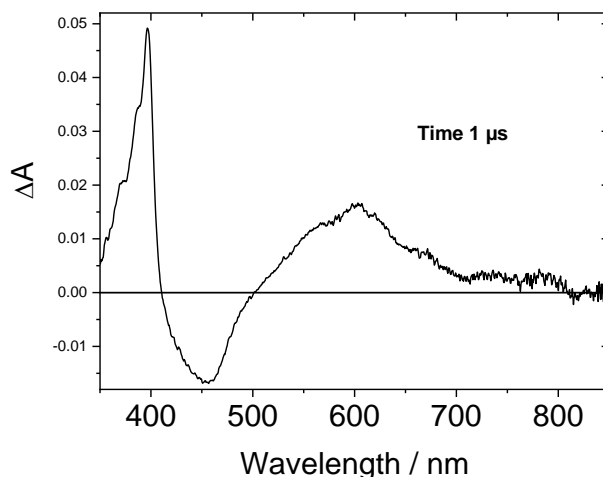
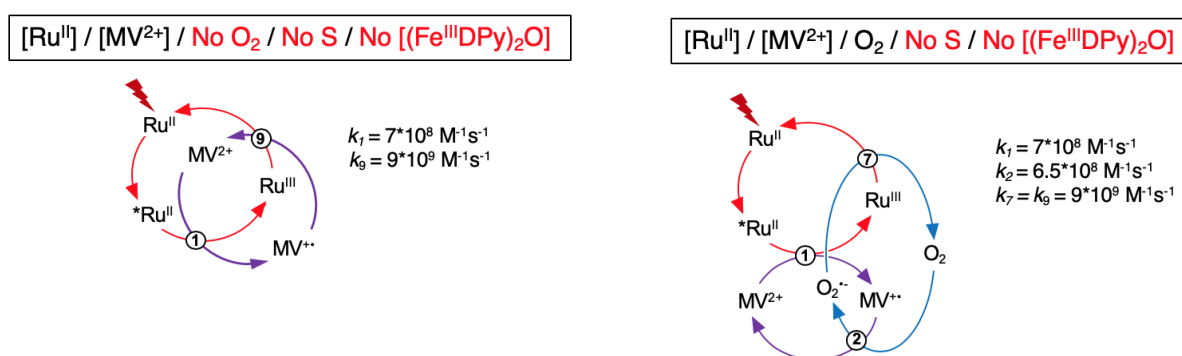


Figure III-7: Transient absorption spectrum from a B&R pH 4 buffer solution of $[Ru(bpy)_3]Cl_2$ ($30 \mu M$), MV^{2+} ($4 mM$) in air at $1 \mu s$ delay after excitation.

However, the faster decay of the $[MV^{+\bullet}]$ radical compared to the $[Ru^{III}]$ species in the presence of O_2 , clearly supports a rapid electron transfer from $[MV^{+\bullet}]$ to O_2 (Figure III-8, black and green).^{140,141} This electron transfer rate $k_2 = 6.5 \cdot 10^8 M^{-1}s^{-1}$ (Scheme 4) was also estimated from the decay time of reduced methyl-viologen in air-saturated solution. Back electron transfer to $[Ru^{III}]$ occurs in a second order reaction rate regenerating the $[Ru^{II}]$ state quantitatively with similar kinetics as back electron transfer from $[MV^{+\bullet}]$ in the absence of O_2 (Scheme 4, Figure III-8, red and blue).



Scheme 4: Proposed mechanism for electron transfer reactions involved in the system containing $[Ru^{II}]$ and MV^{2+} upon light irradiation under argon atmosphere (left) and aerobic atmosphere (right).

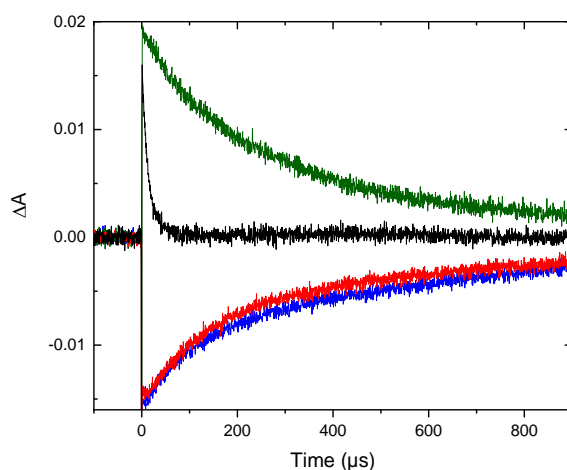


Figure III-8 : Time-resolved absorption changes of a solution of $[Ru(bpy)_3]Cl_2$ ($30 \mu M$) and MV^{2+} ($4 mM$) at $605 nm$ (green) and $450 nm$ (blue) in argon saturated B&R pH 4 buffer; at $605 nm$ (black) and $450 nm$ (red) in B&R pH 4 buffer under aerobic conditions.

Interestingly, in a deaerated solution and in presence of the olefin, we found that the recovery of the $[Ru^{II}]$ is faster than the lifetime of $[MV^{+}]$ (Figure III-9, blue and green). This observation can be assigned to the oxidation of the alkene by $[Ru^{III}]$ through an intermolecular electron transfer process to form an alkenyl radical cation (Scheme 5, step 4).⁹³ The bimolecular rates can be obtained from the regeneration time of the $[Ru^{II}]$ photosensitizer at $450 nm$ in argon-saturated solution (Scheme 5, $k_4 = 8 \cdot 10^4 M^{-1}s^{-1}$).

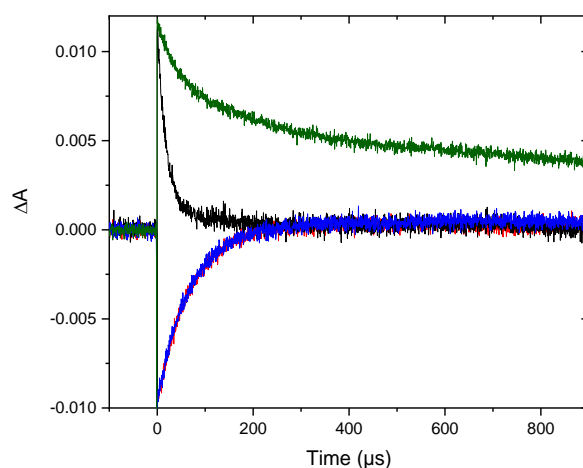


Figure III-9 : Time resolved absorption changes of a B&R (pH 4) buffer solution of $[Ru(bpy)_3]Cl_2$ ($30 \mu M$) and MV^{2+} ($4 mM$) in presence of sodium 4-styrenesulfonate ($100 mM$) at $605 nm$ (green) and $450 nm$ (blue) under argon; at $605 nm$ (black) and $450 nm$ (red) in aerobic conditions.

The chemical oxidation of the alkene by $[\text{Ru}^{\text{III}}]$ complex was performed and confirmed by the EPR detection of an organic radical (Figure III-10) which brings further support for this reaction pathway. Indeed, the EPR signal observed at $g = 2.002$ appears as a doublet, the shape of which can be related to a previously described styrenyl radical cation.¹⁴² In this parent intermediate, the highest hyperfine coupling constant (with β -hydrogens) was found of 1.1 mT, which is very close to the splitting of 1.5 mT measured in our case, while weaker hyperfine coupling were found with α and aromatic protons (0.2 to 0.3 mT) which are probably not well resolved in our case.

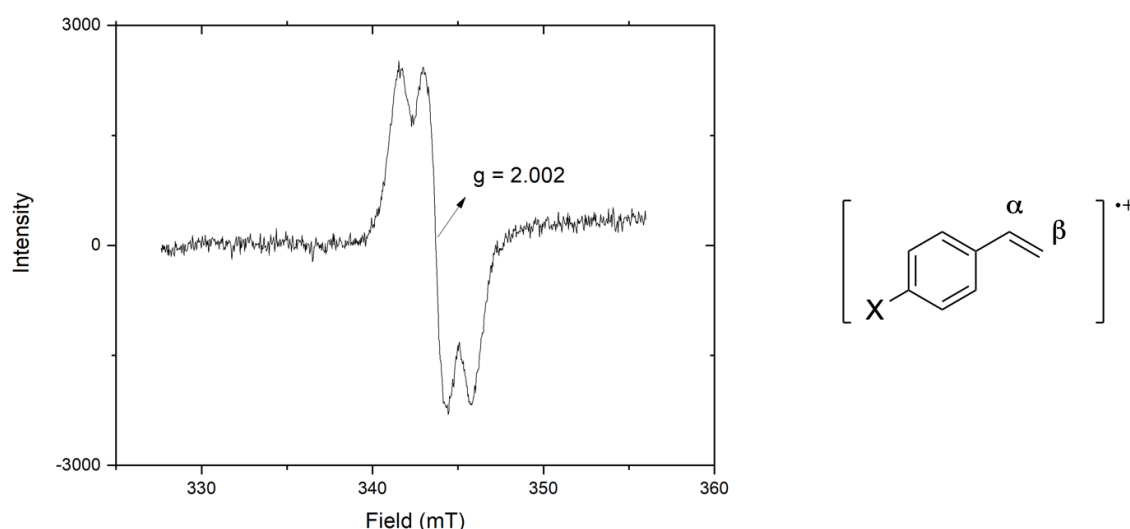
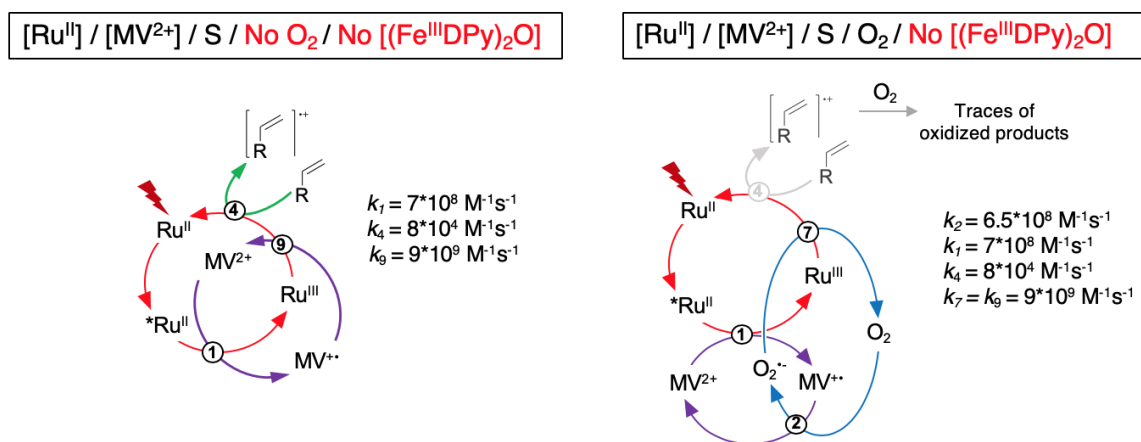


Figure III-10 : (Left) EPR spectrum at 80K of sodium 4-styrenesulfonate radical observed by mixing $[\text{Ru}(\text{bpy})_3](\text{PF}_6)_3$ (1 mM) with sodium 4-styrenesulfonate (10 mM) in B&R pH 4 buffer under argon. (Right) alkenyl radical cation form.

The trace amount of oxidized substrate (<1% of aldehyde) observed in the blank experiment with $[\text{Ru}^{\text{II}}]$, MV^{2+} and substrate in the absence of $[(\text{Fe}^{\text{III}}\text{DPy})_2\text{O}](\text{OTf})_2$ catalyst may thus originate from a minor side reaction of the singly oxidized olefin derivative with O_2 (Table III-2, Entry 3).¹⁴³ In Scheme 5, we recapitulate the photophysical events in the absence of $[(\text{Fe}^{\text{III}}\text{DPy})_2\text{O}](\text{OTf})_2$ complex. In this experimental set, the lack of the iron complex leads to the rapid annihilation of the charge separation state by a major recombination of the superoxide radical with the oxidized photosensitizer ($[\text{Ru}^{\text{III}}]$) (step 7 with kinetic $k_7 = 9.10^9 \text{ M}^{-1}$

$^1\text{s}^{-1}$) and a minor oxidation of olefin by the oxidized photosensitizer ($[\text{Ru}^{\text{III}}]$) (step 4 with kinetic $k_4 = 8 \cdot 10^4 \text{ M}^{-1}\text{s}^{-1}$).



Scheme 5: Proposed mechanism for reactions involved in the blank experiment containing $[\text{Ru}^{\text{II}}]$, substrate and MV^{2+} upon light irradiation under argon atmosphere (left) and aerobic atmosphere (right).

III.2.2.3 Role of catalyst

We then assessed the role of $[(\text{Fe}^{\text{III}}\text{DPy})_2\text{O}](\text{OTf})_2$ complex. The Fe-O bond of μ -oxo diiron(III) can be photoactivated to implicate the formation of a Fe^{II} complex and an active $\text{Fe}^{\text{IV}}=\text{O}$ complex capable of oxygenating alkene and alkane to release Fe^{II} complex in aprotic solvent as previously described by Nocera.¹⁴⁴⁻¹⁴⁶ The photogenerated Fe^{II} complex reacts with dioxygen to form a μ -peroxo diiron(III) intermediate followed by a O-O bond cleavage leading to the formation of an $\text{Fe}^{\text{IV}}=\text{O}$ species.^{57,115,120} However, this photocatalytic activity pathway is probably deactivated in aqueous medium that was confirmed by no oxidized product detected in the blank experiment in presence of $[(\text{Fe}^{\text{III}}\text{DPy})_2\text{O}](\text{OTf})_2$ and without $[\text{MV}^{2+}]$ (Table III-2, Entry 4 & 5).

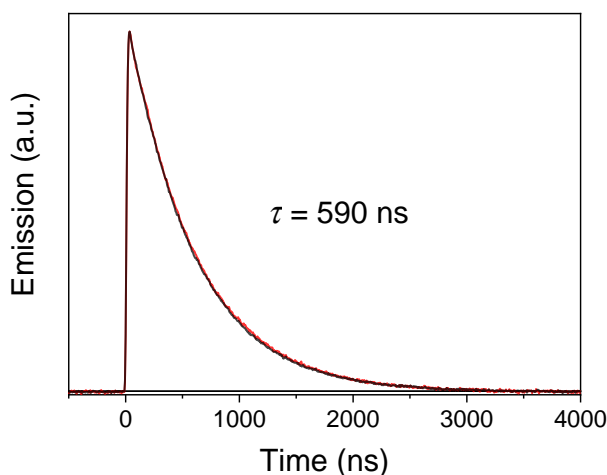


Figure III-11 : Normalized traces of the kinetics of $[Ru^{II*}]$ emission measured at 610 nm in a B&R pH 4 solution of $[Ru(bpy)_3]Cl_2$ ($30 \mu M$) (red) in the absence and (black) presence of $[(Fe^{III}DPy)_2O](OTf)_2$ complex ($30 \mu M$).

In a last control experiment where we omitted $[MV^{2+}]$ but introduced $[(Fe^{III}DPy)_2O](OTf)_2$ complex (Table III-2, Entry 5), no oxidized substrate was detected. This result indicates that no charge shift process is undergoing from the excited state of the photosensitizer to $[(Fe^{III}DPy)_2O](OTf)_2$ complex in agreement with the absence of quenching of the emission life time of $[Ru^{II*}]$ upon addition of $[(Fe^{III}DPy)_2O](OTf)_2$ (Figure III-11).

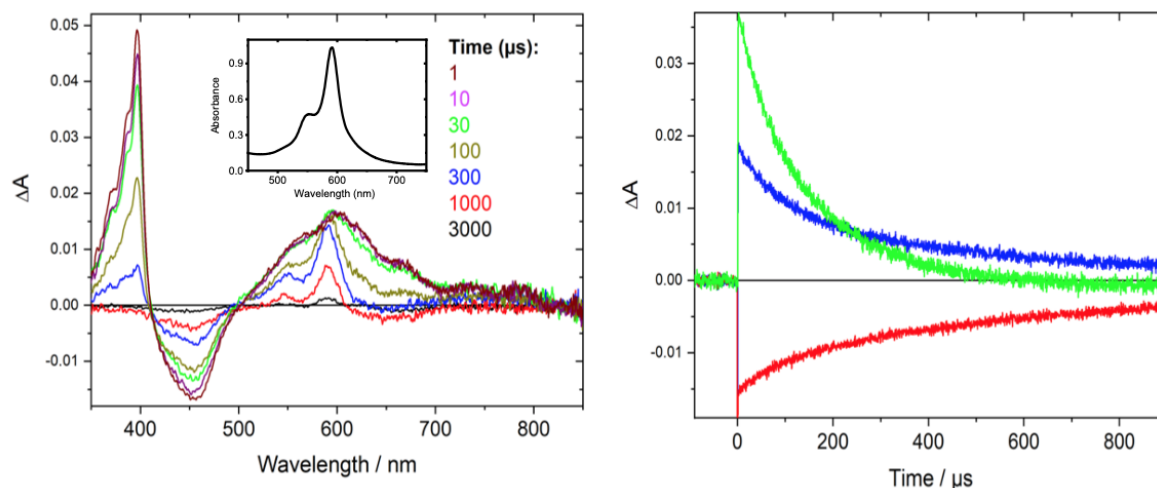


Figure III-12: Left: Transient absorption spectra from an Ar-saturated B&R buffer solution of $[Ru(bpy)_3]^{2+}$ ($30 \mu M$), MV^{2+} ($4 mM$) and $[(Fe^{III}DPy)_2O](OTf)_2$ ($30 \mu M$) at the indicated delay times after excitation and (Inset) UV-visible spectrum of $(DPy)Fe^{II}$ in water under argon. Right: Time resolved absorption changes at 390 nm (green), 450 nm (red) and 605 nm (blue) corresponding to the contribution of $MV^{+•}$, $[Ru^{II}]$, both $MV^{+•}$ and iron(II) complex, respectively.

We then interrogated the role of $[(\text{Fe}^{\text{III}}\text{DPy})_2\text{O}](\text{OTf})_2$ in presence of $[\text{MV}^{2+}]$ based on the laser flash photolysis study of trimolecular system containing the $[\text{Ru}^{\text{II}}]$ photosensitizer, $[(\text{Fe}^{\text{III}}\text{DPy})_2\text{O}](\text{OTf})_2$ complex and $[\text{MV}^{2+}]$. Under an inert atmosphere, the oxidative quenching of the photosensitizer and the formation of $[\text{MV}^{+\bullet}]$ again prevailed. However, a rapid fading of the absorption features of the $[\text{MV}^{+\bullet}]$ radical is observed that matched with the formation of the reduced $(\text{DPy})\text{Fe}^{\text{II}}$, detected by two absorption bands in the visible region at around 550 and 590 nm (Figure III-12, Left). The formation of $(\text{DPy})\text{Fe}^{\text{II}}$ with the increasing of a absorption band at 590 nm explains the different time resolved absorption at 390 nm and 605 nm because the time resolved absorption changes at 390 nm corresponding to the contribution of only $[\text{MV}^{+\bullet}]$, while that at 605 nm corresponding to both $[\text{MV}^{+\bullet}]$ and $(\text{DPy})\text{Fe}^{\text{II}}$ (Figure III-12, right, green and blue). Based on the decay time of $[\text{MV}^{+\bullet}]$ at 395 nm under inert atmosphere, the electron transfer rate between $[\text{MV}^{+\bullet}]$ and $[(\text{Fe}^{\text{III}}\text{DPy})_2\text{O}](\text{OTf})_2$ was estimated with a value $k_2 = 2.3 \times 10^8 \text{ M}^{-1}\text{s}^{-1}$ (Scheme 6). The recovery of $[\text{Ru}^{\text{II}}]$ is quite slow under these conditions and can reasonably be attributed to the re-oxidation of Fe(II) to Fe(III) (compare blue and red traces in Figure III-12, right).

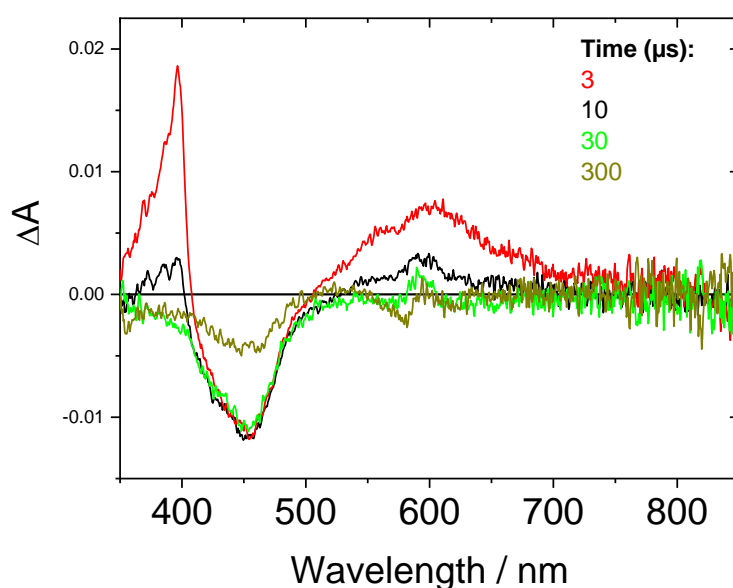
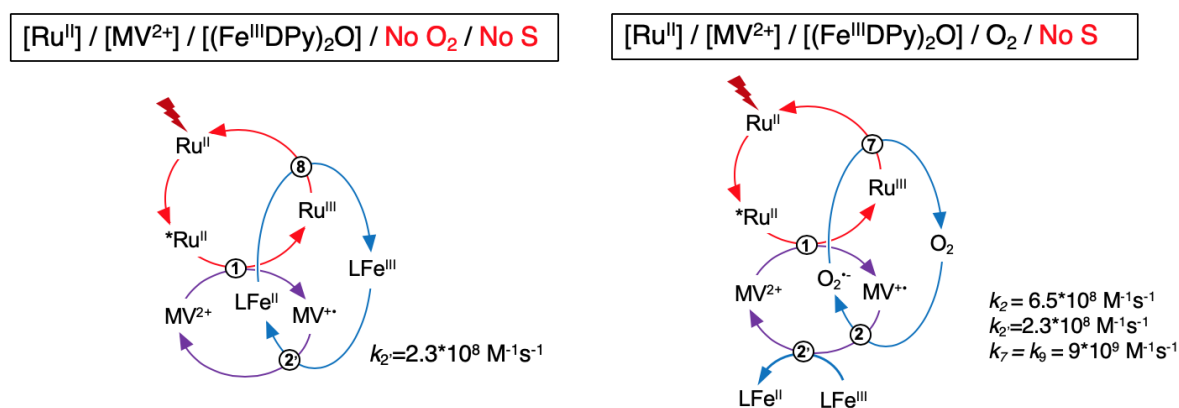


Figure III-13 : : Transient absorption spectra from a B&R pH 4 buffer solution of $[\text{Ru}(\text{bpy})_3]\text{Cl}_2$ ($30 \mu\text{M}$), MV^{2+} (4 mM) and $[(\text{Fe}^{\text{III}}\text{DPy})_2\text{O}](\text{OTf})_2$ complex ($30 \mu\text{M}$) under aerobic conditions at the indicated delay times after excitation.

In presence of O_2 , the electronic absorption signature of the $(\text{DPy})\text{Fe}^{\text{II}}$ can still be detected (Figure III-13) albeit with lower intensity than in the absence of O_2 . The lower yield in

presence of O₂ is compatible with the competitive reduction of [(Fe^{III}DPy)₂O](OTf)₂ vs. O₂ by [MV²⁺] to generate the (DPy)Fe^{II} and O₂^{•-} species respectively with a branching ratio determined essentially by the relative concentrations of [(Fe^{III}DPy)₂O](OTf)₂ (30 μM) and O₂ (around 260 μM in air-equilibrated aqueous solution at 25 °C) due to the similar bimolecular rate of two branches (Scheme 6, k₂ and k₂^{•-}). Consequently, the reaction of [MV²⁺] with O₂ is about 10-20 times more favorable than the reaction of [MV²⁺] with [(Fe^{III}DPy)₂O](OTf)₂ due to concentration of [(Fe^{III}DPy)₂O](OTf)₂ and O₂ that is in agreement with the amplitude of the (DPy)Fe^{II} absorption at 590 nm in absence of O₂ (Figure III-12, left) about 10-20 time more than that in presence of O₂ (Figure III-13).

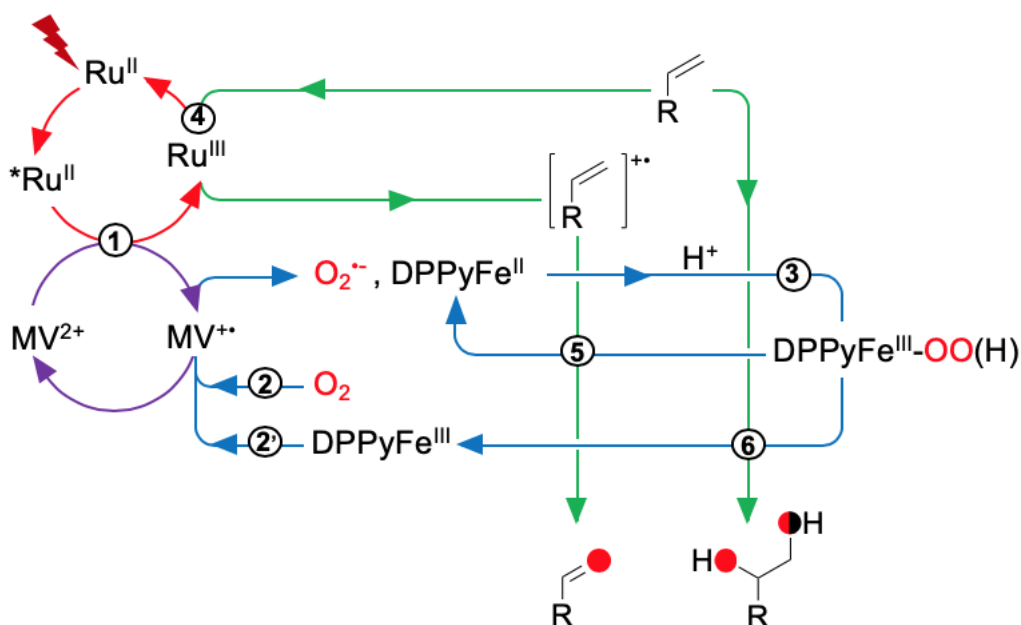


Scheme 6 : Proposed mechanism for reactions involved in the blank experiment containing [Ru^{II}], [(Fe^{III}DPy)₂O](OTf)₂ and MV²⁺ upon light irradiation under argon atmosphere (left) and aerobic atmosphere (right).

III.2.2.4 Proposed mechanism for the full system

Scheme 7 illustrates the different events occurring after excitation of the photosensitizer leading to the formation of the two main oxidized products, which are the diol and benzaldehyde. Importantly, our global photocatalytic cycle is in sharp contrast with the classical photoactivation scheme, inasmuch as there is no intervention of a sacrificial electron donor (SED). Traditionally, the function of the SED serves to aliment the photocatalytic process with electrons for the activation of O₂.¹²³ The first photoinduced sequence relies on

the oxidative quenching of the photosensitizer to form the highly oxidizing $[\text{Ru}^{\text{III}}]$ and the powerful reductant $\text{MV}^{\bullet+}$ (step 1). Laser Flash Photolysis experiments supported by the redox properties of each partner ($E^\circ(\text{MV}^{2+}/\text{MV}^{\bullet+}) = -0.69 \text{ V}$; $E^\circ(\text{O}_2/\text{O}_2^{\bullet-}) = -0.40 \text{ V}$ vs. SCE; $E^\circ(\text{Fe}^{\text{III}}\text{Fe}^{\text{III}}/\text{Fe}^{\text{III}}\text{Fe}^{\text{II}}) = 0.12 \text{ V}$ and $E^\circ(\text{Fe}^{\text{III}}\text{Fe}^{\text{II}}/\text{Fe}^{\text{II}}\text{Fe}^{\text{II}}) = -0.15 \text{ V}$ in ACN/H₂O (95/5 mixture) ascertain that the $\text{MV}^{\bullet+}$ radical can reduce both the iron(III) complex and O₂ (steps 2 and 2' in Scheme 7).



Scheme 7 : Proposed mechanism of the photocatalytic oxidation of sodium styrene-4-sulfonate by the photosensitizer / iron catalyst / methyl-viologen mixture to form the diol and aldehyde products.

The resulting iron(II) complex and O₂•⁻ species ultimately combine to form an iron(III)-peroxo or hydroperoxo type intermediate (step 3). Note that at pH 4, the superoxide radical anion is most likely to be protonated to produce a hydroperoxyl radical ($\text{pK}_a(\text{•OOH}/\text{O}_2^{\bullet-}) = 4.7$)^{148,149, 120}. All attempts to trap the iron(III)-(hydro)peroxo intermediate in aqueous medium from the reaction of a chemically prepared (DPy)Fe^{II} and superoxide anion were unfruitful. However, such intermediates have been caught with other iron complexes, spectroscopically characterized and their reactivity modes were demonstrated in organic media.^{150,151} Therefore, we decided to make an attempt at generating Fe^{III}-OOH species in methanol. The reaction of the prepared (DPy)Fe^{II} and 10 eq H₂O₂ at -40 °C under argon atmosphere was monitored by absorption spectroscopy. Three isosbestic points were clearly observed at 612, 509 and 302

nm, suggesting a clean chemical transformation (Figure III-14). This transformation was completed with 1 min and a new absorption band at 632 nm was observed, and attributed to an active iron species with a life-time $t_{1/2} = 3$ h at -40 °C. The EPR spectrum recorded at 10 K of this species showed an intense signal at $g = 4.3$ (Figure III-15), that might correspond to the formation of a high spin $\text{Fe}^{\text{III}}\text{-OOH}$ species.^{47,152}

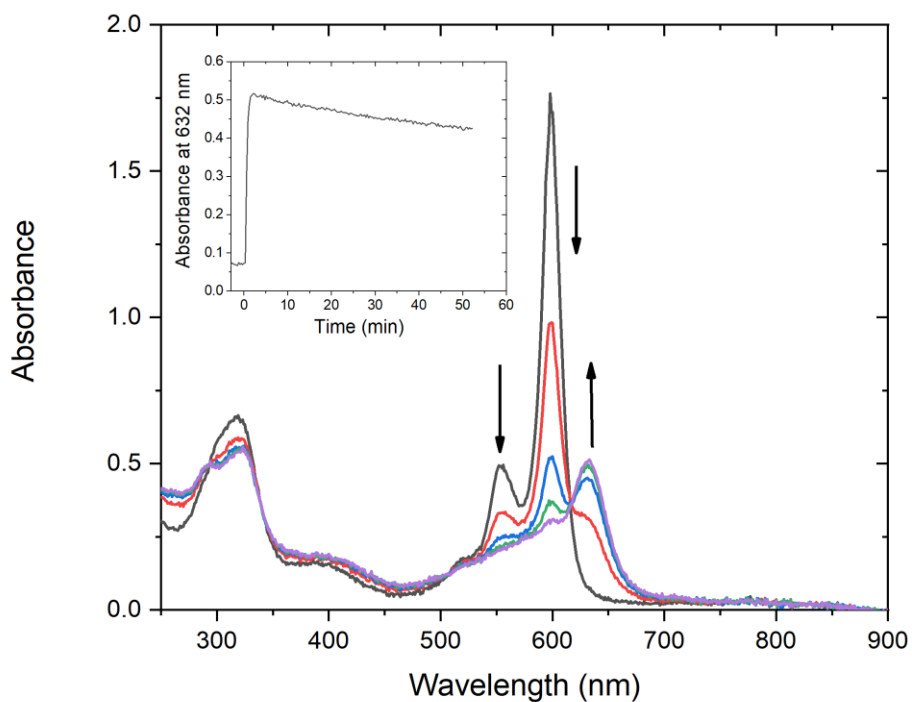


Figure III-14 : UV-visible spectral changes during the reaction of the prepared $(\text{DPy})\text{Fe}^{\text{II}}$ ($50 \mu\text{M}$) (black) and 10 eq H_2O_2 in MeOH at -40 °C under argon atmosphere. Inset: plot of absorbance at 632 nm over time.

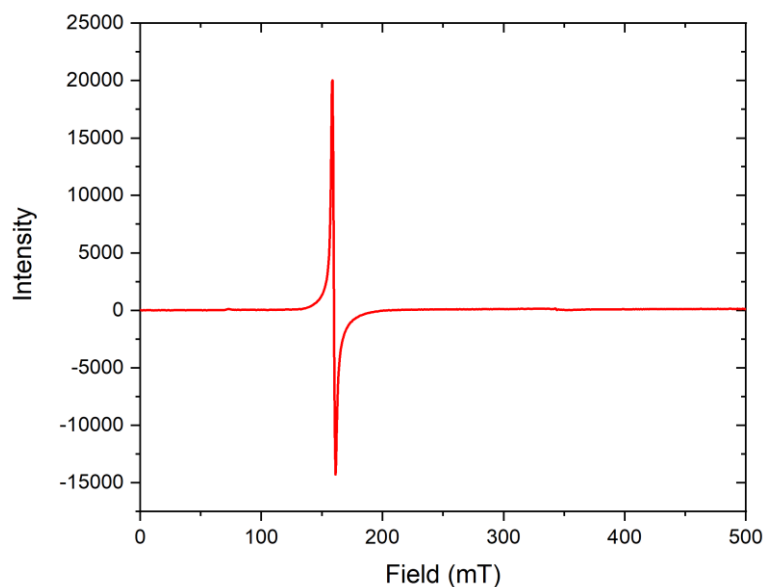
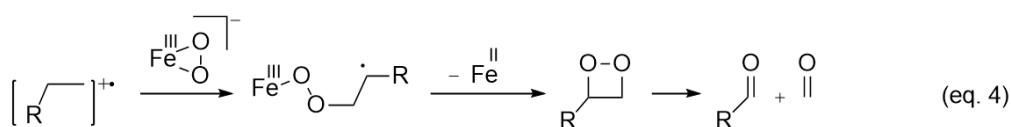
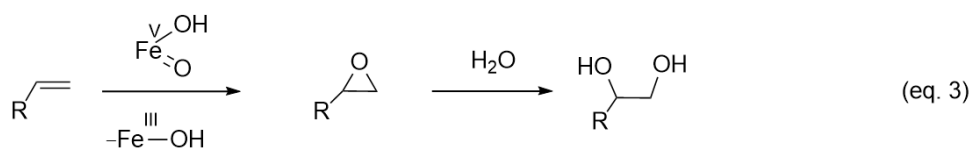
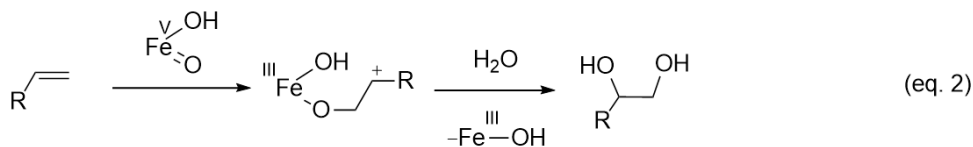


Figure III-15 : EPR Spectrum recorded at 10 K of the iron intermediate obtained from $(DPy)Fe^{II}$ (1 mM) upon addition of 10 eq H_2O_2 at $-40^\circ C$ under argon atmosphere.

Turning our attention to the oxidant issued from the first photophysical event; the $[Ru^{III}]$ species can oxidize the alkene to form an alkenyl radical cation thereby recycling the photosensitizer to its resting state (step 4). The formed organic radical species leads to one of the two main photoproducts that we evidenced, namely the benzaldehyde sulfonate. As already elucidated from previous studies, this product can derive from the formation of an unstable dioxetane species where O-O and C-C bonds cleavage delivers the benzaldehyde derivative. The direct reaction of the superoxide radical anion with the singly oxidized alkenyl radical cation to form the dioxetane intermediate can be ruled out under our experimental conditions. Indeed, as already mentioned, the blank experiment where a mixture of $[Ru^{II}]$, $[MV^{2+}]$, S and O_2 was irradiated only lead to a minute amount of oxidized photoproduct. Henceforth, we can arguably propose that the formation of the dioxetane results from the reaction of the alkenyl radical cation, formed by the electron transfer from the alkene to the oxidized $[Ru^{III}]$ (step 4), with the Fe^{III} -peroxo intermediate (step 5 in Scheme 7 and eq. 4 in Scheme 8). The other characterized photoproduct was the diol derivative (step 6). Its formation emanates from the $Fe^{III}(OOH)$ species which, in turn, can evolve *via* heterolytic O-O cleavage to form an $Fe^V(O)(OH)$ (Scheme 8, eq. 1).¹⁵³⁻¹⁵⁵ This intermediate can concertedly fix two oxygen atoms to the alkene to yield the *cis*-diol product (Scheme 8, eq.

2). Alternatively, the formation of the diol may come from the ring opening of an epoxide formed from the high valent Fe-oxo intermediate (Scheme 8, eq. 3).



Scheme 8 : Proposed mechanism for iron catalyzed sodium 4-styrene sulfonate oxidation.

III.2.2.5 Influence of the pH media

When the photocatalytic run was realized at pH 6, only the epoxide and the aldehyde were revealed (Table III-3). This subtle reactivity control brings further confirmation that the oxygen atom transfer reactions are guided through activated forms of O₂ at the iron center.

pH buffer	[Ru(bpy) ₃]Cl ₂	[(Fe ^{III} DPy) ₂ O](OTf) ₂	MV ²⁺	Substrate	Product yield ^a			TON ^b
					Diol	Benzaldehyde	Epoxyde	
4	30 μM	30 μM	4 mM	10 mM	11.7%	12.7%	traces	81
6	30 μM	30 μM	4 mM	10 mM	traces	10.5%	10.7%	71

Table III-3 : Substrate conversion under different conditions. Oxygenation reactions were carried out under irradiation for 22 hours, under aerobic conditions. ^a The product yield is based on substrate and determined by ¹H-NMR (non isolated). ^b TON: turnover number is calculated over catalyst.

Step 1, 2, 2', 4 in Scheme 8 of the photocatalytic cycle are not modified at pH 6. The oxidative quenching of the photosensitizer still generates the highly oxidized chromophore and the powerful reductant methyl-viologen radical [MV^{•+}] that can then concomitantly reduce the iron(III) complex to the iron(II) form and O₂ to O₂^{•-}. The oxidized photosensitizer is reset to its ground state by oxidizing an alkene substrate to an alkenyl radical cation. However, at pH 6 the superoxide O₂^{•-} is mainly non protonated because of pKa (•OOH/ O₂^{•-}) = 4.7. We can thus propose that the main active species in this case is the iron(III)-peroxo species obtained by the reaction of iron(II) complex and O₂^{•-}, that can further reacts with the olefin to form the epoxide product.¹⁵⁶ Furthermore, the minor iron(III)-peroxo species protonated to iron(III)-hydroperoxo species followed by a O-O bond cleavage to form iron-oxo species transferring oxygen atom to olefin to form epoxide product that is stable at pH 6 solution (eq. 3 in Scheme 8).

III.2.2.6 Limiting step in the proposed mechanism

Based on our proposed mechanism, oxidation of the substrate by the [Ru^{III}] (step 4) is probably the limiting step in the light-induced electron transfer processes because its rate is 10000 times slower than the back-electron transfer rate between the oxidized photosensitizer and superoxide (step 7) or iron (II) complex (step 8). Accordingly, the photocatalytic reaction rate can be accelerated by playing with substrate concentration (Table III-4). The oxidized products ratio is likely not influenced but the reaction rate increases with the concentration of sodium styrene-4-sulfonate.

[Ru(bpy) ₃]Cl ₂	[(Fe ^{III} DPy) ₂ O](OTf) ₂	MV ²⁺	Substrate	Product (mM)			TON ^a	TOF (h ⁻¹)
				Diol	Benzaldehyde	Epoxyde		
30 μM	30 μM	4 mM	5 mM	0.33	0.48	traces	27	1.2
30 μM	30 μM	4 mM	10 mM	1.17	1.27	traces	81	3.7
30 μM	30 μM	4 mM	100 mM	6.92	12.43	0.92	709	32.2

Table III-4 : Substrate conversion under different conditions. Oxygenation reactions were carried out under irradiation for 22 hours under aerobic conditions. ^a TON: turnover number is calculated over catalyst.

III.2.3 Isotope labelling study

¹⁸O isotopic labelling experiments, which carried out at pH 4 B&R buffer were undertaken to interrogate the origin and the pattern of the inserted oxygen atoms into oxidized products. The HPLC-HRMS analysis of the corresponding photocatalytic experiments indeed confirmed that the oxygen atom stems from ¹⁸O₂ (Figure III-16). The isotope labelling study was examined on the cis-diol product because of the fast oxygen exchange between the carbonyl group and water,¹⁵⁷ for the HPLC analysis used as an eluent.

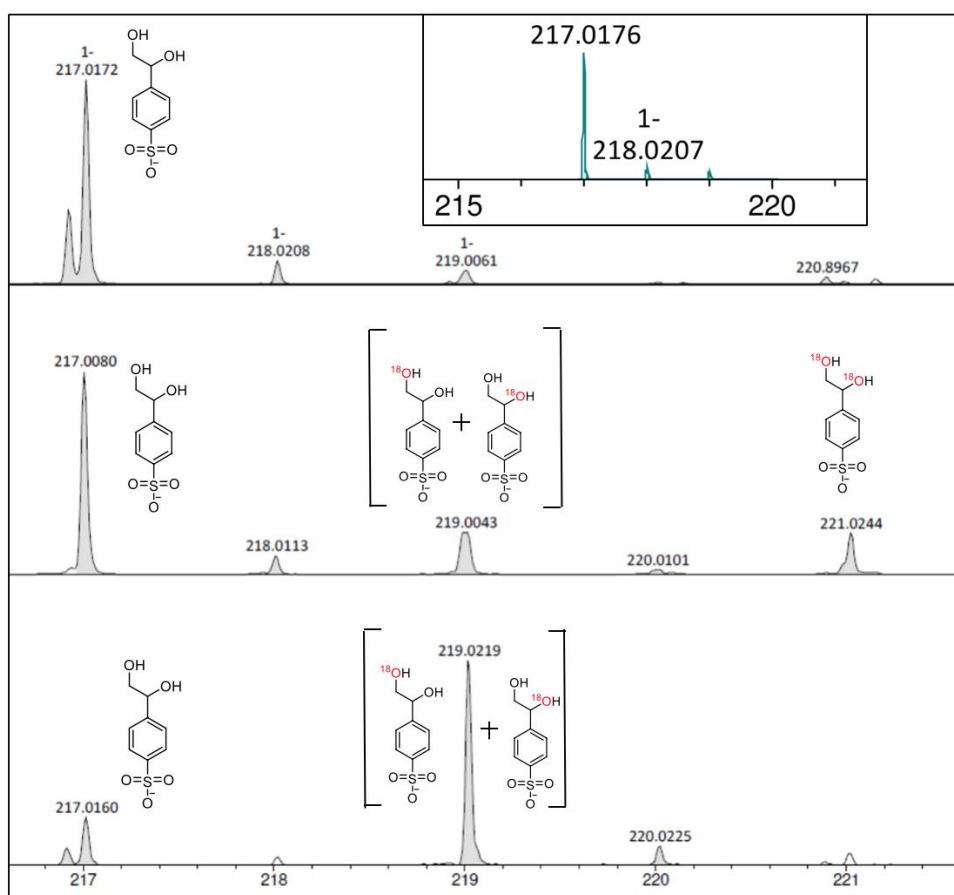


Figure III-16: ESI- - HRMS of diol formed in sodium 4-styrenesulfonate oxygenation under irradiation for 22 hours in B&R pH 4 buffer in presence of $[Ru(bpy)_3Cl_2]$ (30 μM), MV^{2+} (4 mM), $[(Fe^{III}DPy)_2O](OTf)_2$ complex (30 μM) and sodium 4-styrenesulfonate (10 mM) with (Top) H_2O and O_2 , (Middle) H_2O and $^{18}O_2$, (Bottom) $H_2^{18}O$ and O_2 , (inset) theoretical isotopic distribution for unlabelled diol.

When the photocatalytic run was realized in presence of a mixture of $^{18}O_2$ and $^{16}O_2$ in $H_2^{16}O$, the *cis*-diol with two inserted ^{18}O atoms was detected in the HRMS together with the $^{18}O^{16}O$ and $^{16}O^{16}O$ labelled diol products (Figure III-16, middle). This experimental finding clearly supports that O_2 is the actual source of oxygen atoms. The presence of mixed oxygen-labelled diol derivative can be rationalized through dynamic water exchange between an iron-bound hydroxo ligand and bulk water (Figure III-17).^{158–160} When, the photocatalytic experiment was carried out in $H_2^{18}O$ under air atmosphere without $^{18}O_2$, only $^{18}O^{16}O$ and $^{16}O^{16}O$ labelled diol products were detected (Figure III-16, bottom). One inserted ^{18}O probably comes from epoxide opening by a $H_2^{18}O$ molecule (Scheme 8, eq. 3). The lack of the *cis*-diol with two inserted ^{18}O atoms in this experimental condition confirmed that the origin of oxygen atom in oxidized product is dioxygen.

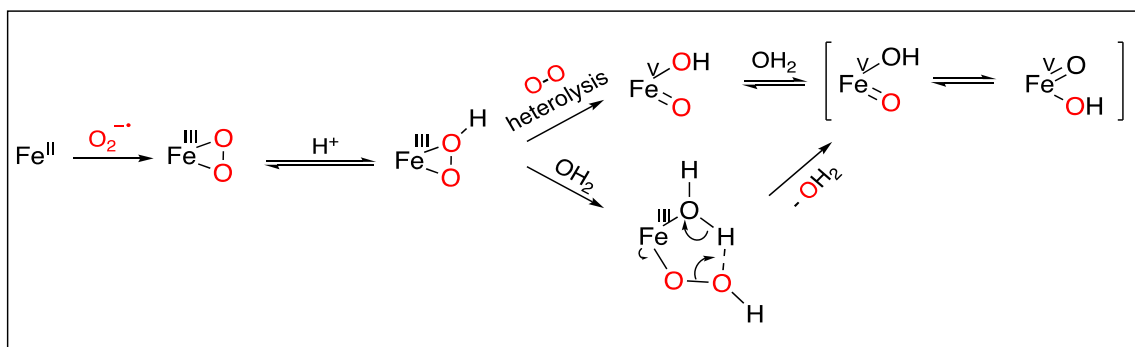


Figure III-17 : Proposed mechanism for the active iron species and oxygen atom exchange.

III.2.4 Quantum yield

The quantum yield for the formation of the oxidized products was calculated by the fraction of the number of reacted electrons and the number of absorbed photons. The number of absorbed photons was estimated as follows. The light intensity emitted by the LED panel was measured with a solar power meter as 1.3 mW/cm^2 and the spectral distribution of the emitted light was measured with an Avantes optical fiber spectrometer showing two bands centered around 450 nm and 560 nm with 30% of the light intensity contained in the 400-500 nm region. The fraction of light absorbed by the $[\text{Ru}(\text{bpy})_3]\text{Cl}_2$ chromophore was estimated from the drop of intensity integrated over the 400-500 nm region of the light transmitted through the sample (Figure III-18).

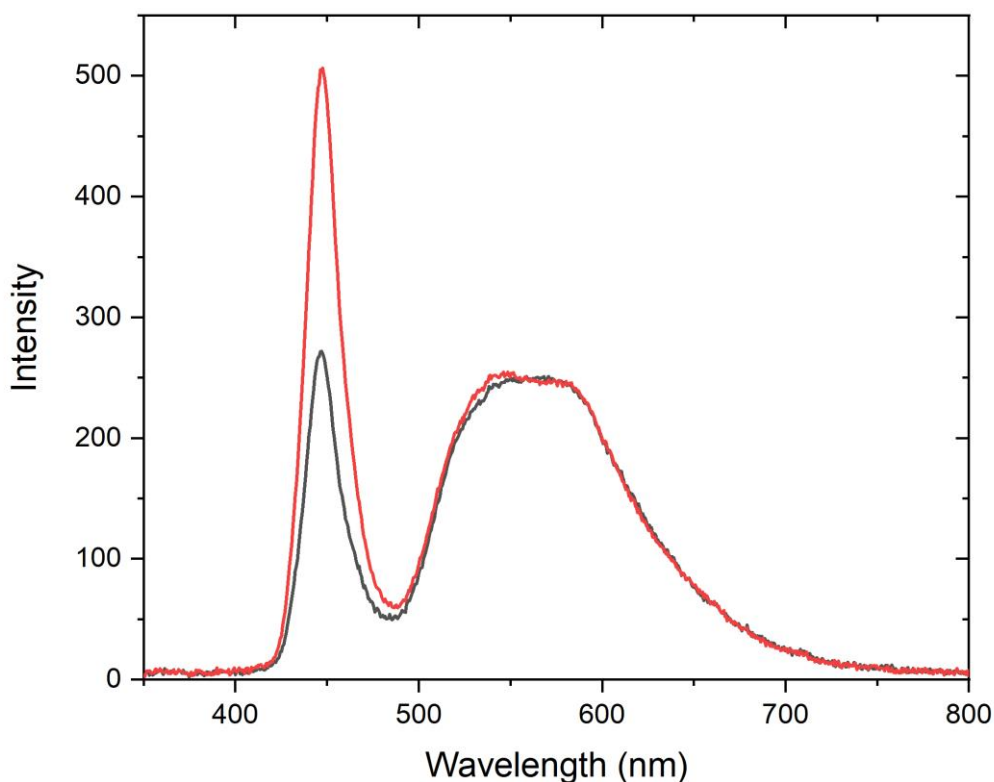


Figure III-18: The spectral distribution of the emitted light without (red) and with sample (black).

The number of absorbed photons is $N_{ph}=5.5 \cdot 10^{14} \text{ s}^{-1}$ or $4.3 \cdot 10^{19}$ for 22 h, as used in the photocatalysis experiments (Table III-1, entry 1). The number of product molecules in the 0.5 mL sample is $N_{diol} = 1.17 \text{ mM} \times 0.5 \text{ mL} \times N_A = 3.5 \cdot 10^{17}$ and $N_{aldehyde} = 1.27 \text{ mM} \times 0.5 \text{ mL} \times N_A = 3.8 \cdot 10^{17}$. Taking into account the number of photons necessary per catalytic cycle (1 for the aldehyde, 2 for the diol) results in an overall quantum yield of $\varphi = \frac{2 \cdot N_{diol} + N_{aldehyde}}{N_{ph}}$ of 2.5%. This quantum yield value falls within the range observed by Nocera's μ -oxo diiron(III) hachman porphyrin where no sacrificial electron donor was present.^{59,161}

III.3 Photosystem using iron(II) catalyst

The above results demonstrated that a reversible electron acceptor, methyl-viologen, can act as electron shuttle to oxidatively quench the photosensitizer, $[\text{Ru}(\text{bpy})_3]^{2+}$, generating the highly oxidized chromophore and the powerful reductant methyl-viologen radical $[\text{MV}^{+\bullet}]$. $[\text{MV}^{+\bullet}]$ can then reduce an iron(III) catalyst to the iron(II) form and concomitantly O_2 to $\text{O}_2^{\bullet-}$ in an aqueous medium to generate an active iron(III)-(hydro)peroxo species responsible for oxygenating substrates. The formation of reduced iron(II) complex by the reaction of iron(III) complex and $\text{MV}^{+\bullet}$ is likely the most important step in photoproduction of iron(III)-(hydro)peroxo species. However, we have evidenced that formation of the Fe(II) was in competition with the reduction of O_2 . Therefore, we reasoned to study a photocatalytic system using an already reduced and stable iron(II) complex with another set of ligand, the $\text{L}_5\text{Fe}^{\text{II}}(\text{OTf})(\text{PF}_6)$ complex where $\text{L}_5 = \text{N-methyl-N,N',N'-tris(2-pyridylmethyl)ethane-1,2-diamine}$ (Figure III-19). $[\text{L}_5\text{Fe}^{\text{II}}]^{2+}$ complex was synthesized and characterized in 1990s,¹⁶² and the corresponding oxidizing species such as iron(III)-(hydro)peroxo, iron(IV)-oxo have been well characterized in organic solvents.¹⁶³⁻¹⁶⁶ Unfortunately, no characterization of these active species was reported in aqueous media to our knowledge.

III.3.1 Reactivity

The mixture of $[\text{Ru}^{\text{II}}]$, S, $[\text{L}_5\text{Fe}^{\text{II}}]^{2+}$ and O_2 was irradiated in absence of MV^{2+} and no oxidized product was detected. As in the case of $[(\text{Fe}^{\text{III}}\text{DPy})_2\text{O}](\text{OTf})_2$ complex, the absence of any oxidized products under such condition corroborates with the lack of photocatalytic activity of the $[\text{L}_5\text{Fe}^{\text{II}}]^{2+}$ complex in aerobic aqueous medium through a dimer μ -peroxo diiron(III) species $\text{Fe}^{\text{III}}\text{-OO-Fe}^{\text{III}}$ obtained by the reaction of $[\text{L}_5\text{Fe}^{\text{II}}]^{2+}$ complex with O_2 then followed by the homolytic O-O cleavage to form the active $\text{Fe}^{\text{IV}}=\text{O}$ species.^{62,115,116} Upon light irradiation of an aqueous mixture of $[\text{Ru}^{\text{II}}]$, S, $[\text{L}_5\text{Fe}^{\text{II}}]^{2+}$ and MV^{2+} under aerobic condition two oxidized products were detected. As seen previously, both the diol and the benzaldehyde derivatives were characterized at pH 4 or the benzaldehyde and the epoxide at pH 6. An overall TOF comparable with that of the above photo-system using $[(\text{Fe}^{\text{III}}\text{DPy})_2\text{O}](\text{OTf})_2$ complex as catalyst was calculated (Table III-5).

pH	$[\text{Ru}(\text{bpy})_3]\text{Cl}_2$	$[\text{L}_5\text{Fe}^{\text{II}}]^{2+}$	MV^{2+}	Substrate	Product (mM)	TON ^a	TOF
----	--	--	------------------	-----------	--------------	------------------	-----

buffer									
					Diol	Benzaldehyde	Epoxide		(h ⁻¹)
4	30 μM	30 μM	4 mM	10 mM	0.83	1.27	traces	70	3.2
6	30 μM	30 μM	4 mM	10 mM	traces	1.17	0.66	61	2.7

Table III-5 : Substrate conversion under different conditions. Oxygenation reactions were carried out under irradiation for 22 under aerobic conditions. ^a TON: turnover number is calculated over catalyst.

III.3.2 Photo-generation of the active iron species.

Previously in the laboratory it was shown that a dyad constituted by a chromophore [Ru(bpy)₃]²⁺ covalently linked to a catalyst L₅Fe^{II} by a triazole moiety can undergo two sequential light-induced electron transfer from the Fe^{II}-OH₂ to the chromophore using [Co(NH₃)₅Cl]²⁺ as sacrificial electron acceptor, generating an Fe^{IV}=O species (Figure III-19).¹⁶⁷ Noteworthy, the formation of the Fe^{IV}=O comes from the two electrons and two protons oxidation process of the precursor Fe^{II}-OH₂ and under anaerobic conditions. In the present study, the photocatalytic runs are performed under aerobic conditions and in presence of a reversible electron acceptor. The questions ahead of us are to underpin the photoactivation pathways for the observed light driven chemical transformation.

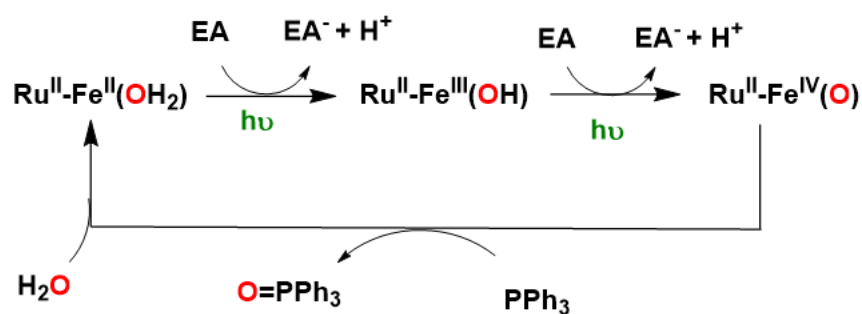
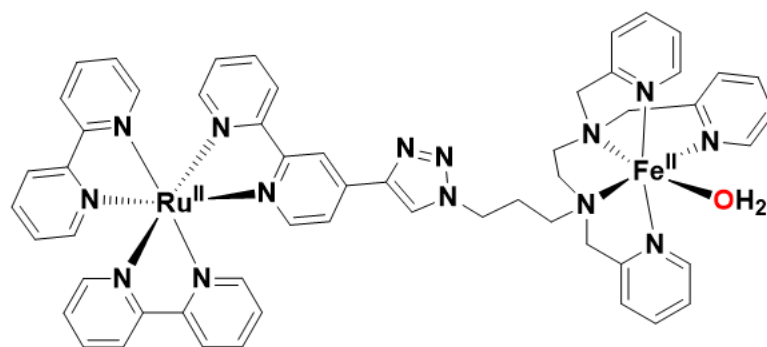


Figure III-19 : Structure of $[Fe^{\text{II}}L_5]^{2+}$ complex (left) and chromophore-catalyst dyad (right).

In presence of $[Fe^{\text{II}}L_5]^{2+}$ in the mixture $[Ru^{\text{II}}]$ photosensitizer and $[MV^{2+}]$, under an inert atmosphere, the oxidative quenching of the photosensitizer and the formation of $[MV^{+\cdot}]$ again prevailed. Laser flash photolysis experiment indeed revealed the characteristic absorption bands of $[MV^{+\cdot}]$ (390 nm and 605 nm) and $[Ru^{\text{II}}]$ (450 nm) shown in Figure III-20, left. However, no oxidation of $[L_5Fe^{\text{II}}]^{2+}$ catalyst by the oxidized photosensitizer was observed under such conditions. Indeed a fast recombination between $[MV^{+\cdot}]$ and $[Ru^{\text{III}}]$ was observed as attested by the simultaneous decay of the absorption band at 450 nm and 605 nm corresponding to $[MV^{+\cdot}]$ and $[Ru^{\text{II}}]$, respectively (comparing red and black in Figure III-20, right).

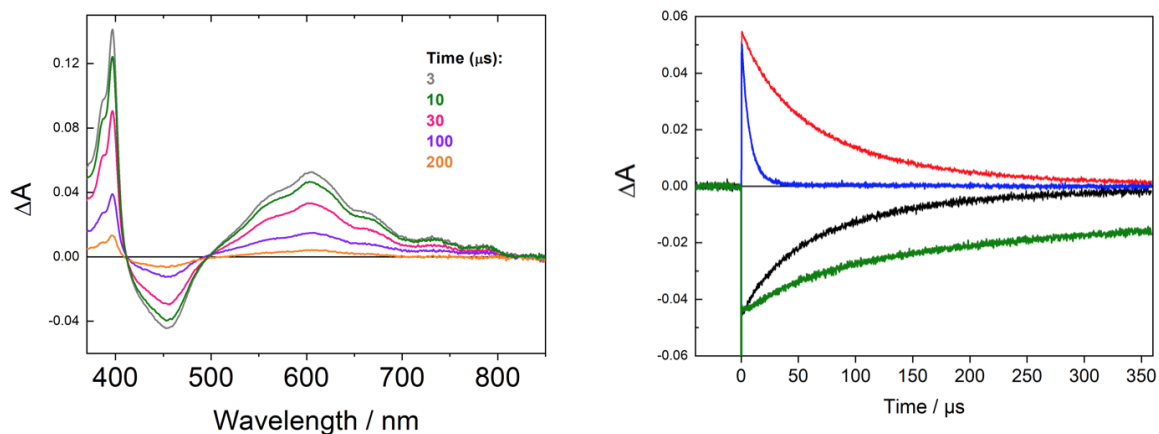
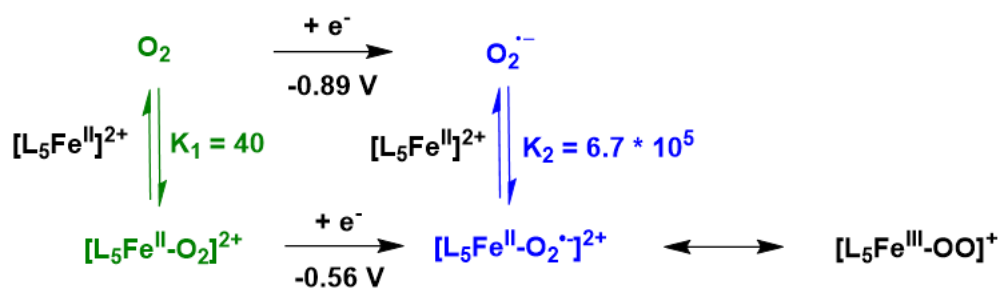


Figure III-20 : Left: Transient absorption spectra from an Ar-saturated pH 4 buffer solution of $[Ru(bpy)_3]^{2+}$ ($30 \mu M$), MV^{2+} ($20 mM$) and $[Fe^{II}L_5]^{2+}$ ($100 \mu M$) at the indicated delay times after excitation. Right: Time-resolved absorption changes at 605 nm (red) and 450 nm (black) in argon saturated pH 4 buffer; at 605 nm (blue) and 450 nm (green) in pH 4 buffer under aerobic conditions.

In presence of O_2 , a fast disappearance of $[MV^{+}]$ at 605 nm was observed, confirming the formation of superoxide $O_2^{\bullet -}$ by the electron transfer from $[MV^{+}]$ to O_2 (Figure III-20, right). Interestingly, the decay of reduced $[MV^{+}]$ was accelerated by addition of $[L_5Fe^{II}]^{2+}$ catalyst (Figure III-21), suggesting a different mechanism with $[L_5Fe^{II}]^{2+}$ catalyst than that in presence of $[Fe^{III}DPy)_2O]^{2+}$ dimer. Dr. Antoine Bohn reported in his thesis that there is an equilibrium between the $[L_5Fe^{II}]^{2+}$ complex and $[L_5Fe^{II}-O_2]^{2+}$ adduct in presence of O_2 and $[L_5Fe^{II}-O_2]^{2+}$ adduct was characterized by electrochemical study.¹⁶⁸ Importantly, the reduction of O_2 to $O_2^{\bullet -}$ at the iron center in the form of $[L_5Fe^{II}-O_2]^{2+}$ adduct was thermodynamically more favored than that without the help of $[L_5Fe^{II}]^{2+}$ complex. Indeed, The $[L_5Fe^{II}-O_2]^{2+}$ form is able to lower the $O_2/O_2^{\bullet -}$ oxidative power from $E^\circ = -0.89 V$ vs SCE to $E^\circ = -0.56 V$ vs SCE in acetonitrile (Scheme 9).



Scheme 9 : Proposed reduction mechanism considered to model experimental CVs for the reaction between O_2 and $[L_5Fe^{II}]^{2+}$ complex.

Consequently, the rapid fading of the absorption features of the $[MV^{+\bullet}]$ radical could be linked to two simultaneous pathways of dioxygen reduction. Firstly, dioxygen is activated at the iron center in the form of $[L_5Fe^{II}-O_2]^{2+}$ by reaction with $[MV^{+\bullet}]$ to generate iron(III)-peroxo species $[L_5Fe^{II}-O_2^{\bullet-}]^{2+}$ or $[L_5Fe^{III}-OO]^+$. Secondly, dioxygen is reduced by $[MV^{+\bullet}]$ to $O_2^{\bullet-}$ to rapidly react with $[L_5Fe^{II}]^{2+}$ catalyst to form the active $[L_5Fe^{III}-OO]^+$ species (Figure III-22).

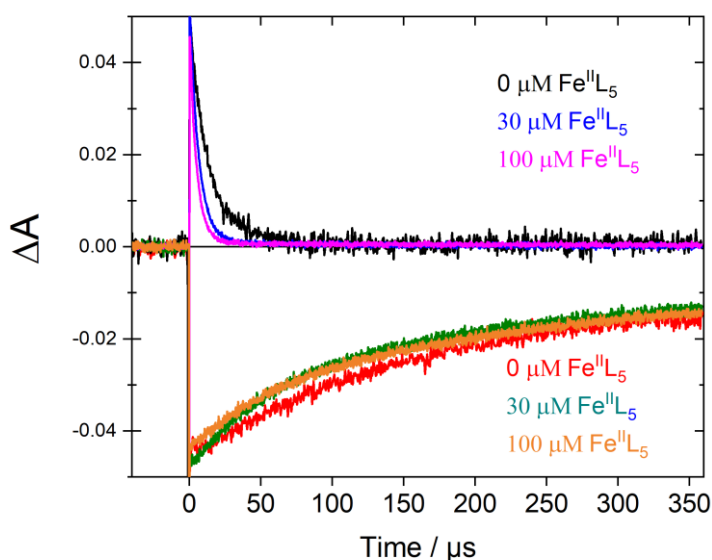
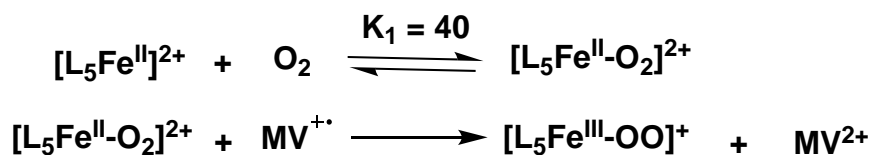


Figure III-21 : Time-resolved absorption changes of the mixture $[Ru(bpy)_3]Cl_2$ (30 μM), MV^{2+} (20 mM) in air-saturated pH 4 buffer without $[Fe^{II}L_5]^{2+}$ complex at 605 nm (black) and 450 nm (red); in presence of $[Fe^{II}L_5]^{2+}$ complex (30 μM) at 605 nm (blue) and 450 nm (green); in presence of $[Fe^{II}L_5]^{2+}$ complex (100 μM) at 605 nm (purple) and 450 nm (orange).

First pathway



Second pathway

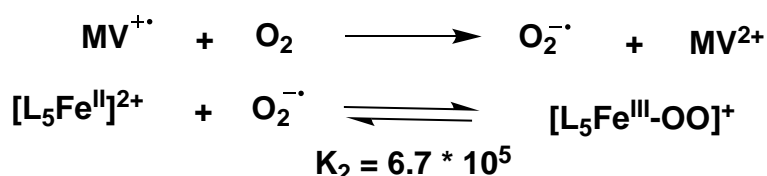


Figure III-22 : Two possible pathways of the reduction of O_2 by $\text{MV}^{+\cdot}$ in presence of $[\text{L}_5\text{Fe}^{\text{II}}]^{2+}$ complex.

This dioxygen activation hypothesis was supported by the appearance of a new broad absorption band centered at 680 nm simultaneously to the disappearance of the absorption features of the $[\text{MV}^{+\cdot}]$ radical (at 395 and 605 nm) and the $[\text{L}_5\text{Fe}^{\text{II}}]^{2+}$ catalyst (at 387 nm) (Figure III-23, Figure III-24). The $[\text{L}_5\text{Fe}^{\text{III}}\text{-OO}]^+$ species was characterized by an absorption band at 740 nm ($\epsilon = 1000 \text{ M}^{-1}\cdot\text{cm}^{-1}$), while $[\text{L}_5\text{Fe}^{\text{III}}\text{-OOH}]^{2+}$ species which was characterized by an absorption band at 537 nm ($\epsilon = 500 \text{ M}^{-1}\cdot\text{cm}^{-1}$) in methanol.¹⁶⁴ Therefore, the broad band centered at 680 nm could be assigned to a mixture of $[\text{L}_5\text{Fe}^{\text{III}}\text{-OO}]^+$ and the protonated $[\text{L}_5\text{Fe}^{\text{III}}\text{-OOH}]^{2+}$ species, due to the acidic medium.

On the other hand, the disappearance of the absorption feature of the $[\text{L}_5\text{Fe}^{\text{II}}]^{2+}$ catalyst (at 387 nm in Figure III-2) could also suggest a water activation by the reaction of $[\text{L}_5\text{Fe}^{\text{II}}(\text{H}_2\text{O})]^{2+}$ catalyst with the oxidized photosensitizer $[\text{Ru}^{\text{III}}]$ to form firstly $[\text{L}_5\text{Fe}^{\text{III}}(\text{OH})]^{2+}$ then probably to $[\text{L}_5\text{Fe}^{\text{IV}}(\text{O})]^{2+}$ by the second oxidation. However, at a delay time of 30 μs after excitation the oxidized photosensitizer $[\text{Ru}^{\text{III}}]$ was not yet reset to the ground state $[\text{Ru}^{\text{II}}]$ (band at 405 nm) while the $[\text{L}_5\text{Fe}^{\text{II}}]^{2+}$ catalyst had disappeared (band at 387 nm). We thus exclude the water oxidation pathway.

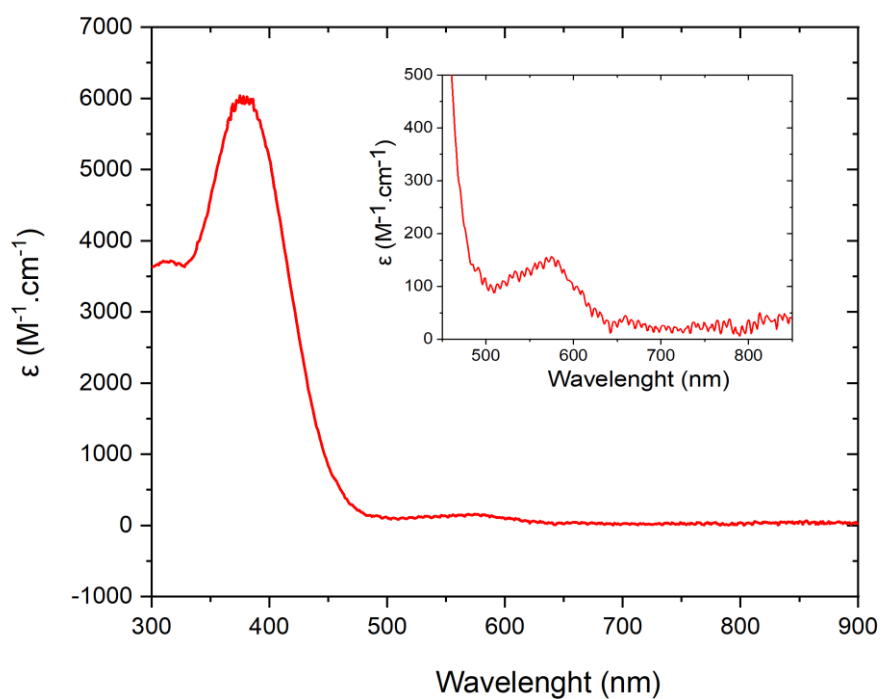


Figure III-23 : UV-visible spectrum of $[L_5Fe^{II}]^{2+}$ complex in B&R pH 4 buffer. Inset: zoom.

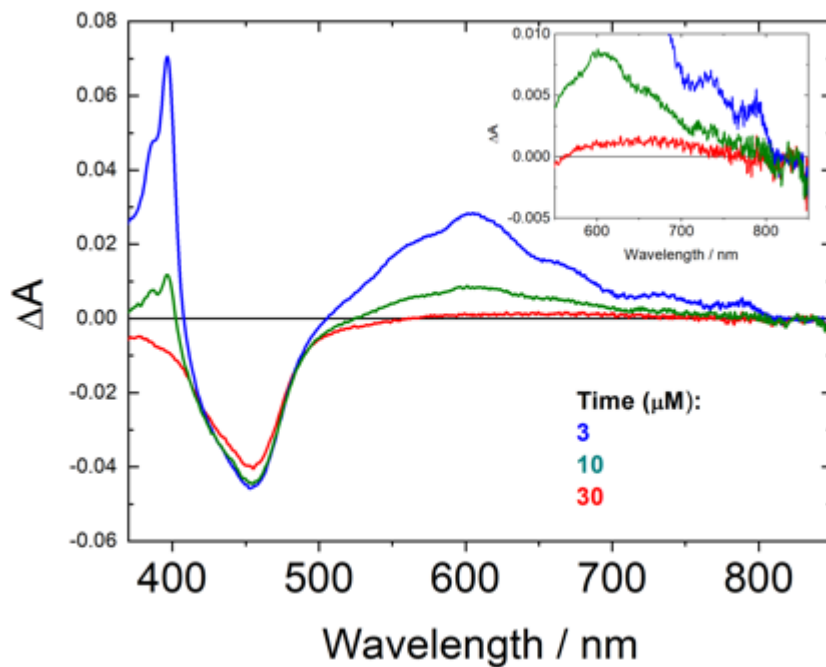


Figure III-24 : Transient absorption spectra from a pH 4 buffer solution of $[Ru(bpy)_3]Cl_2$ ($30 \mu M$), MV^{2+} ($20 mM$) and $[Fe^{II}L_5]^{2+}$ complex ($100 \mu M$) under aerobic conditions at the indicated delay times after excitation. Inset: zoom.

III.3.3 Characterization of the active iron species

To verify this hypothesis, we decided to monitor the reaction of $[\text{L}_5\text{Fe}^{\text{II}}]^{2+}$ catalyst and 1.5 eq. of H_2O_2 in $\text{pH} = 4$ buffer at $0\text{ }^\circ\text{C}$ monitored by absorption spectroscopy. The UV-visible spectra showed a broad absorption band around 700 nm which quickly disappeared (Figure III-25). By using H_2O_2 as oxidant in $\text{pH} 4$ buffer, the formation of the deprotonated iron(III)-peroxo species $[\text{L}_5\text{Fe}^{\text{III}}\text{-OO}]^+$ species can be excluded among the generated species in solution. This absorption band around 700 nm could thus be assigned to a mixture of $[\text{L}_5\text{Fe}^{\text{III}}\text{-OOH}]^{2+}$ and probably their evolution species such as $[\text{L}_5\text{Fe}^{\text{V}}\text{=O}]^{2+}$ obtained by a heterolytic O-O cleavage. $[\text{L}_5\text{Fe}^{\text{IV}}\text{=O}]^{2+}$ species characterized by band at 756 nm in methanol and at 732 nm in acetonitrile was also probably generated in the reaction .^{168,169}

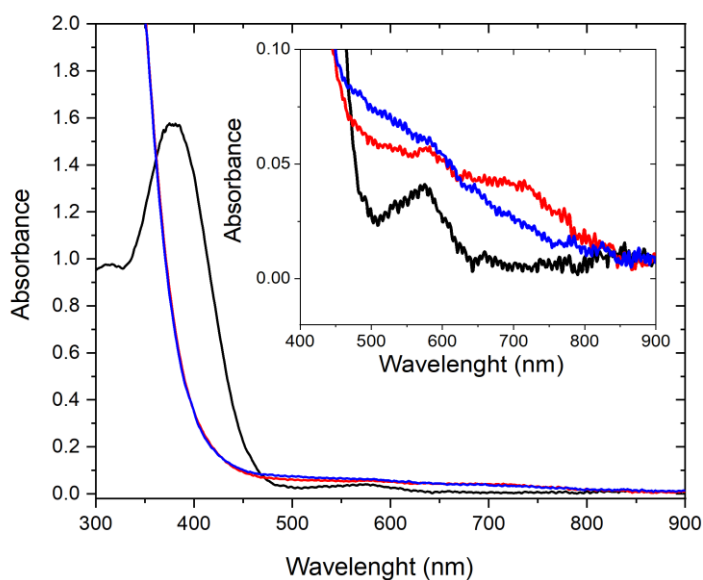


Figure III-25 : UV-visible spectra of $[\text{Fe}^{\text{II}}\text{L}_5]^{2+}$ in $\text{pH} 4$ buffer (black) upon addition of 1.5 eq H_2O_2 (red) and after 1 min (blue).

It is known that the iron(III)-(hydro)peroxo species $[\text{L}_5\text{Fe}^{\text{III}}\text{-OO}]^+$ and $[\text{L}_5\text{Fe}^{\text{III}}\text{-OOH}]^{2+}$ showed very distinct signals by EPR spectroscopy. $[\text{L}_5\text{Fe}^{\text{III}}\text{-OOH}]^{2+}$ species was characterized by EPR signals at $g = 1.97, 2.16$ and 2.21 , indicating a low spin iron(III) species while the high spin $[\text{L}_5\text{Fe}^{\text{III}}\text{-OO}]^+$ species was characterized by EPR signals at $g = 5.6$ and 7.5 . To confirm the formation of an iron(III)-(hydro)peroxo species suggested by our LFP exp, we

thus tried to examine the iron species photo-generated in our photocatalytic system by EPR spectroscopy. The EPR spectrum of a solution containing $[Ru^{II}]$, $[MV^{2+}]$ and $[L_5Fe^{II}]^{2+}$ in pH 4 buffer upon light irradiation for 120 s at air atmosphere showed the signals with g value around 2.13, 2.02 and 1.90 corresponding probably to a low spin iron(III) species (Figure III-26). Firstly, we notice that these signals are very weak, probably because of the competitive back electron process and the high reactivity of iron(III)-(hydro)peroxo species did not allow to accumulate enough intermediate to be detected. Secondly, these EPR signals observed are not sharp, probably due to formation of the crystallin ice during sample freezing. This experiment, that will be reproduced in presence of 10 % glycerol to avoid the formation of ice, will be helpful to identify the photo-generated iron species.

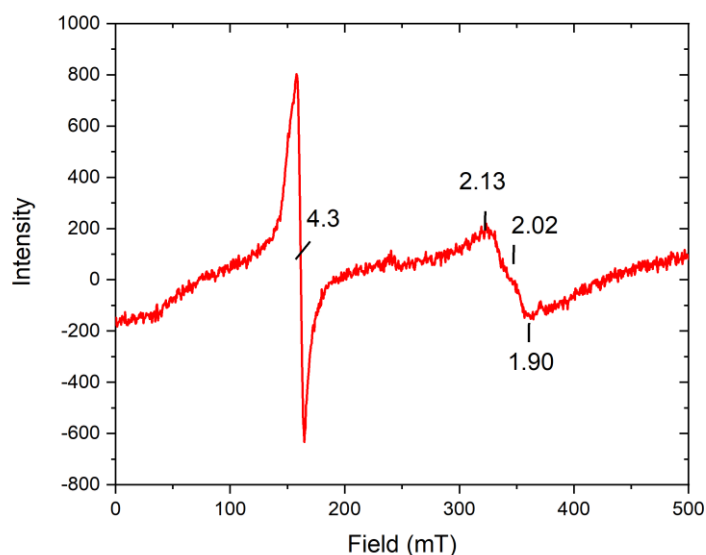
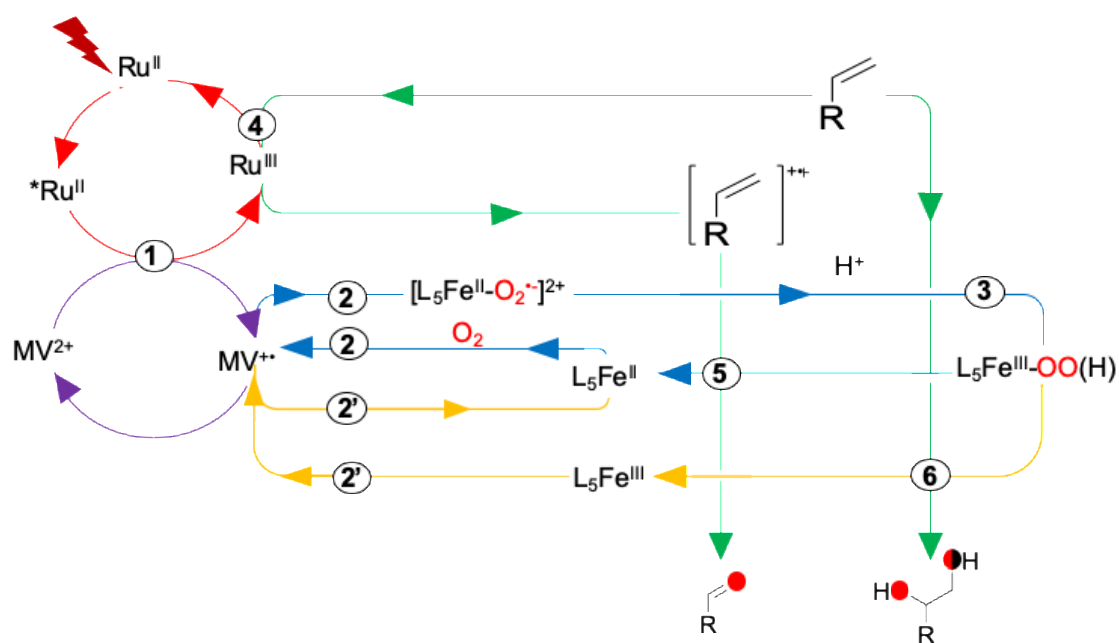


Figure III-26 : EPR spectrum of a solution containing $[Ru^{II}]$, $[MV^{2+}]$ and $[Fe^{II}L_5]^{2+}$ in pH 4 buffer upon light irradiation ($\lambda = 450 \text{ nm}$, power = 15 mW.cm^{-1}) for 120 s at air atmosphere.

III.3.4 Proposed mechanism for the photocatalytic system using $[L_5Fe^{II}]^{2+}$ catalyst

At this point we can recapitulate the events occurring after excitation of the photosensitizer leading to the formation of the oxidized products as depicted in Scheme 10. Unlike when using $[(Fe^{III}DPy)_2O](OTf)_2$ catalyst, at the beginning of photocatalytic reaction, the reduced

methyl-viologen $MV^{+\bullet}$ reduces dioxygen in its free form or at the iron center leading to form the active iron(III)-(hydro)peroxo species responsible for oxygenating olefin (step 2 in Scheme 10). However, the reaction of active iron species with olefin (step 6 in Scheme 10) leads to form the diol product and release an iron(III) complex $[L_5Fe^{III}]^{3+}$. Continuing the photocatalytic cycle, $[L_5Fe^{III}]^{3+}$ is reset to initial complex $[L_5Fe^{II}]^{2+}$ by reaction with reduced methyl-viologen $[MV^{+\bullet}]$ (step 2' in Scheme 10) as previously proposed for $[(Fe^{III}DPy)_2O](OTf)_2$ dimer. Indeed, the reduction of $[L_5Fe^{III}]^{3+}$ by $MV^{+\bullet}$ is allowed by the redox properties of $[Fe^{II}L_5]^{2+}$ complex ($E_{PC}(L_5Fe^{III}-OH_2/ L_5Fe^{II}-OH_2) = 0.13$ V and $E_{PC}(L_5Fe^{III}-OH/ L_5Fe^{II}-OH) = -0.17$ V (Figure III-27)) that have been measured by CV compared to $[MV^{2+}]$ ($E_{PC}(MV^{2+}/ MV^{+\bullet}) = -0.69$ V).¹⁴⁷ In aqueous medium, the initial $[L_5Fe^{II}]^{3+}$ is mainly in the $Fe^{II}-OH_2$ form so the oxidation wave was observed at $E_{P,A} = 0.25$.



Scheme 10 : Proposed mechanism of the photocatalytic oxidation of sodium styrene-4-sulfonate by the photosensitizer / iron catalyst $[Fe^{II}L_5]^{2+}$ / methyl-viologen mixture to form the diol and aldehyde products.

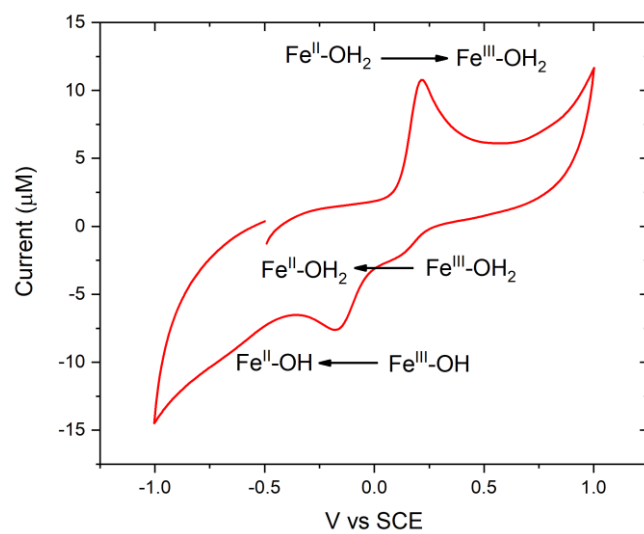


Figure III-27 : CV of $[L_3Fe^{II}]^{2+}$ in pH 6 buffer.

III.4 Conclusion & Perspective

The study we present here provides a new paradigm to perform photoinduced oxygen atom transfer reactions with solely light as energy input and O₂ as oxygen atom source in aqueous solution, without the “evil necessity” of a sacrificial electron donor. An introspection of the photocatalytic cycle points to the crucial role of the reversible charge carrier methyl-viologen to produce O₂^{•-} and reduce an iron(III) complex to iron(II) complex in utilization of [Fe^{III}DPy)₂O]²⁺ dimer as a pre-catalyst. Further reaction between iron(II) complex and O₂^{•-} generates the activated Fe^{III}-(hydro)peroxo as the archetypal OAT reactive species. Meanwhile, the oxidized photosensitizer is reset to its resting state through oxidation of the olefin substrate to produce an alkenyl radical cation. The latter and the olefin can react with the active catalytic species to form oxygenated products.

Using [Fe^{II}L₅]²⁺ complex as a pre-catalyst, the active Fe^{III}-(hydro)peroxo species was generated by reducing the combination of [Fe^{II}L₅]²⁺ and O₂ with the powerful reductant [MV^{•+}] with two possible mechanisms. Dioxygen is reduced under its free form or at the iron center leading to the generation of the Fe^{III}-(hydro)peroxo species. An important experimental fact comes from the observation that the benzaldehyde product is the main product when the photocatalytic run is performed at pH 6. Since the benzaldehyde product is obtained by reaction of the alkenyl radical cation with the Fe^{III}-peroxo species Fe^{III}-OO⁻, while the diol product was formed by oxidizing olefin with an Fe^V=O species, itself evolving from Fe^{III}-hydroperoxo species Fe^{III}-OOH. We can propose that at pH 6 the protonation of the Fe^{III}-peroxo species is less favoured, leading to the selective benzaldehyde formation.

The photocatalytic activity of the [(Fe^{III}DPy)₂O](OTf)₂ complex through homolytic Fe-O cleavage to form the active Fe^{IV}=O species is probably deactivated in aqueous medium. However preliminary study in aerated acetonitrile for 15 h revealed that the oxidation of PPh₃ to O=PPh₃ was accelerated in presence of [(Fe^{III}DPy)₂O](OTf)₂ dimer as pre-catalyst upon light irradiation (λ > 550 nm)(Table III-6). Moreover, the consumption of O₂ during the photo-reaction with [(Fe^{III}DPy)₂O](OTf)₂ dimer was also accelerated (Figure III-28). Therefore, the preliminary results on photocatalytic activity of [(Fe^{III}DPy)₂O](OTf)₂ in organic media are encouraging for further investigation.

$[(\text{Fe}^{\text{III}}\text{DPy})_2\text{O}](\text{OTf})_2$	PPh_3	$\text{O}=\text{PPh}_3$	TON	TOF
25 μM	250 mM	6.3 mM	252	17 h^{-1}
0	250 mM	2.3 mM	x	x

Table III-6 : Substrate conversion. Oxygenation reactions were carried out under irradiation for 15 hours ($\lambda > 550 \text{ nm}$), under aerobic conditions. ^a TON: turnover number is calculated over catalyst.

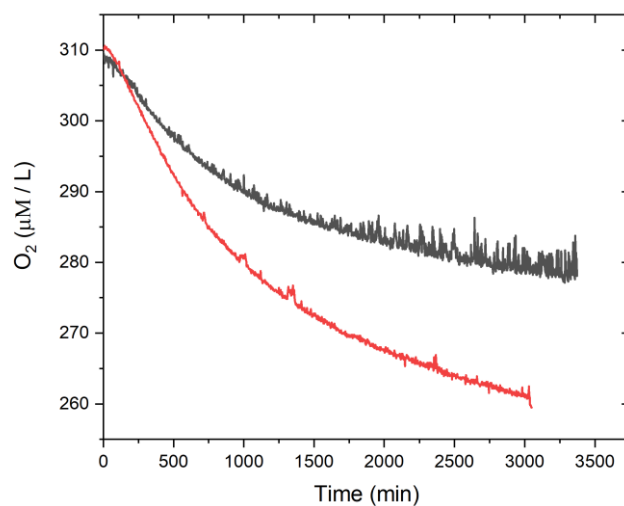


Figure III-28 : Consumption of dioxygen during the photo-oxidation of PPh_3 in presence (red) and absence (black) of $[(\text{Fe}^{\text{III}}\text{DPy})_2\text{O}](\text{OTf})_2$ dimer as pre-catalyst.

Chapter IV : Chemical generation of an
active low oxidation state iron species
based on non-innocent DPy Ligand

IV.1 Low oxidation state iron(III) species related to iron-oxo species

Hydrocarbon oxidation through C-C and C-H bond activation is a real challenging transformation both in biology and chemistry. The active species involved in these transformations have been attributed to highly oxidized metal-oxo intermediates. Although different methods have been used to generate these iron-oxo species, a general synthesis is carried out by oxidizing the iron precursor with an oxygen atom transfer agent such as a mCPBA, NaClO, H₂O₂, PhIO.¹⁷⁰⁻¹⁷² The chemical generation pathway was proposed to proceed through the formation of a low oxidation state iron adduct species containing a Fe-O-X (X = IPh, OH, Cl, OC(O)R) motif followed by a O-X bond cleavage to form a highly oxidized iron-oxo species responsible for oxygenating substrates. In some cases these early intermediates could be characterized and their conversion to iron-oxo species studied, raising the question of multiple oxidant mechanisms.^{173,174}

IV.1.1 Fe-O-X adducts

IV.1.1.1 *Fe-O-Cl*

In 2004, Banse and co-workers reported the spectroscopic characterization of an iron(IV)-oxo species generated by oxidizing iron(II) precursor [L₅Fe^{II}Cl](PF₆) with NaClO as oxidant agent.¹⁶⁹ The Mössbauer spectroscopy obtained at 80 K in absence of an applied magnetic field revealed a major species with the parameters $\delta = 0.01 \text{ mm}\cdot\text{s}^{-1}$ and $\Delta E_Q = 1.2 \text{ mm}\cdot\text{s}^{-1}$ indicating a low-spin Fe^{IV} species. While, the Raman spectrum showed a band at 752 cm^{-1} as a good candidate for a Fe-O vibration. The characteristic absorption band at 756 nm ($\epsilon \approx 300 \text{ M}^{-1}\text{cm}^{-1}$) corresponding to a d-d transition was also observed. To clarify the mechanism of the iron(IV)-oxo formation, stopped-flow absorption experiment was carried out. Upon addition of 100 eq of NaClO to the iron(II) precursor solution, an intermediate characterized by a transient band at 440 nm was first formed and then quickly transformed to a Fe^{IV}=O species in 200 ms. This clean transformation is characterized by a clear isosbestic point at 503 nm. The intermediate absorbing at 440 nm was proposed to be an Fe^{II}-O-Cl adduct by the authors. Accordingly, the proposed mechanism is summarized in Figure IV-1.

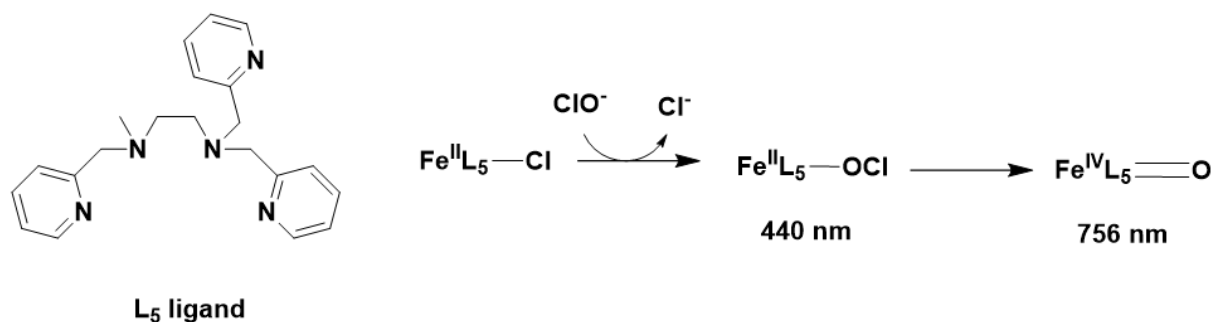


Figure IV-1 : L₅ ligand structure and mechanism proposed for the formation of mononuclear L₅Fe^{IV}=O via the L₅Fe^{II}-OCl species using NaClO.

10 years later, Brown and Visser reported the reaction of [Fe^{II}(MeN4Py)]²⁺ precursor with 2 eq NaClO showing the formation of an Fe^{III}-OCl species and subsequently an Fe^{IV}=O species by homolytic O-Cl cleavage.¹⁷⁵ The Fe^{III}-OCl species was characterized by a absorption band at 480 nm and by an EPR resonance revealing 3 signals with g values at 2.26, 2.15 and 1.97 attributed to a low-spin iron(III) species. The Raman spectrum revealed two strong bands at 653 and 580 cm⁻¹ which were assigned to an Fe-O and an O-Cl stretching modes of the Fe^{III}-OCl species. The need for 2 eq NaClO for the formation of Fe^{III}-OCl species was explained by the following events. First the one-electron oxidation of [Fe^{II}(OH₂)(MeN4Py)]²⁺ into [Fe^{III}(OH)(MeN4Py)]²⁺ is occurred by 0.5 eq of the two-electron oxidant NaClO. Second, the reversible hydroxo substitution by a hypochlorite ligand yields Fe^{III}-OCl species that slowly decomposes into the Fe^{IV}=O species by a homolytic O-Cl cleavage.

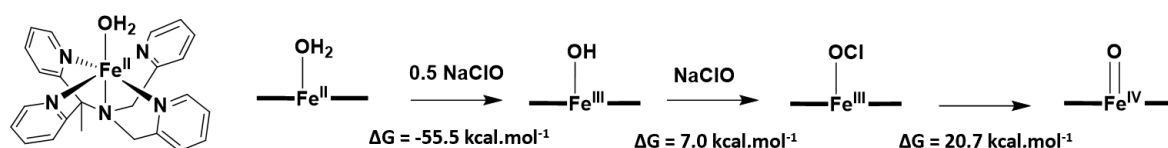


Figure IV-2 : The reaction mechanism for the formation of [Fe^{III}(OCl)(MeN4Py)]²⁺ and [Fe^{IV}(O)(MeN4Py)]²⁺ proposed on the basis of DFT calculations.

In 2012, Fujii reported that an hypochloritoiron(III) porphyrin adduct [Fe^{III}(OCl)₂(TPFP)]¹⁻ could be generated by reacting iron(III) porphyrin with TBAOCl. This intermediate was found to be stable for 1 h at -60 °C and was characterized by a Soret band at 422 nm and a visible band at 534 nm. The [Fe^{III}(OCl)₂(TPFP)]¹⁻ adduct was further characterized by three EPR signals at g = 2.26, 2.14 and 1.96, revealing a low spin (S = ½) iron(III) species. The

energy of the O-Cl vibration in The $[\text{Fe}^{\text{III}}(\text{OCl})_2(\text{TPFP})]^{1-}$ adduct was identified by Raman resonance spectroscopy at 780 cm^{-1} that shifted to 747 cm^{-1} upon labelling with ^{18}O . This adduct slowly decomposed into $[\text{Fe}^{\text{IV}}(\text{O})(\text{TPFP})]$ at $-40\text{ }^\circ\text{C}$ identified by two absorption bands at 414 nm , 546 nm , a silent EPR spectrum and a vibration at 828 cm^{-1} assigned to Fe-O oscillator in $[\text{Fe}^{\text{IV}}(\text{O})(\text{TPFP})]$ species. Interestingly, $[\text{Fe}^{\text{III}}(\text{OCl})_2(\text{TPFP})]^{1-}$ was identified as an active oxidant for sulfoxidation and epoxidation reaction because it oxidized substrates in a few minutes while the corresponding iron-oxo species is formed by decomposition within 90 min at $-20\text{ }^\circ\text{C}$ (Figure IV-3).¹⁷⁶ Indeed, upon addition of thioanisole or cyclohexene, UV-visible spectrum of the $[\text{Fe}^{\text{III}}(\text{OCl})_2(\text{TPFP})]^{1-}$ adduct quickly changed to a spectrum typical of a mixture of the $[\text{Fe}^{\text{III}}(\text{Cl})(\text{TPFP})]$ and $[\text{Fe}^{\text{III}}(\text{OH})(\text{TPFP})]$ complexes. However, the oxidative activity of the $[\text{Fe}^{\text{III}}(\text{OCl})_2(\text{TPFP})]^{1-}$ adduct can be questioned because the presence of substrate probably accelerated the decomposition of the $[\text{Fe}^{\text{III}}(\text{OCl})_2(\text{TPFP})]^{1-}$ adduct into the $[\text{Fe}^{\text{IV}}(\text{O})(\text{TPFP})]$ species that can be responsible for the observed reactivity.

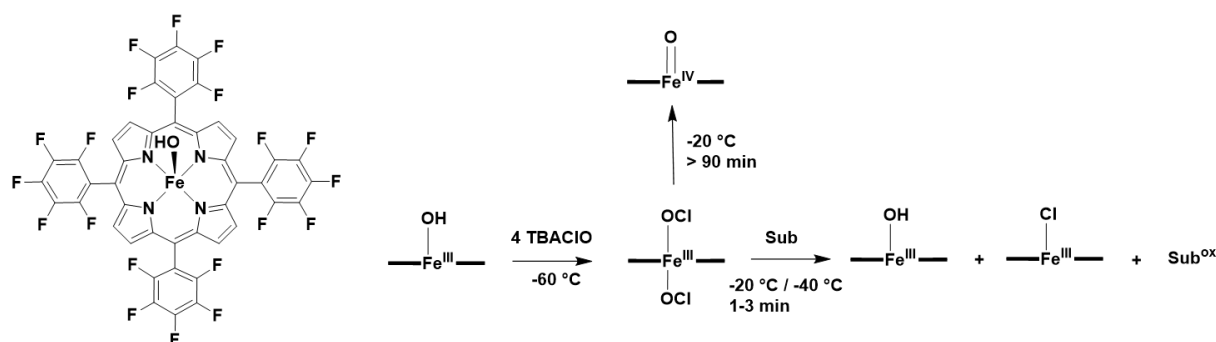


Figure IV-3 : $[\text{Fe}^{\text{III}}(\text{OCl})_2(\text{TPFP})]^{1-}$ adduct involved in oxidation reaction.

IV.1.1.2 Fe-O-OC(O)-R

In 2018, Costas and co-workers reported that the reaction of $[\text{Fe}^{\text{II}}(\text{CF}_3\text{SO}_3)_2(\text{PyNMe}_3)]$ precursor with excess peracetic acid generates a mixture of minor $[\text{Fe}^{\text{III}}(\text{OOAc})(\text{PyNMe}_3)]$ species and major $[\text{Fe}^{\text{V}}=\text{O}(\text{OAc})(\text{PyNMe}_3)]$ species, in which iron-oxo species is formed by a reversible O-O bond cleavage of acylperoxoiron(III) species obtained after the one-electron oxidation of the iron(II) precursor into iron(III) complex (Figure IV-4). Both species were characterized by Mass spectroscopy and EPR revealing two low spin ($S = \frac{1}{2}$) iron(III) and

iron(V) species. The author proposed that the reactivity towards C-H activation comes from the iron(V)-oxo species.

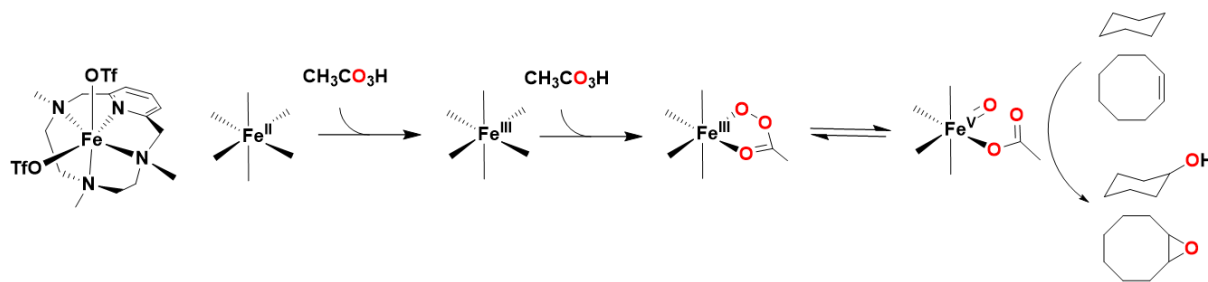


Figure IV-4 : Proposed mechanism for generating active iron species.

IV.1.1.3 Fe-OIAr

Iodosylarenes are another important class of oxygen atom transfer reagents in organic synthesis, often used in conjunction with transition-metal-based catalyst.^{177,178} Oxygen atom transfer from iodosylarenes to iron complex giving the corresponding iron-oxo species was suggested to proceed via the formation of iron-iodosylarene adduct shown in Figure IV-5. The existence of an equilibrium between iron-oxo species and iron-iodosylarene adduct was reported by Nam and co-workers in 2003.¹⁷⁹ They indeed showed that by reaching $[(\text{TDCPP}\bullet)\text{Fe}^{\text{IV}}=\text{O}]^+$ or $[(\text{TDFPP}\bullet)\text{Fe}^{\text{IV}}=\text{O}]^+$ (previously generated using mCPBA as oxidant) with iodobenzene, $[(\text{TDCPP})\text{Fe}^{\text{III}}(\text{OIPh})]^+$ or $[(\text{TDFPP})\text{Fe}^{\text{III}}(\text{OIPh})]^+$, respectively could be formed and detected spectroscopically. Remarkably, the formation of iron-iodosylarene was not observed with any iron-oxo porphyrin species / iodoarene combination. For example, the formation of iron-iodoarene adduct was not observed in the reaction of PhI and $[(\text{TMP}\bullet)\text{Fe}^{\text{IV}}=\text{O}]^+$ based on an electron-rich porphyrin ligand. Nor, the reaction of $[(\text{TDCPP}\bullet)\text{Fe}^{\text{IV}}=\text{O}]^+$ species and the electron-poor $\text{F}_5\text{C}_6\text{I}$. Interestingly, the iron-iodosylarene adducts $[(\text{TDCPP})\text{Fe}^{\text{III}}(\text{OIPh})]^+$ and $[(\text{TDFPP})\text{Fe}^{\text{III}}(\text{OIPh})]^+$ were immediately converted back into the iron(III) porphyrins $[(\text{TDCPP})\text{Fe}^{\text{III}}]^+$ and $[(\text{TDFPP})\text{Fe}^{\text{III}}]^+$ respectively, upon addition of a substrate such as thioanisole and cyclohexene, indicating that these iron-iodoarene adducts seemed to be oxidizing agent. However, the possibility that the small amount of the active iron(IV)-oxo cation radical in equilibrium with the iodoarene adduct could oxidize the substrates, was not excluded.

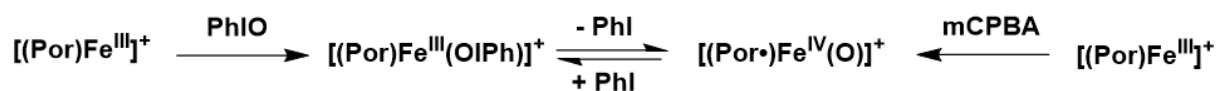


Figure IV-5 : Existence of an equilibrium between iron-oxo porphyrin species and iron-iodosylarene porphyrin adduct.

Three years later, Nam reported that the equilibrium depicted in Figure IV-5 is controlled by factors such as the electronic nature of iron porphyrin and the iodoarenes.¹⁸⁰ The shift forwards iron-iodosylarene adduct occurs readily when iron porphyrin $[(\text{Por})\text{Fe}^{\text{III}}]^+$ is supported by a more electron-deficient porphyrin and the iodoarene is more electron-rich. However, the authors proposed that the $[(\text{Por}\bullet)\text{Fe}^{\text{IV}}=\text{O}]^+$ species is in fact responsible for epoxidizing alkenes when the $[(\text{Por}\bullet)\text{Fe}^{\text{IV}}=\text{O}]^+$ species and the iron(III)-iodosylarene porphyrin adduct are present in reaction by equilibrium. This proposition was based on the similar product ratios obtained in a series of competitive epoxidations (cis-stilbene versus trans-stilbene and cyclooctene versus trans-stilbene) with $\text{Fe}^{\text{III}}\text{TDFPP}$ -iodosylarene adducts prepared by two different pathways: one by the reaction of the $[(\text{TDFPP}\bullet)\text{Fe}^{\text{IV}}=\text{O}]^+$ species with different iodoarenes such as PhI, 4- CH_3Ph , 2,4,6- $(\text{CH}_3)_3\text{PhI}$ and second by the reaction of the $[(\text{TDFPP})\text{Fe}^{\text{III}}]^+$ complex with different iodosylarenes.

Yet, this hypothesis was challenged in the case of a nonheme iron complex that afforded the first X-ray characterization of an iron-iodosylarene intermediate reported by McKenzie in 2012.¹⁸¹ The high-spin seven-coordinated iron(III)-iodosylbenzene was prepared from the reaction of iodosylbenzene (PhIO) with a μ -oxo diiron(III) precursor based on a $\text{N}_3\text{N}'$ -tris(2-pyridylmethyl)ethylenediamine- N' -acetate (tpena⁻) hexadentate ligand (Figure IV-6). Therefore, the nature of the active species involved in the oxygenation of thioanisole to methylphenyl sulfoxide by μ -oxo diiron(III) precursor $[\{\text{Fe}^{\text{III}}(\text{tpenaH})\}_2\text{O}]$ in presence of PhIO as oxidant was questioned. No high-valent iron-oxo species was observed in this case. $[\text{Fe}^{\text{III}}(\text{tpena})(\text{OIPh})]$ could be inactive and play the role of a labile reservoir for the active iron(V)-oxo species or could be an active oxidant transferring oxygen atom to the substrate in a concerted mechanism.¹⁸² The comparison of the decay time of $[\text{Fe}^{\text{III}}(\text{tpena})(\text{OIPh})]^{2+}$ species in absence and presence of one equivalent of thioanisole as a substrate supports the latter hypothesis that the $[\text{Fe}^{\text{III}}(\text{tpena})(\text{OIPh})]^{2+}$ species is able to oxidize the substrate.¹⁸³ The

presence of 1 eq. of thioanisole led to a 260-fold acceleration of the decay time of the $[\text{Fe}^{\text{III}}(\text{tpena})(\text{OIPh})]^{2+}$ species, while the substrate oxidation rate increased with thioanisole concentration. The authors propose that given that the $\text{Fe}^{\text{V}}=\text{O}$ species was not detected, then if it were the active species it would have reacted instantaneously. Therefore no substrate concentration dependence would be observed. Henceforth, the $[\text{Fe}^{\text{III}}(\text{tpena})(\text{OIPh})]^{2+}$ species was postulated as the active species.

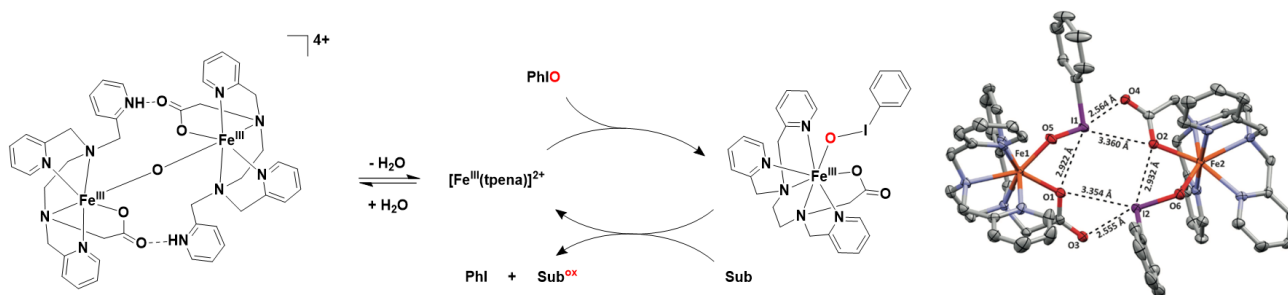


Figure IV-6: (Right) X-ray structure of $[\text{Fe}^{\text{III}}(\text{tpena})(\text{OIPh})]^{2+}$; (Left) Proposed mechanism for oxidation of a substrate (Sub) by iodosylbenzene catalyzed by $[\{\text{Fe}^{\text{III}}(\text{tpenaH})_2\text{O}\}]^{4+}$.

One could ask if the nature of the active species can depend on the the nature of the ligand. In fact, in 2014 Nam and co-workers came back on their initial mechanistic proposal in the case of a nonheme ligand. They demonstrated that the reaction rate of oxidation of substrates such as thioanisole, cumene, by $[(13\text{-TMC})\text{Fe}^{\text{III}}\text{-OI C}_6\text{F}_5]^{3+}$ was not influenced by the addition of $\text{C}_6\text{F}_5\text{I}$.¹⁸⁴ If the iron-oxo species was the only active oxidant capable of oxygenating substrate, then the presence of an excess amount of iodoarene should decrease the oxidation rate. Therefrom, the iron-iodosylarene adduct was proposed to be as the oxidizing agent. However, this hypothesis was based on the assumption that an equilibrium between the iron-iodosylarene porphyrin adduct and the iron-oxo cation radical porphyrin exists although while no evidence for this equilibrium was reported with nonheme iron complex was reported.

Furthermore, when $[(13\text{-TMC})\text{Fe}^{\text{II}}]^{2+}$ was used in combination with the chiral iodosylarene ($^c\text{PhIO}$), chalcone was converted to chalcone oxide as major product with 76 % enantioselectivity (Figure IV-7).¹⁸⁵ Because the iron(IV)-oxo or iron(V)-oxo species obtained by homolytic or heterolytic O-I bond cleavage do not possess a chiral center, the reaction of iron-oxo species with chalcone would have led to a racemic mixture product. Nam and co-workers thus propose that the active intermediate responsible for oxidation reaction in these

cases is the iron-iodosylarene adduct, not iron-oxo species. However, one can not exclude a minor participation of an iron-oxo species

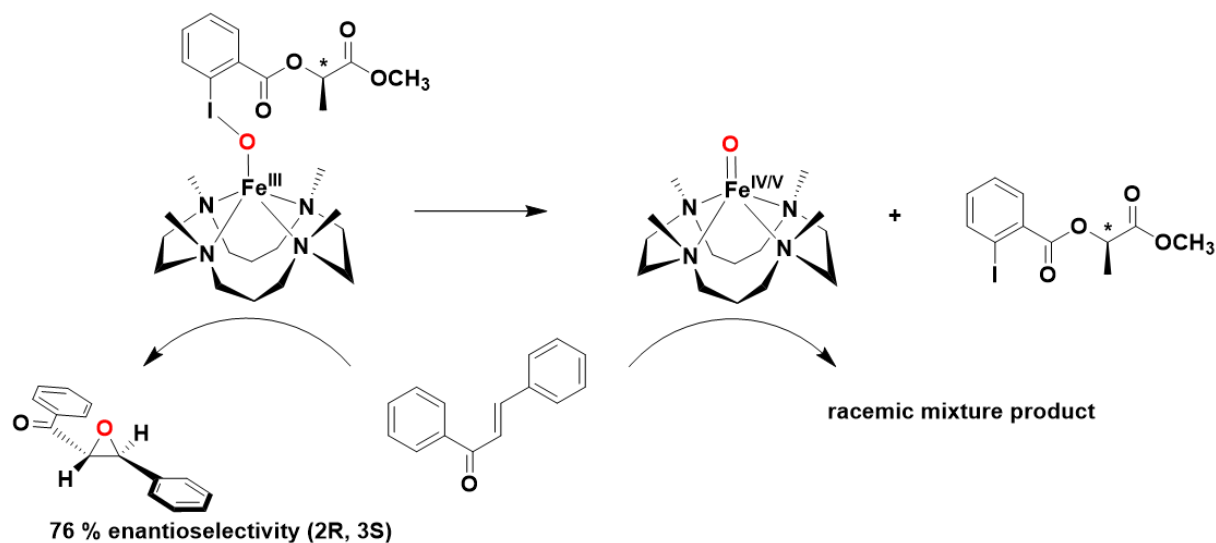


Figure IV-7: Proposed iron-iodosylarene adduct and iron-oxo species in olefin epoxidation reaction.

IV.1.2 Ligand-oxygenated iron(III) species

Iron intermediates where the ligand have undergone self-oxidation were detected in the reaction of an iron precursor with oxidizing agent. In 1986, Groves and Watanabe reported on an iron(III) N-oxide porphyrin species obtained by oxidizing $[\text{Fe}^{\text{II}}(\text{TMP})]^+$ in toluene by 2 eq. of m-CPBA.^{186–188} The reaction was monitored at -50°C by UV-visible spectroscopy, showing the immediate formation of iron(III)-m-CPBA adduct followed by a relatively slow decomposition to iron(III) porphyrin N-oxide species. The formation of iron(III) porphyrin N-oxide species was proposed to account for the equimolar formation of diacyl peroxide, occurring through an homolytic O-O bond cleavage and the formation of N-(benzoxo) iron(III) porphyrin intermediate as shown in Figure IV-8.

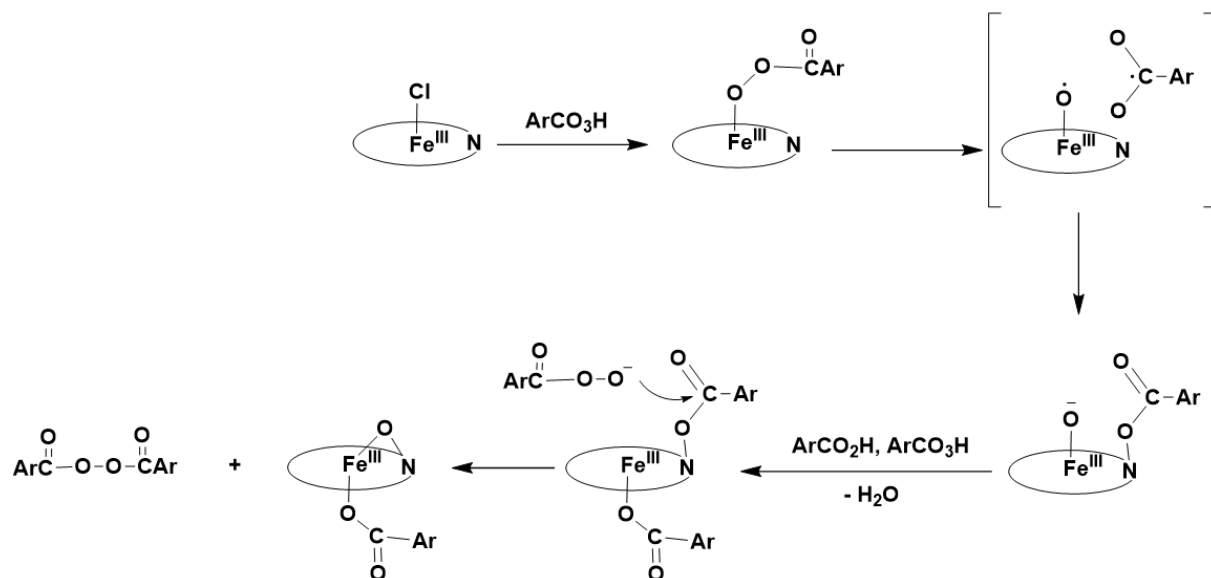


Figure IV-8 : Proposed mechanism for iron(III) porphyrin N-oxide formation in toluene..

In 2006 McKenzie reported two degradation products in the reaction of the iron(III) complex based on the carboxylate-containing pentadentate ligand with tertbutyl peroxide ${}^t\text{BuOOH}$.¹⁸⁹ These degraded products, which were isolated and characterized by X-Ray diffraction analysis were proposed to be the products of the aromatic hydroxylation and the N-oxygenation by a $\text{Fe}^{\text{V}}=\text{O}$ moiety. Of note, no observation of the $\text{Fe}^{\text{V}}=\text{O}$ species was reported.

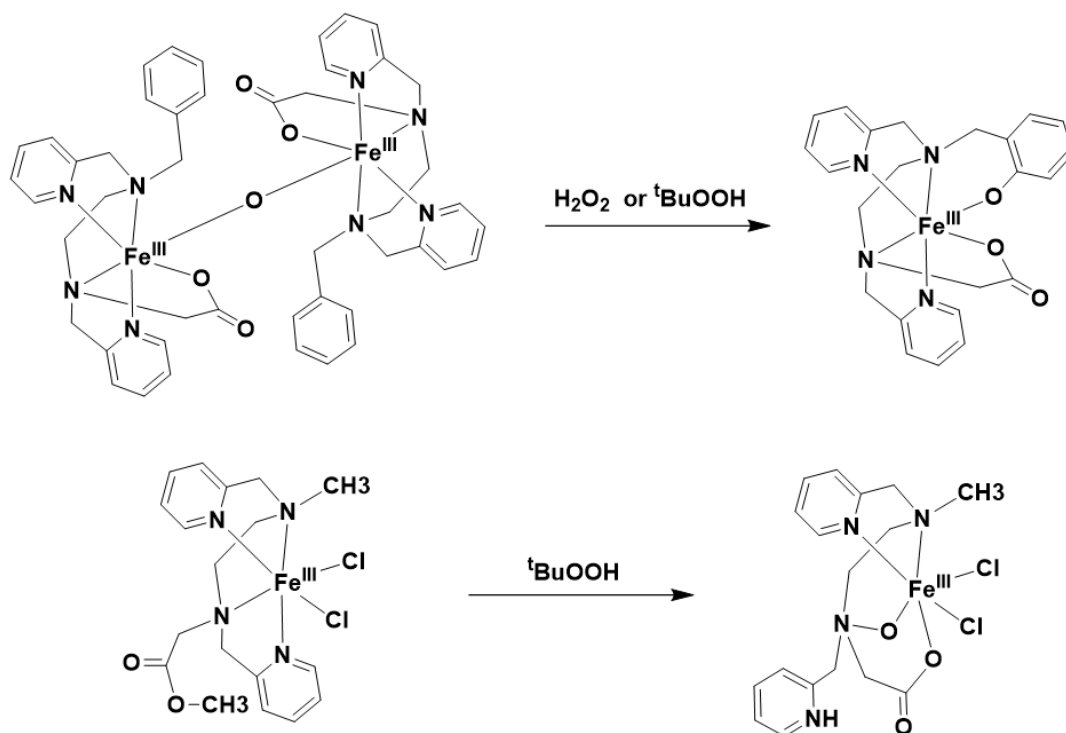


Figure IV-9: Two ligand-oxygenated iron(III) species reported by McKenzie.

More recently, in 2017, Kovacs reported a sulfonate-ligated iron(III) species $[\text{Fe}^{\text{III}}(\eta^2\text{-S}^{\text{Me}_2}\text{O})(\text{S}^{\text{Me}_2}\text{N}_3(\text{Pr},\text{Pr}))]^+$ which was isolated from the reaction of the five-coordinate dithiolate iron(III) $[\text{Fe}^{\text{III}}(\text{S}_2^{\text{Me}_2}\text{N}_3(\text{Pr},\text{Pr}))]^+$ with PhIO at $-30\text{ }^\circ\text{C}$. The UV-visible spectral evolution during this reaction at $-70\text{ }^\circ\text{C}$ revealed that the dithiolate precursor was converted to a new species characterized by a band at 677 nm. This intermediate was assigned to an iron(III)-iodosylarene adduct or an iron(V)-oxo species before turning into the sulfonate form ($\lambda_{\text{max}} = 510\text{ nm}$). Importantly, the authors made no mention if $[\text{Fe}^{\text{III}}(\eta^2\text{-S}^{\text{Me}_2}\text{O})(\text{S}^{\text{Me}_2}\text{N}_3(\text{Pr},\text{Pr}))]^+$ was able to further transfer the oxygen atom to an exogenous substrate. However, it was only observed and isolated at low temperature, indicating that this intermediate can further react.

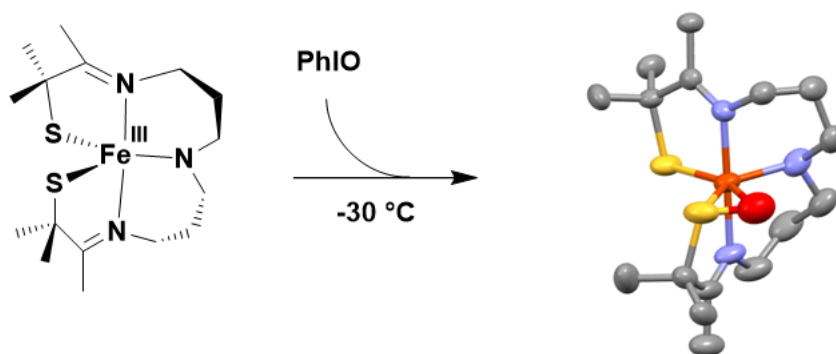


Figure IV-10: X-Ray structure of $[Fe^{III}(\eta^2-S^{Me_2}O)(S^{Me_2}N_3(Pr,Pr))]^+$.

The multiple active oxidant mechanism possibly involving the low oxidation state iron species have challenged the hypothesis that the highly oxidized iron-oxo species are the only species responsible for iron-catalyzed OAT reaction. Indeed, the nature of the active species depends on both the ligand set and the oxidant. Therefore, further attempts to understand the nature of active species responsible for substrate oxygenation by a given system is indispensable to enhance the reactivity of synthetic catalysts. In this chapter, we will report the generation and characterization of new active iron species using different oxidant and study their reactivity in organic medium. Because the μ -oxo diiron(III) $[(Fe^{III}DPy)_2O](OTf)_2$ probably converts to monomer iron(III) complex before reacting with oxidant agent,^{181,183,189} we used the well-defined monomer $Fe^{III}DPyCl_2$ in this study.

IV.2 Chemical oxidation of Fe^{III}DPyCl₂ and evidence of a reversible ligand oxidation

The oxidation of the iron(III) complex to form active species was studied by using oxygenated chemical oxidants. Three oxidants were tested: iodosylbenzene (PhIO), sodium hypochlorite (NaClO) and meta-chloroperbenzoic acid (mCPBA). These reagents are all known to allow the formation of highly oxidized iron-oxo species or an active low-oxidation-state iron intermediates. Our strategy was first to seek the conditions allowing us to well characterize the oxidized form of [Fe^{III}DPy]²⁺ complex and then to evaluate its reactivity.

IV.2.1 Oxidation with m-CPBA

The reaction of Fe^{III}DPyCl₂ with an excess of m-CPBA (10 eq) in acetonitrile at room temperature leads to the disappearance of all absorption bands characterizing Fe^{III}DPyCl₂ complex in 10 min and without the apparition of new bands that would attest the accumulation of an oxidized species (Figure IV-11). m-CPBA is a two-electron oxidant agent which should oxidize the iron(III) precursor to generate probably an iron(V)-oxo species [Fe^V=O(DPy)]²⁺ or an iron(IV)-oxo ligand cation radical species [Fe^{IV}=O(DPy[•])]²⁺, due to the non-innocent semi hemic DPy ligand. Based on the literature, the synthetic iron(V) and iron(IV) oxo species can be identified by an absorption band around 600–800 nm with a moderate extinction molar coefficient ($\epsilon = 100\text{--}4000 \text{ M}^{-1}\text{cm}^{-1}$) corresponding to a d-d transition.¹⁹⁰ If such a species was formed it is possible that this characteristic weak absorption band would be hidden by the strong $\pi\text{-}\pi^*$ absorption band of the Fe^{III}DPyCl₂ precursor at 666 and 584 nm ($\epsilon = 10118$ and $21680 \text{ M}^{-1}\text{cm}^{-1}$, respectively). The short lifetime of the oxidized iron species at room temperature compared to its slow generation by m-CPBA in 10 min also prevented its detection. The reaction of Fe^{III}DPyCl₂ with m-CPBA at low temperature (-40 °C) was not helpful to observe the characteristic band of the active species, probably because both the formation and the degradation of the oxidized species were slow down.

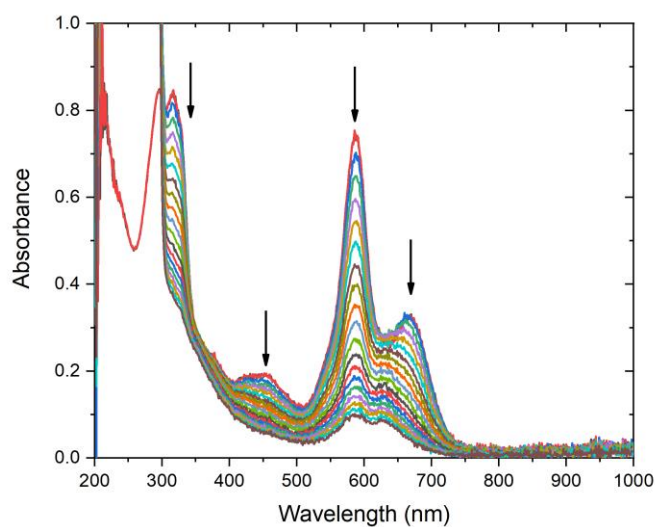


Figure IV-11: UV-visible spectral changes of a $\text{Fe}^{\text{III}}\text{DPyCl}_2$ ($25 \mu\text{M}$) solution after addition of 10 eq *m*-CPBA in acetonitrile at room temperature over 10 min.

The reactional mixture of $\text{Fe}^{\text{III}}\text{DPyCl}_2$ and 10 eq *m*-CPBA was stirred for 1 min and frozen in liquid nitrogen before EPR studied. The X-band EPR spectrum at 10 K showed a signal at $g = 4.3$ attributed to a high spin ($S = 5/2$) iron(III) species in a low symmetry environment, while only traces of the tree signals with g value at 9.0, 5.1 and 3.7 characterizing the $\text{Fe}^{\text{III}}\text{DPyCl}_2$ precursor were observed (Figure IV-12). This could indicate the rapid formation of an iron(III)-*m*CPBA adduct in less than 1 min. In addition, a broad signal with g value at 2.0 was also observed. This last signal could correspond to a radical cation ligand coordinated on iron center such as $[\text{Fe}^{\text{IV}}=\text{O}(\text{DPy}^\bullet)]^{2+}$ or a low spin iron(V) species $[\text{Fe}^{\text{V}}=\text{O}(\text{DPy})]^{2+}$ obtained by a heterolytic O-O bond cleavage. Remarkably, this EPR matched with the one obtained from the electrolysis of the $\text{Fe}^{\text{III}}\text{DPyCl}_2$ complex at 1.6 V in wet acetonitrile (Figure IV-12).

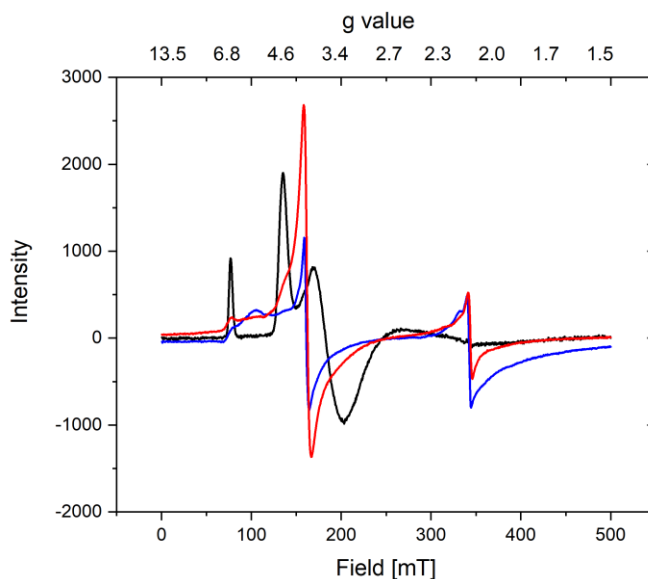


Figure IV-12: EPR spectra recorded at 10 K of the $\text{Fe}^{\text{III}}\text{DPyCl}_2$ complex solution (1 mM) (black), upon oxidation with 10 eq *m*-CPBA (red) or electrolyzing at 1.6 V vs SCE (blue).

In the case of iron porphyrin, the nature of the O-O bond cleavage seemed to be conditioned by the nature of the solvent. Indeed, Nam and co-workers reported that the nature of the anionic axial ligand can affect the O-O cleavage of iron(III)-*m*-CPBA adduct.¹⁹¹ Strong electron donors such as Cl^- , OH^- and MeO^- favor the homolytic O-O cleavage leading to form iron(III) N-oxide species while the weak electron donors, for example CF_3SO_3^- and NO_3^- , favor the formation of highly oxidized iron-oxo species $[\text{Fe}^{\text{IV}}=\text{O}(\text{Por}\bullet)]^+$ through a heterolytic O-O bond cleavage (Figure IV-13). In an attempt to trap all possible active iron species supported by this new DPy ligand class; we decided to test the influence of the solvent and the axial ligand.

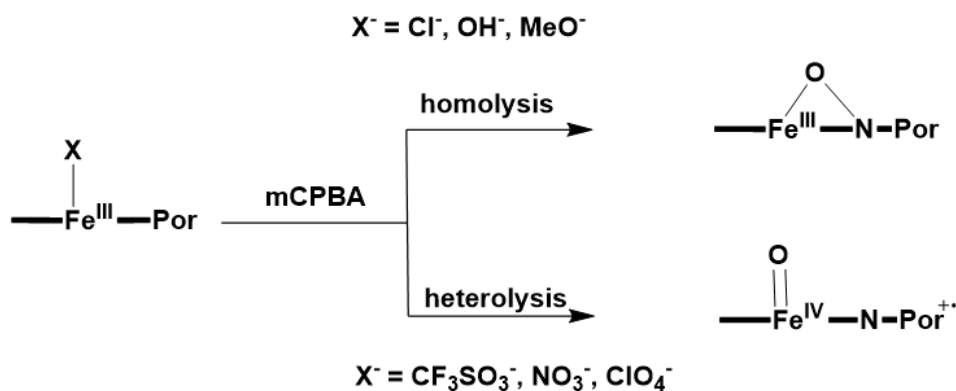


Figure IV-13 : Influence of anionic axial ligands on the locus of the oxidation of iron porphyrins by *m*-CPBA.

Solubilizing Fe^{III}DPyCl₂ in MeOH led to replacement of chloride by methanolate ligand as attested by ESI-MS analysis. Two peaks with *m/z* value at 550.0499 and 604.0570 were detected and assigned respectively to monocharged [Fe^{III}DPy(OMe)]⁺ and [Fe^{III}DPy(OMe)₂Na]⁺ with methanolate as anionic axial ligand. Likewise, the UV-visible absorption of Fe^{III}DPyCl₂ was changed in MeOH. In fact, the Fe^{III}DPy(OMe)₂ formed in-situ by Fe^{III}DPyCl₂ complex in MeOH was characterized by an intense absorption band at 630 nm ($\epsilon = 38\,600\text{ M}^{-1}\text{cm}^{-1}$) and a shoulder at 585 nm. Noteworthy, the Fe^{III}DPyCl₂ absorbs at 666 nm and 584 nm in acetonitrile. However, the EPR spectrum at 10 K of Fe^{III}DPy(OMe)₂ showed also three signals with *g* value at 9.0, 5.1 and 3.7 as for the Fe^{III}DPyCl₂ complex in acetonitrile. This is probably because methanolate ligand, which is also a π -electron donor ligand as chloride ligand, creates a similar electronic ligand field (Figure IV-15). Accordingly, the reaction of Fe^{III}DPy(OMe)₂ with *m*-CPBA in MeOH at room temperature was followed by UV-vis spectroscopy and showed similar changes as in acetonitrile. Upon addition of 10 eq *m*-CPBA, no new absorption band was observed and the initial bands of iron(III) precursor decayed within 10 min (Figure IV-14).

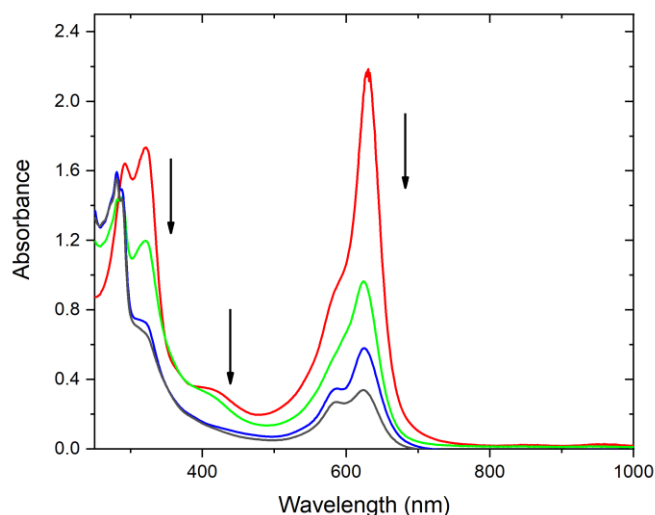


Figure IV-14 : : UV-visible spectral changes of Fe^{III}DPyCl₂ (50 μM) after addition 10 eq *m*-CPBA in MeOH at room temperature over 10 min.

Similarly, the reaction mixture of $\text{Fe}^{\text{III}}\text{DPy}(\text{OMe})_2$ complex with 10 eq m-CPBA in MeOH after mixing for 1 min was frozen and analyzed by EPR spectroscopy. The EPR spectrum at 10 K also showed a signal with g value at 4.3 attributed to a high spin ($S = 5/2$) iron(III) species and a non-identified positive broad signal at 2.01 (Figure IV-15). With the strong electron donor methanolate ligand in axial position, similar oxidation and degraded mechanisms thus seem to occur as with chloride ligand in acetonitrile.

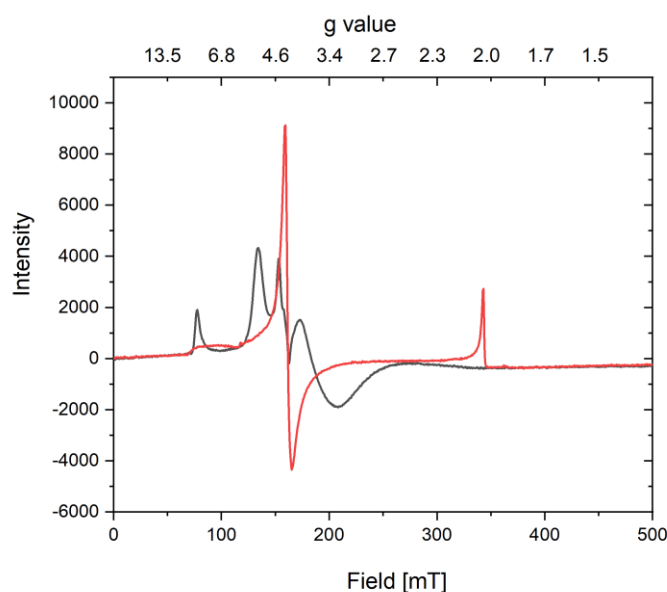


Figure IV-15 : EPR spectra recorded at 10 K of $\text{Fe}^{\text{III}}\text{DPy}(\text{OMe})_2$ (1 mM) prepared by dissolving $\text{Fe}^{\text{III}}\text{DPyCl}_2$ in MeOH (black) and oxidized species obtained by reacting with 10 eq m-CPBA (red).

We then attempted to displace the chloride ligand with less donating triflate (OTf) ligands. As already described in Chapter II, this strategy indeed lead to the formation of a dimeric, $[(\text{Fe}^{\text{III}}\text{DPy})_2\text{O}](\text{OTf})_2$ dimer. Upon addition of 10 eq m-CPBA into $[(\text{Fe}^{\text{III}}\text{DPy})_2\text{O}](\text{OTf})_2$ solution in acetonitrile, the absorption bands characterizing $[(\text{Fe}^{\text{III}}\text{DPy})_2\text{O}](\text{OTf})_2$ dimer at 616 nm and 588 nm slowly disappeared upon 10 min, and new absorption band at 633 nm was observed after mixing for 1 min then slowly disappeared (Figure IV-16). Two isosbestic points at 346 and 424 nm were observed within 1 min, indicating a clean chemical transformation.

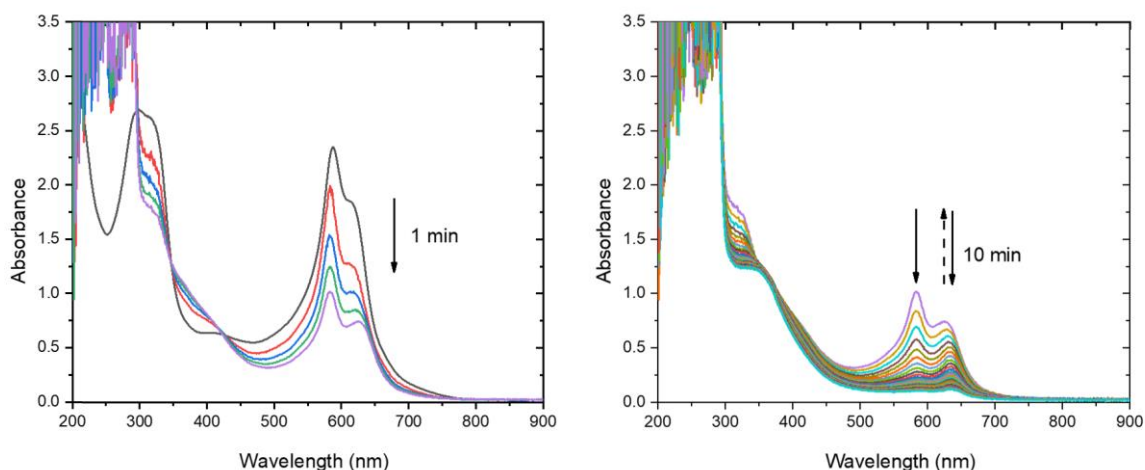


Figure IV-16: UV-visible spectral changes of $[(\text{Fe}^{\text{III}}\text{DPy})_2\text{O}](\text{OTf})_2$ ($100 \mu\text{M}$) after addition 10 eq m-CPBA in acetonitrile at room temperature over 1 min (left) and 10 min (right).

The reaction mixture obtained after mixing $[(\text{Fe}^{\text{III}}\text{DPy})_2\text{O}](\text{OTf})_2$ dimer and 10 eq m-CPBA in acetonitrile for 1 min was analyzed by EPR spectroscopy. EPR signals were detected suggesting that monomeric iron species were formed. This can be explained by the liberation of the acid allowing the μ -oxo dimer to break down as shown in chapter II. As before, an EPR signal at $g = 4.3$ attributed for a high spin iron(III) species and a broad symmetric EPR signal at $g = 2.0$ corresponding probably to metalloradical species such as $[\text{Fe}^{\text{IV}}=\text{O}(\text{DPy}^\bullet)]^{2+}$ intermediates were observed. In addition, three signals with g values at 2.15, 2.07 and 1.95 were detected. They can be tentatively assigned probably to an iron(V)-oxo species $[\text{Fe}^{\text{V}}=\text{O}(\text{DPy})]^{2+}$ obtained by a heterolytic O-O cleavage pathway.

In brief, $[\text{Fe}^{\text{III}}\text{DPy}]\text{X}_2$ (X: Cl, MeO, OTf) complexes react with mCPBA under different conditions. Absorption spectroscopy was of little help to monitor the chemical reaction but tends to support that no single species was accumulated overtime. EPR spectroscopy showed at least 2 species coexist in solution that were probably a high spin $[\text{Fe}^{\text{III}}(\text{DPy})(\text{mCPBA})]^+$ adduct and a low spin $[\text{Fe}^{\text{IV}}=\text{O}(\text{DPy}^\bullet)]^{2+}$ or $[\text{Fe}^{\text{V}}=\text{O}(\text{DPy})]^{2+}$ species obtained by heterolytic O-O cleavage. Axial ligand substitution led to subtle changes in the high field area that we are not able to explain at this stage. However, the reaction of $[\text{Fe}^{\text{III}}\text{DPy}]^{2+}$ precursor and excess of m-CPBA was relatively slow even at room temperature and not only the generated active iron species was degraded but also the $[\text{Fe}^{\text{III}}\text{DPy}]^{2+}$ precursor was completely altered in the

absence of substrate. Therefore, the m-CPBA was eliminated as the oxidant for further studies of the oxidized forms of $[\text{Fe}^{\text{III}}\text{DPy}]^{2+}$ complex.

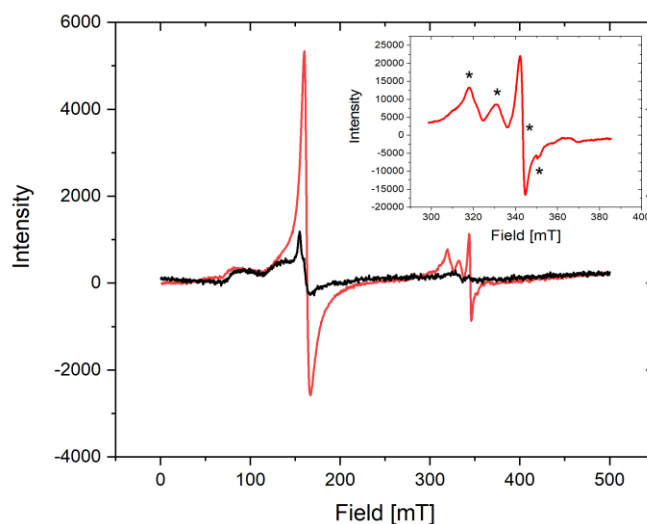


Figure IV-17 : EPR spectra recorded at 10 K of $[\text{Fe}^{\text{III}}\text{DPy}]_2\text{O}(\text{OTf})_2$ dimer (1 mM) (black), oxidized species obtained by reacting with 10 eq m-CPBA (red) and zoom at the high field area with 10 scans (inset).

IV.2.2 Oxidation with NaClO

Next, we decided to generate and characterize the oxidized forms of $\text{Fe}^{\text{III}}\text{DPyCl}_2$ complex using NaClO which is also a two-electron oxidant agent as mCPBA.

IV.2.2.1 Characterization of the generated iron species

IV.2.2.1.1 UV-visible spectroscopy

Upon addition of 2 eq. of NaClO in water to the initial blue solution of $\text{Fe}^{\text{III}}\text{DPyCl}_2$ precursor, a quick color change to cyan followed by a slow evolution to blue over 30 min was observed. Accordingly, the UV-vis spectroscopy showed the quick apparition of a new band at 631 nm with an extinction molar coefficient of $30\,700\text{ M}^{-1}\text{cm}^{-1}$ assigned to an active iron species. This band decayed with a lifetime $t_{1/2}$ of 15 min to yield a new spectrum different from the initial with a new absorption band at 615 nm, different from the initial band at 666 nm (Figure IV-18). Based on the band intensity, the initial iron(III) precursor $[\text{Fe}^{\text{III}}\text{DPy}]^{2+}$ was not fully

degraded as in the case of mCPBA. However, an altered species was obtained, which could be a complex with aqua or hydroxo ligand in axial position $[\text{Fe}^{\text{III}}\text{Dpy}(\text{H}_2\text{O})_n(\text{OH})_m]^{(2-m)+}$ due to the presence of water. Indeed, a similar UV-vis spectrum was obtained upon addition of 10 % water into $\text{Fe}^{\text{III}}\text{DPyCl}_2$ precursor in acetonitrile (Figure IV-19). The formation of μ -oxo diiron(III) complex $[(\text{Fe}^{\text{III}}\text{DPy})_2\text{O}](\text{OTf})_2$ showing very close absorption band in acetonitrile may also be envisioned.

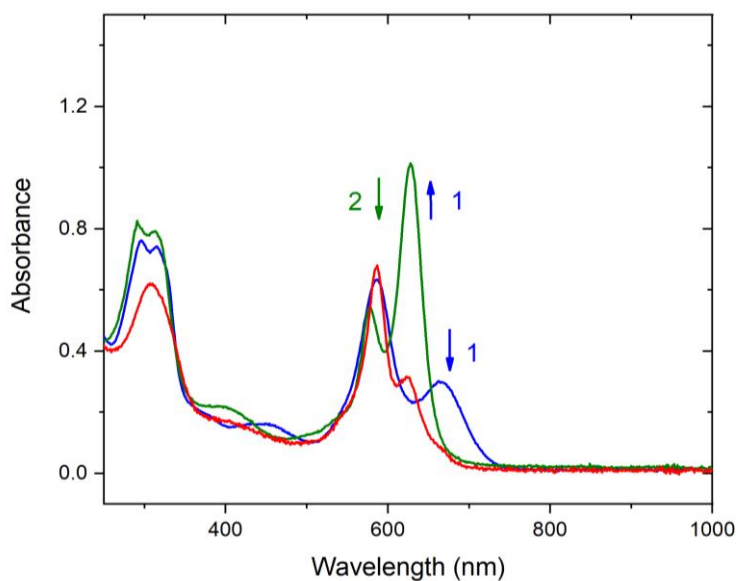


Figure IV-18 : UV-vis spectra showing the formation and decomposition of active iron species generated by oxidizing $\text{Fe}^{\text{III}}\text{DPyCl}_2$ (25 μM) with NaClO in acetonitrile/water ($v/v = 99/1$). Blue: the initial $\text{Fe}^{\text{III}}\text{DPyCl}_2$ precursor, Green: after adding of 2 eq. of NaClO and Red: evolution after 30 min.

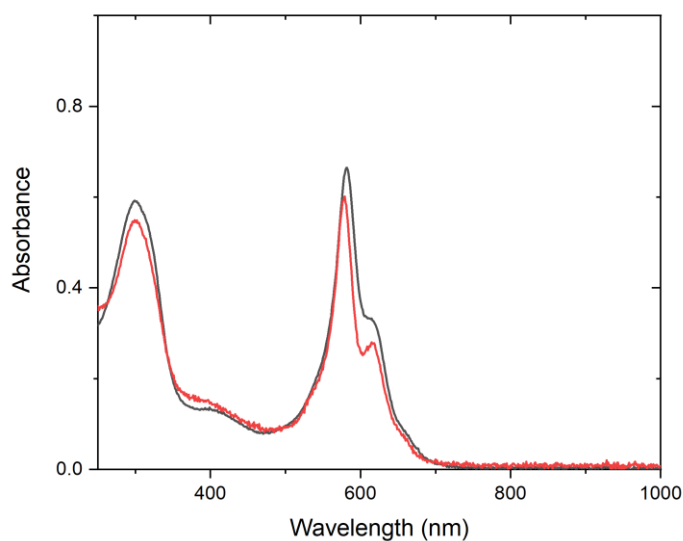


Figure IV-19 : UV-vis spectra of $Fe^{III}DPyCl_2$ ($25 \mu M$) in acetonitrile / water ($v/v = 9/1$) (black) and decomposed species obtained after oxidizing $Fe^{III}DPyCl_2$ ($25 \mu M$) in acetonitrile / water ($v/v = 99/1$) with 2 eq. of $NaClO$.

IV.2.2.1.2 EPR spectroscopy

The magnetic properties of the intermediate were characterized by X-band EPR at 10K to identify the iron species detected by UV-visible spectroscopy. The initial rhombic signal of the iron(III) precursor was replaced by a broad isotropic signal at $g=4.3$ in perpendicular mode and no signal was detected in parallel mode (Figure IV-20). The EPR signal at $g = 4.3$ assigned to a high spin ($S = 5/2$) iron(III) species reminisces the species obtained in the case of mCPBA that was also characterized by EPR signal at 4.3.

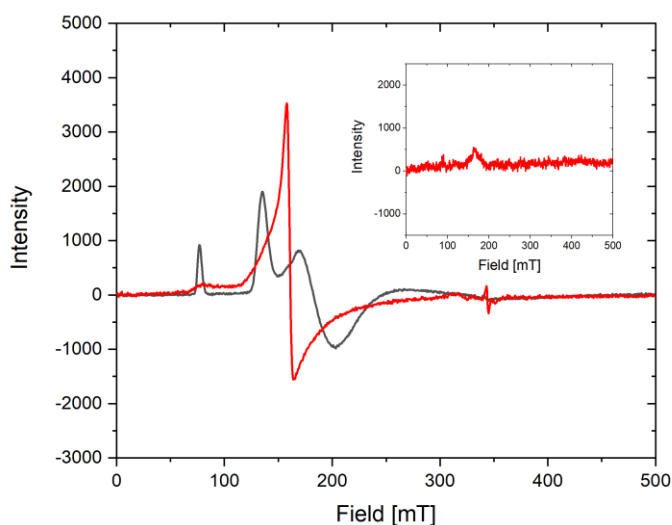


Figure IV-20: EPR spectra in perpendicular mode before (black) and after (red) oxidation of $\text{Fe}^{\text{III}}\text{DPyCl}_2$ by NaClO . Inset: EPR spectrum in parallel mode.

IV.2.2.1.3 High resolution mass spectroscopy (HRMS)

ESI⁺-HRMS analysis of the frozen solution obtained after adding NaClO showed a peak at $m/z = 569.9948$ with a charge and isotopic distribution agreeing with monocharged $[\text{Fe}(\text{DPy})\text{Cl} + \text{O}]^+$ formula (Figure IV-22, Top). Upon addition of ^{18}O labelled water to the previous sample, a new peak was detected at $m/z = 571.9993$ proving the oxygen atom in the detected species readily exchanges (Figure IV-22, Bottom). Using NaClO as terminal oxidant, the detected formula $[\text{Fe}(\text{DPy})\text{Cl} + \text{O}]^+$ can correspond to four different species: a $[\text{Fe}^{\text{III}}(\text{DPy})(\text{OCl})]^+$ adduct, two $[\text{Fe}^{\text{V}}=\text{O}(\text{DPy})(\text{Cl})]^+$ or $[\text{Fe}^{\text{IV}}=\text{O}(\text{DPy}\bullet)(\text{Cl})]^+$ iron-oxo species and a N-oxide iron(III) $[\text{Fe}^{\text{III}}(\text{DPyNO})]^+$ species. In fact, the $\text{Fe}-\text{N}_{\text{Pyridine}}$ distances in $\text{Fe}^{\text{III}}\text{DPyCl}_2$ precursor exhibited in the solid state being rather long, one could expect some degree of lability allowing such an oxygen atom insertion, suggesting the possibility to have oxidized one of the pyridines of the ligand to form an iron(III) N-oxide species $[\text{Fe}^{\text{III}}(\text{DPyN}_{\text{Py}}\text{O})]^{2+}$.

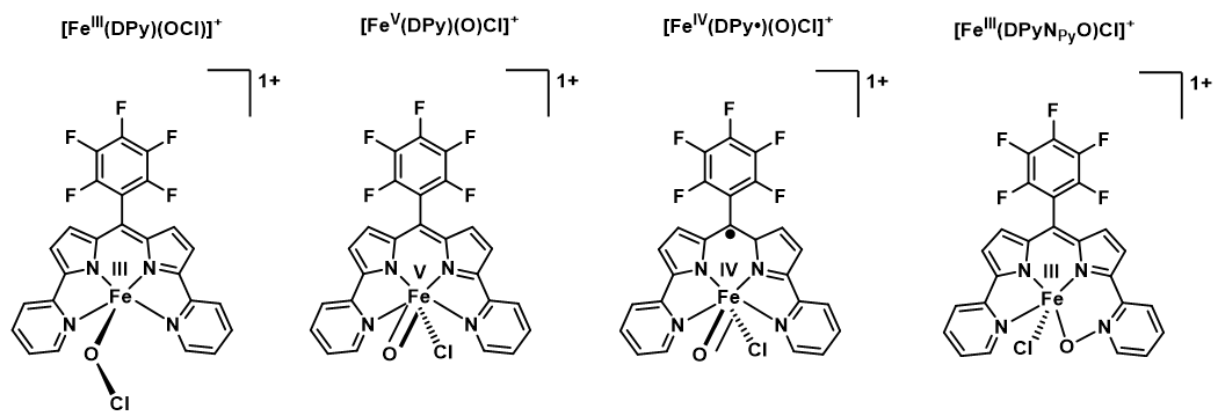


Figure IV-21: Structural assignment for $m/z = 569.9948$.

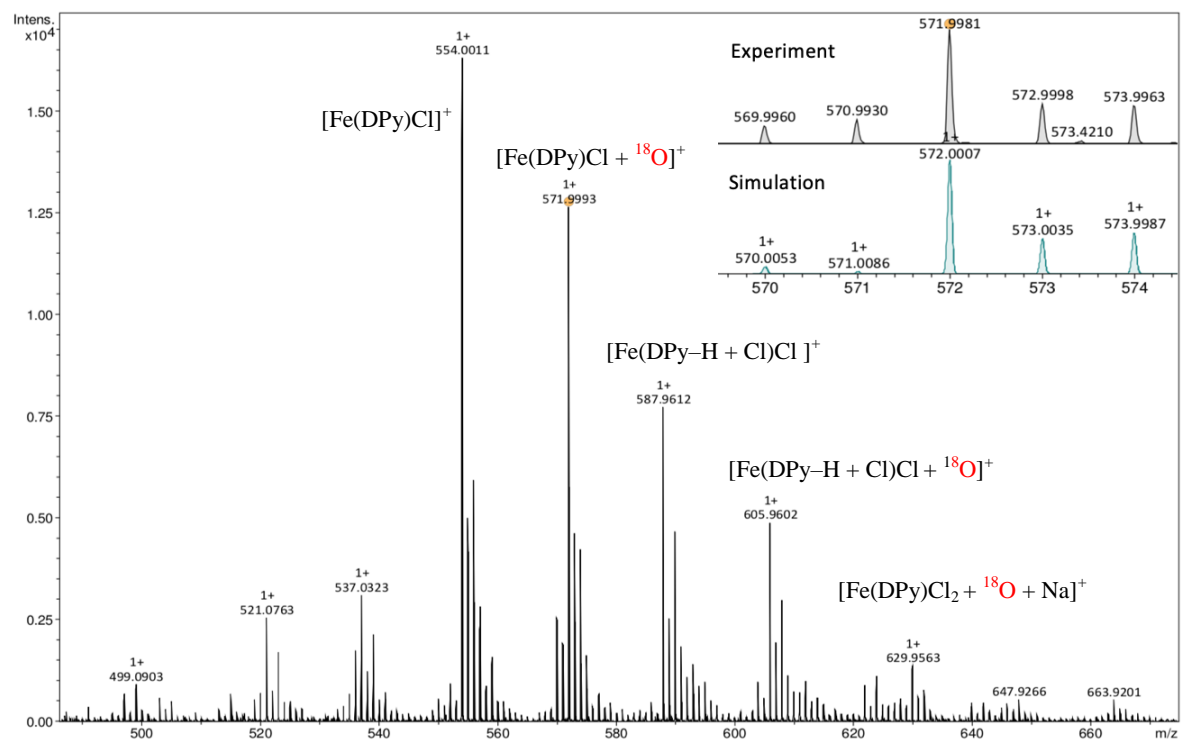
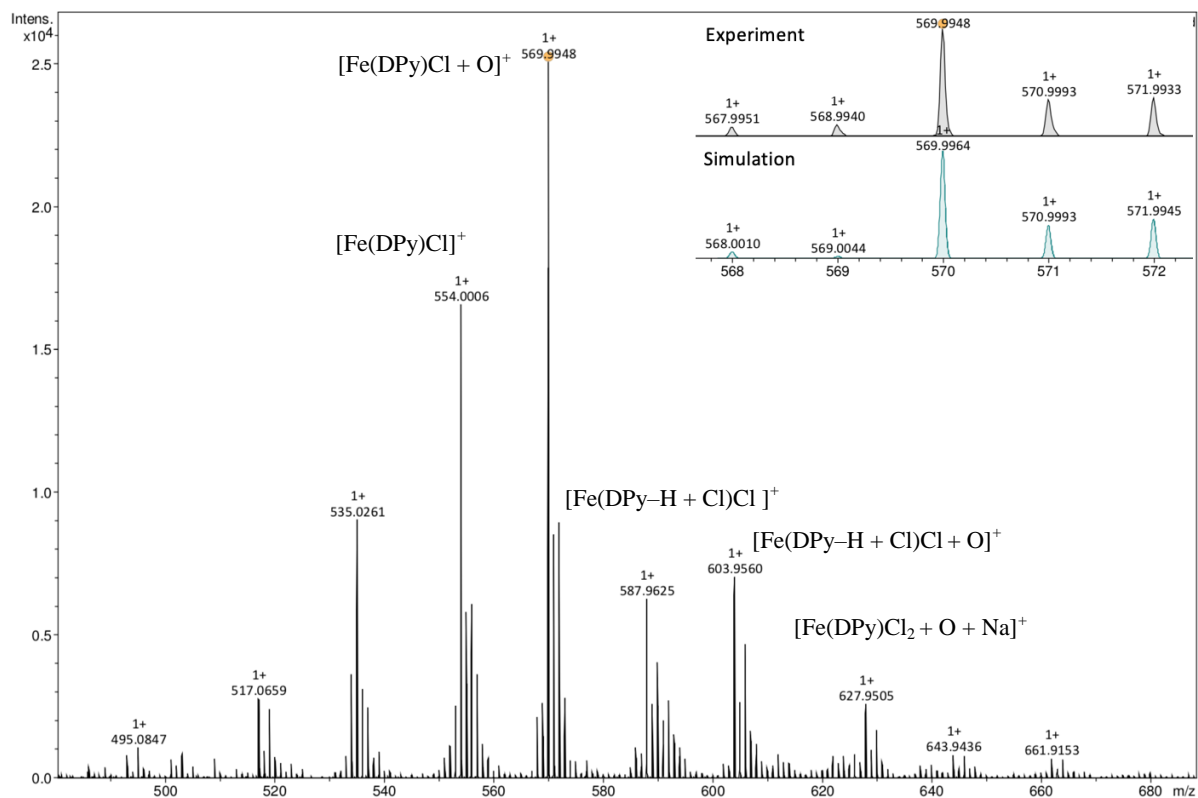


Figure IV-22 : ESI⁺-HRMS analyses of (Fe^{III}DPyCl₂ + NaClO) frozen solution in acetonitrile without (Top) and with (Bottom) H₂¹⁸O. Inset: Experimental and simulated isotopic distribution of detected species at m/z =569.9948 and 571.9981.

Combining the above HRMS and EPR results, the active iron species generated by NaClO is an iron(III) species that can be $[\text{Fe}^{\text{III}}(\text{DPy})(\text{OCl})]^+$ adduct or the N-oxide iron(III) $[\text{Fe}^{\text{III}}(\text{DPyN}_{\text{Py}}\text{O})\text{Cl}]^+$ species. When the ESI⁺-HRMS analysis was performed in a methanol diluted solution, a peak with m/z value at 566.0437 corresponding to $[\text{Fe}^{\text{III}}(\text{DPy})(\text{OMe}) + \text{O}]^+$ formula was detected, showing that the chloride ligand was rather linked to the metal than the oxygen, allowing its replacement by a MeOH ligand (Figure IV-23). Since axial chloride ligand can be replaced by methanolate ligand in presence of methanol. Therefore the $[\text{Fe}^{\text{III}}(\text{DPy})(\text{OCl})]^+$ adduct was excluded and the iron intermediate is proposed to be a N-oxide iron(III) $[\text{Fe}^{\text{III}}(\text{DPyN}_{\text{Py}}\text{O})]^{2+}$ species. Of note, a high spin $[\text{Fe}^{\text{III}}(\text{DPyN}_{\text{Py}}\text{O})(\text{Cl})]^+$ iron(III) N-oxide species in a distorted geometry is expected, which is in good agreement with EPR signal at $g = 4.3$. Besides, it is possible that the $[\text{Fe}^{\text{III}}(\text{DPyN}_{\text{Py}}\text{O})(\text{Cl})]^+$ species was also formed in the reaction of the $\text{Fe}^{\text{III}}\text{DPyCl}_2$ complex with mCPBA since similar EPR signal was detected.

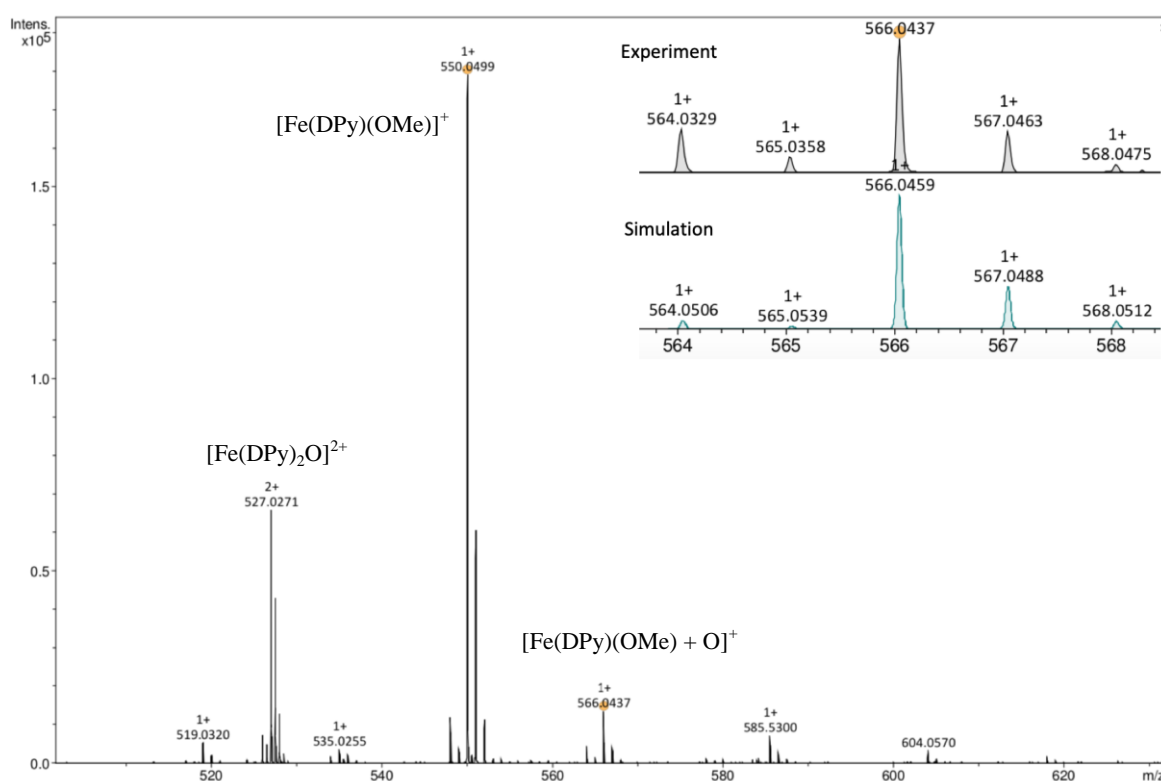


Figure IV-23 : ESI⁺-HRMS analysis of $(\text{Fe}^{\text{III}}\text{DPyCl}_2 + \text{NaClO})$ solution diluted in MeOH and frozen. Inset: Experimental and simulated isotopic distribution of detected species at $m/z = 566.0437$.

Attempting to identify the other peaks observed in HRMS analyses, we found that the peaks at $m/z = 587.9612$ and 603.9560 could probably correspond to non-desired chlorinated

products (Figure IV-24), suggesting the formation of the chloride radical due to homolytic O-Cl.

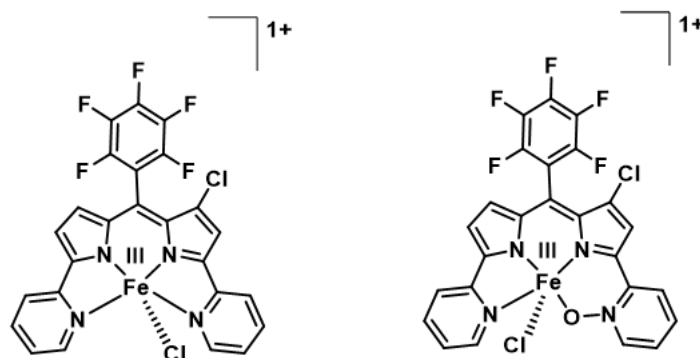


Figure IV-24: Proposed structural assigned for $m/z = 587.9612$ (left) and 603.9560 (right)

IV.2.2.1.4 Infra-red spectroscopy

To confirm, the existence of N-O bound in the detected intermediate its characterization by infrared spectroscopy was performed. Upon oxidation of the $\text{Fe}^{\text{III}}\text{DPyCl}_2$ precursor by NaClO , new vibration bands were observed around 855 and 1230 cm^{-1} that matched well with the N-O stretching and the N-O bending vibrations reported for Fe(III) hexa(pyridine-N-oxide) complex (839 and 1214 cm^{-1} , respectively) (Figure IV-25).^{192,193} Unfortunately, upon addition of ^{18}O labelled water, the bands sensitive to ^{18}O labelling could not be clearly evidenced due to too many changes in the whole spectrum.

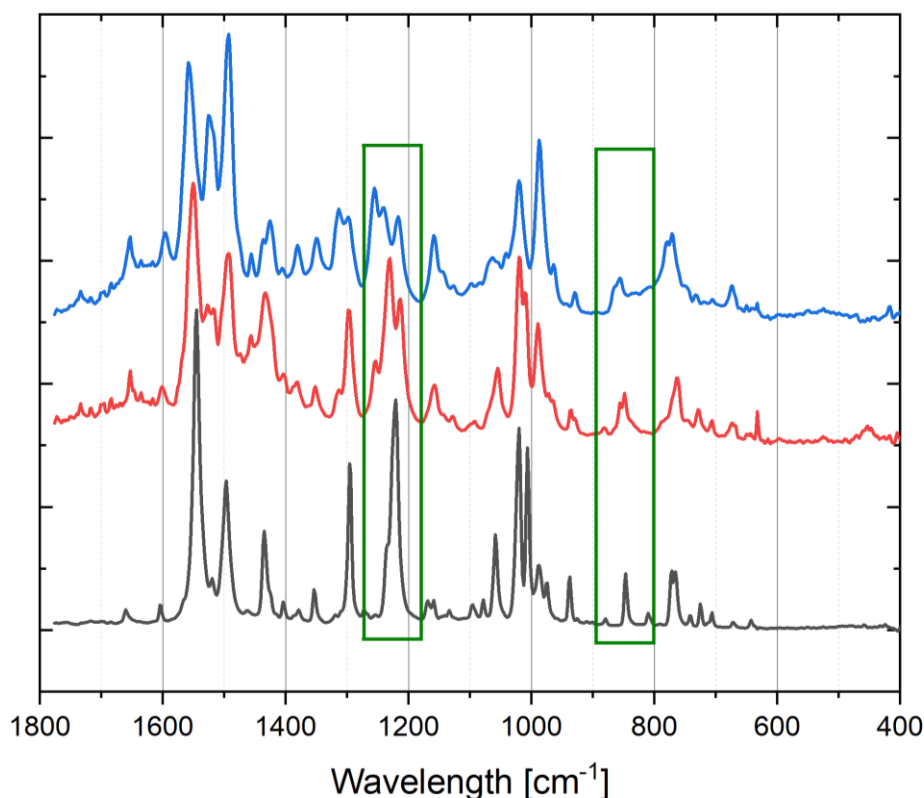


Figure IV-25 : Infrared spectra of $\text{Fe}^{\text{III}}\text{DPyCl}_2$ precursor (black), after adding NaClO (red) and previous solution added with H_2^{18}O (blue).

Although $\text{Fe}^{\text{III}}(\text{DPy})(\text{OCl})\text{Cl}$ adduct and $[\text{Fe}^{\text{V}}=\text{O}(\text{DPy})\text{Cl}]\text{Cl}$ iron-oxo species were not spectroscopically trapped at room temperature, the formation of $\text{Fe}^{\text{III}}(\text{DPyN}_{\text{Py}}\text{O})\text{Cl}_2$ iron(III) N-oxide species probably proceeds via the formation of $\text{Fe}^{\text{III}}(\text{DPy})(\text{OCl})\text{Cl}$ adduct followed by a heterolytic O-Cl bond cleavage to form $[\text{Fe}^{\text{V}}=\text{O}(\text{DPy})\text{Cl}]\text{Cl}$ iron-oxo species, then followed by an intramolecular interaction to generate $\text{Fe}^{\text{III}}(\text{DPyN}_{\text{Py}}\text{O})\text{Cl}_2$ species. Unfortunately, all attempts made to detect the iron-hypochlorite adduct and the iron-oxo species by UV-vis, EPR at low temperature ($-40\text{ }^\circ\text{C}$) and stopped-flow absorption spectroscopy were not conclusive, probably due to their highly reactivity. At $-40\text{ }^\circ\text{C}$, similar absorption bands than that at room temperature were detected. Notably, the intense band at 631 nm characteristic of the $\text{Fe}^{\text{III}}(\text{DPyN}_{\text{Py}}\text{O})\text{Cl}_2$ iron N-oxide species persisted at low temperature ($t_{1/2} \approx 8\text{ h}$), and the EPR spectrum measured on an aliquot of the reactional mixture taken when maximum intensity of the band at 631 nm at $-40\text{ }^\circ\text{C}$ reached, showed similarly a broad signal at $g = 4.3$. We thus propose that the formation of $\text{Fe}^{\text{III}}(\text{DPyN}_{\text{Py}}\text{O})\text{Cl}_2$ iron(III) N-oxide species either proceeds via the concerted O-Cl bond, or the Fe-O-N bond

formation is too rapid to allow the detection of intermediates involved in a stepwise mechanism even at low temperature.

IV.2.2.2 Studying the reactivity of the N-oxide iron(III) species

Upon addition of 2 eq PPh₃ into the solution of the intermediate generated, the UV-vis spectrum of the precursor was recovered, suggesting that the detected iron intermediate is able to oxidize PPh₃ to O=PPh₃ (Figure IV-26). This was confirmed by the HRMS detection of O=PPh₃. We can propose that the iron intermediate characterized by the absorption band at 631 nm is active in oxygen atom transfer.

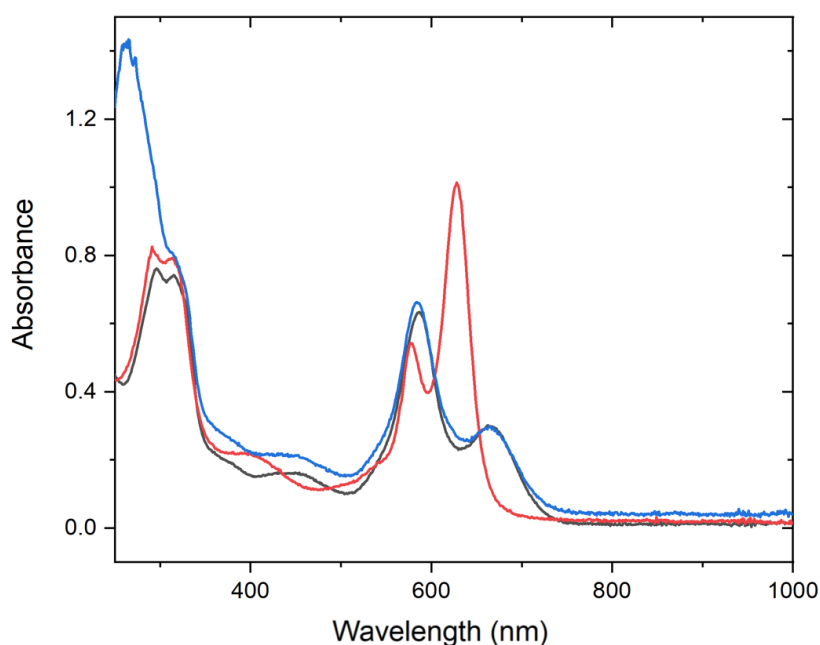


Figure IV-26 : UV-vis spectral changes during the oxidation of the Fe^{III}DPyCl₂ complex (black) by 2 eq. of NaClO (red) and its reaction with 2 eq. of PPh₃ (blue)

Remarkably, the iron(III) precursor regenerated after the first catalytic oxidation cycle can react a second time by adding more NaClO to generate the active iron species characterized by the absorption band at 631 nm and then PPh₃ to recover the initial iron(III) precursor (Figure IV-27).

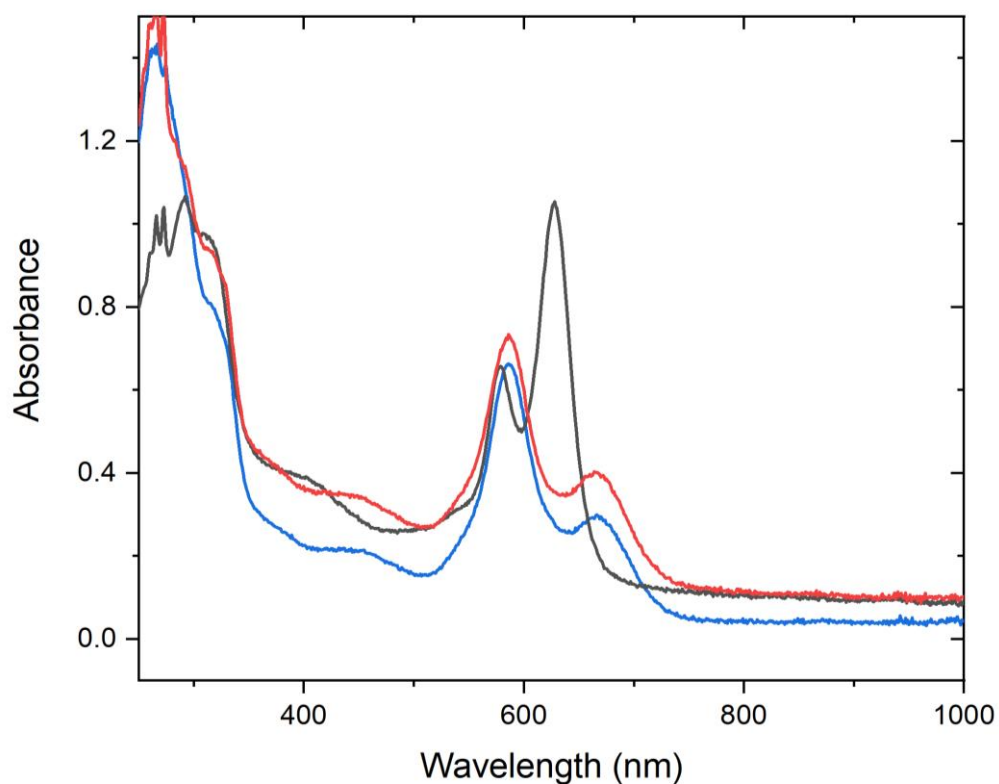


Figure IV-27 : Second catalytic oxidation cycle. Blue: regenerated iron(III) precursor after the first cycle, black : oxidation with 2 eq. NaClO, red : after reaction with 2 eq. PPh₃.

These experiments were repeated with 4-MePhSMe as a substrate. When added in excess amount, similar results were obtained. When stoichiometric amount was used the reaction was slower but allowed the observation of isosbestic points at 603 and 657 nm (Figure IV-28). Again, HRMS confirmed the formation of the corresponding sulfoxide.

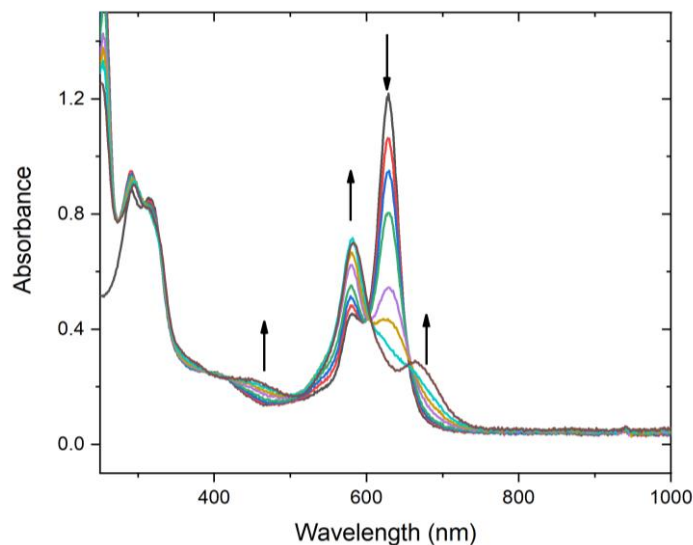


Figure IV-28 : UV-visible changes during the reaction of the iron intermediate generated by NaClO with stoichiometric 4-MeSPhMe over 30 min.

IV.2.2.3 Catalytic tests

The catalytic activity of $\text{Fe}^{\text{III}}\text{DPyCl}_2$ was evaluated in presence of 1000 eq. of substrate and 1000 eq NaClO in deuteriated acetonitrile at room temperature. After 5 min, the oxidized products O=PPh_3 and 4-Me(SO)PhMe were respectively quantified by ^{31}P NMR and ^1H NMR (Figure IV-29). Turnover number (TON) of 780 and 510 corresponding to turnover frequencies (TOF) of 2.6 s^{-1} and 1.7 s^{-1} were calculated for PPh_3 and 4-MeSPhMe oxidation, respectively (Table IV-1).

$\text{Fe}^{\text{III}}\text{DPCl}_2$	Substrates	NaClO	Time	Yield ^a	TON ^b	TOF ^b
0	50 mM PPh_3	50 mM	5 min	38%	x	x
50 μM	50 mM PPh_3	50 mM	5 min	78%	780	2.6 s^{-1}
50 μM	50 mM 4-MeSPhMe	50 mM	5 min	51%	510	1.7 s^{-1}

Table IV-1: Substrate conversion.^a Yield based on substrate, ^b TON and TOF are calculated over $\text{Fe}^{\text{III}}\text{DPyCl}_2$ catalyst.

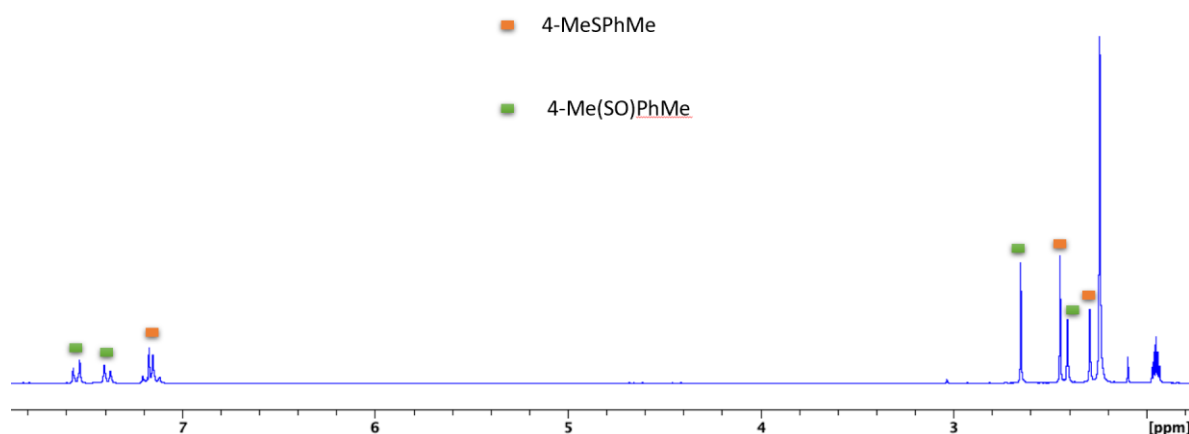
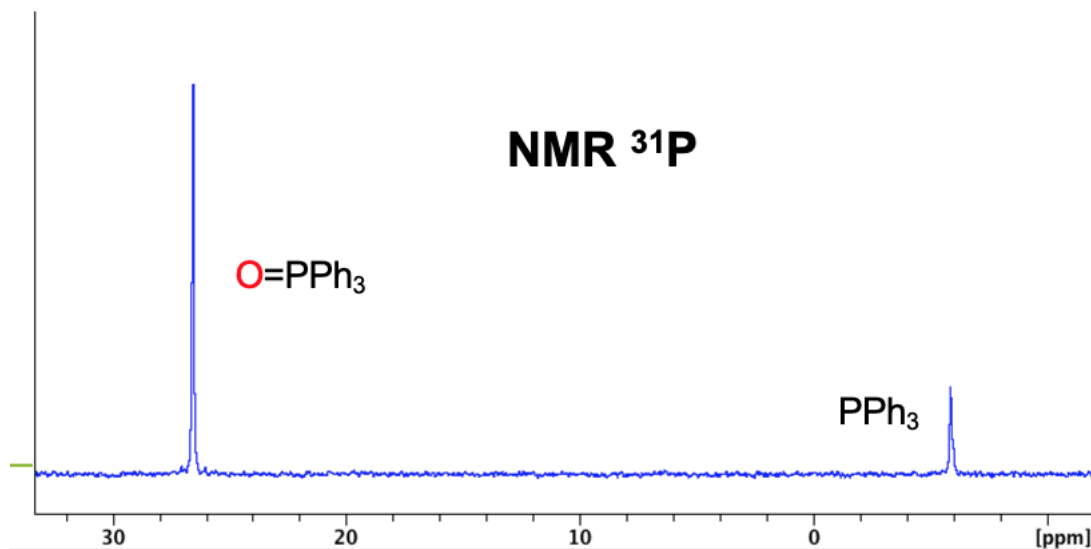


Figure IV-29 : (Top) ^{31}P NMR of catalytic reaction with PPh_3 as substrate and (Bottom) ^1H NMR with 4-MeSPhMe as substrate.

In brief, the $\text{Fe}^{\text{III}}\text{DPyCl}_2$ complex reacts with NaClO under different conditions. The formation of a high spin ($S = 5/2$) iron(III) intermediate with insertion of an oxygen atom in an Fe-N bond is proposed based on the following spectroscopic facts:

- the detection of an absorption band at 631 nm
- an EPR signal at $g = 4.3$ (rule out the Fe(V) formulation)
- the HRMS analysis (Cl exchange with MeOH)
- and the vibration energy of the N-O bond detected by IR.

Interestingly, this $[\text{Fe}^{\text{III}}(\text{DPyN}_{\text{Py}}\text{O})\text{Cl}_2]$ iron species is able to oxidize substrates such as PPh_3 and thioanisole and allow the initial iron precursor to be recovered after transferring the oxygen atom to the substrates. However, NaClO is a non-innocent oxidant that led to the formation of non-desired iron species such as $[\text{Fe}^{\text{III}}(\text{Cl-DPy})]^+$ and $[\text{Fe}^{\text{III}}(\text{Cl-DPyNO})]^+$. We thus decided to further investigate the oxidation of the $\text{Fe}^{\text{III}}\text{DPyCl}_2$ complex with the classical oxidant, Iodosylarene.

IV.2.3 Oxidation with iodosylarenes

Iodosylbenzene (PhIO) is an efficient terminal oxidant for the generation of active metal species such as metal-oxo species and metal-iodosylbenzene adduct. Unlike NaClO it is not basic and does not react alone with modest substrates such as PPh_3 . However, its weak solubility in non protic solvent can prevent a good control of its reactivity.

IV.2.3.1 Characterization of generated iron species

IV.2.3.1.1 UV-visible spectroscopy

The reaction of $\text{Fe}^{\text{III}}\text{DPyCl}_2$ with PhIO in acetonitrile in absence of substrate was monitored by different spectroscopic techniques. Mixing the two reactants at room temperature in ACN resulted in the apparition of a new transition band at 636 nm reminiscing the $[\text{Fe}^{\text{III}}(\text{DPyN}_{\text{Py}}\text{O})]^{2+}$ iron N-oxide species generated by NaClO . Interestingly the new absorption feature faded slowly in about 15 min and the initial $\text{Fe}^{\text{III}}\text{DPyCl}_2$ spectrum was recovered this time albeit with slightly lower intensity (Figure IV-30). In the presence of triphenylphosphine, the decay was accelerated by at least a factor of 3 and triphenylphosphine oxide was detected by HRMS suggesting that this intermediate species is capable of transferring an oxygen atom, as in the case of NaClO .

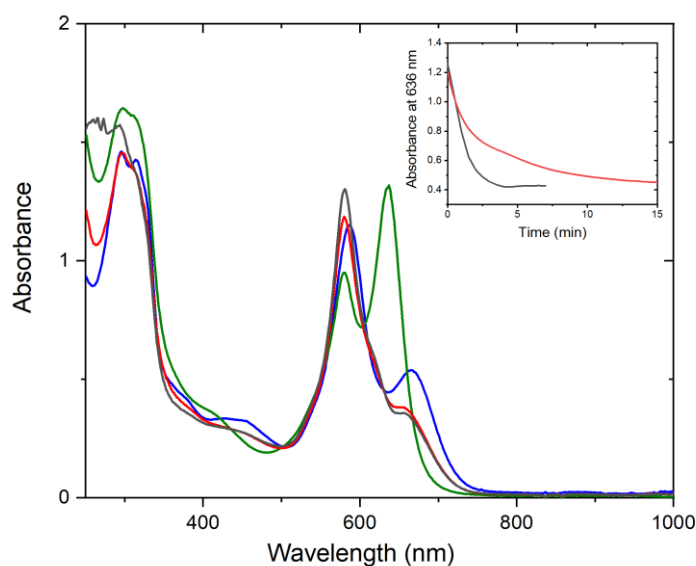


Figure IV-30 : UV-vis spectra changes during oxidation of $Fe^{III}DPyCl_2$ complex (blue) by PhIO (green), its evolution after 15 min in absence of substrate (red) and its reaction with PPh_3 (black). Inset: (red) Decay of absorption band at 636 nm with (black) and without PPh_3 over time.

IV.2.3.1.2 EPR spectroscopy

The magnetic properties of the intermediate were also characterized by X-band EPR at 10K. The initial rhombic signal of the iron(III) precursor was replaced by a broad isotropic signal at $g=4.3$ attributed to a high spin ($S = 5/2$) iron species as detected with NaClO with an estimated conversion of around 60% (Figure IV-31). No signal was detected in parallel mode. Again, the initial characteristic signals of the iron(III) precursor were slowly recovered in absence of substrate while the recovery was accelerated by adding triphenylphosphine as observed by UV-visible spectroscopy. Like in UV-visible spectroscopy, the EPR signals of iron(III) precursor was not totally regenerated probably due to formation a silent iron species in EPR such as μ -oxo diiron(III) complex especially in absence of substrate.

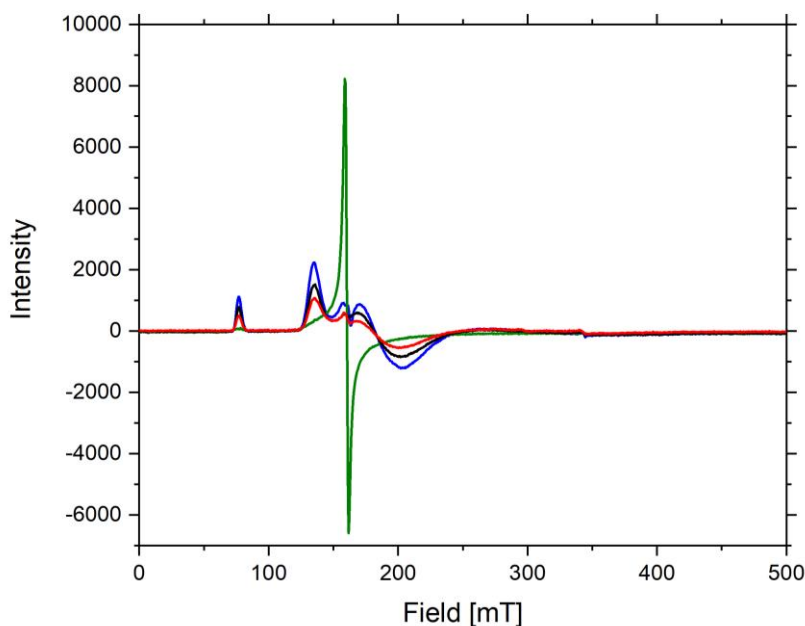


Figure IV-31 : EPR spectra changes during oxidation of $\text{Fe}^{\text{III}}\text{DPyCl}_2$ complex (blue) by PhIO (green), its evolution at room temperature after 16 h in absence of substrate (red) and a few seconds after adding PPh_3 (black).

IV.2.3.1.3 Mössbauer spectroscopy

The iron(III) species intermediate species generated by reaction with PhIO was also studied by Mössbauer analysis of the ^{57}Fe enriched iron(III) samples. The spectrum revealed a main signal (73%) that could be fitted with an isotropic shift (δ) of $0.48 \text{ mm}\cdot\text{s}^{-1}$ and a quadrupolar splitting (ΔE) of $1.53 \text{ mm}\cdot\text{s}^{-1}$, and a minor signal ($\delta = 0.40 \text{ mm}\cdot\text{s}^{-1}$ and $\Delta E = 0.38 \text{ mm}\cdot\text{s}^{-1}$), both compatible with a high spin iron(III) species (Figure IV-32). No highly oxidized iron intermediate was thus detected. In this experiment we did not get the chance to add a substrate to identify the signal associated with an active species. However, given previous experiments followed by UV it is quite reasonable to think that at least the main signal corresponds to an active species that is the $[\text{Fe}^{\text{III}}(\text{DPyNO})]^{2+}$ iron N-oxide intermediate. In a second spectrum, measured on the previous solution let to evolve 2 h at room temperature, the weaker signal had disappeared. Therefore, we can propose that it corresponds to an active species too, possibly an $\text{Fe}^{\text{III}}\text{-OIPh}$ intermediate. As already mentioned such an intermediate has been postulated by Nam and McKenzie and shown to be active too in OAT reactions.^{181,183–185}

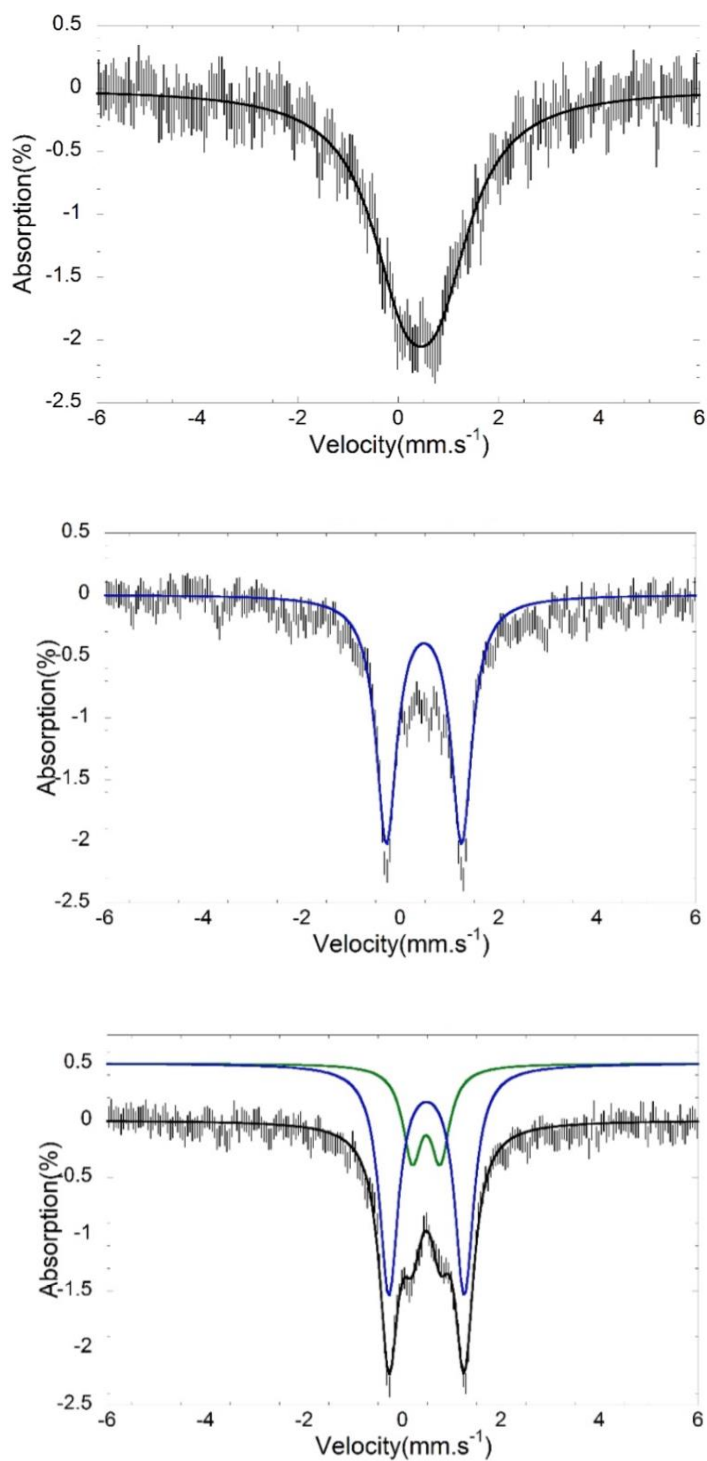


Figure IV-32 : Zero-field Mössbauer spectra of frozen acetonitrile solutions of iron intermediates generated by oxidizing $Fe^{III}DPyCl_2$ (2 mM) (Top) with PhIO (middle) at 80 K and its evolution without substrate after 2 h under inert atmosphere at room temperature (bottom). Black, Blue and green line are simulations of experimental spectra.

The evolution of these two active species led after 2 hours under inert atmosphere and room temperature to two new sets of signals. The major signal (72 %) could coincidentally be fitted with close isotropic shift (0.49 mm.s^{-1}) and quadrupolar splitting (1.53 mm.s^{-1}) to the main signal observed before evolution. Knowing that the main active species has a $t_{1/2}$ life-time of 15 min, as demonstrated by absorption band at 636 nm. It thus cannot correspond to the same active species but rather to resting forms for example the initial precursor with a different axial ligand like acetonitrile. Similarly, the minor signal (38 %) that was fitted with an isotropic shift of 0.48 mm.s^{-1} and a quadrupolar splitting of 0.57 mm.s^{-1} , probably corresponds to another high spin resting iron(III) species that we have not yet characterized.

IV.2.3.1.4 HRMS

ESI-HRMS analyses of oxidized solution with PhIO showed two peaks at $m/z = 569.9954$ and 580.0242 corresponding respectively to $[\text{Fe}(\text{DPy})\text{Cl} + \text{O}]^+$ and $[\text{Fe}(\text{DPy})(\text{OAc}) + \text{O}]^+$ formula. Acetate ligand was found in this experiment because sodium acetate was used for calibration of the HRMS shortly before the experiment (Figure IV-33). These peaks cannot be assigned to high oxidized iron-oxo species $[\text{Fe}^{\text{V}}=\text{O}(\text{DPy})\text{Cl}]^+$ and $[\text{Fe}^{\text{V}}=\text{O}(\text{DPy})(\text{OAc})]^+$ due to results found by EPR and Mössbauer analyses, we thus reason that these peaks can be attributed to iron(III) N-oxide species $[\text{Fe}^{\text{III}}(\text{DPyNO})\text{Cl}]^+$ and $[\text{Fe}^{\text{III}}(\text{DPyNO})(\text{OAc})]^+$. Moreover, a peak at $m/z = 503.0879$ with charge and isotopic distribution agreeing with $[(\text{DPyH}) + \text{O} + \text{Na}]^+$ formula was observed which probably comes from iron(III) N-oxide species demetallation under HRMS condition. Upon addition of ^{18}O labelled water to the previous sample, two new peaks were detected at 571.9988 and 582.0262 corresponding respectively to $[\text{Fe}(\text{DPy})\text{Cl} + ^{18}\text{O}]^+$ and $[\text{Fe}(\text{DPy})(\text{OAc}) + ^{18}\text{O}]^+$ formula, proving the lability of the metal bound oxygen atom in the detected species (Figure IV-33).

Moreover, the formation of an iron(III)-iodosylbenzene adduct was revealed by the detection of a peak at $m/z = 773.9389$ attributed for $[\text{Fe}(\text{DPy})\text{Cl}(\text{OIPh})]^+$ ion. However, the peak corresponding to $[\text{Fe}(\text{DPy})\text{Cl}(^{18}\text{OIPh})]^+$ was not found upon addition of ^{18}O labelled water. The existence of iron(III)-iodosylbenzene adduct is reasonable because its formation is believed to be the first step in oxidation reaction with PhIO. As a consequence, one can propose that the oxidized solution contains both iron(III)-iodosylbenzene adduct and iron(III)

N-oxide species, which agrees with the detection of two iron(III) species by Mössbauer spectroscopy.

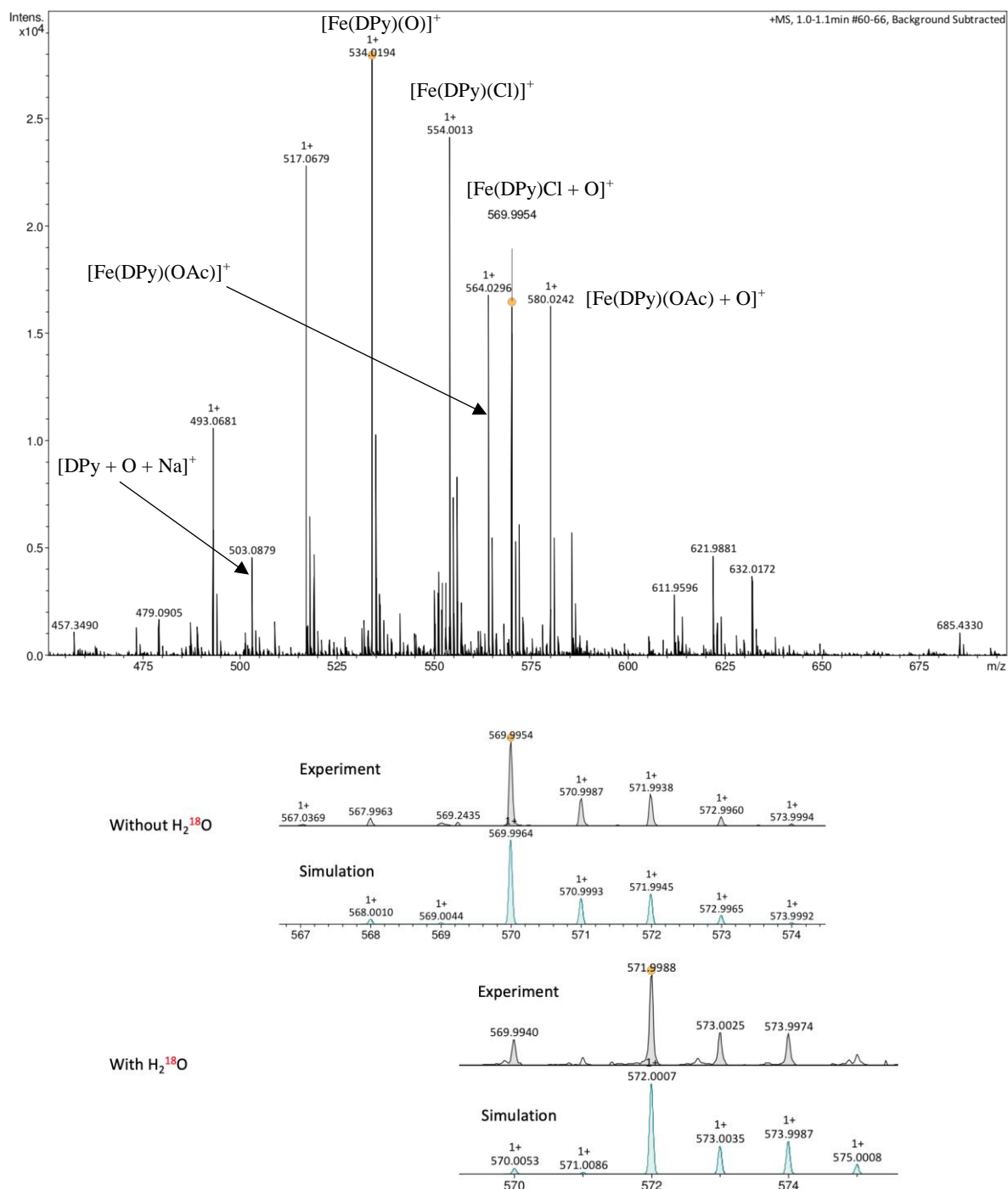


Figure IV-33 : ESI⁺-HRMS analyses of oxidation of the Fe^{III}DPyCl₂ by PhIO in acetonitrile (Top) Zoom of the peaks of interest in the absence and presence of H₂¹⁸O (Bottom).

Other peaks were present in the reaction mixture that we tried to identify. One of the major one at 534.0194 was found to have the charge and the isotopic distribution compatible with a $[\text{Fe}(\text{DPy}) + \text{O-H}]^+$ formula. Due to the lability of coordinated pyridine in iron(III) precursor as mentioned in chapter II, one C-H bond of a pyridine could be activated leading by oxygen insertion and deprotonation to the formation of $[\text{Fe}^{\text{III}}(\text{DPyO})]^+$ species (Figure IV-34). This irreversible degradation pathway by aromatic hydroxylation has been reported by others,^{189,194} and cannot be considered as active for oxygen atom transfer reaction.

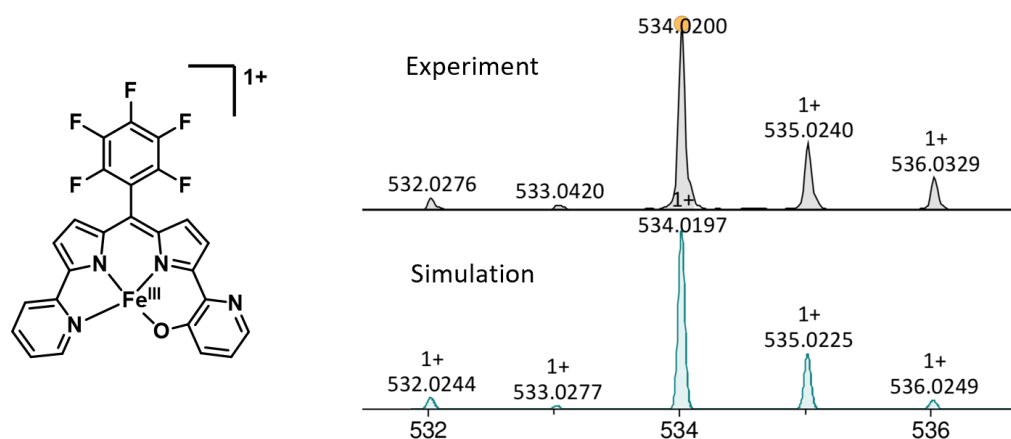


Figure IV-34: (left) Structure of $[\text{Fe}^{\text{III}}(\text{DPyO})]^+$ ion and (right) isotopic distribution of $[\text{Fe}^{\text{III}}(\text{DPyO})]^+$.

In order to check this hypothesis, ESI-HRMS analysis was performed on the reactional mixture left to evolve a few hours. To our satisfaction, peaks assigned to the active species at 569.9954, 580.0242 and 503.0879 were absent, while the initial $[\text{Fe}^{\text{III}}\text{DPy}]^{2+}$ precursor was detected by the presence of two peaks at 554.0006 and 564.0299 attributed to two $[\text{Fe}(\text{DPy})\text{Cl}]^+$ and $[\text{Fe}(\text{DPy})(\text{OAc})]^+$ chemical species, respectively (Figure IV-35). Therefore, the recovery of iron(III) precursor observed by UV-vis, EPR, Mössbauer was also confirmed by HRMS, revealing the iron(III) N-oxide species was also active. However, the peak at 534.0200 was absent. A possibility is that such a species would dimerize after a while as previously observed with the manganese $[\text{MnDPy}]^+$ (Figure II-1).⁹⁴ This degradation pathway might explain why spectral features are not fully recovered after quenching of the active species (Figure IV-30 and Figure IV-31).

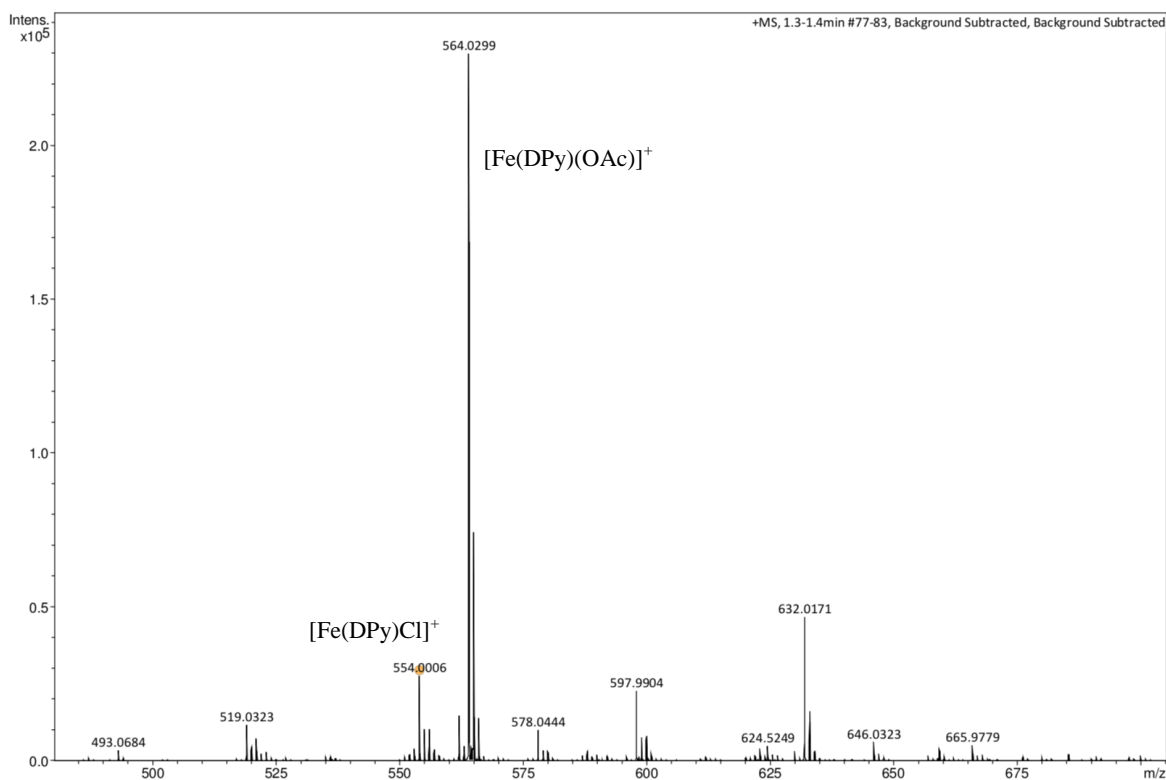


Figure IV-35 : ESI⁺-HRMS analyses of (Fe^{III}DPyCl₂ + PhIO) sample taken 16 h after mixing.

IV.2.3.1.5 Infrared spectroscopy

The existence of a N-O bond in the iron N-oxide intermediate [Fe^{III}(DPyN_{Py}O)]²⁺ was probed by Infrared spectroscopy. This time, two vibration bands sensitive to ¹⁸O labelling were clearly observed. The first at a frequency of 1226 cm⁻¹ was assigned to the N-O stretching vibration and the second at 845 cm⁻¹ was attributed to N-O bending by comparison with the N-O vibrations reported for Fe(III) hexa(pyridine-N-oxide) complex (Figure IV-36). Upon ¹⁸O labelling these bands were shifted to 1213 and 800 cm⁻¹ respectively thus clearly indicating the implication of an exchangeable oxygen atom.

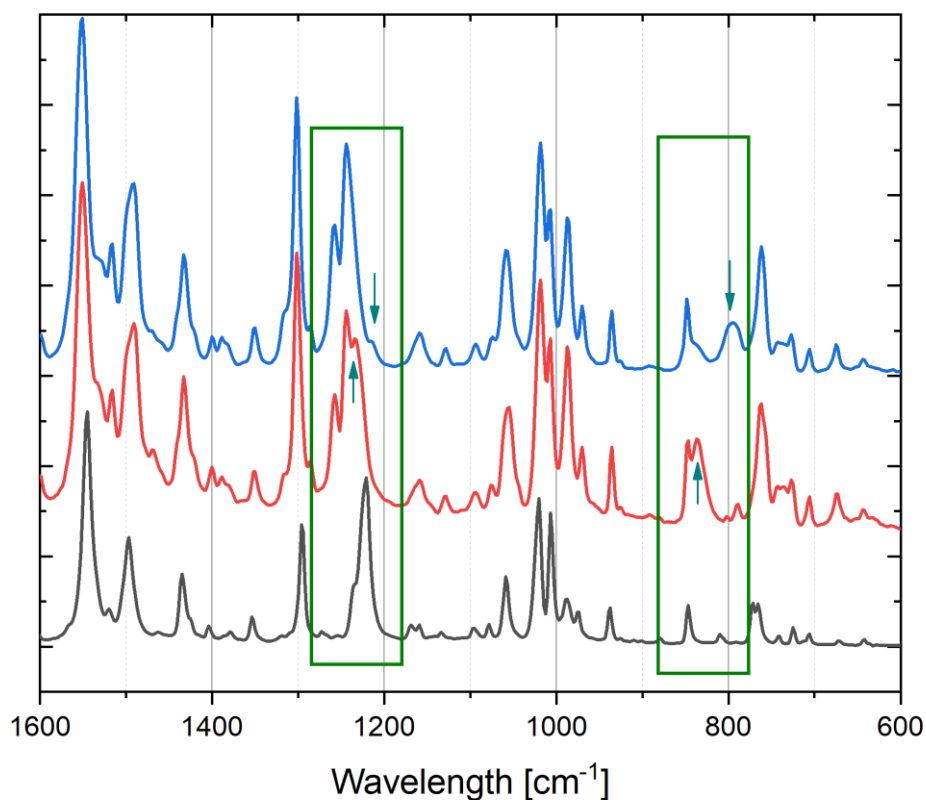


Figure IV-36: Infrared spectra of $\text{Fe}^{\text{III}}\text{DPyCl}_2$ precursor (black), upon addition of PhIO (red) and then H_2^{18}O (blue).

Comparing the IR spectra obtained by oxidation of $\text{Fe}^{\text{III}}\text{DPyCl}_2$ with PhIO and NaClO revealed quasi identical features except in these specific area (Figure IV-37). Small changes observed might come from slightly different intermediates. In the case of NaClO a different axial ligand such as hydroxyl (OH) or weak interaction with a sodium might change subtly the vibration energy of the Fe-O-N bonds.

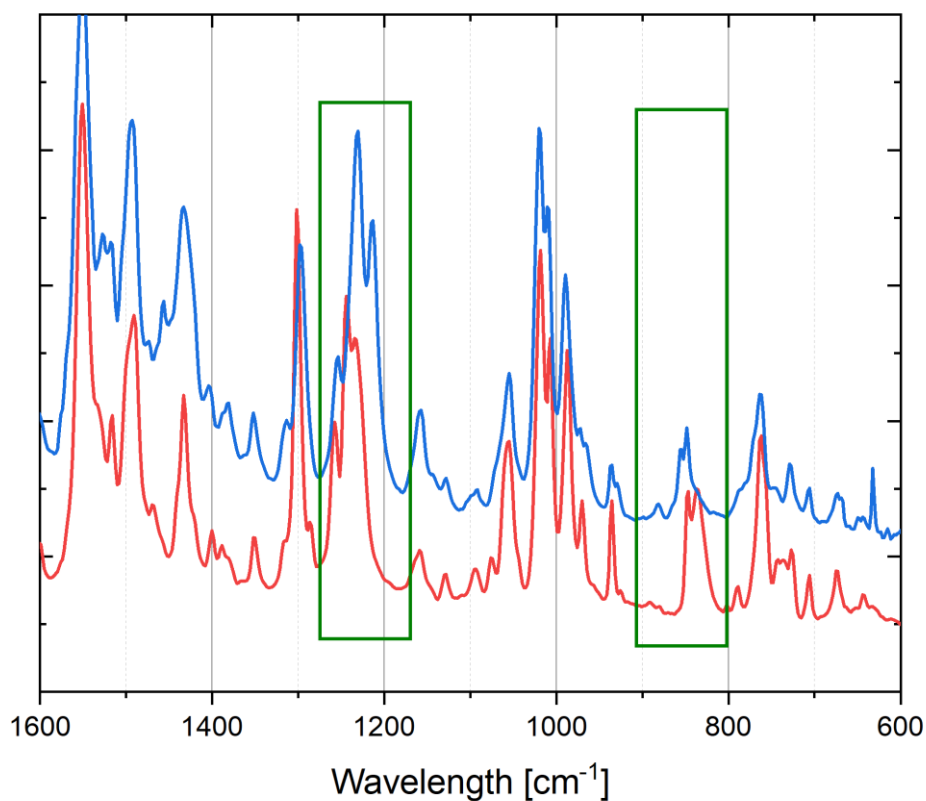


Figure IV-37: : Comparison of the infrared spectra of iron intermediates generated by PhIO (red) and by NaClO (blue).

IR bands	N-O	N- ¹⁸ O
NaClO	855 cm ⁻¹	Non-identified
	1231 cm ⁻¹	Non-identified
PhIO	845 cm ⁻¹	800 cm ⁻¹
	1226 cm ⁻¹	1213 cm ⁻¹

Table IV-2: Comparison of the characteristic frequencies attributed to N-O-Fe vibrations in the iron intermediate generated by NaClO and PhIO.

IV.2.3.1.5 Resonance Raman spectroscopy

Having detected such a possible intermediate by HRMS, we also tried to detect the presence of $[\text{Fe}^{\text{III}}(\text{DPy})(\text{OIPh})]^{2+}$ adduct as a precursor of $[\text{Fe}^{\text{III}}(\text{DPyN}_{\text{Py}}\text{O})]^{2+}$ species. Very few Fe-OIPh species have been characterized. Interestingly, the groups of Nam and Latour were able to identify such a species by Raman spectroscopy. In their case, a ^{18}O labelled sensitive transition band was detected at 783 cm^{-1} .

The Raman spectra of our sample recorded in collaboration with Dr. Thomas Pino and Dr. Thi Minh Huong Nguyen from Institut des Sciences Moléculaires d'Orsay (ISMO), showed two new bands at frequencies of 1218 cm^{-1} and 790 cm^{-1} upon excitation at 532 nm . Although the band at 790 cm^{-1} was compatible with the O-I vibration of the iron cyclam iodosylbenzene adduct $[\text{Fe}^{\text{III}}(13\text{-TMC})(\text{OIPh})]^{3+}$ reported by Nam and Latour,¹⁸⁴ attempt to detect a shift upon addition of ^{18}O labelling water was hampered by the poor quality of the signal (Figure IV-38). It is thus difficult to affirm that such a species is quantitatively accumulated under our condition.

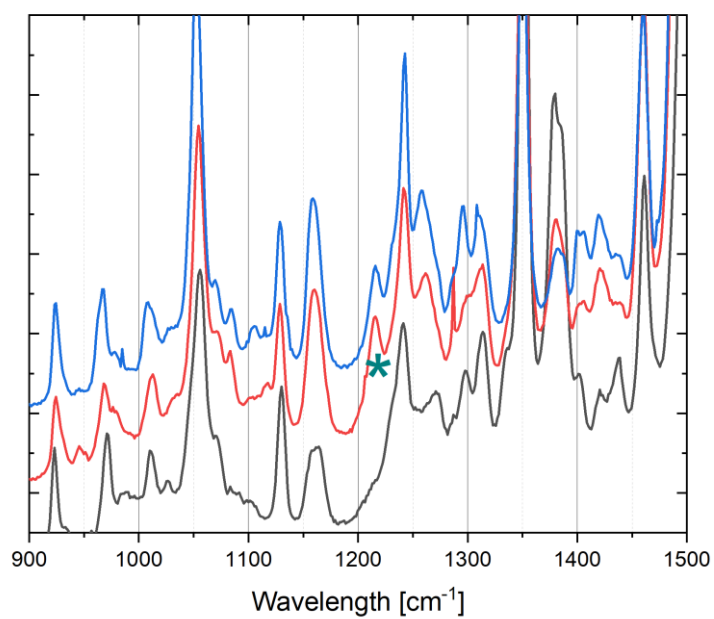
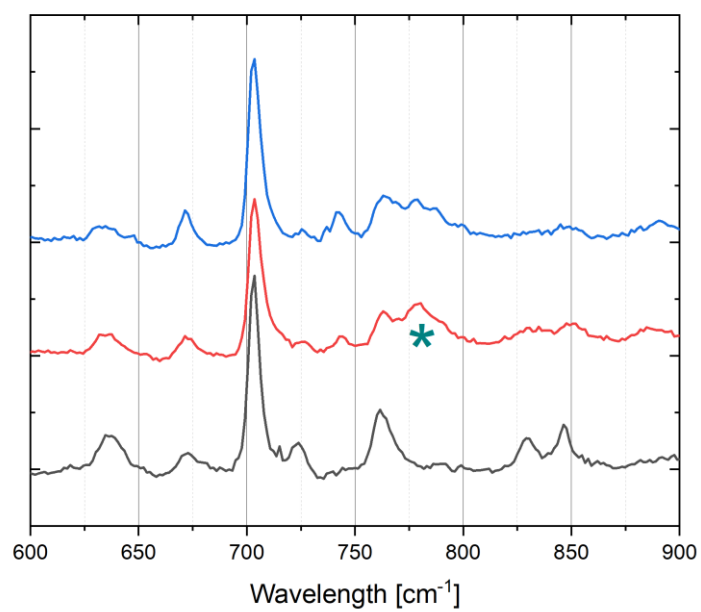


Figure IV-38: Raman resonance of $Fe^{III}DPyCl_2$ precursor (black), upon addition of PhIO (red) and then $H_2^{18}O$ (blue).

IV.2.3.1.6 DFT Calculation

In brief, UV-vis, EPR, MS and IR spectroscopy experiments all point to the formation of an Fe(III) active species in which the ligand has been oxidized. To further support our hypothesis and to propose a geometry for this unusual intermediate, DFT calculations were performed by Dr. Marie Sircoglou. The method was calibrated on the stable precursor and the lability of the ligand was evaluated (Figure IV-39). The activation energy required for the decoordination of one pyridine was found of 9 kcal.mol⁻¹ in the gas phase which, seems sufficiently accessible to allow intramolecular ligand oxidation at room temperature.

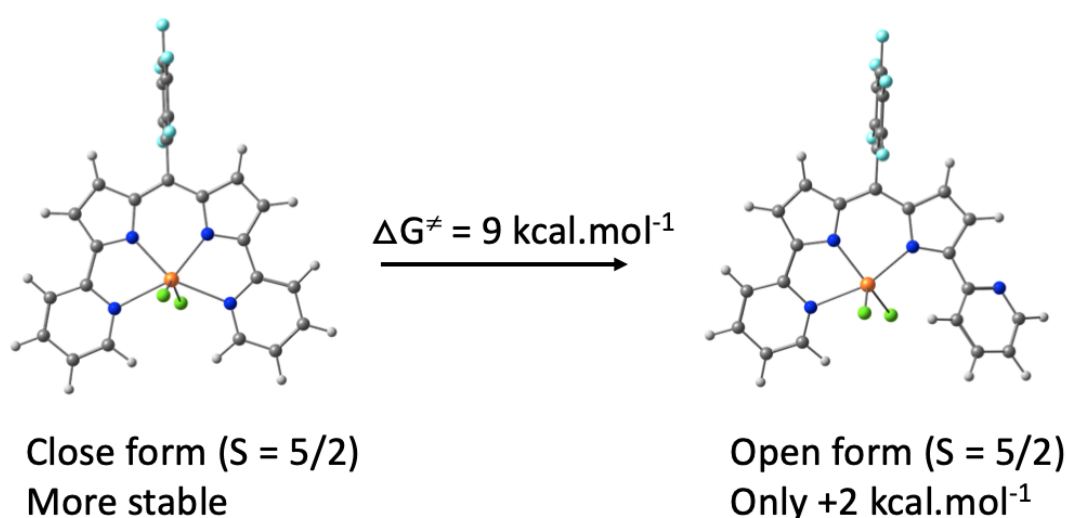


Figure IV-39: DFT optimized structure of two Fe^{III}DPyCl₂ complex

Next, the structure of Fe^{III}(DPyNO)Cl₂ and the other possible oxidized species such as [Fe^{III}(DPy)(OCl)]⁺ adduct, [Fe^V=O(DPy)(Cl)]⁺ iron(V)-oxo species were investigated (Figure IV-40). The most stable geometry we localized features the insertion of an oxygen atom in one of the N_{pyridine}-Fe bond. The iron center hardly deviates from the N₄ plane (d(Fe-N₄)=0,22Å) while the pyridine-N-oxide ring tilts by 27° from N₄ plane to allow the bent N-O-Fe 4e-3center interaction to establish (Fe-O = 2.087 Å , N-O = 1.315 Å , NOFe = 122.9°). Meanwhile the Fe-Cl bonds are bent away by 10° from their original axial position. The calculated frequencies associated with this geometry allowed evidencing two vibration modes involving the O atom at 852 and 1233 cm⁻¹ that were isotopically shifted to higher energies). These results nicely reproduce the trends observed experimentally.

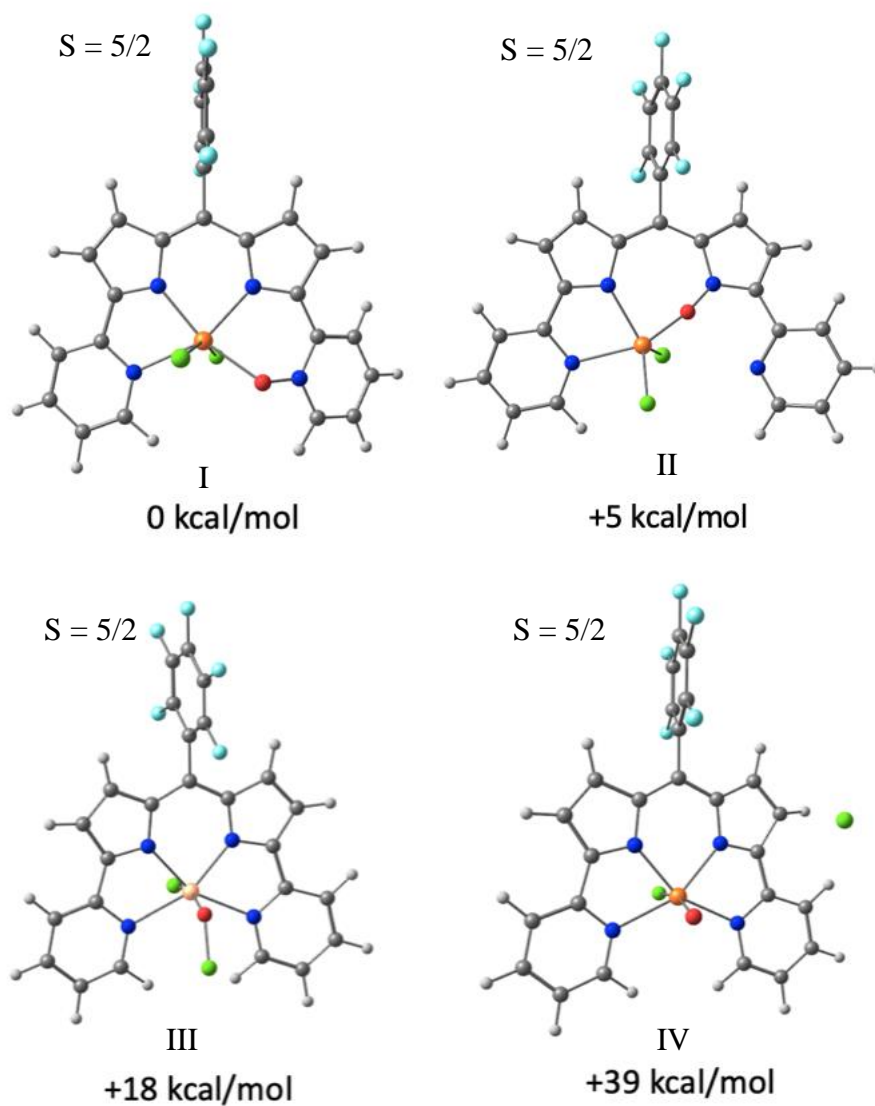


Figure IV-40 : Modelisation of 4 structures that could be obtained upon oxidation of $Fe^{III}DPyCl_2$ by. Relative thermal free energies at 298 K are given under each structure.

IR-bands	N-O	N-O	N- ¹⁸ O
Experiment	Fe ^{III} DPyCl ₂ + NaClO	Fe ^{III} DPyCl ₂ + PhIO	Fe ^{III} DPyCl ₂ + PhIO + H ₂ ¹⁸ O
	855 cm ⁻¹ 1231 cm ⁻¹	845 cm ⁻¹ 1226 cm ⁻¹	800 cm ⁻¹ 1213 cm ⁻¹
DFT	852 cm ⁻¹ 1233 cm ⁻¹		840 cm ⁻¹ 1223 cm ⁻¹

Table IV-3: Comparison of the characteristic frequencies attributed to N-O-Fe vibrations found experimentally and theoretically.

Another possibility could be the insertion of an oxygen atom in one of the N_{pyrrole}-Fe bonds. The structure of the Fe^{III}(DPyN_{pyrrole}O)Cl₂ species was also investigated (Figure IV-40). Indeed form II was found very close in energy to form I by DFT calculation. However, no vibration related to the Fe-O-N_{pyrrole} bounds were calculated in the range observed experimentally. Accordingly, we can exclude the Fe^{III}(DPyN_{pyrrole}O)Cl₂ species.

IV.2.3.2 Preparation of oxidized DPyN_{py}O ligand

With the target to isolate the oxidized DPyN_{py}O ligand, we used the mixture of acetic acid and chlorhydric acid (4/1), as reported by Groves,¹⁸⁸ to demetalliated the [Fe^{III}(DPyN_{py}O)]²⁺ intermediate. The isolation of DPyN_{py}O was unsuccessful probably due to its short lifetime in concentrated acid solution. However, we obtained a chlorinated product determined by X-Ray diffraction on single crystal, reminiscing the chlorinated product observed by HRMS analysis of the frozen Fe^{III}DPyCl₂ solution in acetonitrile after adding NaClO (Figure IV-22 and Figure IV-24). The structure is not presented here due to low quality of the mono-crystals.

IV.2.3.3 Catalytic activity study

The catalytic activity of $\text{Fe}^{\text{III}}\text{DPyCl}_2$ was evaluated in presence of 800 eq. of different substrates and 20 eq. of PhIO in acetonitrile at room temperature. The catalyst and the substrates were dissolved in acetonitrile, then solid PhIO was added portion wise and the suspension was stirred for the time indicated (Figure IV-4). The oxidized products were analyzed and quantified by HPGC using an internal standard. Of note, PhIO cannot oxidize the substrates in this study by itself. Quantitative oxidation of thioanisole was observed within 2 h. Among the three alkenes used as substrate, cyclooctene was oxidized to cyclooctene oxide, affording a conversion of 46 % and 100 % of selectivity for epoxidation. The oxidation of cyclohexene and styrene afforded over 100 % conversion calculated on oxidant with a modest selectivity for epoxidation, suggesting an auto-oxidation process occurring under air atmosphere.⁶⁴ Indeed, the catalytic experiment run under inert atmosphere showed a conversion of 19 % for cyclohexene oxidation with high selectivity towards the epoxide product (Table IV-5).

The conversion for toluene oxidation was not changed under inert atmosphere compared with that under air atmosphere, suggesting that the alkene hydroxylation was not an auto-oxidation process. The oxidation of toluene was achieved with a conversion of 100 % within 24 h while other alkanes afforded 5 to 35 % conversion. Noticeably, even cyclohexane was oxidized albeit with a modest conversion.

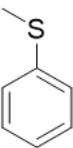
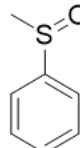
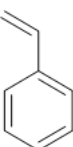
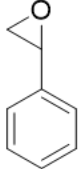
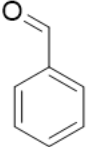
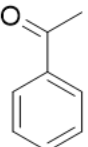
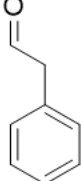
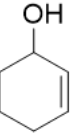
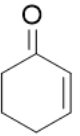
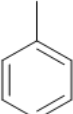
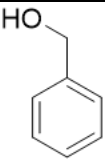
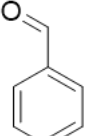
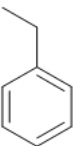
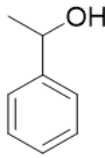
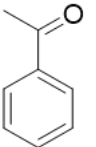
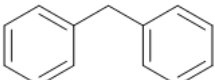
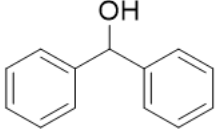
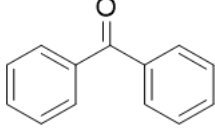
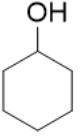
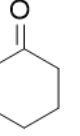
Substrate	Products / conversion	Reaction time (h)	Total conversion
		2	95 %
		2 / 24	30 % / 46 %
	 3 %  31 %  38 %  92 %	2	164 %
	 71 %  128 %  11 %	2	210 %
	 53 % / 93 %  2 % / 7 %	2 / 24	55 % / 100 %
	 5 % / 14 %  7 % / 21 %	2 / 24	12 % / 35 %
	 7 % / 15 %  3 % / 8 %	2 / 24	10 % / 23 %
	 2 % / 3 %  1 % / 2 %	2 / 24	3 % / 5 %

Table IV-4: Catalytic oxidation towards the different substrates under air atmosphere. $Fe^{III}DPyCl_2 / PhIO / Substrate = 1 / 20 / 800$. Conversion is calculated based on PhIO.

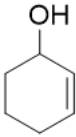
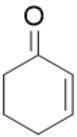
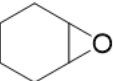
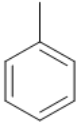
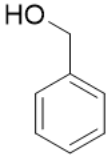
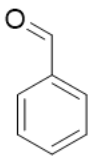
Substrate	Products / conversion			Reaction time (h)	Total conversion
	 4 %	 3 %	 12 %	2	19 %
	 51%	 1 %		2	52 %

Table IV-5: Catalytic oxidation towards the different substrates under argon atmosphere. $Fe^{III}DPyCl_2$ / PhIO / Substrate = 1 / 20 / 800. Conversion is calculated on PhIO.

IV.3 Conclusion

The $\text{Fe}^{\text{III}}\text{DPyCl}_2$ complex was oxidized by different oxidants agents to generate the active iron intermediate species. The reaction with mCPBA probably led to a mixture of many iron intermediates such as $[\text{Fe}^{\text{III}}(\text{DPy})\text{mCPBA}]^{2+}$ adduct, $[\text{Fe}^{\text{IV}}(\text{DPy}\bullet)\text{O}]^{2+}$ and $[\text{Fe}^{\text{III}}(\text{DPyN}_{\text{Py}}\text{O})]^{2+}$ species but the slow formation of these species compared to their life-times under these conditions prevented the characterization. Moreover, The $\text{Fe}^{\text{III}}\text{DPyCl}_2$ precursor was completely destroyed with mCPBA over 10 min. While, NaClO and PhIO could oxidize the $\text{Fe}^{\text{III}}\text{DPyCl}_2$ complex to form an identical iron intermediate. The spectroscopic analyses revealed that one of the two pyridine arms was probably oxidized, leading the formation of the N-oxide high spin ($S = 5/2$) iron(III) species $[\text{Fe}^{\text{III}}(\text{DPyNO})]^{2+}$ species. It is possible that there is an equilibrium between this $[\text{Fe}^{\text{III}}(\text{DPyNO})]^{2+}$ species and the $[\text{Fe}^{\text{III}}(\text{DPy})(\text{OCl})]^+$ or $[\text{Fe}^{\text{III}}(\text{DPy})\text{OIPh}]^{2+}$ adduct in solution respectively, but further experiments would be need to confirm this hypothesis.

The oxidation of DPy ligand to form $[\text{Fe}^{\text{III}}(\text{DPyNO})]^{2+}$ species is not a negative point in catalytic oxidation compared to other systems, as reported by McKenzie.¹⁸⁹ The initial iron(III) precursor could be recovered after transferring oxygen atom to substrate, encouraging for further investigation in improving their catalytic activity. For example, an optimized temperature can accelerate the oxidation rate.

Chapter V : Conclusion & Perspectives

In the context of the ANR project MULTIPLET, this thesis focused on the study of new oxidation catalysts for clean photooxidation transformations. Inspired by the highly oxidized iron-oxo species involved in natural oxidative processes, we sought to generate an active iron(V)-oxo species. To this end, we chose, as a precatalyst, an iron(III) complex based on an anionic hemiporphyrinic dipyrin-dipyridine DPy ligand, recently developed in our lab (Chapter II). This DPy ligand was designed to combine the structural features of well-known catalyst platforms such as porphyrins and poly-nitrogen ligands. The $\text{Fe}^{\text{III}}\text{DPyCl}_2$ complex was synthesized and characterized by a variety of spectroscopic techniques. X-Ray diffraction on single crystal revealed that the structure of this complex in the solid state is in a distorted octahedral geometry with four coordinated nitrogen in equatorial position and two chloride in axial position. An identical formula was found in solution as confirmed by HRMS. The EPR and Mössbauer spectroscopy indicated the high spin character of the iron(III) center and suggested that at least two iron(III) complexes with very close geometries coexist. Based on the structural parameters measured by X-ray diffraction and DFT calculation, the hemilability of one pyridine arm is proposed to lead to different conformers of the complex in solution.

The electrochemical study of $\text{Fe}^{\text{III}}\text{DPyCl}_2$ coupled to EPR analysis revealed that the ligand is redox non-innocent. For instance, the locus of the first reduction is at the iron(III) center while the second concerns the DPy ligand. A preliminary study showed that as hemicatalysts, the $\text{Fe}^{\text{III}}\text{DPyCl}_2$ complex is capable of reducing CO_2 to CO at -1.7 V vs SCE, albeit with a modest selectivity compared to the competitive proton reduction. Towards oxidation, several processes were found to occur at very close potentials, and we were not able to clearly distinguish them. However, they allow the formation of a highly oxidized species able to promote water oxidation at 1.5 V vs SCE.

To enhance the reactivity of this first complex, we synthesized a second iron(III) complex with triflate as weaker electron donor ligands in place of chloride. However, the formation of a μ -oxo diiron(III) complex was obtained instead of the monomer. The $[\text{Fe}^{\text{III}}(\text{DPy})_2\text{O}](\text{OTf})_2$ was characterized by HRMS, UV-vis absorption spectroscopy and X-Ray diffraction on single crystal, confirming the lability of the triflate anion in coordinating solvents. Like the $\text{Fe}^{\text{III}}\text{DPyCl}_2$ complex, this dimer is able to activate water. Besides, the Fe-O bond in this

dimer is not inert and can be activated under certain conditions such as temperature, or the presence of acid, suggesting promising application in oxygen atom transfer reaction.

In Chapter III, this promising complex was tested as part of a photocatalytic system to promote the aerobic photooxidation of styrene into diol and benzaldehyde, in a completely new and counter-intuitive approach. Sacrificial electron acceptors are usually needed for the activation of the catalyst by the photosensitizer. But they are an “evil necessity” since they are non-atom economic and can deactivate the photocatalyst. In an attempt to exclude the use of sacrificial electron acceptor, we found that methyl viologen MV^{2+} as a reversible electron acceptor produces superoxide in pH 4 B&R buffer under aerobic condition, which can, by the mediation of our catalyst, transfer oxygen atom to an organic substrate. The implication of an homolytic Fe-O cleavage to form an iron(IV)-oxo species was excluded by control experiment. While, the Flash laser photolysis experiments revealed that the excited state of the $[Ru^{II}]$ chromophore is quenched by MV^{2+} to form the reduced $MV^{+\bullet}$ which can transfer an electron to both O_2 and Fe^{III} precursor to form $O_2^{\bullet-}$ and Fe^{II} species. Further reaction between Fe^{II} complex and $O_2^{\bullet-}$ generates the activated Fe^{III} -(hydro)peroxo as the archetypal OAT reactive species. Meanwhile, the oxidized photosensitizer $[Ru^{III}]$ oxidizes the 4-styrene sulfonate substrate to produce an alkenyl radical cation and release the ground state photosensitizer. While, alkenyl radical cation reacts with the active catalytic species Fe^{III} -(hydro)peroxo to form benzaldehyde. On the other side, the olefin is oxidized by the $Fe^V=O$ species, generated from Fe^{III} -hydroperoxo species, to form the diol product. When the photocatalytic run was performed at pH 6 the benzaldehyde product was found as the main product, since the protonation of the Fe^{III} -peroxo was disfavored in such condition.

All attempt to chase the Fe^{III} -(hydro)peroxo and Fe^V -oxo DPy species were unsuccessful in aqueous medium, probably due to their short lifetime. We decided to generate the active iron DPy species by the reaction of H_2O_2 and the prepared $[Fe^{II}DPy]^+$ complex in MeOH at -40° . The formation of an active iron species was observed within few seconds by the detection of a band at 632 nm and an EPR signal at $g = 4.3$ assigned to a rhombic high spin iron(III) species.

To investigate further this new approach, we utilized the $[L_5Fe^{II}]^{2+}$ complex as catalyst. In this case; $MV^{+\bullet}$ reduces the combination of $[L_5Fe^{II}]^{2+}$ and O_2 to form the Fe^{III} -(hydro)peroxo L_5 species by a mechanism that can be envisioned in two different ways. Either, the $[L_5Fe^{II}(O_2)]^{2+}$ adduct is formed by the reaction of the $[L_5Fe^{II}]^{2+}$ and O_2 then followed by

reaction with $MV^{+\bullet}$ to form the Fe^{III} -(hydro)peroxo L_5 species, or, the $[L_5Fe^{II}]^{2+}$ reacts with $O_2^{\bullet-}$, as a product of the reduction of O_2 by $MV^{+\bullet}$. The LFP experiment revealed the formation of a mixture of iron oxygenated species, that could be $[L_5Fe^{IV}(O)]^{2+}$, $[Fe^{II}(O_2)L_5]^{1+}$ and $[L_5Fe^{II}(OOH)]^{1+}$, according to the UV-vis spectral observed.

In chapter IV, by testing different two-electron oxidants we sought to generate and characterize potent oxidizing species derived from $Fe^{III}DPyCl_2$. mCPBA slowly degrades the complex preventing the clear detection of relevant intermediate. NaClO reacts with the $Fe^{III}DPyCl_2$ complex at room temperature to form an iron active species detected by a new absorption band at 631 nm associated with a life time $t_{1/2} = 15$ min. The EPR analysis revealed that the active species generated by NaClO is a rhombic high spin Fe(III) complex characterized by a broad signal at 4.3 and thus cannot be an Fe(V) oxo species as expected. HRMS analysis indicates that one oxygen atom has yet been added to the iron species. After ruling out a possible $Fe^{III}-OCl$ intermediate, we proposed that the oxygen insertion takes place in a $N_{Pyridine}-Fe$ bond, yielding a $[Fe^{III}(DPyNO)]^{2+}$ species, due to the hemilability of the ligand. Our proposition was supported by the vibration energies detected at 855 and 1231 cm^{-1} by Infrared spectroscopy, which are close to the energies reported for the Fe-O-N vibration in the hexa(pyridine-N-oxide) iron(III) complex. To our satisfaction, this intermediate was found to be a potent oxygen atom transfer agent to triphenylphosphine and thioanisole. However, we also detected degraded chlorinated complex by HRMS, precluding the application of NaClO as an oxidant in catalysis. PhIO, as a more selective reagent was picked in the next study.

Iodosylbenzene oxidizes the $Fe^{III}DPyCl_2$ complex to generate an active species which seems identical to the $[Fe^{III}(DPyNO)]^{2+}$ generated by NaClO, based on UV-vis absorption, Mass and EPR spectroscopies. Two vibration energies at 840 and 1223 cm^{-1} , sensitive to ^{18}O labelling were also identified. DFT calculation nicely corroborated our experimental results and allowed us to propose a geometry for the $[Fe^{III}(DPyNO)]^{2+}$ intermediate. Finally, we showed that this intermediate is probably involved in the catalytic oxidation of a variety of substrates, among which the challenging cyclohexane.

As a perspective of this work we could envision to explore the next generation of ligand. Preliminary study on a ligand bearing methyl benzimidazole groups instead of pyridines groups indeed revealed a promising reactivity. The reaction of the $Fe^{III}BIMCl_2$ complex with

NaClO led to the formation of an iron intermediate characterized at 670 nm, reminiscent to that obtained with the $\text{Fe}^{\text{III}}\text{DPyCl}_2$ complex. This iron intermediate reacts with the stoichiometric amount of 4-MePhSMe within 3 min compared to 30 min in the case of the $\text{Fe}^{\text{III}}\text{DPyCl}_2$ complex. Moreover, based on UV-visible spectroscopy, the initial iron(III) precursor is fully recovered. However, one could ask if the oxygen atom can be inserted in the Fe-N_{BIM} bonds. Such a new reactivity pattern will be further investigated in the group.

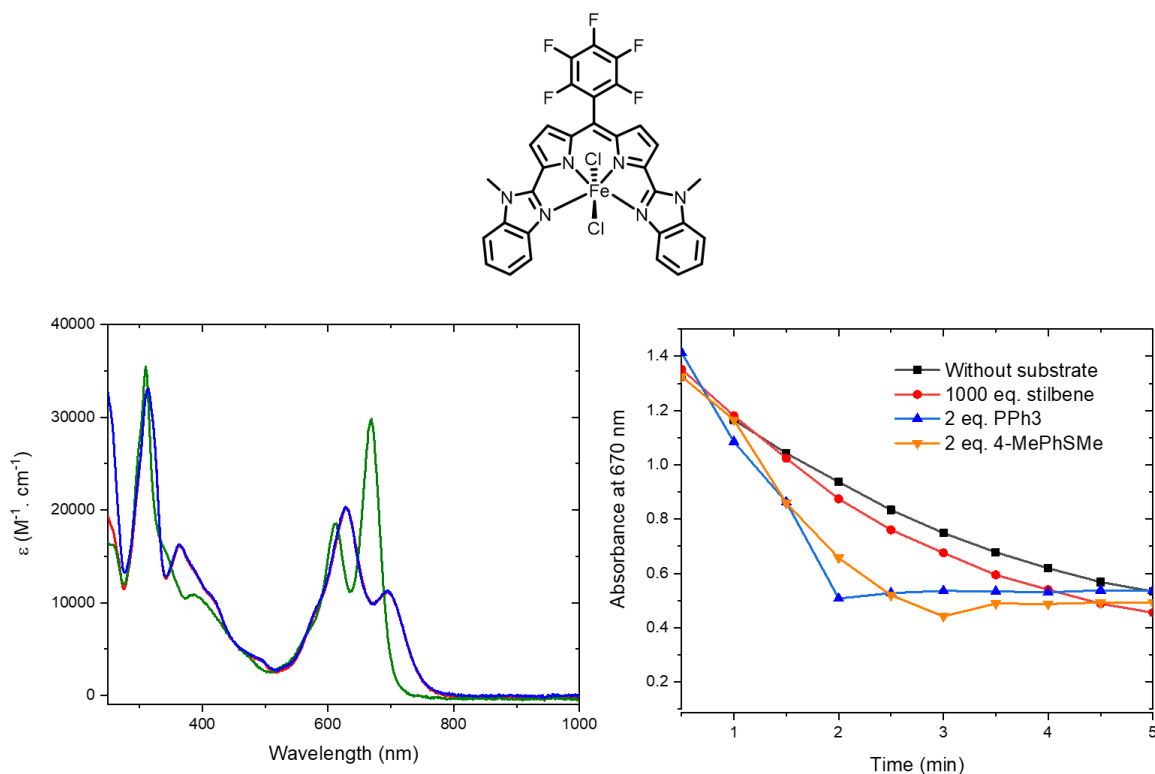


Figure V-1: (Top) structural drawing of the $\text{Fe}^{\text{III}}\text{BIMCl}_2$ complex; (Bottom, left) UV-vis spectral changes during the oxidation of the $\text{Fe}^{\text{III}}\text{BIMCl}_2$ complex (red) by 2 eq. of NaClO (green) and its reaction with 2 eq. of PPh_3 (blue); (Bottom, right) Absorption band at 670 nm with and without substrates.

Experimental section

Instrumentation

UV-visible Absorption spectrometry

UV-visible absorption spectra were recorded in solution using 1 cm quartz cuvettes on a Varian Cary 60 UV-vis spectrophotometer. The measures at low temperature (-40°C) were recorded on a Varian Cary 60 UV-vis spectrophotometer equipped with an UNISOKU cryostat system (UPS-203; UNISOKU, Japan) under nitrogen atmosphere to avoid condensation.

Nuclear magnetic resonance spectrometry

^1H , ^{19}F and ^{31}P NMR spectra were performed on Bruker Avance III 400 MHz, Bruker Avance I 360 MHz, Bruker Avance I 300 MHz or Bruker DPX 250 MHz. All results from NMR spectra were treated by Topspin software and the chemical shifts δ were described in ppm. Deuterated solvents (deuterated acetonitrile, deuterated acetone or deuterated oxide) were used as the reference.

Electrospray ionization mass spectrometry

The Thermo Scientific DSQ 2004 model from Thermo Fischer Scientific Company was employed for recording the electrospray ionization mass spectrometry experiments with an ESI⁺ or ESI⁻ method. Samples were prepared in a 100–200 μM solution with methanol or acetonitrile as solvent to directly inject into the spectrometer. For intermediate species, the samples were frozen in liquid nitrogen after preparation, then allowed to melt at room temperature just a few seconds before injection it in the device.

Electronic paramagnetic resonance spectrometry

X-band (9.47 GHz) EPR measurements were measured by using a Bruker Elexsys E 500 spectrometer with an Oxford ESR9 liquid helium (5 K) flow cryostat using a gold-chromel thermocouple directly below the sample position. Sample concentration were typically 1 mM. The complexes and intermediates were prepared in acetonitrile with 0.1 M TBAPF₆ then transferred to a degassed EPR tube and frozen to 77 K.

Electrochemistry

Cyclic voltammetry and controlled potential electrolysis experiments were performed using an Autolab 204 potentiostat monitored by the NOVA 1.10 software. A standard three electrodes electrochemical cell was used. Potentials were referenced to a Saturated Calomel Electrode. The working electrode was a 3 mm diameter vitreous carbon electrode polished with 1 mm diamond paste. The counter electrode was a platinum electrode. For the controlled potential electrolysis experiment, the working electrode was a carbon felt linked to a carbon stick or a glassy carbon plate with a copper thread used to connect the electrode. The counter electrode was a platinum wire. Electrochemical measurements were run under an argon atmosphere at room temperature using the commercial dried solvents and the recrystallized TBAPF₆ as an electrolyte. The solution was degassed for 10 min to achieve a saturated gas (argon or carbon dioxide) before running the experiments.

Mössbauer spectrometry

Mössbauer spectra were recorded at 4.2 K and 80 K, either on a low field Mössbauer spectrometer equipped with a Janis SVT-400 cryostat or on a strong-field Mössbauer spectrometer equipped with an Oxford Instruments Spectromag 4000 cryostat containing an 8T split-pair superconducting magnet. Both spectrometers were operated in a constant acceleration mode in transmission geometry. The isomer shifts are referenced against that of a room-temperature metallic iron foil. Analysis of the data was performed with the program WMOSS (WEB Research).

Led Lamp used for photocatalytic experiments

A white LED from METAPHASE TECHNOLOGY (light power = 1.3 mW.cm⁻¹) equipped with a Wratten 2E filter (blocking $\lambda < 415$ nm) was used to irradiate reactional mixtures (Figure 0-1).



Figure 0-1: LED panel used for photocatalytic experiment

High performance liquid chromatography

The high-performance liquid chromatography experiments (HPLC) were performed on a 1260 infinity II LC system from Agilent Technologies with a Zorbax Eclipse Plus C18 column (10 cm, 4.6 mm, 3.5 μm).

High performance gas chromatography

The performance gas chromatography experiments (HPGC) were performed on a GC-2010 system from Shimadzu with a Zebron ZB Semi-Volatiles column (25 m, 0.25 mm, 0.25 μm). The Shimadzu GC software is used to perform analyses.

Laser Flash Photolysis

Samples were prepared in 1 cm quartz cuvettes. Transient absorption and emission measurements were recorded on an Edinburgh Instruments LP920 flash photolysis spectrometer. Laser excitation pulses were generated from a Continuum Surelite OPO laser (5 ns pulses duration, typical energy 10 mJ per flash) for excitation at 460 nm. The probe source is a pulsed 450 W Xenon lamp and the detectors are either a Hamamatsu photomultiplier tube (PMT) or a water cooled Andor intensified charge coupled device (ICCD) camera.

Infra-Red spectrometry

Infra-red spectra were recorded on an attenuated total reflectance-infrared (ATR-IR) Thermo-Nicolet 6700 FTIR spectrometer, equipped with a mercury-cadmium-telluride (MCT)

detector. 5 μL of the sample solution (1 mM) was dropped onto the diamond prism of ATR-IR. The solvent was allowed to evaporate in a stream of nitrogen gas until a dry film is deposited. 200 sample scans were recorded with a resolution of 4 cm^{-1} , recorded for the range of 4000 cm^{-1} to 500 cm^{-1} with a speed of 1.8988 kHz and aperture of 10 mm.

Resonance Raman spectrometry

rRaman spectra were measured on a home-made Raman spectrometer at 532 nm excitation wavelength, the spectrum being acquired with a fiber spectrometer coupled to a CCD camera (IsoPlane SCT 320 mounted with a PIXIS, using a 1800 lines grating; Princeton Inst.). An interferential filter was used to cut the elastic scattering. The spectral resolution was set to 6 cm^{-1} . The laser power was adjusted to about 1-2 mW on the sample to avoid laser damage. The sample was deposited onto a quartz plate by dropping the sample solution (4 mM) then evaporate solvent under a stream of nitrogen.

Experimental procedures

Synthesis

2-(N-Boc-1H-pyrrol-2-yl)pyridine: 2-bromopyridine (2.26 mL, 23.60 mmol, 1 equiv.) were dissolved in the mixture of dioxane (100 mL), ethanol (50 mL) and water (50 mL). This solution was degased within 1h by Argon. Then $[\text{Pd}(\text{PPh}_3)_4]$ (2.73 g, 2.36 mmol, 0.1 equiv.) and (N-Boc-2-pyrrolyl)boronic acid (5.00 g, 23.6 mmol, 1 equiv.) were added under Argon. The mixture was stirred in 20 min. K_2CO_3 (10.00 g, 0.24 mol, 10 equiv.) was then added, and the reactional mixture was stirred vigorously and heated at $107\text{ }^\circ\text{C}$ for 2 h. After cooling to room temperature, solvents were evaporated. The obtained solid was dissolved in 200 mL ethyl acetate then extracted with 200 mL K_2CO_3 1 M (3 times). The organic phase was dried with Na_2SO_4 then filtered and concentrated. 2-(N-Boc-1H-pyrrol-2-yl)pyridine as a yellow oil was purified by column chromatography on silica gel (petroleum ether/ethyl acetate, 9:1) to yield 1 as a yellow oil (3.9 g, 68%). ^1H NMR (CDCl_3 , 250 MHz): $\delta = 1.36$ (s, 9 H, CH_3), 6.25 (t, $J = 3.3\text{ Hz}$, 1 H), 6.42 (dd, $J = 3.3, 1.8\text{ Hz}$, 1 H), 7.20 (ddd, $J = 12, 4.8, 1.2\text{ Hz}$, 1 H), 7.36–7.43 (m, 2 H), 7.68 (td, $J = 7.5, 1.8\text{ Hz}$, 1 H), 8.60–8.64 (m, 1 H) ppm.

2-(2-Pyrrolyl)pyridine: 2-(N-Boc-1H-pyrrol-2-yl)pyridine (3.9 g, 16.05 mmol) was dissolved in CH₂Cl₂ (30 mL), and aqueous HCl 3 M (30 mL) was added. The biphasic mixture was vigorously stirred at room temperature for 60 h. The solution was neutralized by adding the saturated solution of NaHCO₃ and extracted with 100 mL of water (3 times). The organic phase was dried with Na₂SO₄ and filtered. The solution was concentrated to yield 2-(2-Pyrrolyl)pyridine as a white solid (2.28 g, 95 %). ¹H NMR (CDCl₃, 360 MHz): δ = 6.30 (dt, J = 2.6, 3.6 Hz, 1 H), 6.7 (m, 1 H), 6.9 (m, 2 H), 7.03 (dd, J = 2.0, 5.5 Hz, 1 H), 7.54 (d, J = 7.7 Hz, 2 H), 7.62 (td, J = 7.7, 1.6 Hz, 1 H), 8.45 (d, J = 5 Hz, 1 H), 9.8 (br. s, NH) ppm.

DPy: p-toluensulfonic acid (4.5 g, 23.7 mmol, 3 equiv.) was dissolved in toluene (50 mL). The Dean stark method was used to eliminate water in the solution. 2-(2-Pyrrolyl)pyridine (2.28 g, 15.8 mmol, 2 equiv.), pentafluorobenzaldehyde (1.55 g, 7.9 mmol, 1 equiv.) and 1,1,2,2-tetrachloroethane (50 mL) were then added. The mixture was heated at 138 °C under argon for 7 day, after which it was basified with aqueous K₂CO₃ (1 M). The aqueous phase was extracted with chloroform, and the combined organic phases were concentrated and dissolved in dichloromethane (100 mL). The dissolved 2,3-dichloro-5,6-dicyano-1,4-benzoquinone (10.5 g, 47.4 mmol, 6 equiv.) in tetrahydrofurane (80 mL) was then added dropwise. The reactional mixture was stirred overnight at room temperature. The solvents were evaporated. The obtained solid was dissolved in 200 mL chloroform, then extracted with 200 mL K₂CO₃ 1 M (3 times). The organic phase was dried with Na₂SO₄ and filtered then concentrated. DPy (2 g, 54 %) as a brown solid was precipitated in methanol (30 mL) at -20 °C (freezer). ¹H NMR (CDCl₃, 250 MHz): δ = 6.59 (d, J = 4.4 Hz, 2 H, Hpyrrol), 7.10 (d, J = 4.4 Hz, 2 H, Hpyrrol), 7.29 (m, 2 H), 7.82 (dd, J = 7.8, 1.6 Hz, 2 H), 8.20 (d, J = 8.1 Hz, 2 H), 8.72 (d, J = 4.7 Hz, 2 H), 13.70 (br. s, 1 H, NH) ppm.

Fe^{III}DPyCl₂: A solution of DPy ligand (100 mg, 215 μmol, 1 equiv.) in methanol (20 mL) was added dropwise to FeCl₃·6H₂O (58.3 mg, 215 μmol, 1 equiv.) in methanol (10 mL) at room temperature then diethyl ether (50 mL) was added to precipitate a solid. The brown residue was filtered and dried under vacuum to give complex Fe^{III}DpyCl₂ (116 mg, 197 μmol, 91%). Single crystals were obtained by diffusing slowly diethyl ether to a saturated solution of complex I in acetonitrile. ESI⁺-HRMS: calcd. For [C₂₅H₁₂ClF₅FeN₄]⁺ 554.0015; found 553.9995. UV-vis (CH₃CN): 668 nm, 589 nm, 320 nm, 298 nm.

[{Fe^{III}DPy(EtOH)}₂O](OTf)₂: A solution of DPy ligand (100 mg, 215 μ mol, 1 eq.) in methanol (20 mL) was added dropwise to Fe(OTf)₂ (89 mg, 215 μ mol, 1 eq.) in methanol (5 mL) at room temperature under argon atmosphere in a glove box. The instant color change from red to blue confirmed the formation of Fe^{II}(DPy)(OTf) complex. Then, a cyan solution was obtained by aerating for 1 hour under stirring. A brown residue was obtained by evaporation and dried under vacuum for 8 hours. The complex [{Fe^{III}DPy(EtOH)}₂O](OTf)₂ was recrystallized by slowly diffusing pentane into a saturated solution in ethanol (132 mg, 85%). ESI⁺-HRMS: calculation for [C₅₀H₂₄F₁₀N₈O₁Fe₂]²⁺ 527.0301; found 527.0287. UV-vis (MeOH): 624 nm ($\epsilon = 23000 \text{ M}^{-1} \cdot \text{cm}^{-1}$), 588 nm ($\epsilon = 32000 \text{ M}^{-1} \cdot \text{cm}^{-1}$), 317 nm ($\epsilon = 32000 \text{ M}^{-1} \cdot \text{cm}^{-1}$).

[Ru(bpy)₃](PF₆)₃:¹⁹⁵ [Ru(bpy)₃]Cl₂ (60 mg, 0.08 mmol, 1.00 eq) was diluted in aq. H₂SO₄ (3 mL, 7 M) then MnO₂ (9 mg, 0.10 mol, 1.25 eq) was added. The mixture was mixed for 1 hours at room temperature in the dark. A green precipitate was formed after the addition of saturated KPF₆ (2.5 mL). After filtration and washing with cold water, the product was obtained as a green solid (69 mg, 0.07 mmol, 85 %).

Crystal structure determination

X-ray diffraction data for compounds $\text{Fe}^{\text{III}}\text{DPyCl}_2$, $[\{\text{Fe}^{\text{III}}\text{DPy}(\text{EtOH})\}_2\text{O}](\text{OTf})_2$ and $\text{Fe}^{\text{III}}\text{DPy}(\text{OTf})_2$ was collected by using a VENTURE PHOTON100 CMOS Bruker diffractometer with Micro-focus IuS source Mo $\text{K}\alpha$ radiation. Crystals were mounted on a CryoLoop (Hampton Research) with Paratone-N (Hampton Research) as cryoprotectant and then flashfrozen in a nitrogen-gas stream at 100 K. The temperature of the crystal was maintained at the selected value by means of an N-Helix cooling device to within an accuracy of $\pm 1\text{K}$. The data were corrected for Lorentz polarization, and absorption effects. The structures were solved by direct methods using SHELXS-97¹⁹⁶ and refined against F^2 by full-matrix least-squares techniques using SHELXL-2018¹⁹⁷ with anisotropic displacement parameters for all non-hydrogen atoms. Hydrogen atoms were located on a difference Fourier map and introduced into the calculations as a riding model with isotropic thermal parameters. All calculations were performed by using the Crystal Structure crystallographic software package WINGX.¹⁹⁸

$\text{Fe}^{\text{III}}\text{DPyCl}_2$

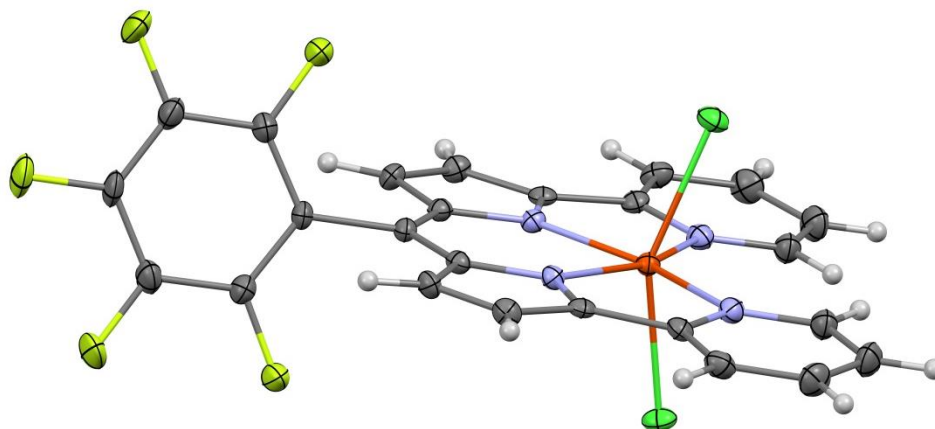


Figure 0-2 : ORTEP representation at 30 % of probability of X-Ray structure of $\text{Fe}^{\text{III}}\text{DPyCl}_2$ complex.

The presence of solvent molecules could easily be seen by residual peaks located in closed spherical cavities (Figure 0-3).

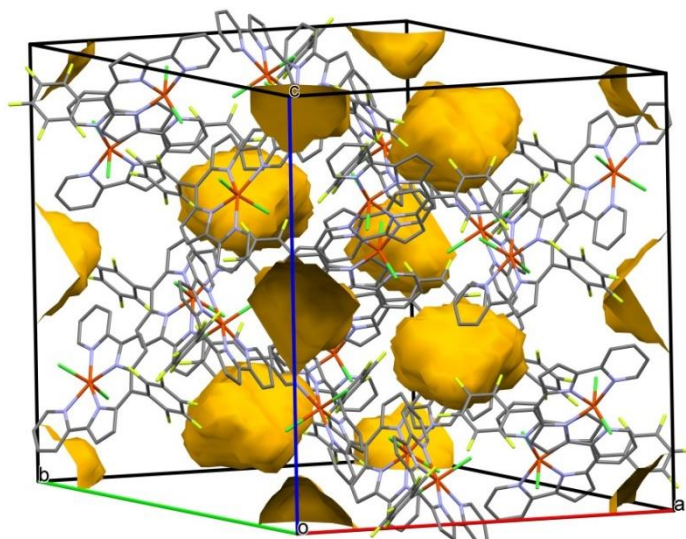


Figure 0-3 : Crystal packing displaying space occupied by solvent molecules.

Unfortunately, they were disordered so badly that it could not be modeled even with restraints. Consequently, SQUEEZE³ (from PLATON) was used to calculate the void space, the electron count and to get a new HKL file. According to the SQUEEZE results and the different experimental evidences a total number 14 CH₃CN solvent molecules (308 electrons) was considered per unit cell.

Without solvent molecules: R1= 0.0848 for 3835 reflections of $I > 2\sigma(I)$ and wR2= 0.2502 for all data. With solvent molecules (SQUEEZE): R1= 0.0784 for 3835 reflections of $I > 2\sigma(I)$ and wR2= 0.1902 for all data, the volume fraction was calculated to 1203 Å³ which corresponds to 11% of the unit cell volume, and to 305 electrons per unit cell allocated to solvent molecules. The crystal data collection and refinement parameters are given in Table 0-1

Compound	Fe^{III}DPyCl₂
Empirical Formula	C ₂₅ H ₁₂ Cl ₂ F ₅ FeN ₄ [+ 7/9 (C ₂ H ₃ N)]
<i>M_r</i>	590.14
Crystal size, mm ³	0.08 x 0.08 x 0.04
Crystal system	trigonal
Space group	<i>R</i> -3 c
a, Å	22.4084(16)
b, Å	22.4084(16)
c, Å	25.9110(19)
α, °	90
β, °	90
γ, °	120
Cell volume, Å ³	11267.7(18)
Z ; Z'	18 ; 1/2
T, K	100 (1)
Radiation type ; wavelength Å	MoKα; 0.71073
F ₀₀₀	5310
μ, mm ⁻¹	0.868
θ range, °	2.623–30.530
Reflection collected	100 553
Reflections unique	3 835
R _{int}	0.1980
GOF	1.023
Refl. Obs. (<i>I</i> >2σ(<i>I</i>))	2 070
Parameters	170
wR ₂ (all data)	0.1902
R value (<i>I</i> >2σ(<i>I</i>))	0.0784
Largest diff. peak and hole (e ⁻ .Å ⁻³)	0.901 ; -0.511

Table 0-1 : Crystallographic data and structure refinement details.

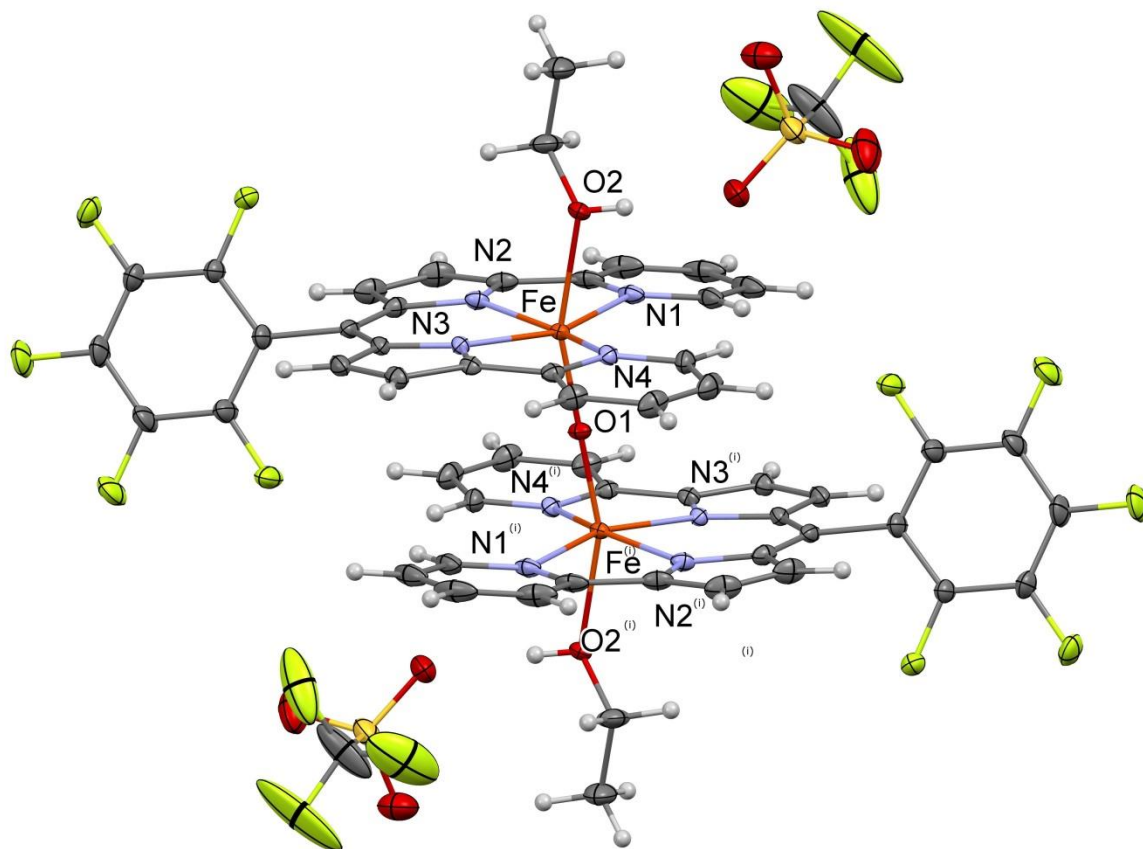


Figure 0-4: An ORTEP drawing of compound complex $[\{\text{Fe}^{\text{III}}\text{DPy}(\text{EtOH})\}_2\text{O}](\text{OTf})_2$. Thermal ellipsoids are shown at the 30% level. (symmetry codes: (i) $-x, -y, -z$).

The central O1 atom is located at the crystallographic inversion center. The crystal data collection and refinement parameters are given in Table 0-2.

Compound	$[\{\text{Fe}^{\text{III}}\text{DPy}(\text{EtOH})\}_2\text{O}](\text{OTf})_2$
CCDC	1911145
Empirical Formula	$\text{C}_{54} \text{H}_{36} \text{F}_{10} \text{Fe}_2 \text{N}_8 \text{O}_3, 2(\text{C} \text{F}_3 \text{O}_3 \text{S})$
M_r	1444.75
Crystal size, mm^3	0.12 x 0.09 x 0.06
Crystal color	orange
Crystal system	monoclinic
Space group	$P 2_1/n$
a, Å	10.6564(9)
b, Å	21.4716(17)
c, Å	12.5861(12)
α , °	90
β , °	94.915(3)
γ , °	90
Cell volume, Å ³	2869.2(4)
Z ; Z'	2 ; 1/2
T, K	100 (1)
Radiation type ; wavelength Å	MoK α ; 1.54178
F_{000}	1456
μ , mm^{-1}	0.696
θ range, °	2.405–30.586
Reflections collected	114 256
Reflections unique	8 791
R_{int}	0.0948
GOF	0.862
Refl. Obs. ($I > 2\sigma(I)$)	6 278
Parameters	427
w R_2 (all data)	0.1999
R value ($I > 2\sigma(I)$)	0.0665
Largest diff. peak and hole ($\text{e} \cdot \text{\AA}^{-3}$)	1.689 ; -1.286

Table 0-2 : Crystallographic data and structure refinement details.

$\text{Fe}^{\text{III}}\text{DPy}(\text{OTf})_2$

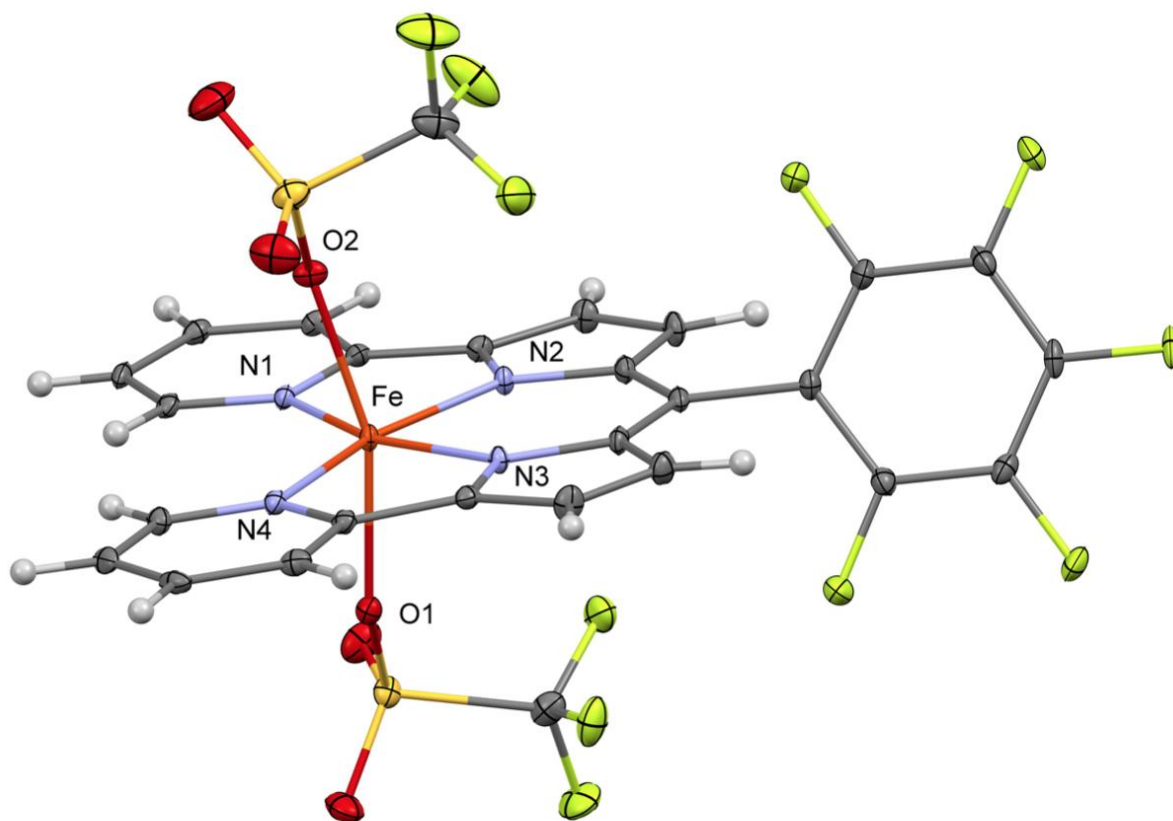


Figure 0-5 : ORTEP representation at 30 % of probability of X-Ray structure of $\text{Fe}^{\text{III}}\text{DPy}(\text{OTf})_2$ complex.

The crystal data collection and refinement parameters are given in Table 0-3.

Compound	Fe^{III}DPy(OTf)₂
CCDC	Unpublished-yet
Empirical Formula	C ₂₇ H ₁₂ F ₁₁ Fe N ₄ O ₆ S ₂
<i>M_r</i>	817.38
Crystal size, mm ³	0.09 x 0.06 x 0.02
Crystal system	triclinic
Space group	<i>P</i> -1
a, Å	8.2592(5)
b, Å	12.9292(8)
c, Å	15.0173(9)
α, °	87.401(3)
β, °	75.093(2)
γ, °	72.263(2)
Cell volume, Å ³	1475.04(16)
Z ; Z'	2 ; 1
T, K	100 (1)
Radiation type ; wavelength Å	MoKα; 0.71073
F ₀₀₀	814
μ, mm ⁻¹	0.774
θ range, °	2.208–31.130
Reflection collected	90 232
Reflections unique	9 337
R _{int}	0.2021
GOF	0.999
Refl. Obs. (<i>I</i> >2σ(<i>I</i>))	4 806
Parameters	460
wR ₂ (all data)	0.1374
R value (<i>I</i> >2σ(<i>I</i>))	0.0587
Largest diff. peak and hole (e ⁻ .Å ⁻³)	0.890 ; -0.776

Table 0-3 : Crystallographic data and structure refinement details.

Catalytic procedure

Catalytic experiments in chapter IV were carried out in a glass vial (3 mL) containing 1 mL acetonitrile solution of 1 mM Fe^{III}DPyCl₂ (1 eq.) and 800 mM substrate. 20 eq. of PhIO was added to solution. After stirring for 2 h at room temperature, 3 μL of internal standard solution (2 mM final) was added to the reactional solution. The resulting solution was filtered through a short silica gel column (on a Pasteur pipette). 1.5 mL MeOH was used to collect all remaining organic product from the silica gel column. The obtained solution was injected into HPGC to detect and quantify the oxidized product.

Quantification of oxidized products by HPGC

2 mM acetophenone was used as an internal standard in the catalytic experiments towards the oxidation of cyclohexane, cyclooctene, diphenylmethane and thioanisole, while 2 mM anisole was used as an internal standard for the oxidation of cyclohexene, toluene and ethylbenzene. The HPGC conditions is detailed in Table 0-4. Concentration of the oxidized products was calculated by the following equation:

$$[Product] = [Standard] \times \frac{k(Standard)}{k(Product)} \times \frac{Area(Product)}{Area(Standard)}$$

k in this equation is a constant which is obtained from the slope of the calibration curves. The retention time (rt) and k value for the oxidized products was presented in Table 0-5.

Substrates	Rate (°C/min)	Temperature (°C)	Hold time (min)
Thioanisole	-	100	0
	5	130	0
	50	220	4
cyclooctene	-	100	0
	20	160	1
	40	220	1
cyclohexene	-	50	0
	20	180	0
	50	220	2
Styrene	-	60	0
	20	220	3
	0	0	0
Toluene	-	50	0
	25	220	2
	0	0	0
Ethylbenzene	-	100	0
	3	130	0
	50	220	3
Diphenylmethane	-	100	0
	50	220	3
	0	0	0
cyclohexane	-	50	0
	2	70	0
	50	220	2

Table 0-4: HPGC conditions used in the quantification of the oxidized products.

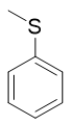
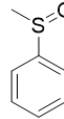
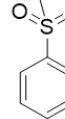
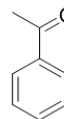
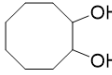
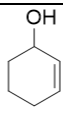
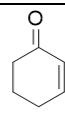
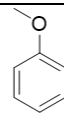
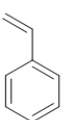
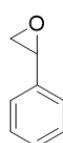
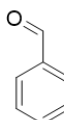
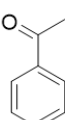
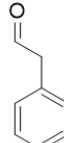
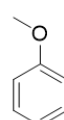
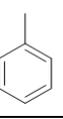
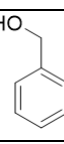
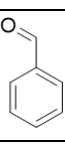
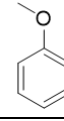
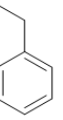
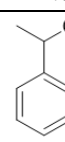
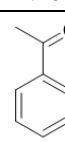
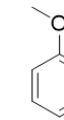
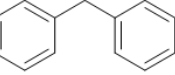
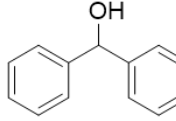
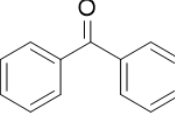
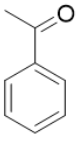
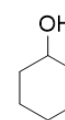
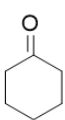
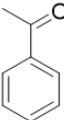
						
Retention time (min)	4.32	7.56	8.04	4.03		
Constant k (10^{13} mol^{-1})	x	2.07	2.19	2.12		
						
Retention time (min)	2.36	4.95	3.36	3.6		
Constant k (10^{13} mol^{-1})	x	2.49	2.31	2.12		
						
Retention time (min)	2.09	3.40	3.75	3.17	3.63	4.92
Constant k (10^{13} mol^{-1})	x	1.69	1.42	1.62	2.09	1.71
						
Retention time (min)	3.09	4.48	3.59	4.41	4.25	3.22
Constant k (10^{13} mol^{-1})	x	2.53	1.42	2.12	1.85	2.09
						
Retention time (min)	2.45	4.22	3.73	3.35		
Constant k (10^{13} mol^{-1})	x	2.00	2.10	2.09		
						
Retention time (min)	2.42	4.19	4.33	2.72		
Constant k (10^{13} mol^{-1})	x	2.26	2.12	2.09		
						
Retention time (min)	3.70	2.55	4.29	2.55		
Constant k (10^{13} mol^{-1})	x	3.23	4.33	2.12		
						
Retention time (min)	2.27	6.44	6.60	11.71		
Constant k (10^{13} mol^{-1})	x	1.85	1.90	2.12		

Table 0-5: Retention time and constant k of each substrate and the corresponding oxidized products.

Photocatalytic procedure

Photocatalytic experiments in chapter III were carried out in a glassy vial (1.5 mL) containing typically 30 μM $[\text{Ru}(\text{bpy})_3]\text{Cl}_2$, 30 μM $[(\text{Fe}^{\text{III}}\text{DPy})_2\text{O}](\text{OTf})_2$, 4 mM MV^{2+} and 10 mM 4-styrene sulfonate sodium in 0.5 mL Britton & Robinson buffer pH 4.0 at 25 °C. The samples were placed on a white LED (1.3 $\text{mW}\cdot\text{cm}^{-1}$) equipped a filter ($T=0$ for $\lambda < 415$ nm). at room temperature, under air, covered with a black box, and irradiated for 22 h. The products were identified and quantified by ^1H NMR (see below).

Photocatalytic experiments under $^{18}\text{O}_2$ atmosphere were run in a Schlenk tube. The reaction mixture in 1 mL B&R buffer was subjected to 3 vacuum / argon cycles then 1 vacuum / $^{18}\text{O}_2$ oxygenation. After photo-reaction, samples were treated with 1 mL HCl 1M then extracted with 1 mL ethyl acetate (3 times). Ethyl acetate was removed by air flow to avoid product loss then the residue was redissolved in 50 μL water. 30 μL of solution were injected in HPLC. The ^{18}O labeling products formed were separated by preparative HPLC in presence of solvent gradient detailed in Table 0-6. The retention time for p-styrene sulfonate and the corresponding oxidized products is presented in Table 0-7. Each product was collected separately and analysed by HRMS-ESI without dilution.

Time (min)	$\text{H}_2\text{O} + 0.05\% \text{HCOOH}$	$\text{MeCN} + 0.1\% \text{HCOOH}$
0	95	5
2	95	5
5	90	10
10	0	100
15	0	100
17	95	5
20	95	5

Table 0-6: Solvent gradient used for HPLC analysis.

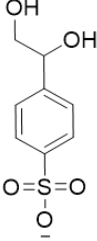
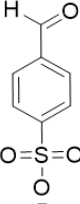
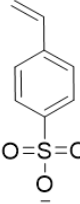
			
Retention time (min)	3.3	5.9	11.8

Table 0-7: Retention times for sulfonic *p*-styrene acid and the corresponding oxidized products.

Quantification of photo-oxidized products by ¹NMR

10 % deuterium oxide was added in the samples after irradiation to be used as a reference. ¹NMR spectra were recorded with a water suppression program. The starting compound and oxidized products were identified by ¹NMR (Styrene sulfonate by doublet at 6.75 ppm, benzaldehyde by singlet at 9.11 ppm, diol by doublet at 7.37 ppm, epoxide by doublet at 7.42 ppm) and quantified by the following equations, with I: Peak integration:

$$\% \text{ benzaldehyde} = \frac{2 * I (\text{benzaldehyde}) * 100\%}{[2 * I (\text{benzaldehyde}) + I (\text{diol}) + \text{intergration} (\text{epoxide}) + 2 * I (\text{S. Styrene})]}$$

$$\% \text{ diol} = \frac{I (\text{diol}) * 100\%}{[2 * I (\text{benzaldehyde}) + I (\text{diol}) + \text{intergration} (\text{epoxide}) + 2 * I (\text{S. Styrene})]}$$

$$\% \text{ epoxide} = \frac{I (\text{epoxide}) * 100\%}{[2 * I (\text{benzaldehyde}) + I (\text{diol}) + \text{intergration} (\text{epoxide}) + 2 * I (\text{S. Styrene})]}$$

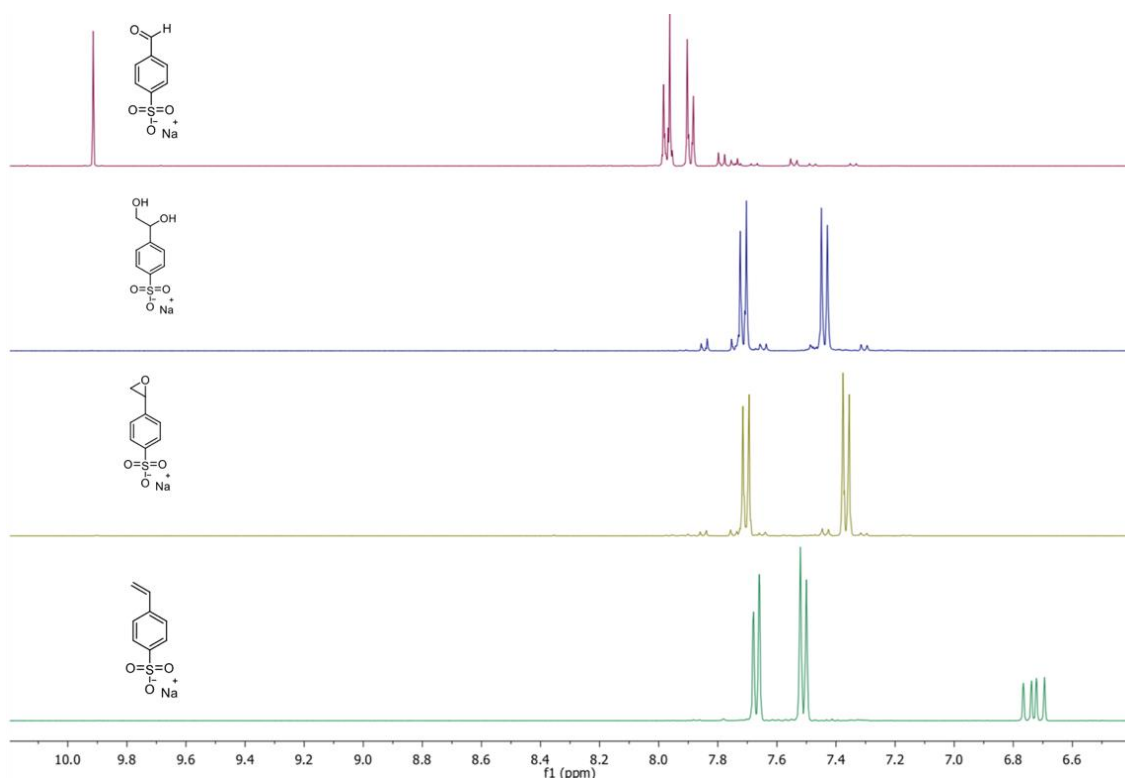


Figure 0-6: Extracts of the $^1\text{H-NMR}$ spectra of 4-styrenesulfonate, 4-(1,2-dihydroxyethyl)benzenesulfonate, 4-(oxiranyl)benzenesulfonate, 4-formylbenzenesulfonate in presence of: D_2O .

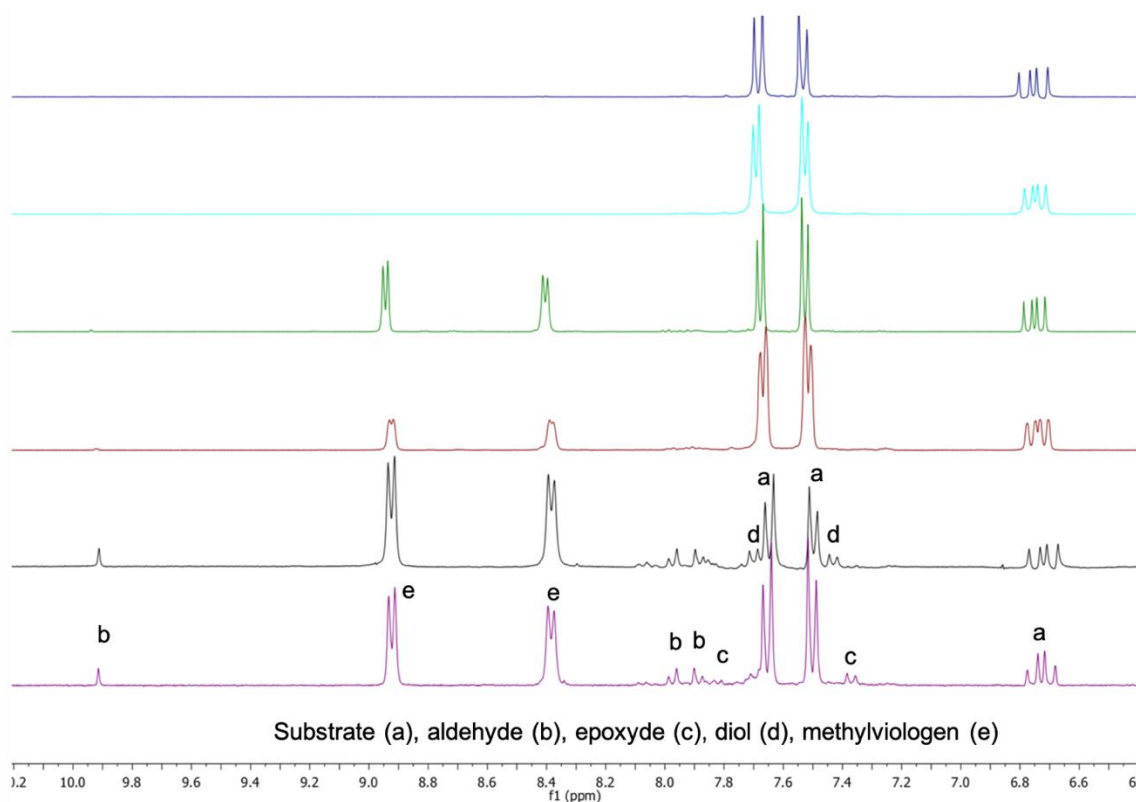
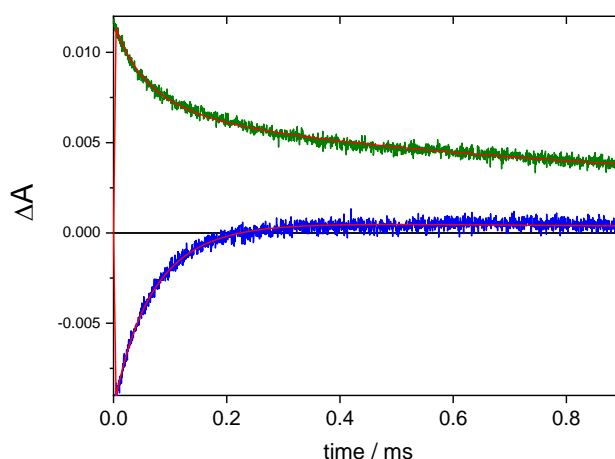


Figure 0-7: Extracts of the $^1\text{H-NMR}$ spectra of crude reaction mixtures in H_2O and 10 % D_2O obtained upon light irradiation of sodium 4-styrenesulfonate (10 mM) for 22 hours under aerobic conditions. (Blue) with $[\text{Ru}^{\text{II}}]$ (30 μM) in B&R pH 4; (Cyan) with $[\text{Ru}^{\text{II}}]$ (30 μM) and complex **I** (30 μM) in B&R pH 4; (Green) with $[\text{Ru}^{\text{II}}]$ (30 μM) and MV^{2+} (4 mM) in B&R pH 4; (Red) with $[\text{Ru}^{\text{II}}]$ (30 μM), FeCl_3 (60 μM), MV^{2+} (4 mM) in B&R pH 4; (Black) with $[\text{Ru}^{\text{II}}]$ (30 μM), complex **I** (30 μM), MV^{2+} (4 mM) in B&R pH 4; (Purple) with $[\text{Ru}^{\text{II}}]$ (30 μM), complex **I** (30 μM), MV^{2+} (4 mM) in B&R pH 6.

Oxidizing the $\text{Fe}^{\text{III}}\text{DPyCl}_2$ complex by PhIO

10 eq. of solid PhIO (1.1 mg) was added into 10 mL solution of 50 μM $\text{Fe}^{\text{III}}\text{DPyCl}_2$ complex under air atmosphere and at room temperature. The reaction mixture was sonicated for 10 s, then the insoluble PhIO was filtered by a syringe filter.



Simulation of kinetic traces

Simulation of the kinetics of the substrate (4-styrene sulfonate sodium) photo-oxidation in the presence of typically 30 μM $[\text{Ru}(\text{bpy})_3]\text{Cl}_2$ and 4 mM MV^{2+} in absence of dioxygen, was performed using the KinTek Explorer simulation program.^{199,200} A reaction scheme was used including the following reaction sequence:

- | | |
|---|---|
| 1. $\text{Ru}^{\text{II}} + \text{light} \rightarrow \text{Ru}^{\text{II}*}$ | 1. excitation |
| 2. $\text{Ru}^{\text{II}*} \rightarrow \text{Ru}^{\text{II}}$ | 2. intrinsic excited state decay |
| 3. $\text{Ru}^{\text{II}*} + \text{MV}^{2+} \rightarrow \text{Ru}^{\text{III}} + \text{MV}^{\bullet+}$ | 3. oxidative quenching by MV^{2+} |
| 4. $\text{Ru}^{\text{III}} + \text{MV}^{\bullet+} \rightarrow \text{Ru}^{\text{II}} + \text{MV}^{2+}$ | 4. charge recombination |
| 5. $\text{Ru}^{\text{II}*} + \text{MV}^{\bullet+} \rightarrow \text{Ru} + \text{MV}^{\bullet+*} \rightarrow \text{Ru} + \text{MV}^{\bullet+}$ | 5. quenching of $\text{Ru}^{\text{II}*}$ by energy transfer to $\text{MV}^{\bullet+}$ |
| 6. $\text{Ru}^{\text{III}} + \text{S} \rightarrow \text{Ru}^{\text{II}} + \text{S}^{\bullet+}$ | 6. oxidation of electron donor (substrate) |

where:

- Ru^{II} , $\text{Ru}^{\text{II}*}$ and Ru^{III} stand for the ground state, triplet excited state and oxidized state of the $[\text{Ru}(\text{bpy})_3]^{2+}$ chromophore,
- S and $\text{S}^{\bullet+}$ are the substrate and the corresponding oxidized state
- MV^{2+} and $\text{MV}^{\bullet+}$ are the oxidized and reduced state of the methyl viologen.

All reactions are considered irreversible. Initial concentrations are those used in the experiment. For the reactions noted in blue, rate constants are known from independent laser

flash kinetic measurements: intrinsic excited state decay of $\text{Ru}^{\text{II}*}$: $k_2=1.9 \cdot 10^6 \text{ s}^{-1}$; energy transfer quenching of $\text{Ru}^{\text{II}*}$ by $\text{MV}^{+\bullet}$: $k_5=6 \cdot 10^9 \text{ M}^{-1}\text{s}^{-1}$.

References

1. Davies, H. M. L. & Morton, D. Recent Advances in C–H Functionalization. *J. Org. Chem.* **81**, 343–350 (2016).
2. Hartwig, J. F. & Larsen, M. A. Undirected, Homogeneous C–H Bond Functionalization: Challenges and Opportunities. *ACS Cent. Sci.* **2**, 281–292 (2016).
3. Ortiz de Montellano, P. R. *Cytochrome P450*. (Springer International Publishing, 2015).
4. Ullrich, V. Cytochrome P450 and biological hydroxylation reactions. in *Blood Vessels* (eds. Effert, S. & Meyer-Erkelenz, J. D.) vol. 83 67–104 (Springer-Verlag, 1979).
5. Jung, C. The mystery of cytochrome P450 Compound I. *Biochim. Biophys. Acta BBA - Proteins Proteomics* **1814**, 46–57 (2011).
6. Green, M. T. Evidence for Sulfur-Based Radicals in Thiolate Compound I Intermediates. *J. Am. Chem. Soc.* **121**, 7939–7940 (1999).
7. Loew, G. H. & Harris, D. L. Role of the Heme Active Site and Protein Environment in Structure, Spectra, and Function of the Cytochrome P450s. *Chem. Rev.* **100**, 407–420 (2000).
8. Hausinger, R. P. Fe(II)/ α -Ketoglutarate-Dependent Hydroxylases and Related Enzymes. *Crit. Rev. Biochem. Mol. Biol.* **39**, 21–68 (2004).
9. Harlos, K. *et al.* Structural origins of the selectivity of the trifunctional oxygenase clavaminic acid synthase. *Nat. Struct. Biol.* **7**, 127–133 (2000).
10. Ryle, M. J., Padmakumar, R. & Hausinger, R. P. Stopped-Flow Kinetic Analysis of *Escherichia coli* Taurine/ α -Ketoglutarate Dioxygenase: Interactions with α -Ketoglutarate, Taurine, and Oxygen[†]. *Biochemistry* **38**, 15278–15286 (1999).
11. Zhou, J., Gunsior, M., Bachmann, B. O., Townsend, C. A. & Solomon, E. I. Substrate Binding to the α -Ketoglutarate-Dependent Non-Heme Iron Enzyme Clavamate Synthase 2: Coupling Mechanism of Oxidative Decarboxylation and Hydroxylation. *J. Am. Chem. Soc.* **120**, 13539–13540 (1998).
12. Price, J. C., Barr, E. W., Tirupati, B., Bollinger, J. M. & Krebs, C. The First Direct

Characterization of a High-Valent Iron Intermediate in the Reaction of an α -Ketoglutarate-Dependent Dioxygenase: A High-Spin Fe(IV) Complex in Taurine/ α -Ketoglutarate Dioxygenase (TauD) from *Escherichia coli* †. *Biochemistry* **42**, 7497–7508 (2003).

13. Proshlyakov, D. A., Henshaw, T. F., Monterosso, G. R., Ryle, M. J. & Hausinger, R. P. Direct Detection of Oxygen Intermediates in the Non-Heme Fe Enzyme Taurine/ α -Ketoglutarate Dioxygenase. *J. Am. Chem. Soc.* **126**, 1022–1023 (2004).

14. Wallar, B. J. & Lipscomb, J. D. Dioxygen Activation by Enzymes Containing Binuclear Non-Heme Iron Clusters. *Chem. Rev.* **96**, 2625–2658 (1996).

15. Tinberg, C. E. & Lippard, S. J. Dioxygen Activation in Soluble Methane Monooxygenase. *Acc. Chem. Res.* **44**, 280–288 (2011).

16. Banerjee, R., Proshlyakov, Y., Lipscomb, J. D. & Proshlyakov, D. A. Structure of the key species in the enzymatic oxidation of methane to methanol. *Nature* **518**, 431–434 (2015).

17. Lee, S. K., Fox, B. G., Froland, W. A., Lipscomb, J. D. & Munck, E. A transient intermediate of the methane monooxygenase catalytic cycle containing an FeIVFeIV cluster. *J. Am. Chem. Soc.* **115**, 6450–6451 (1993).

18. Werck-Reichhart, D., Hehn, A. & Didierjean, L. Cytochromes P450 for engineering herbicide tolerance. *Trends Plant Sci.* **5**, 116–123 (2000).

19. Groves, J. T., Nemo, T. E. & Myers, R. S. Hydroxylation and epoxidation catalyzed by iron-porphine complexes. Oxygen transfer from iodosylbenzene. *J. Am. Chem. Soc.* **101**, 1032–1033 (1979).

20. Battersby, A. R. & Howson, W. Model Studies on the Active Site of Cytochrome P-450: an FeII-Porphyrin carrying a Strapped Thiolate Ligand. *J. CHEM SOC* 1266–1268 (1982).

21. Collman, J. P. & Groh, S. E. ‘Mercaptan-tail’ porphyrins: synthetic analogs for the active site of cytochrome P-450. *J. Am. Chem. Soc.* **104**, 1391–1403 (1982).

22. Higuchi, T., Uzu, S. & Hirobe, M. Synthesis of a highly stable iron porphyrin coordinated by alkylthiolate anion as a model for cytochrome P-450 and its catalytic activity

in oxygen-oxygen bond cleavage. *J. Am. Chem. Soc.* **112**, 7051–7053 (1990).

23. Dawson, J. H. *et al.* Magnetic circular dichroism studies. 43. Oxidized cytochrome P-450. Magnetic circular dichroism evidence for thiolate ligation in the substrate-bound form. Implications for the catalytic mechanism. *J. Am. Chem. Soc.* **98**, 3707–3709 (1976).

24. Woggon, W.-D. Metalloporphyrines as Active Site Analogues Lessons from Enzymes and Enzyme Models. *Acc. Chem. Res.* **38**, 127–136 (2005).

25. Hessenauer-Ilicheva, N., Franke, A., Wolak, M., Higuchi, T. & van Eldik, R. Spectroscopic and Mechanistic Studies on Oxidation Reactions Catalyzed by the Functional Model SR Complex for Cytochrome P450: Influence of Oxidant, Substrate, and Solvent. *Chem. - Eur. J.* **15**, 12447–12459 (2009).

26. Porhiel, E., Bondon, A. & Leroy, J. β -Octafluoro-meso-tetraarylporphyrin iron complexes as catalysts for monooxygenation reactions. *Tetrahedron Lett.* **39**, 4829–4830 (1998).

27. Shan, X. & Que, L. High-valent nonheme iron-oxo species in biomimetic oxidations. *J. Inorg. Biochem.* **100**, 421–433 (2006).

28. Mehn, M. P., Fujisawa, K., Hegg, E. L. & Que, L. Oxygen Activation by Nonheme Iron(II) Complexes: α -Keto Carboxylate versus Carboxylate. *J. Am. Chem. Soc.* **125**, 7828–7842 (2003).

29. Paria, S., Chatterjee, S. & Paine, T. K. Reactivity of an Iron–Oxygen Oxidant Generated upon Oxidative Decarboxylation of Biomimetic Iron(II) α -Hydroxy Acid Complexes. *Inorg. Chem.* **53**, 2810–2821 (2014).

30. Katsuki, T. Some Recent Advances in MetalloSalen Chemistry. *Synlett* 0281–0297 (2003).

31. Cozzi, P. G. Metal–Salen Schiff base complexes in catalysis: practical aspects. *Chem Soc Rev* **33**, 410–421 (2004).

32. Jacobsen, E. N., Zhang, W., Muci, A. R., Ecker, J. R. & Deng, L. Highly enantioselective epoxidation catalysts derived from 1,2-diaminocyclohexane. *J. Am. Chem.*

Soc. **113**, 7063–7064 (1991).

33. Hinz, F. P. & Margerum, D. W. Ligand solvation and the macrocyclic effect. Nickel(II)-tetramine complexes. *Inorg. Chem.* **13**, 2941–2949 (1974).

34. Collins, T. J. Designing Ligands for Oxidizing Complexes. *Acc. Chem. Res.* **27**, 279–285 (1994).

35. Collins, T. J. TAML Oxidant Activators: A New Approach to the Activation of Hydrogen Peroxide for Environmentally Significant Problems. *Acc. Chem. Res.* **35**, 782–790 (2002).

36. Anson, F. C. *et al.* Oxidative and hydrolytic decomposition of a polyanionic chelating ligand. *Inorg. Chem.* **26**, 1161–1168 (1987).

37. Collins, T. J. & Ryabov, A. D. Targeting of High-Valent Iron-TAML Activators at Hydrocarbons and Beyond. *Chem. Rev.* **117**, 9140–9162 (2017).

38. Ghosh, M. *et al.* Formation of a Room Temperature Stable Fe^V(O) Complex: Reactivity Toward Unactivated C–H Bonds. *J. Am. Chem. Soc.* **136**, 9524–9527 (2014).

39. Oloo, W. N. & Que, L. Bioinspired Nonheme Iron Catalysts for C–H and C=C Bond Oxidation: Insights into the Nature of the Metal-Based Oxidants. *Acc. Chem. Res.* **48**, 2612–2621 (2015).

40. Engelmann, X., Monte-Pérez, I. & Ray, K. Oxidation Reactions with Bioinspired Mononuclear Non-Heme Metal-Oxo Complexes. *Angew. Chem. Int. Ed.* **55**, 7632–7649 (2016).

41. Serrano-Plana, J. *et al.* Trapping a Highly Reactive Nonheme Iron Intermediate That Oxygenates Strong C–H Bonds with Stereoretention. *J. Am. Chem. Soc.* **137**, 15833–15842 (2015).

42. Sastri, C. V. *et al.* Axial ligand tuning of a nonheme iron(IV) oxo unit for hydrogen atom abstraction. *Proc. Natl. Acad. Sci.* **104**, 19181–19186 (2007).

43. Que, L. The Road to Non-Heme Oxoferryls and Beyond[†]. *Acc. Chem. Res.* **40**, 493–

500 (2007).

44. Chen, K. & Que, L. cis-Dihydroxylation of Olefins by a Non-Heme Iron Catalyst: A Functional Model for Rieske Dioxygenases. *Angew. Chem. Int. Ed.* **38**, 2227–2229 (1999).
45. Hölzl, S. M., Altmann, P. J., Kück, J. W. & Kühn, F. E. Speciation in iron epoxidation catalysis: A perspective on the discovery and role of non-heme iron(III)-hydroperoxo species in iron-catalyzed oxidation reactions. *Coord. Chem. Rev.* **352**, 517–536 (2017).
46. Hitomi, Y., Arakawa, K., Funabiki, T. & Kodera, M. An Iron(III)-Monoamidate Complex Catalyst for Selective Hydroxylation of Alkane C–H Bonds with Hydrogen Peroxide. *Angew. Chem. Int. Ed.* **51**, 3448–3452 (2012).
47. Li, F. *et al.* Characterization of a High-Spin Non-Heme Fe^{III}–OOH Intermediate and Its Quantitative Conversion to an Fe^{IV}=O Complex. *J. Am. Chem. Soc.* **133**, 7256–7259 (2011).
48. Bukowski, M. R. *et al.* Catalytic Epoxidation and 1,2-Dihydroxylation of Olefins with Bispidine–Iron(II)/H₂O₂ Systems. *Angew. Chem. Int. Ed.* **45**, 3446–3449 (2006).
49. Solomon, E. I., Decker, A. & Lehnert, N. Non-heme iron enzymes: Contrasts to heme catalysis. *Proc. Natl. Acad. Sci.* **100**, 3589–3594 (2003).
50. Li, F., England, J. & Que, L. Near-Stoichiometric Conversion of H₂O₂ to Fe^{IV}=O at a Nonheme Iron(II) Center. Insights into the O–O Bond Cleavage Step. *J. Am. Chem. Soc.* **132**, 2134–2135 (2010).
51. Eser, B. E. *et al.* Direct Spectroscopic Evidence for a High-Spin Fe(IV) Intermediate in Tyrosine Hydroxylase. *J. Am. Chem. Soc.* **129**, 11334–11335 (2007).
52. Thibon, A. *et al.* Proton- and Reductant-Assisted Dioxygen Activation by a Nonheme Iron(II) Complex to Form an Oxoiron(IV) Intermediate. *Angew. Chem. Int. Ed.* **47**, 7064–7067 (2008).
53. Horwitz, C. P., Creager, S. E. & Murray, R. W. Electrocatalytic olefin epoxidation using manganese Schiff-base complexes and dioxygen. *Inorg. Chem.* **29**, 1006–1011 (1990).

54. Sengupta, K., Chatterjee, S., Samanta, S. & Dey, A. Direct observation of intermediates formed during steady-state electrocatalytic O₂ reduction by iron porphyrins. *Proc. Natl. Acad. Sci.* **110**, 8431–8436 (2013).
55. Ségaud, N. *et al.* Electrochemical study of a nonheme Fe(II) complex in the presence of dioxygen. Insights into the reductive activation of O₂ at Fe(II) centers. *Chem. Sci.* **6**, 639–647 (2015).
56. Chin, D.-H., La Mar, G. N. & Balch, A. L. Role of ferryl (FeO₂⁺) complexes in oxygen atom transfer reactions. Mechanism of iron(II) porphyrin catalyzed oxygenation of triphenylphosphine. *J. Am. Chem. Soc.* **102**, 5945–5947 (1980).
57. Balch, A. L. *et al.* Oxygenation patterns for iron(II) porphyrins. Peroxo and ferryl (FeIVO) intermediates detected by proton nuclear magnetic resonance spectroscopy during the oxygenation of (tetramesitylporphyrin)iron(II). *J. Am. Chem. Soc.* **106**, 7779–7785 (1984).
58. Chin, D.-H., Balch, A. L. & La Mar, G. N. Formation of porphyrin ferryl (FeO₂⁺) complexes through the addition of nitrogen bases to peroxo-bridged iron(III) porphyrins. *J. Am. Chem. Soc.* **102**, 1446–1448 (1980).
59. Pistorio, B. J., Chang, C. J. & Nocera, D. G. A Phototriggered Molecular Spring for Aerobic Catalytic Oxidation Reactions. *J. Am. Chem. Soc.* **124**, 7884–7885 (2002).
60. Rosenthal, J., Pistorio, B. J., Chng, L. L. & Nocera, D. G. Aerobic Catalytic Photooxidation of Olefins by an Electron-Deficient Pacman Bisiron(III) μ -Oxo Porphyrin. *J. Org. Chem.* **70**, 1885–1888 (2005).
61. Rosenthal, J., Luckett, T. D., Hodgkiss, J. M. & Nocera, D. G. Photocatalytic Oxidation of Hydrocarbons by a Bis-iron(III)- μ -oxo Pacman Porphyrin Using O₂ and Visible Light. *J. Am. Chem. Soc.* **128**, 6546–6547 (2006).
62. Kim, S. O., Sastri, C. V., Seo, M. S., Kim, J. & Nam, W. Dioxygen Activation and Catalytic Aerobic Oxidation by a Mononuclear Nonheme Iron(II) Complex. *J. Am. Chem. Soc.* **127**, 4178–4179 (2005).
63. Ghosh, A. *et al.* Catalytically Active μ -Oxodiiron(IV) Oxidants from Iron(III) and

Dioxygen. *J. Am. Chem. Soc.* **127**, 2505–2513 (2005).

64. Sankaralingam, M., Lee, Y.-M., Nam, W. & Fukuzumi, S. Selective Oxygenation of Cyclohexene by Dioxygen via an Iron(V)-Oxo Complex-Autocatalyzed Reaction. *Inorg. Chem.* **56**, 5096–5104 (2017).

65. Singh, K. K., Tiwari, M. k., Dhar, B. B., Vanka, K. & Sen Gupta, S. Mechanism of Oxygen Atom Transfer from Fe^V (O) to Olefins at Room Temperature. *Inorg. Chem.* **54**, 6112–6121 (2015).

66. Meyer, T. J., Huynh, M. H. V. & Thorp, H. H. The Possible Role of Proton-Coupled Electron Transfer (PCET) in Water Oxidation by Photosystem II. *Angew. Chem. Int. Ed.* **46**, 5284–5304 (2007).

67. McEvoy, J. P. & Brudvig, G. W. Water-Splitting Chemistry of Photosystem II. *Chem. Rev.* **106**, 4455–4483 (2006).

68. Lee, Y.-M. *et al.* Water as an Oxygen Source in the Generation of Mononuclear Nonheme Iron(IV) Oxo Complexes. *Angew. Chem. Int. Ed.* **48**, 1803–1806 (2009).

69. Kotani, H., Suenobu, T., Lee, Y.-M., Nam, W. & Fukuzumi, S. Photocatalytic Generation of a Non-Heme Oxoiron(IV) Complex with Water as an Oxygen Source. *J. Am. Chem. Soc.* **133**, 3249–3251 (2011).

70. Ellis, W. C., McDaniel, N. D., Bernhard, S. & Collins, T. J. Fast Water Oxidation Using Iron. *J. Am. Chem. Soc.* **132**, 10990–10991 (2010).

71. Panda, C. *et al.* Homogeneous Photochemical Water Oxidation by Biuret-Modified Fe-TAML: Evidence of Fe^V (O) Intermediate. *J. Am. Chem. Soc.* **136**, 12273–12282 (2014).

72. Das, A., Nutting, J. E. & Stahl, S. S. Electrochemical C–H oxygenation and alcohol dehydrogenation involving Fe-oxo species using water as the oxygen source. *Chem. Sci.* **10**, 7542–7548 (2019).

73. Wang, D. *et al.* Nonheme oxoiron(IV) complexes of pentadentate N5 ligands: spectroscopy, electrochemistry, and oxidative reactivity. *Chem Sci* **4**, 282–291 (2013).

74. Collins, M. J., Ray, K. & Que, L. Electrochemical Generation of a Nonheme Oxoiron(IV) Complex. *Inorg. Chem.* **45**, 8009–8011 (2006).
75. Groves, J. T., Haushalter, R. C., Nakamura, M., Nemo, T. E. & Evans, B. J. High-valent iron-porphyrin complexes related to peroxidase and cytochrome P-450. *J. Am. Chem. Soc.* **103**, 2884–2886 (1981).
76. Mandon, D. *et al.* Models for peroxidase compound I: generation and spectroscopic characterization of new oxoferryl porphyrin .pi. cation radical species. *Inorg. Chem.* **31**, 4404–4409 (1992).
77. Penner-Hahn, J. E. *et al.* Structural characterization of horseradish peroxidase using EXAFS spectroscopy. Evidence for Fe = O ligation in compounds I and II. *J. Am. Chem. Soc.* **108**, 7819–7825 (1986).
78. Hashimoto, S., Tatsuno, Y. & Kitagawa, T. Observation of the FeIV=O stretching Raman band for a ferryl porphyrin .pi. cation radical. *J. Am. Chem. Soc.* **109**, 8096–8097 (1987).
79. Fujii, H. Electronic structure and reactivity of high-valent oxo iron porphyrins. *Coord. Chem. Rev.* **226**, 51–60 (2002).
80. Costas, M. Selective C–H oxidation catalyzed by metalloporphyrins. *Coord. Chem. Rev.* **255**, 2912–2932 (2011).
81. Niwa, T. & Nakada, M. A Non-Heme Iron(III) Complex with Porphyrin-like Properties That Catalyzes Asymmetric Epoxidation. *J. Am. Chem. Soc.* **134**, 13538–13541 (2012).
82. Bell, S. R. & Groves, J. T. A Highly Reactive P450 Model Compound I. *J. Am. Chem. Soc.* **131**, 9640–9641 (2009).
83. Groves, J. T. & Watanabe, Yoshihito. The mechanism of olefin epoxidation by oxo-iron porphyrins. Direct observation of an intermediate. *J. Am. Chem. Soc.* **108**, 507–508 (1986).
84. Grapperhaus, C. A., Mienert, B., Bill, E., Weyhermüller, T. & Wieghardt, K.

Mononuclear (Nitrido)iron(V) and (Oxo)iron(IV) Complexes via Photolysis of [(cyclam-acetato)Fe^{III}(N₃)]⁺ and Ozonolysis of [(cyclam-acetato)Fe^{III}(O₃SCF₃)]⁺ in Water/Acetone Mixtures ‡. *Inorg. Chem.* **39**, 5306–5317 (2000).

85. Rohde, J.-U. Crystallographic and Spectroscopic Characterization of a Nonheme Fe(IV)=O Complex. *Science* **299**, 1037–1039 (2003).

86. Coggins, M. K., Zhang, M.-T., Vannucci, A. K., Dares, C. J. & Meyer, T. J. Electrocatalytic Water Oxidation by a Monomeric Amidate-Ligated Fe(III)–Aqua Complex. *J. Am. Chem. Soc.* **136**, 5531–5534 (2014).

87. de Oliveira, F. T. *et al.* Chemical and Spectroscopic Evidence for an FeV-Oxo Complex. *Science* **315**, 835–838 (2007).

88. Lyakin, O. Y., Bryliakov, K. P., Britovsek, G. J. P. & Talsi, E. P. EPR Spectroscopic Trapping of the Active Species of Nonheme Iron-Catalyzed Oxidation. *J. Am. Chem. Soc.* **131**, 10798–10799 (2009).

89. Lyakin, O. Y., Bryliakov, K. P. & Talsi, E. P. EPR, ¹H and ²H NMR, and Reactivity Studies of the Iron–Oxygen Intermediates in Bioinspired Catalyst Systems. *Inorg. Chem.* **50**, 5526–5538 (2011).

90. Lyakin, O. Y., Ottenbacher, R. V., Bryliakov, K. P. & Talsi, E. P. Asymmetric Epoxidations with H₂O₂ on Fe and Mn Aminopyridine Catalysts: Probing the Nature of Active Species by Combined Electron Paramagnetic Resonance and Enantioselectivity Study. *ACS Catal.* **2**, 1196–1202 (2012).

91. Lyakin, O. Y., Prat, I., Bryliakov, K. P., Costas, M. & Talsi, E. P. EPR detection of Fe(V)=O active species in nonheme iron-catalyzed oxidations. *Catal. Commun.* **29**, 105–108 (2012).

92. Van Heuvelen, K. M. *et al.* One-electron oxidation of an oxoiron(IV) complex to form an [O=Fe^V=NR]⁺ center. *Proc. Natl. Acad. Sci.* **109**, 11933–11938 (2012).

93. Schneider, L. *et al.* Visible-Light-Driven Oxidation of Organic Substrates with Dioxygen Mediated by a [Ru(bpy)₃]²⁺/Laccase System. *ChemSusChem* **8**, 3048–3051

(2015).

94. El Ghachtouli, S. *et al.* Dipyrinphenol–Mn(III) complex: synthesis, electrochemistry, spectroscopic characterisation and reactivity. *Dalton Trans.* **40**, 9090 (2011).
95. Ducloiset, C. *et al.* Monoanionic Dipyrin-Pyridine Ligands: Synthesis, Structure and Photophysical Properties: Monoanionic Dipyrin-Pyridine Ligands. *Eur. J. Inorg. Chem.* **2015**, 5405–5410 (2015).
96. Nishida, Y., Kino, K. & Kida, S. Crystal structures of low- and high-spin iron(III) complexes with quadridentate Schiff bases. *J. Chem. Soc. Dalton Trans.* 1157–1161 (1987).
97. Zang, Y. *et al.* Models for Nonheme Iron Intermediates: Structural Basis for Tuning the Spin States of Fe(TPA) Complexes. *J. Am. Chem. Soc.* **119**, 4197–4205 (1997).
98. Guillemot, M., Toupet, L. & Simonneaux, G. X-ray Crystallographic Structure of (*meso*-Tetraphenylporphinato)bis(phenylphosphinic methyl ester)iron(III) Perchlorate: A New High-Spin Six-Coordinate Ferric Porphyrin. *Inorg. Chem.* **35**, 6334–6336 (1996).
99. Mashiko, T., Kastner, M. E., Spartalian, K., Scheidt, W. R. & Reed, C. A. Six coordination in high-spin ferric porphyrins. A new structural type and models for aquomethemoglobin. *J. Am. Chem. Soc.* **100**, 6354–6362 (1978).
100. Zang, Y. *et al.* Models for Nonheme Iron Intermediates: Structural Basis for Tuning the Spin States of Fe(TPA) Complexes. *J. Am. Chem. Soc.* **119**, 4197–4205 (1997).
101. Draksharapu, A. *et al.* Ligand Exchange and Spin State Equilibria of Fe^{II} (N4Py) and Related Complexes in Aqueous Media. *Inorg. Chem.* **51**, 900–913 (2012).
102. Hoard, J. L., Cohen, G. H. & Glick, M. D. The Stereochemistry of the Coordination Group in an Iron(III) Derivative of Tetraphenylporphine. *J. Am. Chem. Soc.* **89**, 1992–1996 (1967).
103. Pawlicki, M. & Latos-Grażyński, L. Iron Complexes of 5,10,15,20-Tetraphenyl-21-oxaporphyrin. *Inorg. Chem.* **41**, 5866–5873 (2002).
104. Malek, Andrzej., Latos-Grazynski, Lechoslaw., Bartczak, T. J. & Zadło, Andrzej.

Reactions of the iron(III) tetraphenylporphyrin .pi. cation radical with triphenylphosphine and the nitrite anion. Formation of .beta.-substituted iron(III) porphyrins. *Inorg. Chem.* **30**, 3222–3230 (1991).

105. Wickramasinghe, L. D. *et al.* Iron Complexes of Square Planar Tetradentate Polypyridyl-Type Ligands as Catalysts for Water Oxidation. *J. Am. Chem. Soc.* **137**, 13260–13263 (2015).

106. Bhugun, I., Lexa, D. & Saveant, J.-M. Ultraefficient selective homogeneous catalysis of the electrochemical reduction of carbon dioxide by an iron(0) porphyrin associated with a weak Brønsted acid cocatalyst. *J. Am. Chem. Soc.* **116**, 5015–5016 (1994).

107. Bhugun, I., Lexa, D. & Savéant, J.-M. Catalysis of the Electrochemical Reduction of Carbon Dioxide by Iron(0) Porphyrins: Synergistic Effect of Weak Brønsted Acids. *J. Am. Chem. Soc.* **118**, 1769–1776 (1996).

108. *Standard potentials in aqueous solution.* (M. Dekker, 1985).

109. Chen, Z. *et al.* Concerted O atom-proton transfer in the O–O bond forming step in water oxidation. *Proc. Natl. Acad. Sci.* **107**, 7225–7229 (2010).

110. Chen, Z. *et al.* Nonaqueous Catalytic Water Oxidation. *J. Am. Chem. Soc.* **132**, 17670–17673 (2010).

111. Butter, E. N. N. Greenwood, A. Earnshaw: Chemistry of the elements. *Cryst. Res. Technol.* **20**, 662–662 (1985).

112. Wang, X., Wang, S., Li, L., Sundberg, E. B. & Gacho, G. P. Synthesis, Structure, and Catalytic Activity of Mononuclear Iron and (μ -Oxo)diiron Complexes with the Ligand 2,6-Bis(*N*-methylbenzimidazol-2-yl)pyridine. *Inorg. Chem.* **42**, 7799–7808 (2003).

113. Plowman, J. E., Loehr, T. M., Schauer, C. K. & Anderson, O. P. Crystal and molecular structure of the (μ -oxo)bis[aquobis(phenanthroline)iron(III)] complex, a Raman spectroscopic model for the binuclear iron site in hemerythrin and ribonucleotide reductase. *Inorg. Chem.* **23**, 3553–3559 (1984).

114. Takahashi, K., Nishida, Y., Maeda, Y. & Kida, S. Crystal structures and magnetism of

binuclear iron(III) complexes with a linear oxo-bridge, $[\text{Fe}_2\text{O}(\text{bbimae})_2\text{X}_2][\text{NO}_3]_2$ {bbimae = 2-[bis(benzimidazol-2-ylmethyl)amino]ethanol, X = Cl or NCS}. *J. Chem. Soc. Dalton Trans.* 2375 (1985).

115. Chin, D.-H., La Mar, G. N. & Balch, A. L. Mechanism of autoxidation of iron(II) porphyrins. Detection of a peroxo-bridged iron(III) porphyrin dimer and the mechanism of its thermal decomposition to the oxo-bridged iron(III) porphyrin dimer. *J. Am. Chem. Soc.* **102**, 4344–4350 (1980).

116. Chin, D.-H., Gaudio, J. D., La Mar, G. N. & Balch, A. L. Detection and Characterization of the Long-Postulated Fe- μ -Fe Intermediate in the Autoxidation of Ferrous Porphyrins. *J. Am. Chem. Soc.* **99**, 5486–5488 (1977).

117. McLendon, George., Motekaitis, R. J. & Martell, A. E. Kinetics and mechanism of μ -oxo dimer formation by ethylenediaminetetraacetatoiron(III) [FeEDTA]. *Inorg. Chem.* **15**, 2306–2308 (1976).

118. Kurtz, D. M. Oxo- and hydroxo-bridged diiron complexes: a chemical perspective on a biological unit. *Chem. Rev.* **90**, 585–606 (1990).

119. Wilkins, R. G. & Yelin, R. E. Kinetics of monomer-dimer interconversion of iron(III) ethylenediaminetetraacetate and related chelates. *Inorg. Chem.* **8**, 1470–1473 (1969).

120. Hong, S., Lee, Y.-M., Shin, W., Fukuzumi, S. & Nam, W. Dioxygen Activation by Mononuclear Nonheme Iron(II) Complexes Generates Iron–Oxygen Intermediates in the Presence of an NADH Analogue and Proton. *J. Am. Chem. Soc.* **131**, 13910–13911 (2009).

121. Avenier, F. *et al.* Photoassisted Generation of a Dinuclear Iron(III) Peroxo Species and Oxygen-Atom Transfer. *Angew. Chem. Int. Ed.* **52**, 3634–3637 (2013).

122. Iali, W. *et al.* A Ruthenium(II)-Copper(II) Dyad for the Photocatalytic Oxygenation of Organic Substrates Mediated by Dioxygen Activation. *Angew. Chem. Int. Ed.* **54**, 8415–8419 (2015).

123. Pellegrin, Y. & Odobel, F. Sacrificial electron donor reagents for solar fuel production. *Comptes Rendus Chim.* **20**, 283–295 (2017).

124. Mühlendorf, B. & Wolf, R. C-H Photooxygenation of Alkyl Benzenes Catalyzed by Riboflavin Tetraacetate and a Non-Heme Iron Catalyst. *Angew. Chem. Int. Ed.* **55**, 427–430 (2016).
125. Mühlendorf, B. & Wolf, R. Photocatalytic benzylic C–H bond oxidation with a flavin scandium complex. *Chem. Commun.* **51**, 8425–8428 (2015).
126. Lechner, R., Kümmel, S. & König, B. Visible light flavin photo-oxidation of methylbenzenes, styrenes and phenylacetic acids. *Photochem. Photobiol. Sci.* **9**, 1367 (2010).
127. Ismail, K. Z. & Weber, S. G. Tris(2,2'-bipyridine)ruthenium(II) as a peroxide-producing replacement for enzymes as chemical labels. *Biosens. Bioelectron.* **6**, 699–705 (1991).
128. Kitajima, N., Ito, M., Fukui, H. & Moro-oka, Y. Hydroxylation of Alkanes and Arenes using Molecular Oxygen. *J Chem Soc Chem Commun* **0**, 102–104 (1991).
129. Maid, H. *et al.* Iron Catalysis for In Situ Regeneration of Oxidized Cofactors by Activation and Reduction of Molecular Oxygen: A Synthetic Metalloporphyrin as a Biomimetic NAD(P)H Oxidase. *Angew. Chem. Int. Ed.* **50**, 2397–2400 (2011).
130. Jaafar, H., Vileno, B., Thibon, A. & Mandon, D. Tuning the conversion of cyclohexane into cyclohexanol/one by molecular dioxygen, protons and reducing agents at a single non-porphyrinic iron centre and chemical versatility of the tris(2-pyridylmethyl)amine $\text{TPAFe}^{\text{II}}\text{Cl}_2$ complex in mild oxidation chemistry. *Dalton Trans* **40**, 92–106 (2011).
131. Schugar, H. J., Walling, Cheves., Jones, R. B. & Gray, H. B. The structure of iron(III) in aqueous solution. *J. Am. Chem. Soc.* **89**, 3712–3720 (1967).
132. Vaidyalingam, A. & Dutta, P. K. Analysis of the Photodecomposition Products of $\text{Ru}(\text{bpy})_3^{2+}$ in Various Buffers and upon Zeolite Encapsulation. *Anal. Chem.* **72**, 5219–5224 (2000).
133. Sala, X. *et al.* The $\text{cis-}[\text{RuII}(\text{bpy})_2(\text{H}_2\text{O})_2]^{2+}$ Water-Oxidation Catalyst Revisited. *Angew. Chem. Int. Ed.* **49**, 7745–7747 (2010).
134. Buettner, G. R. The Pecking Order of Free Radicals and Antioxidants: Lipid

- Peroxidation, α -Tocopherol, and Ascorbate. *Arch. Biochem. Biophys.* **300**, 535–543 (1993).
135. Richardson, W. H., Montgomery, F. C., Yelvington, M. B. & O'Neal, H. E. Kinetics of the thermal decomposition of 3,3-diphenyl- and 3,3-dibenzyl-1,2-dioxetane. Consideration of stepwise and concerted mechanisms. *J. Am. Chem. Soc.* **96**, 7525–7532 (1974).
136. Boyd, J. D. & Foote, C. S. Chemistry of singlet oxygen. 32. Unusual products from low-temperature photooxygenation of indenenes and trans-stilbene. *J. Am. Chem. Soc.* **101**, 6758–6759 (1979).
137. *Organic Free Radicals*. vol. 69 (AMERICAN CHEMICAL SOCIETY, 1978).
138. Kalyanasundaram, K. Photophysics, photochemistry and solar energy conversion with tris(bipyridyl)ruthenium(II) and its analogues. *Coord. Chem. Rev.* **46**, 159–244 (1982).
139. Watanabe, T. & Honda, K. Measurement of the extinction coefficient of the methylviologen cation radical and the efficiency of its formation by semiconductor photocatalysis. *J. Phys. Chem.* **86**, 2617–2619 (1982).
140. Stradowski, C. Methylviologen cation radical as probe of oxygen diffusion through polymer. *J. Appl. Polym. Sci.* **41**, 2511–2512 (1990).
141. Thorneley, R. N. F. A convenient electrochemical preparation of reduced methylviologen and a kinetic study of the reaction with oxygen using an anaerobic stopped-flow apparatus. *Biochim. Biophys. Acta BBA - Bioenerg.* **333**, 487–496 (1974).
142. Bonazzola, L. *et al.* An ESR Study of Aromatic Olefin Radical Cations. *Bull. Chem. Soc. Jpn.* **63**, 347–352 (1990).
143. Dean, A. M. & Bozzelli, J. W. Hydrocarbon Radical Reactions with O_2 : Comparison of Allyl, Formyl, and Vinyl to Ethyl. *J. Phys. Chem.* **97**, 4427–4441 (1993).
144. Rosenthal, J., Pistorio, B. J., Chng, L. L. & Nocera, D. G. Aerobic Catalytic Photooxidation of Olefins by an Electron-Deficient Pacman Bisiron(III) μ -Oxo Porphyrin. *J. Org. Chem.* **70**, 1885–1888 (2005).
145. Rosenthal, J., Lockett, T. D., Hodgkiss, J. M. & Nocera, D. G. Photocatalytic

Oxidation of Hydrocarbons by a Bis-iron(III)- μ -oxo Pacman Porphyrin Using O₂ and Visible Light. *J. Am. Chem. Soc.* **128**, 6546–6547 (2006).

146. Chang, C. J. *et al.* Structural, Spectroscopic, and Reactivity Comparison of Xanthene- and Dibenzofuran-Bridged Cofacial Bisporphyrins. *Inorg. Chem.* **41**, 3102–3109 (2002).

147. Heyrovský, M. The electroreduction of methyl viologen. *J Chem Soc Chem Commun* 1856–1857 (1987).

148. Sawyer, D. T. & Valentine, J. S. How super is superoxide? *Acc. Chem. Res.* **14**, 393–400 (1981).

149. Nosaka, Y. & Nosaka, A. Y. Generation and Detection of Reactive Oxygen Species in Photocatalysis. *Chem. Rev.* **117**, 11302–11336 (2017).

150. Nam, W. Synthetic Mononuclear Nonheme Iron–Oxygen Intermediates. *Acc. Chem. Res.* **48**, 2415–2423 (2015).

151. Girerd, J.-J., Banse, F. & Simaan, A. J. Characterization and Properties of Non-Heme Iron Peroxo Complexes. *Struc Bond* **97**, 145–177 (2000).

152. Cho, J. *et al.* Structure and reactivity of a mononuclear non-haem iron(III)–peroxo complex. *Nature* **478**, 502–505 (2011).

153. Chen, K. & Que, L. cis-Dihydroxylation of Olefins by a Non-Heme Iron Catalyst: A Functional Model for Rieske Dioxygenases. *Angew. Chem. Int. Ed.* **38**, 2227–2229 (1999).

154. Oloo, W. N., Fielding, A. J. & Que, L. Rate-Determining Water-Assisted O–O Bond Cleavage of an Fe^{III}-OOH Intermediate in a Bio-inspired Nonheme Iron-Catalyzed Oxidation. *J. Am. Chem. Soc.* **135**, 6438–6441 (2013).

155. Gamba, I., Codolà, Z., Lloret-Fillol, J. & Costas, M. Making and breaking of the OO bond at iron complexes. *Coord. Chem. Rev.* **334**, 2–24 (2017).

156. Selke, M., Sisemore, M. F. & Valentine, J. S. The Diverse Reactivity of Peroxy Ferric Porphyrin Complexes of Electron-Rich and Electron-Poor Porphyrins. *J. Am. Chem. Soc.* **118**, 2008–2012 (1996).

157. Samuel, D. & Silver, B. L. Oxygen Isotope Exchange Reactions of Organic Compounds. in *Advances in Physical Organic Chemistry* vol. 3 123–186 (Elsevier, 1965).
158. Oloo, W. N. & Que, L. Bioinspired Nonheme Iron Catalysts for C–H and C=C Bond Oxidation: Insights into the Nature of the Metal-Based Oxidants. *Acc. Chem. Res.* **48**, 2612–2621 (2015).
159. Puri, M., Company, A., Sabenya, G., Costas, M. & Que, L. Oxygen Atom Exchange between H₂O and Non-Heme Oxoiron(IV) Complexes: Ligand Dependence and Mechanism. *Inorg. Chem.* **55**, 5818–5827 (2016).
160. Feng, Y., England, J. & Que, L. Iron-Catalyzed Olefin Epoxidation and cis-Dihydroxylation by Tetraalkylcyclam Complexes: the Importance of cis-Labile Sites. *ACS Catal.* **1**, 1035–1042 (2011).
161. Rosenthal, J., Lockett, T. D., Hodgkiss, J. M. & Nocera, D. G. Photocatalytic Oxidation of Hydrocarbons by a Bis-iron(III)-μ-oxo Pacman Porphyrin Using O₂ and Visible Light. *J. Am. Chem. Soc.* **128**, 6546–6547 (2006).
162. Bernal, I. *et al.* Iron(II) complexes of polydentate aminopyridyl ligands and an exchangeable sixth ligand; reactions with peroxides. Crystal structure of [FeL¹(H₂O)][PF₆]₂·H₂O [L¹ = N,N'-bis-(6-methyl-2-pyridylmethyl)-N,N'-bis(2-pyridylmethyl)ethane-1,2-diamine]. *J Chem Soc Dalton Trans* 3667–3675 (1995).
163. Simaan, A. J., Banse, F., Girerd, J.-J., Wieghardt, K. & Bill, E. The Electronic Structure of Non-Heme Iron(III)–Hydroperoxo and Iron(III)–Peroxo Model Complexes Studied by Mössbauer and Electron Paramagnetic Resonance Spectroscopies. *Inorg. Chem.* **40**, 6538–6540 (2001).
164. Simaan, A. J. *et al.* Characterization of a Nonheme Mononuclear Peroxoiron(III) Intermediate by UV/Vis and EPR Spectroscopy and Mass Spectrometry. *Eur J Inorg Chem* 993–996 (1999).
165. Balland, V. *et al.* Spectroscopic Characterization of an FeIV Intermediate Generated by Reaction of XO⁻ (X = Cl, Br) with an FeII Complex Bearing a Pentadentate Non-Porphyrinic Ligand– Hydroxylation and Epoxidation Activity. *Eur. J. Inorg. Chem.* **2004**,

301–308 (2004).

166. Martinho, M. *et al.* Preparation and Characterization of a Microcrystalline Non-Heme FeIII(OOH) Complex Powder: EPR Reinvestigation of FeIII(OOH) Complexes—Improvement of the Perturbation Equations for the Tensor of Low-Spin FeIII. *Chem. - Eur. J.* **14**, 3182–3188 (2008).

167. Herrero, C. *et al.* Successive light-induced two electron transfers in a Ru–Fe supramolecular assembly: from Ru–Fe(II)–OH₂ to Ru–Fe(IV)–oxo. *Chem. Sci.* **6**, 2323–2327 (2015).

168. Approche électrochimique de l'activation réductrice du dioxygène à l'aide d'un complexe de fer(II) non hémique. Bohn, A., PhD defended the 7th of December 2018.

169. Balland, V. *et al.* Spectroscopic Characterization of an FeIV Intermediate Generated by Reaction of XO[–] (X = Cl, Br) with an FeII Complex Bearing a Pentadentate Non-Porphyrinic Ligand—Hydroxylation and Epoxidation Activity. *Eur. J. Inorg. Chem.* **2004**, 301–308 (2004).

170. Que, L. The Road to Non-Heme Oxoferryls and Beyond †. *Acc. Chem. Res.* **40**, 493–500 (2007).

171. Hitomi, Y., Arakawa, K. & Kodera, M. Electronic Tuning of Iron-Oxo-Mediated C–H Activation: Effect of Electron-Donating Ligand on Selectivity. *Chem. - Eur. J.* **19**, 14697–14701 (2013).

172. Mills, M. R., Weitz, A. C., Hendrich, M. P., Ryabov, A. D. & Collins, T. J. NaClO-Generated Iron(IV)oxo and Iron(V)oxo TAMLs in Pure Water. *J. Am. Chem. Soc.* **138**, 13866–13869 (2016).

173. Collman, J. P., Zeng, L. & Decréau, R. A. Multiple active oxidants in competitive epoxidations catalyzed by porphyrins and corroles. *Chem Commun* 2974–2975 (2003).

174. Collman, J. P., Chien, A. S., Eberspacher, T. A. & Brauman, J. I. Multiple Active Oxidants in Cytochrome P-450 Model Oxidations. *J. Am. Chem. Soc.* **122**, 11098–11100 (2000).

175. Draksharapu, A. *et al.* Identification and Spectroscopic Characterization of Nonheme Iron(III) Hypochlorite Intermediates. *Angew. Chem. Int. Ed Engl.* **54**, 4357–4361 (2015).
176. Cong, Z. *et al.* Synthesis, Characterization, and Reactivity of Hypochloritoiron(III) Porphyrin Complexes. *J. Am. Chem. Soc.* **134**, 20617–20620 (2012).
177. Costas, M. Selective C–H oxidation catalyzed by metalloporphyrins. *Coord. Chem. Rev.* **255**, 2912–2932 (2011).
178. Yusubov, M. S., Nemykin, V. N. & Zhdankin, V. V. Transition metal-mediated oxidations utilizing monomeric iodosyl- and iodylarene species. *Tetrahedron* **66**, 5745–5752 (2010).
179. Nam, W. *et al.* Reversible Formation of Iodosylbenzene±Iron Porphyrin Intermediates in the Reaction of Oxoiron(IV) Porphyrin π -Cation Radicals and Iodobenzene. *Angew. Chem.* **115**, 113–115 (2003).
180. Song, W. J., Sun, Y. J., Choi, S. K. & Nam, W. Mechanistic Insights into the Reversible Formation of Iodosylarene-Iron Porphyrin Complexes in the Reactions of Oxoiron(IV) Porphyrin π -Cation Radicals and Iodoarenes: Equilibrium, Epoxidizing Intermediate, and Oxygen Exchange. *Chem. - Eur. J.* **12**, 130–137 (2006).
181. Lennartson, A. & McKenzie, C. J. An Iron(III) Iodosylbenzene Complex: A Masked Non-Heme Fe^V O. *Angew. Chem. Int. Ed.* **51**, 6767–6770 (2012).
182. Wang, S. H. *et al.* Catalytic Sulfoxidation and Epoxidation with a Mn(III) Triazacorrole: Evidence for A “Third Oxidant” in High-Valent Porphyrinoid Oxidations. *J. Am. Chem. Soc.* **126**, 18–19 (2004).
183. de Sousa, D. P. *et al.* Halogen-Bonding-Assisted Iodosylbenzene Activation by a Homogenous Iron Catalyst. *Chem. - Eur. J.* **22**, 3810–3820 (2016).
184. Hong, S. *et al.* Highly Reactive Nonheme Iron(III) Iodosylarene Complexes in Alkane Hydroxylation and Sulfoxidation Reactions. *Angew. Chem. Int. Ed.* **53**, 6388–6392 (2014).
185. Wang, B., Lee, Y.-M., Seo, M. S. & Nam, W. Mononuclear Nonheme Iron(III)-Iodosylarene and High-Valent Iron-Oxo Complexes in Olefin Epoxidation Reactions. *Angew.*

Chem. **127**, 11906–11910 (2015).

186. Zilm, K. W., Merrill, R. A., Kummer, M. W. & Kubas, G. J. Characterization of transition-metal molecular hydrogen complexes by solid-state proton NMR. *J. Am. Chem. Soc.* **108**, 7837–7839 (1986).

187. Machii, K., Watanabe, Y. & Morishima, I. Acylperoxo-Iron(III) Porphyrin Complexes: A New Entry of Potent Oxidants for the Alkene Epoxidation. *J. Am. Chem. Soc.* **117**, 6691–6697 (1995).

188. Groves, J. T. & Watanabe, Yoshihito. Reactive iron porphyrin derivatives related to the catalytic cycles of cytochrome P-450 and peroxidase. Studies of the mechanism of oxygen activation. *J. Am. Chem. Soc.* **110**, 8443–8452 (1988).

189. Nielsen, A., Larsen, F. B., Bond, A. D. & McKenzie, C. J. Regiospecific Ligand Oxygenation in Iron Complexes of a Carboxylate-Containing Ligand Mediated by a Proposed FeV–Oxo Species. *Angew. Chem.* **118**, 1632–1636 (2006).

190. Decker, A., Rohde, J.-U., Que, Lawrence & Solomon, E. I. Spectroscopic and Quantum Chemical Characterization of the Electronic Structure and Bonding in a Non-Heme FeIVO Complex. *J. Am. Chem. Soc.* **126**, 5378–5379 (2004).

191. Nam, W., Lim, M. H. & Oh, S.-Y. Effect of Anionic Axial Ligands on the Formation of Oxoiron(IV) Porphyrin Intermediates. *Inorg. Chem.* **39**, 5572–5575 (2000).

192. Reedijk, J. The ligand properties of pyridine-N-oxide. Extension and discussion. *Recl. Trav. Chim. Pays-Bas* **88**, 499–512 (2010).

193. Kida, S., Quagliano, J. V., Walmsley, J. A. & Tyree, S. Y. Infra-red studies of pyridine N-oxide and its Co(II), Ni(II), Cu(II), Zn(II), Al(III), Cr(III), Fe(II), Fe(III) and Sn(IV) complexes in the 3–15 μ region. *Spectrochim. Acta* **19**, 189–199 (1963).

194. Mekmouche, Y., Toia-Duboc, C., Fontecave, M., Galey, J.-B. & Lebrun, C. H₂O₂-Dependent Fe-Catalyzed Oxidations: Control of the Active Species*. **40**, 949–952 (2001).

195. Biner, M., Büergi, H. B., Ludi, A. & Roehr, C. Crystal and molecular structures of [Ru(bpy)₃](PF₆)₃ and [Ru(bpy)₃](PF₆)₂ at 105 K. *J. Am. Chem. Soc.* **114**, 5197–5203 (1992).

196. Sheldrick, G. M. Program for Crystal Structure Solution. *Acta Crystallogr. A* **64**, (1997).
197. Sheldrick, G. M. A short history of *SHELX*. *Acta Crystallogr. A* **64**, 112–122 (2008).
198. Farrugia, L. J. *WinGX* suite for small-molecule single-crystal crystallography. *J. Appl. Crystallogr.* **32**, 837–838 (1999).
199. Johnson, K. A., Simpson, Z. B. & Blom, T. FitSpace Explorer: An algorithm to evaluate multidimensional parameter space in fitting kinetic data. *Anal. Biochem.* **387**, 30–41 (2009).
200. Johnson, K. A., Simpson, Z. B. & Blom, T. Global Kinetic Explorer: A new computer program for dynamic simulation and fitting of kinetic data. *Anal. Biochem.* **387**, 20–29 (2009).

Titre : Complexe de fer(III) semi-hémique bioinspiré pour les réactions chimiques et photochimiques de transfert d'atome d'oxygène

Mots clés : complexe de fer, activation de dioxygène, transfert de multi-électron, transfert d'atome d'oxygène, catalyses, photo-catalyses

Résumé : L'oxydation des hydrocarbures est une transformation chimique difficile aussi bien en biologie qu'en chimie. Les espèces active métal-oxo en de haut degré d'oxydation sont des intermédiaires capables d'effectuer ces transformations. Dans ce manuscrit, nous rapportons la synthèse et la caractérisation d'un complexe de fer (III) supporté par un ligand hémi-porphyrinique non innocent, construit avec un fragment dipyrriane et deux fonctions pyridines. Les complexes de fer (III) ont été préparés et caractérisés, en mettant l'accent sur leur comportement électrochimique et leur utilisation potentielle en tant que catalyseurs pouvant achever des sources d'oxygène vertes telles que le dioxygène et l'eau en vue d'oxyder des hydrocarbures. Nous avons constaté que ces complexes peuvent catalyser l'oxydation d'une grande variété de substrats en utilisant un agent oxydant tel que l'iodosylbenzène. Curieusement, nos résultats rassemblés suggèrent un schéma de réactivité

qui découle d'une espèce de fer de bas degré d'oxydation. Les analyses de résonance paramagnétique électronique et de Mössbauer confirment l'existence d'une espèce réactive de fer (III) haut spin. De plus, les données de spectrométrie de masse et de spectroscopie infrarouge appuyées par des calculs de DFT nous ont aidés à proposer la formulation chimique de cet intermédiaire généré chimiquement où le ligand a été oxydé de manière réversible. En outre, ces complexes ont été utilisés comme catalyseurs dans un système photocatalytique utilisant un accepteur d'électron réversible permettant d'éviter le recours néfaste à un donneur d'électrons sacrificiel. Notre étude fournit un nouveau paradigme pour effectuer des réactions photoinduites de transfert d'atome d'oxygène utilisant la lumière comme la source d'énergie et de l'O₂ comme la source d'atome d'oxygène en solution aqueuse.

Title : Bioinspired semi-hemic iron(III) complex for chemical and photochemical oxygen atom transfer reactions

Keywords : iron complex, dioxygen activation, multielectron transfer, oxygen atom transfer, catalysis, photocatalysis

Abstract : Hydrocarbon oxidation is a real challenging chemical transformation both in biology and chemistry. Highly oxidized metal-oxo species are the active intermediates to perform these transformations. In this manuscript we report the synthesis and characterization of an iron(III) complex supported by a non-innocent hemi-porphyrinic ligand, constructed with a dipyrriane fragment and two pyridine functions. The iron(III) complexes have been prepared and characterized, with a focus on their electrochemical behavior and their potential use as catalysts in the activation of green oxygen source such as dioxygen and water for hydrocarbon oxidation. We found that these complexes can catalyze the oxidation of a fair variety of substrates using oxidant agent such as iodosylbenzene.

Intriguingly, our gathered results point to a reactivity pattern that stems from a low-oxidation state iron species. Electron Paramagnetic Resonance and Mössbauer analyses support a high spin iron(III) reactive species. Furthermore, data from mass spectrometry and Infra-red spectroscopy supported by DFT calculations helped us to propose the chemical formulation of this chemically generated intermediate where the ligand has been reversibly oxidized. Additionally, these complexes were used as catalysts in a photocatalytic system using a reversible electron acceptor to preclude the "evil necessity" of a sacrificial electron donor. Our study provides a new paradigm to perform photoinduced oxygen atom transfer reactions with solely light as energy input and O₂ as oxygen atom source in aqueous solution.

